Table of Contents

List of Figures

List of Tables

Names and Formulas of Minerals

NAME	FORMULA
γ-Fe	Gamma-iron (Austenite)
α-Fe	Alpha-iron (Ferrite)
Awaruite	Ni, Fe
Biotite	$K(Mg, Fe)_3AlSi_3O_{10}(OH, F)_2$
Chalcocite	Cu_2S
Chalcopyrite	$CuFeS_2$
Chromite	$FeCr_2O_4$
Covellite	CuS
Digenite	$Cu_{9-x}S_5$
Feldspar	$(K, Ca, Na)AlSi_3O_8$
Heazlewoodite	Ni_3S_2
Idaite	Cu_3FeS_4
Intermediate solid solution	$(Cu, Fe)_xS$
Keilite	(Fe, Mg, Mn, Ca, Cr)S
Magnetite	Fe_3O_4
Millerite	NiS
Monosulfide solid solution	$(Fe, Ni)_{1-x}S$
Niningerite	(Mg, Fe, Mn, Ca, Cr)S
Pentlandite	$(Fe, Ni)_9S_8$
Plagioclase	$(Na, Ca)(Mg, Fe, Al)(Al, Si)_2O_6$
Pyrite	FeS_2
Pyroxene	$(Na, Ca)(Si, Al)_4O_8$
Pyrrhotite	$Fe_{1-x}S$
Troilite	FeS

List of Abbreviations

BSE	Back-scattered electron
CAF	Coal Ash Fusion
CaS	Calcium sulfide
CS_2	Carbon disulfide
Cu_2S	Copper sulfide
Cu_xFe_yS	Copper iron sulfide
EDS	Energy dispersive spectroscopy
EPMA	Electron probe micro analyser
FeNi	Iron nickel alloy
FeS	Iron sulfide
Fe_xNi_ySi	Iron nickel silicide
HG	High grade isostatically pressed dense graphite
ICP	Inductively coupled plasma
Matte-A	Amplats-Waterval matte
Matte-L	Lonmin matte
Matte-P	Amplats-Polokwane matte
Matte-S	Synthetic matte
MIC	Matte inside crucible
MOC	Matte outside crucible - penetrated matte
MPC	Micropore carbon
NiS	Nickel sulfide
OM	Optical microscope
PGM	Platinum group metals
SEM	Scanning electron microscope
SG	Low grade porous graphite
XRD	X-ray diffraction
XRF	X-ray fluorescence
XRM	X-ray micro tomography

List of symbols

Symbol	Description	Units
D	= pore diameter	m
g	= acceleration gravity	9.81 $m.s^{-2}$
h	= depth of the fluid	m
k	= thermal conductivity	$W.m^{-1}.K^{-1}$
l	= distance	m
q	= rate of energy transfer	$W.m^{-2}$
R_T	= thermal resistance	$K.W^{-1}$
T	= temperature	°C
t	= time	s
η	= viscosity of liquid	Pa.s
θ	= contact angle	°
ρ	= density	$kg.m^{-3}$
σ or ɣ	= surface tension/interfacial tension	$N.m^{-1}$

1 Introduction

1.1 Platinum group metals (PGMs)

The world's reserves of platinum group metals/elements (PGMs) are estimated at 100 million kilograms, of which over 80 percent is contained in South Africa's Bushveld Igneous Complex [Junge et al. 2015]. Summary of the PGMs reserves by country is shown in Table 1-1 [Jewell et al. 2015]. PGMs are a group of six elements namely; iridium, osmium, platinum, palladium, rhodium and ruthenium [Glaister et al. 2010]. PGMs together with gold and silver are classified as noble metals because of their high corrosion and oxidation resistance [Glaister et al. 2010, Xiao et al. 2004]. PGMs are used in a number of industrial processes and commercial applications, such as; automotives, jewellery, electronics, dentistry and investments amongst others [Jewell et al. 2015, Jones 2005].

Table 1-1: World's PGMs reserves [Jewell et al. 2015]

Country	PGM reserves (kg)
United states	900 000
Canada	310 000
Russia	1 100 000
South Africa	63 000 000
Other countries	800 000
World total (rounded)	66 000 000

The principal sources of PGMs are sulfide and arsenide minerals such as $PtAs_2$, PtS, (Pt, Pd)S, RuS_2, PdSb and elemental ruthenium [Xiao et al. 2004]. Noble metals together with cobalt (Co), copper (Cu), iron (Fe) and nickel (Ni) belong to the class of transition metals in the periodic table [Jones 2005]. Geologically, PGMs associate with base metal sulfides such as chalcopyrite ($CuFeS_2$), millerite (NiS), pentlandite $(Fe, Ni)_9S_8$, pyrite (FeS_2) and pyrrhotite ($Fe_{1-x}S$) [Xiao et al. 2004, Jones 1999]. Gangue minerals associated with PGM containing minerals are feldspar, biotite, plagioclase and pyroxene [Jones 1999]. To liberate the PGM-rich minerals from gangue minerals the PGM ore is crushed and milled prior to concentration processes

[Habashi 2002]. The milled PGM-ore is treated using gravity separators and flotation to produce a sulfide-rich PGM concentrate [Jones 2005, Mudd 2012]. To separate the PGM-rich sulfides from the gangue minerals, smelting is used. Rectangular six-in-line or circular three-electrode electric furnaces are typical in the PGM industry [Jones 1999]. During smelting of the PGM containing concentrate two liquid phases of distinct relative densities form, a lighter fayalitic-fosteritic ($[Mg, Fe]_2SiO_4$) slag and a denser matte. Matte is rich in iron-copper-nickel sulfides and it serves as a collector for PGMs [Liddell et al. 1986].

Due to high operating temperatures (1350 °C to >1600 °C) [Eksteen 2011] associated with PGM smelting the smelter has to be lined with refractories at the hot-face. To prolong the service life of the refractories, sufficient cooling of the refractories is required at the cold-face of the refractory wall. Copper waffle coolers are typically used on the cold-face of the refractories to extract heat away from the refractories [McDougall 2012]. Due to high operating temperature and corrosiveness of the PGM containing melt, failure of the copper waffle coolers has been experienced in PGM smelters in the upper sidewall region [Thethwayo 2010]. Failure of copper waffle coolers causes explosions, loss of production and costs associated with furnace rebuild. The failure of copper waffle coolers was preceded by the consumption of conventional refractory bricks (MgO_x-CrO_x) that were used to form the furnace lining. To prevent the occurrences of copper waffle cooler failures, conventional bricks have been replaced by the graphite blocks in recent designs of PGM smelter refractory walls. Graphite blocks are only applied at the hot-face upper sidewall (against the concentrate and the slag-zone). Graphite blocks have increased the service life of the copper waffle coolers [Thethwayo 2010]. It is desired to extend the graphite blocks to the lower sidewall of the PGM smelter refractory wall against the matte zone. There is virtually no data published on the behaviour of graphite when it is in contact with liquid PGM matte.

1.2 Aims of study

Owing to high infiltration of furnace melt in the slag-matte tidal zone (with graphite lined smelters), the refractory lining of the lower side wall has to be redesigned such that the refractory material at the hot-face has high resistance towards melt penetration. It is envisaged that using

carbon-based refractory at the hot-face of the matte zone (lower side-wall) will improve the service life of the furnace lining in PGM smelters.

The behaviour of graphite when in contact with liquid PGM matte has not been covered in the literature. The objectives of this work are the following:

- Determine the most prominent refractory-wear mechanism when selected carbon-based refractories are in contact with liquid PGM-furnace melt at typical furnace operating temperatures. In this context; prominent wear mechanism of a refractory is a wear mechanism that causes the most degradation/dissolution/penetration or erosion of a refractory.
- Determine the compatibility of carbon-based refractories (graphite and micropore carbon) with PGM melt (matte and slag).

1.2.1 Approach

The research question for this study is as follows:

"Which is the most prominent refractory wear mechanism when carbon-based refractories are exposed to a liquid PGM furnace melt?"

The research question is subdivided into 4 questions:

1. "Does a PGM melt (matte and slag) wet graphite?"
2. "What is the most prominent wear mechanism of graphite when graphite is exposed to a liquid PGM melt (matte and slag)?"
3. "Does matte form a protective frozen skull when graphite is cooled sufficiently?"
4. "Does a micropore carbon perform better than graphite when exposed to a PGM matte?"

To address the research questions wettability tests and crucible tests were performed.

Wettability of graphite by matte and slag was investigated by determining the contact angle between a refractory substrate and a molten droplet.

Crucible tests were executed to determine the compatibility of primary PGM matte with the carbonaceous refractory. Refractories tested were graphite and micropore carbon. Graphite was exposed to synthetic PGM matte, industrial PGM matte and industrial PGM slag. The micropore carbon was exposed to synthetic and industrial matte.

The interaction between the refractory and the primary matte and slag was assessed by measuring the following:

- The extent of matte and slag penetration through a refractory
- The dissolution of a refractory by the matte (change in liquid composition)
- The degree of erosion of a refractory at the matte-slag interface

1.2.2 Rationale and significance

The outcome of this work provides data on possible wear mechanisms of carbon-based refractories when they are exposed to a primary PGM matte and slag. Such data enables the smelter designers to make informed decisions as to which refractory is most compatible with a process. Such information prevents implementation of refractories that are incompatible with the melt; this leads to premature failures of the refractory wall and subsequent losses of production and incurred costs associated with furnace rebuilt. Based on the outcome of this study the current designs of PGM smelter refractory wall can be improved in a cost-effective way. The data on the behaviour of tested refractories and melt add to the body of knowledge since there is no data available on the open literature that addresses this topic. The study of the behaviour of industrial PGM matte provides answers to the phenomenon that are already observed in the smelters such as the deposition of matte species on the cold-face of the refractory.

1.2.3 Thesis organization

Section _ Title	***Contents***
1 _ Context and aims	The introductory information, aims, motivation, approach, relevance and significance of the study are discussed in this section.
2 _ Background	In this section the description of the PGM ore, PGM smelting process, challenges associated with the smelting of PGMs and the design of a typical PGM smelter sidewall are given,
3 _ Literature	Literature review contains the description of the refractories tested, the refractory wear mechanisms and refractory testing methods. Previous work on the interaction of carbon with sulfides and silicates is discussed. The sulfidation of silicates in the presence of carbon is also discussed. Foaming phenomenon of melts is discussed.
4 _ Materials and methods	Description of the analytical techniques used for the characterisation of materials is given in this section. The properties of the materials used for the test work (refractories, PGM matte and slag) are described. The apparatus used for the lab work, (coal ash fusion furnace and a vertical tube furnace) are described. Experimental procedures for all the tests done are outlined.
5 _ Results A	Results for wettability tests and crucible tests of graphite exposure to matte and slag are reported. The interaction of graphite with synthetic matte, industrial matte and industrial slag is reported. The effect of cooling graphite when exposed to industrial matte is reported in this section.
6 _ Results B	The interaction between a micropore carbon and matte (synthetic and industrial) is reported in this section.
7 _ Discussion	Results A and B are discussed in this section, the results are compared with the literature discussed in Section 3.
8 _ Conclusions and recommendations	The findings from this work are summarised in this section. The recommended actions based on the findings are discussed in this section.
9 _ References	The list of the bibliography used in this work is given in this section.
Appendix	The post-mortem analysis of a used graphite block is in Appendix A. The procedure and results for the synthesis of a CuFe-Al, S phase are in Appendix B. The matte penetration tests done on a CAF furnace are reported in Appendix C.

2 Background

2.1 The PGM ore

In South Africa, the PGM ore is mined in the western and eastern limb of the Bushveld Igneous Complex [Eksteen 2011]. Within the Bushveld Igneous Complex, the Merensky reef, Platreef and Upper Group 2 (UG2) reef are exploited for platinum production [Junge et al. 2015, Amplats annual report 2013, Forrest et al. 2006]. Merensky and Platreef have similar chemical and mineral composition [Nell 2004, Jones 2005]. These reefs typically have fairly low contents of total sulfides. UG2 differ from the two reefs, in that it has low nickel and copper content, and a large amount of $FeCr_2O_4$ (> 30 mass percent) [Xiao et al. 2004]. The Cr_2O_3 content in the Merensky and Platreef can be less than 1 mass percent [Nell 2004]. A typical mineralogy of the Merensky and UG2 from the western limb is shown in Table 2-1 (extract from Eksteen 2011).

Table 2-1: Sulfide and gangue mineralogy of the Merensky and the UG2 concentrates [Eksteen 2011]

	Western UG2	**Western Merensky**
Amphibole/tremolite/actinolite	2.3	4.1
Biotite/phlogopite	0.8	0.5
Carbonates and other minor minerals	0.4	0.3
Chalcopyrite	1.7	9.1
Chlorite	1.7	0.4
Chromite spinel	4.1	0.6
Clinopyroxene	6.1	6.1
Magnetite spinel	0.3	0.2
Olivine	0.2	0.1
Orthopyroxene	50.3	35.4
Other sulfides	0.3	0.8
Pentlandite	3.6	15.1
Plagioclase/anorthite	5.4	4.6
Pyrite	0.9	0.9
Pyrrhotite	0.8	16.7
Quartz	0.4	0.5
Serpentine	2.6	0.1
Talc	16.7	2.7

2.2 PGM ore processing: an overview

Typical process route for treating PGM ore is shown in Figure 2-1, [Habashi 2002, Hayes 2003], with the approximate PGM grade in each process (extracted from Jones 1999).

The PGM ore is initially crushed and milled to liberate the valuable minerals [Habashi 2002]. The milled PGM-ore is treated using gravity separators and flotation cells to produce a sulfide-rich PGM concentrate [Jones 2005, Mudd 2012].

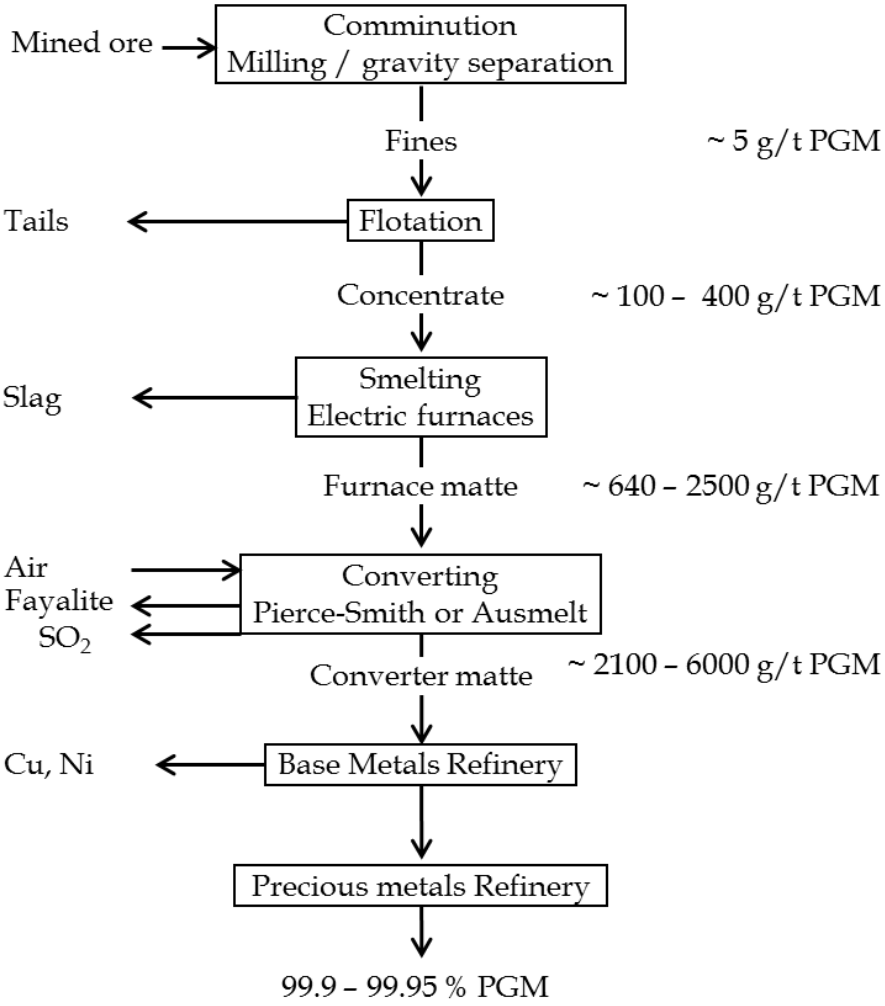

Figure 2-1: Typical process-flow diagram for a PGM-ore processing [Jones 1999]

Typical composition of UG2 and Merensky flotation concentrate is shown in Table 2-2 [extracted from Liddell et al. 1986]. The UG2 concentrate has a higher chrome content when compared to a Merensky concentrate as seen in Table 2-2. The UG2 concentrate also has a higher PGM content than the Merensky concentrate.

After the flotation step, the PGM concentrate from the flotation cells is dried and smelted to separate the sulfides from the silicates. After smelting, the furnace matte is treated in converters to remove iron and some sulfur by oxidation. Iron is removed as a fayalitic slag and sulfur is removed as sulfur dioxide [Jones 2005]. The converter matte is treated in the base metals refinery (BMR) to remove the copper, nickel and cobalt. The PGM concentrate from the BMR is treated in the precious metals refinery where PGMs are separated into final products. The current work focuses on the PGM-ore smelting process.

Table 2-2: Typical composition of the Merensky and the UG2 concentrate [Liddell et al. 1986]

	Al_2O_3	CaO	Cr_2O_3	Cu	FeO	MgO	Ni	S	SiO_2	PGM (g/t)
Merensky	1.6	2.2	0.3	2.1	22.3	18.2	3.2	9	41.4	100 - 250
UG2	5.0	2.4	2.9	0.8	12.6	21.0	1.7	3.6	44.0	300 - 600

2.3 PGM ore smelting

Smelting is a high-temperature process step where the sulfides (valuable minerals) are separated from the silicates (gangue minerals). The energy required for melting the concentrate is provided by Joule heating when an electric current is passed through the resistive slag [Habashi 2002].

Graphite electrodes are used for electrical connections between the power supply and the bath. Graphite electrodes are inserted into the resistive bath such that when a current is applied through the electrodes, thermal energy is generated [Jones 2005, Habashi 2002].

The feed ports are openings in the roof of the smelter through which the PGM concentrate is introduced into the smelter. The concentrate forms a thick bed (~400 mm) on top of the molten bath. The heat generated in the resistive bath causes the concentrate bed to melt gradually [Eksteen 2011].

The operating temperature of the smelter at the concentrate-zone can range from 600 °C to 900 °C [Eksteen et al. 2011]. The liquidus temperature of base metal sulfides associated with PGMs is 850 °C to 875 °C, whereas that of the corresponding silicates is approximately 1350 °C [Eksteen et al. 2011]. The sulfides in a PGM concentrate start melting at the concentrate bed since the temperature at the concentrate-zone can exceed the liquidus temperature of the sulfides.

The silicate minerals melt when they reach the molten bath (concentrate-slag interface). The silicates and sulfides are immiscible; upon melting they form two separate layers. The molten silicates and oxides form a slag layer while the PGM containing sulfides settle to form the matte layer [Eksteen et al. 2011].

The specific gravity of matte ranges from 4.8 to 5.6, that of slag ranges from 2.8 to 3.8 [Habashi 2002, Jones 2005]. Owing to the difference in specific gravities of matte and slag, the slag forms a top layer. Matte being denser than slag falls through the slag layer and settles underneath the slag. Matte consists of base metal sulfides (cobalt, copper, iron and nickel). Matte serves as a collector for the PGMs [Hayes 2003, Jones 2005].

Operating temperature of matte and slag varies with the composition of the concentrate [Eksteen 2011]. Typical smelter operating temperature for matte varies from 1380 °C to 1600 °C and that of slag varies from 1500 °C to 1680 °C [Eksteen 2011].

The molten slag and matte are tapped out of the smelter through the tap-holes situated at the end-walls of the furnace. After tapping the matte can either be fed directly to the converters as tapped or it can be granulated before the conversion step, matte treatment varies with the producers.

2.3.1 Industrial PGM-furnace matte

Anglo American Platinum (Amplats), Impala Platinum (Implats), and Lonmin are three major producers of PGMs in South Africa [Ryan 2014]. Typical compositions of matte from selected smelters are shown in Table 2-3. Matte from different smelters seems to have comparable amounts of major components (Cu, Fe, Ni and S). The slight difference is that the amount of iron in Amplats matte is slightly higher than the iron in a Lonmin matte (Table 2-3).

Table 2-3: Typical chemical composition of industrial matte from selected smelters (mass percent) [Jones 1999]

	Co	Cr	Cu	Fe	Ni	S
Amplats-Waterval	0.5	0.5	9.0	41.0	17.0	27.0
Lonmin-Merensky/UG2	0.5	0.2	9.7	37.0	17.0	28.0
Lonmin-UG2	0.5	0.3	9.8	35.0	17.0	28.0

2.3.2 Industrial PGM-furnace slag

Gangue minerals associated with PGM containing minerals are feldspar, biotite, plagioclase and pyroxene ($[Ca, Na]Al_{1-2}Si_{3-2}O_8$) [Jones 1999]. During smelting, these gangue minerals form a slag that is a silicate-rich liquid phase. Typical composition of the PGM-furnace slag from different smelters is shown in Table 2-4 [extracted from Jones 1999]. The oxide compounds in Amplats and Lonmin-Merensky slag are comparable, Lonmin-UG2 slag has higher Cr_2O_3, CaO and MgO, its FeO content is significantly lower when compared to the slag from Amplats and Lonmin-Merensky ore.

Table 2-4: Typical chemical composition of industrial slag from different smelters (mass percent)

	Al_2O_3	CaO	Co	Cr_2O_3	Cu	FeO	MgO	Ni	S	SiO_2
Amplats-Waterval	3.3	6.4	0.1	0.8	0.1	31.0	15.0	0.2	0.5	46.0
Lonmin-Merensky	2.0	9.8	0.1	1.2	0.1	28.0	19.0	0.2	0.0	44.0
Lonmin-UG2	3.9	13.0	0.0	2.4	0.1	9.2	22.0	0.1	0.0	47.0

2.3.3 Challenges associated with smelting high chromite concentrate

South African PGM producers generally process a Merensky concentrate where available; otherwise the Merensky and UG2 concentrates are blended together to achieve the required feed composition for the smelter. In recent years, the depletion of the Merensky reef has forced the PGM producers to mine the UG-2 reef that has up to 60 percent chromite. As a consequence, the flotation concentrate has higher chrome content than the chrome amount that the smelters are designed to handle. In reducing conditions, the operating temperature limits the solubility of Cr_2O_3 in a typical slag. At 1450 °C to 1650 °C the solubility of Cr_2O_3 in slag is limited to

1.8 mass percent. As such, the smelters have battled with numerous challenges owing to the treatment of a high chrome concentrate [Coetzee 2006]. The challenges associated with high chrome feed to the smelter are the following:

- Formation of chromite spinels which are insoluble in slag [Coetzee 2006]
- Chromite spinels have high melting points as such they increase the liquidus temperature of the slag and they lower the fluidity of the slag [Coetzee 2006]
- The operating temperature must be increased, as a consequence the overall temperature of the constituents (slag and matte) increases [Eksteen 2011, Hundermark et al. 2011]
- When the matte temperature is above the liquidus temperature of the slag freeze-lining, the matte dissolves the freeze-lining, this leads to corrosion of the refractories by corrosive matte and slag [Eksteen 2011, Hundermark et al. 2011]
- There are FeO based spinels and CrO based spinels, the proportion of Fe and Cr in the spinel may vary, as such there are spinels that have a higher density than the matte and the spinels that are slightly lighter than matte. Spinels which are denser than matte settle on the hearth, the accumulation of spinels on the hearth reduce the volume of the furnace [Eksteen 2011, Hundermark et al. 2011]
- Spinels with intermediate density form a "mushy" layer at the slag-matte interface, this leads to the entrainment of matte in slag, [Eksteen 2011, Hundermark et al. 2011]
- High chrome decreases electrical conductivity of the bath, this leads to electrical control problems in the furnace [Coetzee 2006]
- High chrome levels affect the matte temperatures during conversion step, matte temperatures above 1355 °C has been observed; this causes damage to the refractory lining. Cold dope (revert) is normally used to lower the temperature of the matte during conversion [Coetzee 2006, Eksteen et al. 2011]

A number of approaches have been investigated to deal with the chrome problem. The following actions have eased chromite problem in the smelters:

- Deep electrode immersion and operating at high power densities causes sufficient mixing which keeps the solids in suspension [Eksteen 2011, Liddell et al. 2012]. High power densities increases the operating temperature which adversely affect the refractory life [Coetzee 2006]

- Some producers stopped feeding the converter slag to the furnaces since the converter slag has high chrome content [Coetzee 2006, Hundermark et al. 2011]
- The flux addition in the furnace was discontinued, lower CaO levels increased the solubility of the chromite in the slag [Coetzee 2006, Hundermark et al. 2011]
- The control of furnace inputs and control of furnace parameters (power, furnace availability) is essential in controlling chrome content [Coetzee 2006]
- Selective reduction, improves the solubility of chromium in the slag [Nelson et al. 2005 in Hundermark et al. 2011]
- Tapping out the intermediate layer intentionally [Barnes et al. 2006]
- Decreasing the chromium input to the smelters [Hundermark et al. 2011]
- Another innovation able to manage chrome-rich ores is the ConRoast process. This process involves removing and capturing sulfur from the concentrate prior to smelting in a DC-arc furnace. Roasting a concentrate makes smelting more environmentally friendly; it also enables furnaces to accept any proportion of chromite, resulting in more efficient and cost-effective platinum production [Jones et al. 2011]. The ConRoast process is a radical departure from current practice, this process is not considered in this thesis.

2.4 PGM smelter

The smelting process is carried out in alternating current, electrical furnaces. Circular 3-electrode or rectangular 6-in-line electrode furnaces are used for PGM smelting [Eksteen et al. 2011, Jones 2005]. A schematic diagram of a typical PGM smelter is shown in Figure 2-2 (a) cross section of a 3-electrode circular furnace, (b) rectangular 6-in-line electrode furnace (extracted from King 1975).

A typical PGM smelter has a hearth, lower sidewall (matte zone), upper sidewall (slag-zone and feed/concentrate-zone) and a freeboard (roof) [McDougall et al. 2012]. The roof typically has electrode ports, view ports and feed ports. The electrode ports are where the electrodes enter the furnace. View ports are used during smelter visual inspections. Feed port is where the feed pipes enter the smelter.

The concentrate, slag and matte layers are annotated as such in Figure 2-2. The hearth is the base of the smelter. The matte tap-hole is placed above the hearth level while the slag tap-hole is placed just above the matte level; tap holes are indicated as launder in Figure 2-2(b) [King 1975].

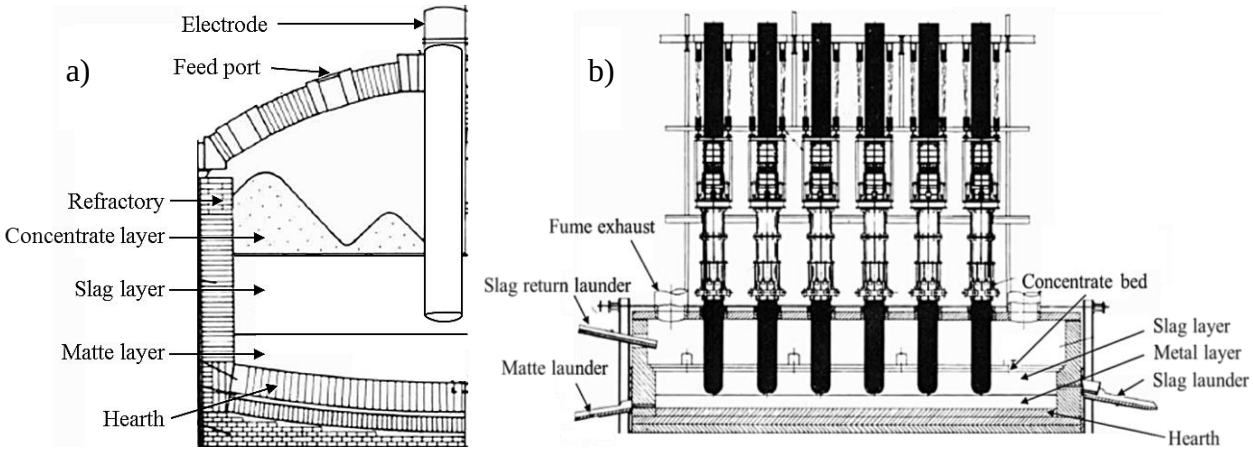

Figure 2-2: a) Typical circular 3-electrode, b) rectangular 6-in-line electrode matte-smelting furnace, the important features of the smelter are annotated in the diagrams [King 1975]

2.5 Sidewall lining design of a typical PGM smelter

In a smelter, lining is a system comprising of a shell, cooling medium, refractories and the process itself [Duncanson et al. 2004]. The insulating concept and the freeze-lining concept are refractory lining concepts that are adopted in industry. The insulating concept applies the mass versus time principle, the refractory is corroded over time, and the primary purpose is to protect the furnace shell. The refractory material with less than 20 percent carbon content is considered insulating [Duncanson et al. 2004]. In conventional designs of a typical PGM-smelter, an insulating lining concept is adopted in the design of a refractory-wall.

The refractory materials used in a typical PGM smelter wall differ from the roof to the hearth [McDougall et al. 2012]. In the conventional design alumina-silicate based refractory bricks are used at the freeboard, magnesia-chromium bricks are used at the hot-face of the upper side-wall, lower side-wall and the hearth. Water-cooled copper waffle coolers are used at the cold-face of the upper sidewall to extract the heat away from the refractories [McDougall et al. 2012].

2.5.1 Challenges with the conventional lining design (MgO_x-CrO_x brick)

Previously, MgO_x-CrO_x bricks were commonly used at the hot-face in front of the copper waffle coolers to provide insulation for the copper waffle coolers. This conventional lining design had short falls; the refractory brick at the hot-face of the upper-side wall had low resistance to chemical attack by liquid matte and slag. As such, the refractories used in PGM smelters had a short life span [Thethwayo 2010]. The insulating lining (MgO_x-CrO_x bricks) performed poorly when used in high operating temperatures associated with high chrome content of the smelter feed. The smelter designers are shifting to the application of the freeze lining concept in PGM smelter refractory wall design [Thethwayo 2010].

2.5.2 The freeze lining concept

The freeze lining refers to a system in which the lining has an ability to freeze the process materials and form a protective accretion "skull" on the hot-face of the refractory [Duncanson et al. 2004]. The formation of a frozen skull at the hot-face of a refractory is a function of the refractory temperature and the solidus temperature of the process material. The composition and thickness of the skull primarily depend on the process temperature and the rate at which the refractory can extract the heat away from the hot-face [Duncanson et al. 2004]. If the temperature at the hot-face of the refractory is below the freezing point of the process material, the process material begins to freeze forming a protective skull. If the temperature at the hot-face of the refractory is above the solidus temperature of the frozen skull, the protective skull starts melting and its thickness decreases [Duncanson et al. 2004]. For the frozen skull to be stable the hot-face temperature must be sufficiently below the solidus temperature of one or more of the process materials. The stable frozen skull protects the refractory and provides an insulating layer to maintain low temperatures. If refractory temperatures are kept low, refractory wear is prevented. The temperature dependency of the protective skull is summarised below;

$T_{hot} < T_{melt\ solidus}$; the melt freezes on the refractory surface forming a protective skull

$T_{hot} > T_{melt\ solidus}$; the protective skull melts.

For the protective layer to be stable there should be sufficient heat transfer from the hot-face to the cooling system. Thermal resistance through the lining should be low for the heat transfer through the refractory to be sufficient [Duncanson et al. 2004]. The following conditions must be met in a true freeze lining system: [Duncanson et al. 2004].

- Robust cooling system
- Refractory materials with high thermal conductivity
- Intimate contact between the cooling system and the refractory

Robust cooling is essential to sufficiently extract the heat from the hot-face such that the hot-face temperature is maintained below the liquidus temperature of the furnace contents [Duncanson et al. 2004]. Copper waffle coolers are used at the cold-face of the recent designs of the refractory wall of the PGM smelter. Copper waffle coolers provide cooling of the refractory, such that a frozen skull forms at the hot-face of the lining. The frozen skull prevents refractory wear by hot furnace contents [McDougall et al. 2012].

Carbon-based materials (such as graphite), offer low thermal resistance due to their relatively high thermal conductivity [Duncanson et al. 2004]. They have high refractoriness, moderate thermal expansion and high resistance towards chemical attack in reducing conditions [Tomala et al. 2007]. In this context, carbon-based materials refer to materials with >20 mass percent carbon [Duncanson et al. 2004].

2.5.3 The current design of a PGM smelter refractory wall (graphite block)

Graphite has replaced the MgO_x-CrO_x bricks in recent refractory wall designs of PGM smelters. A schematic diagram of a refractory-wall cross section is shown in Figure 2-3, this is a current design. Graphite is used at the hot-face upper sidewall of the refractory wall of the smelter as shown in Figure 2-3. Graphite is in contact with cooled copper waffle coolers. Copper waffle coolers have a base and knobs that protrude on both sides of the base. A typical matte zone refractory wall has a copper plate cooler in contact with the MgO_x-CrO_x brick [McDougall et al. 2012], other smelters have a rammable or a castable in the hot-face of the lower side-wall.

Graphite has performed very well at the upper sidewall of the refractory wall of the smelter. A graphite block used in a particular smelter was assessed after 6 months in operation

[Thethwayo 2010]. The graphite block was analysed from the top (feed level) to the bottom (slag-matte interface). BSE images of the graphite hot-face at the concentrate-slag interface and at the slag-matte interface are shown in Figure 2-4 and Figure 2-5 respectively.

At the graphite hot-face, the melt penetration was up-to 1 mm into the graphite wall. The melt penetration depth of 1 mm after six months exposure is considered minimal since it is not always possible to maintain the hot-face temperature below the solidus temperature of the melt. At the spaces between the graphite blocks, the melt penetration was up-to the cold-face of the graphite block [Thethwayo 2010].

In cooled refractories, there is a temperature gradient from the hot-face to the cold-face of the refractory. Liquid penetrant freezes when the refractory wall temperature falls below the solidus temperature of the penetrant. Liquid solidification creates a protective skull that causes the liquid penetration to cease [Carniglia et al. 1992, Lee et al. 1999 and Jansson et al. 2004]. Therefore, in the refractory in Figure 2-4 and Figure 2-5 the formation of the frozen skull was due to the efficient cooling of the lining which caused the melt to freeze at the hot-face.

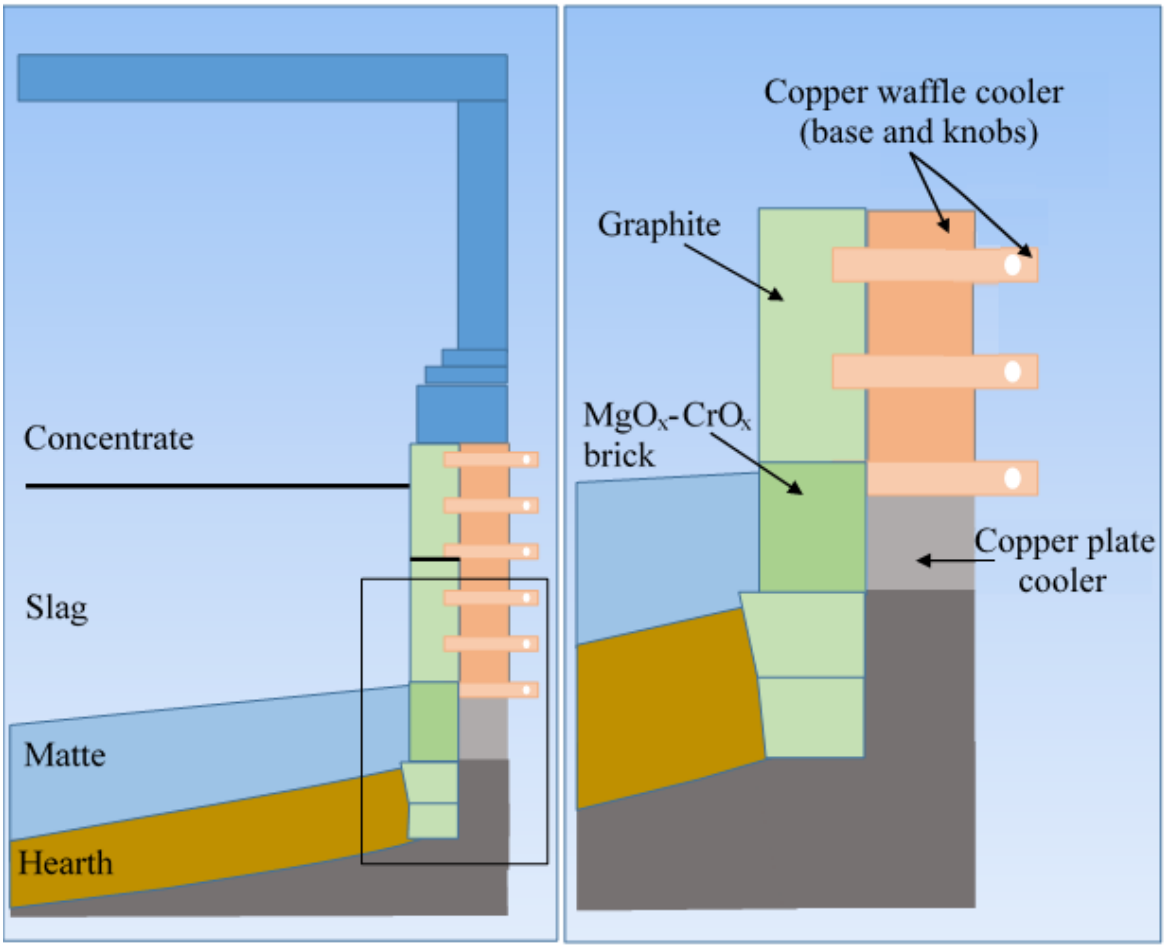

Figure 2-3: A cross-section of the current design of a PGM smelter refractory-wall: the cold-face is lined with copper waffle coolers at the upper-sidewall and copper plate cooler at the matte zone, the hot-face has graphite at the upper-sidewall and MgO_x-CrO_x brick at the matte zone [McDougall et al. 2012]

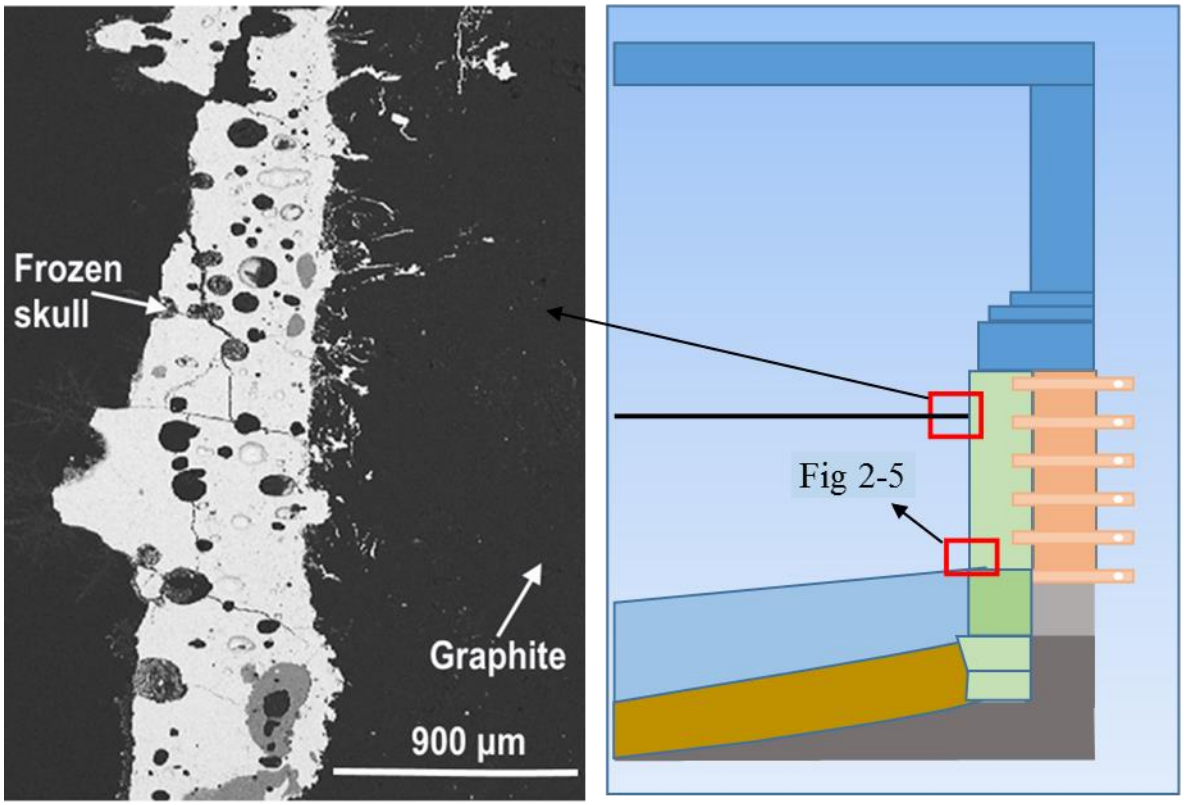

Figure 2-4: Graphite-lined refractory wall of a PGM smelter after 6 months in service at the hot-face of the upper-sidewall (concentrate-slag interface), on the left is the BSE image where a frozen skull and graphite are annotated, on the right is a schematic, the positions of the samples are annotated here [Thethwayo 2010]

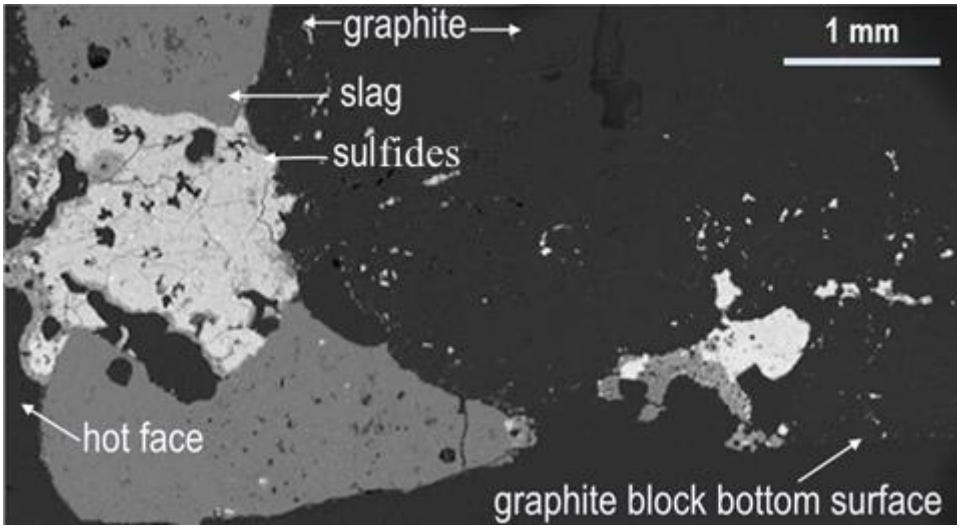

Figure 2-5: Graphite-lined refractory wall of the PGM smelter after 6 months in service at the hot-face (slag-matte zone) BSE image, the frozen skull and graphite are annotated [Thethwayo 2010]

2.5.3.1 The formation of a frozen skull at the hot-face of the graphite

To determine the mechanism of skull formation the elemental composition of the frozen skull (Figure 2-4 and Figure 2-5) was acquired using electron probe micro analyser (EPMA). The constituents of the frozen skull would differentiate whether the frozen skull formed as a result of the interaction of graphite with the melt (reduction) or deposition of the melt due to the surface temperature of the graphite [Thethwayo 2010]. The composition of the frozen skull is summarised in Table 2-5 [extracted from Thethwayo 2010].

Sulfide phases were abundant in the frozen skull at the feed-slag zone (Figure 2-4). Both slag and sulfide phases were detected in the frozen skull at the slag-matte zone (Figure 2-5). Metal phases were not detected in the frozen skull [Thethwayo 2010]. The frozen skull constituted the melt that solidified due to the surface temperature of the graphite that was lower than the solidus temperature of the melt. The composition and thickness of the skull (at the surface of graphite) varied with the depth of the refractory lining from the concentrate-zone (Figure 2-4) to the matte zone (Figure 2-5). The skull at the concentrate zone was thin (~1 mm) and at the base of the slag-matte interface the skull was thicker (~2 mm) [Thethwayo 2010].

The composition and thickness of the frozen skull depend on the hot-face temperature of the refractory [Duncanson et al. 2004]. Therefore the mechanism of the skull formation was a function of the temperature of the graphite hot-face and the composition of the melt.

Table 2-5: Composition of the frozen skull in Figure 2-4 and Figure 2-5, EPMA analysis (mass percent)

Ca	**Cr**	**Cu**	**Fe**	**Mg**	**Ni**	**S**	**Si**	**O**	**Stoichiometry**
-	-	-	25.0	-	28.0	47.0	-	-	$(Fe, Ni)_xS$
-	-	22.0	32.0	-	1.0	45.0	-	-	$(CuFe)_xS$
-	-	45.5	9.5	-	-	45.0	-	-	$CuFe_xS$
7.9	1.3	-	11.8	16.6	-	-	33.8	28.6	$(Mg, Fe, Ca)_xSiO_y$

Base metal sulfides start melting at the concentrate bed since the concentrate bed temperatures can exceed the liquidus temperature (875 °C) of the base metal sulfides [Eksteen 2011]. The highest projected temperature at the concentrate-zone is about 900 °C [Eksteen 2011].

The liquidus temperature of the silicates is about 1550 °C depending on the composition [Eksteen 2011], therefore the silicates remain solid at the concentrate-zone. The silicates start melting at the slag-zone where the operating temperature is higher (1550 °C) [Eksteen 2011].

A temperature gradient exists from the concentrate bed to the electrode tips and from the electrode tips to the hearth. The critical temperatures at different points in the PGM smelter are shown in Figure 2-6. In Figure 2-6, T_1, T_2 and T_3 are the operating temperatures at different levels inside the smelter; T_1 is at the concentrate level, T_2 is at the tip of the electrodes and T_3 is at the matte layer. T_h, T_m and T_c are estimated temperatures of the refractory wall; T_h is the hot-face temperature, T_m is the graphite-copper interface temperature, and Tc is the temperature at the cold-face of the copper waffle cooler.

The temperature of the graphite hot-face increases from the concentrate-zone to the slag-zone. At the concentrate-zone, the hot-face temperature is below the solidus temperature of the silicate phases. At the slag-zone, the hot-face temperature is above the solidus temperature of matte; as such matte phases will remain liquid at the graphite hot-face of the slag-zone. In contrast, the hot-face temperature of the slag-zone may be lower than the slag solidus temperature, therefore when slag comes in contact with the graphite hot-face it would solidify.

The proposed mechanism of skull formation in the graphite surface is summarised below;

$T_{h\text{-}1} < T_{\text{sulfide solidus}}$; sulfide solidifies

$T_{h\text{-}2} > T_{\text{sulfide solidus}}$; sulfide melts

$T_{h\text{-}2} < T_{\text{slag solidus;}}$ slag solidifies

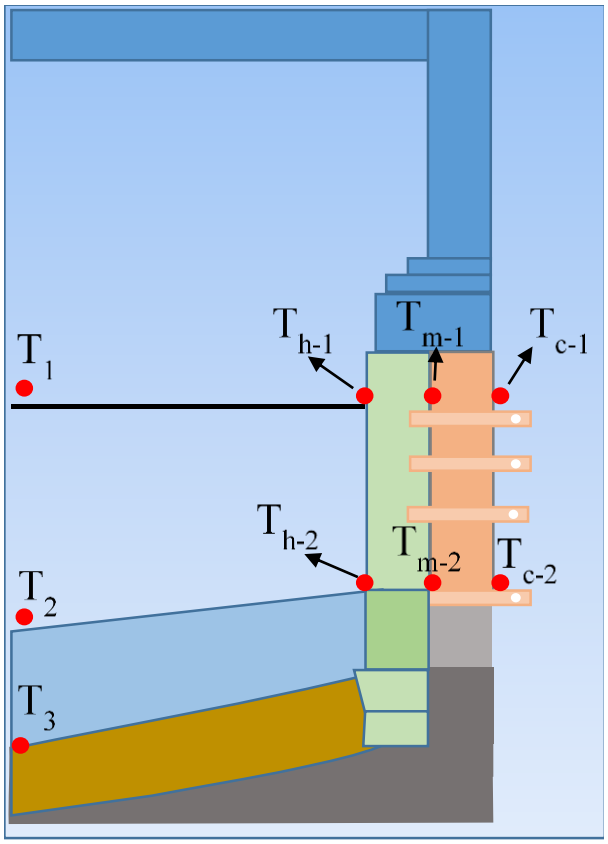

Figure 2-6: Critical temperatures in a typical PGM smelter, T_1= operating temperature at the concentrate-zone, T_2 = temperature at the tip of the electrodes (slag-zone), T_3 = temperature at the matte layer, T_h = hot-face temperature, T_m = temperature at graphite-cooler interface, T_c = cold-face temperature

2.5.3.2 Wear of graphite at the slag-matte interface

In cooled refractories there is a steep temperature gradient from the hot-face to the cold-face of the refractory [Carniglia et al. 1992, Lee et al. 1999 and Jansson et al. 2004]. The heat flux through the furnace lining can be estimated from Equation 1. Heat flux is the same through each component, therefore it can be used to calculate temperature drop in each component [Duncanson et al. 2004].

$$q = \frac{kA\Delta T}{l} \qquad \text{Equation 1}$$

q = rate of heat transfer (W), k = thermal conductivity ($W.m^{-1}.K^{-1}$), A = area of heat transfer (m^2), ΔT = temperature difference across a thermal system (K), l = distance of heat transfer (m), l/k = thermal resistance (R_T),

The temperature at the graphite-copper interface (T_{m_1} and T_{m_2} in Figure 2-6), was estimated using Equation 1. The parameters used for the calculation were the following,

k_{Cu} = 360 $W.m^{-1}.k^{-1}$, thickness of copper = 3.5 cm, $k_{graphite}$ = 150 $W.m^{-1}.k^{-1}$, thickness of graphite = 16 cm.

The assumptions for this calculation were the following: the cold-face temperature is 40 °C and the heat flux is at steady state. The estimated interface temperatures were as follows [Figure 2-6];

At T_{h_1} = 900 °C, T_{m_1} = 112 °C

At T_{h_2} = 1550 °C, T_{m_2} = 166 °C

Based on the calculated values of the graphite-copper interface temperature, the surface of the copper waffle cooler can be as hot as 166 °C at the slag-zone. It has been reported that at temperatures above 100 °C copper can be severely corroded by sulfur [Thethwayo 2010]. This indicates that when the sulfur vapour and sulfide gases get in contact with the surface of the copper, chemical reactions between the copper waffle coolers and the process gas will occur.

Proposed mechanisms for higher wear of graphite at the slag-matte interface are outlined below:

- High temperature at the slag-zone makes the environment conducive for reduction reactions between graphite and furnace melt
- The slag and matte levels move up and down during tapping. This area is therefore exposed to significant mechanical turbulence which can lead to refractory erosion [McDougall et al. 2012]
- Matte and slag have different chemical and thermal properties, for this reason, the frozen skull in the tidal zone may not form a stable thickness as it is constantly exposed to these phases. Eksteen discussed the solubility of oxides (CrO and FeO) in the matte [Eksteen 2011]. If there is a composition gradient between the frozen skull and the melt, and if the melt is not in equilibrium with the frozen skull, the frozen skull can be dissolved by the melt [Eksteen 2011].

- The slag is typically at a higher temperature than the solidus temperature of the frozen skull, in such a case the frozen skull will be dissolved by the melt.

2.5.3.3 Future design of the PGM smelter refractory wall

Due to the challenges observed with the current refractory lining design, it is desired to extend the graphite blocks to the matte layer as shown in Figure 2-7.

If graphite is compatible with the liquid PGM matte, graphite will be used as a refractory at the hot-face of the matte zone refractory wall. The copper waffle coolers will be used at the cold-face from the upper sidewall to the lower sidewall as drawn in Figure 2-7.

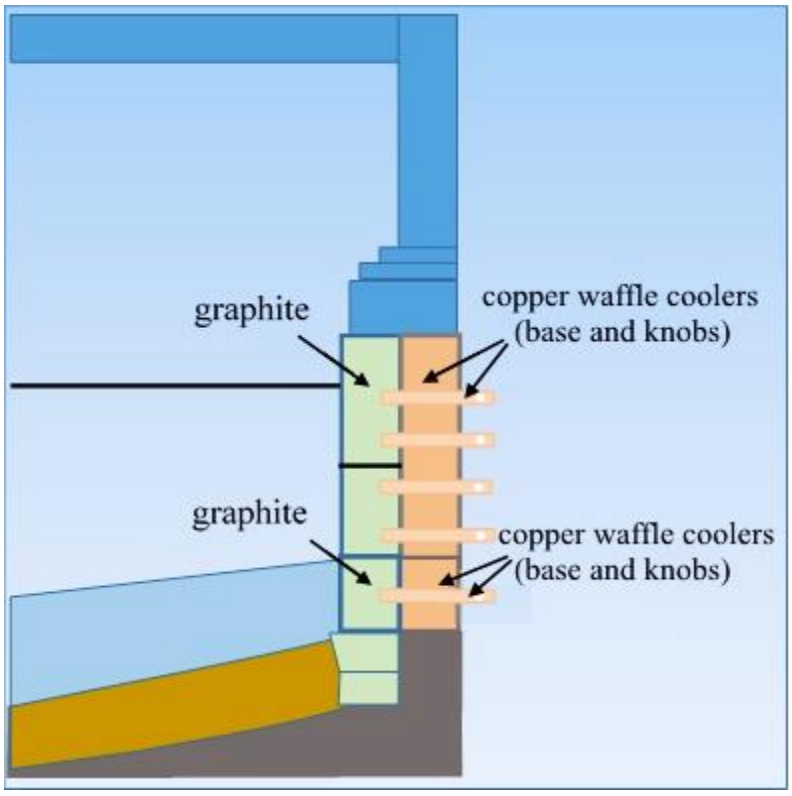

Figure 2-7: A cross-section of the PGM smelter refractory-wall: future design, graphite will be lined at the hot-face upper-sidewall and lower-sidewall; water-cooled copper waffle coolers will be lined at the cold-face upper-sidewall and lower-sidewall.

2.6 Summary

The background section entailed the description of the PGM ore, typical compositions of the PGM concentrate from various producers and an overview of the PGM ore processing. The smelting of PGMs, the layout of the smelter, the liquid smelting products and challenges associated with processing high chromite ore were discussed.

The focus of the current work is to determine the wear mechanisms of carbon-based refractories when in contact with a liquid PGM matte and slag. The challenges associated with the conventional refractory wall design have been discussed. The application of graphite on the upper sidewall of the PGM smelter has been successful, it is desired to extend the graphite lining to the lower sidewall of the PGM furnace refractory wall. The next section will review the literature on the selected refractories, the refractory testing methods, the properties of the matte and slag, the interaction of carbon with sulfides and silicates as well as the melt foaming phenomenon.

3 Literature

Application of graphite as a refractory in PGM smelters is a recent development. As such the open literature has limited data on the behaviour of carbon-based refractories when in contact with a PGM melt (matte and slag). Hence, the focus of the current work was to study the behaviour of graphite and micropore carbon when in contact with a liquid PGM melt (matte and slag).

The literature review covers the following topics:

- Refractories; the definition of refractories, the manufacturing processes of the refractories tested in this work, the refractory wear mechanisms, the prevention of refractory wear using cooling, and the refractory-wear testing methods.
- Factors affecting matte flow rate through a graphite tap-hole; the work done on this topic was reviewed with an aim of determining the parameters for the current work.
- Phase relations in the Cu-Fe-S and Fe-Ni-S system; the phase transformation in the Cu-Fe-Ni-S system was reviewed since the matte samples used in the current work are composed of the Cu-Fe-S and Fe-Ni-S compounds.
- The interaction of carbon with sulfides; the previous work done on the interaction of iron-nickel sulfide with carbon was reviewed since solubility of carbon in matte was one of the research questions in the current work. No literature was found on the interaction of carbon with iron-copper sulfide, but there is one reference to the solubility of carbon in a Cu-Fe melt and the effect of carbon solubility in the wettability of carbon by a melt.
- The interaction of sulfides with silicates in the presence of carbon; previous work done on the sulfide-silicate-carbon system was discussed in this section. This topic was relevant to the current work because the graphite was exposed to matte (sulfides) and slag (silicates), therefore the interaction between the sulfide and silicate in the presence of carbon had to be understood.
- Interaction of sulfides with gas bubbles; this section reviewed the conditions under which compound drops form and the effect of matte entrainment in gas bubbles. The release of process gas was expected during the exposure of matte to graphite, this topic was reviewed to understand what would happen when the matte came in contact with the gas.

- Melt foaming; this section reviewed the conditions that cause a melt to foam. Since slag and matte were in contact with graphite, formation of a CO gas was envisaged, hence studying the possibility of slag/matte foaming.

3.1 Refractories

Refractories are structural materials that can resist destructive forces at high temperatures. Refractories typically have high melting point in order to withstand high temperatures during application. Refractories can be classified as acidic (e.g. SiO_2), basic (e.g. CaO/MgO), or amphoteric (e.g. Al_2O_3 or Cr_2O_3). Amphoteric refractories can react with either an acid or a base. Graphite does not fall under any of these categories, it is a neutral refractory; it is chemically stable in contact with both acids and bases [Habashi 2002].

Graphite is one of the most refractory substances known, but it oxidizes at high temperatures, it is extensively used in metallurgical furnaces where oxidation can be controlled [Habashi 2002]. Graphite has a high thermal conductivity; it is not easily wetted by matte, and it can withstand high operating temperatures under reducing conditions [McDougall et al. 2012].

3.1.1 Carbon-based refractories

The carbon-based refractories tested in this work included extruded porous graphite (SG), isostatically pressed (dense) graphite (HG) and a micropore carbon (MPC). The aim of comparing these refractories was to identify the material most compatible with the liquid PGM furnace melt.

Criteria used to select these refractories were based on the performance of similar materials used in industry. SG graphite is used at the hot-face of recently designed refractory linings in PGM smelters at the upper sidewall [Thethwayo 2010]. HG graphite was tested for comparative reasons. Micropore carbon is used in steel making blast furnaces and it has improved the service life of these furnaces [Nitta et al. 2008]. The aim of testing a micropore carbon was to determine whether it will resist the liquid PGM matte thereby improving the integrity of the lining of the

PGM smelter. Typical manufacturing processes and properties of graphite and micropore carbon are discussed in turn.

3.1.2 Synthetic (moulded) graphite

Synthetic graphite is carbon material that has been treated at temperatures above 2700 °C. The raw materials used in making synthetic graphite are fillers, binders, impregnators and additives. Fillers are materials such as coke, recycled graphite, natural graphite and carbon black. They serve as aggregate in the synthetic graphite structure. Binders consolidate the aggregate particles. Coal-tar pitch and petroleum pitch are typical binders used in making synthetic graphite [Pierson 1993]. Typical production flow diagram for a moulded graphite is shown in Figure 3-1**.**

3.1.2.1 Manufacturing of a synthetic graphite

Fillers and binders are milled to the required particle sizes after which they are mixed and blended at typically 170 °C. The mixture is cooled to about 125 °C and moulded to shape. Three forming techniques used for moulding graphite are; extrusion, compression and isostatic pressing. Following forming, the binder is carbonized by heating the shapes to temperatures of up to 1200 °C in an inert atmosphere, this process is called carbonization. During carbonization, the product becomes porous due to the loss of volatile material. To achieve the required porosity and quality the product is impregnated with coal-tar pitch or polymers in a high-pressure autoclave. Impregnation and carbonization are repeated until the required properties are met. The products are treated at temperatures of up to 3000 °C in resistance or induction furnaces to convert the carbon to a graphitic structure. Graphitization increases the thermal and electrical conductivity of the material and the resistance to thermal shock and chemical attack. During graphitization puffing may occur, a condition in which the shaped graphite expands due to the release of volatile species. Puffing causes cracks and other structural defects [Pierson 1993]. The properties of the final product are influenced by the forming technique. Extrusion produces a non-uniform, anisotropic, low-cost material. Isostatic pressing produces a material with more uniform isotropic structure and fewer defects [Pierson 1993].

The extruded (low grade) graphite and an isostatically pressed (high grade) graphite were graphite types tested in this work. In this report the extruded graphite is denoted as SG and the isostatically pressed graphite is denoted as HG.

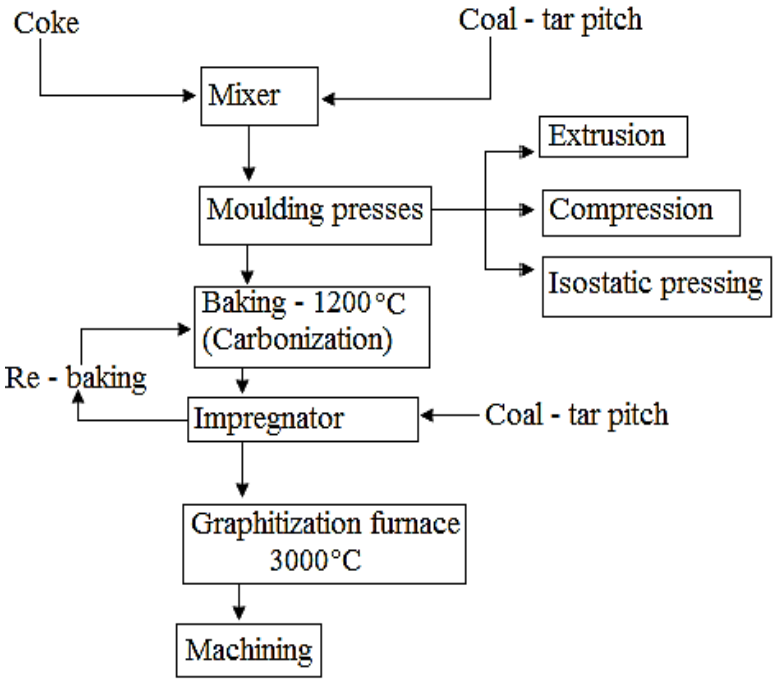

Figure 3-1: Typical production - process flow diagram for a moulded graphite [Pierson 1993]

3.1.3 Micropore carbon (MPC)

Carbon blocks have been used in blast furnace lining since the 19th century [Nitta et al. 2008]. Micropore carbon is a carbon-based material that is characterised by low porosity, high resistance to metal corrosion and high thermal conductivity. Micropore carbon has improved the service life of iron-producing blast furnaces [Nitta et al. 2008].

Micropore carbon was tested in this work to determine whether it can improve the service life of the refractory lining of the PGM producing smelters as it has performed well in the blast furnaces. Comparative tests were done to determine whether the MPC would perform better than the graphite.

3.1.3.1 Manufacturing of a micropore carbon

The original carbon block used in blast furnaces consisted of roasted anthracite and artificial graphite flakes that were bonded with tar [Nitta et al. 2008, Tomala et al. 2007]. Roasted anthracite forms the aggregate of the block; artificial graphite scraps or flakes are added to improve the thermal conductivity and the resistance of the block against alkali attack [Tomala et al. 2007, Chen et al. 2010]. Additives such as alumina compounds and fine ground silicon are added to the carbon block recipe to improve the properties of the block [Nitta et al. 2008, Tomala et al. 2007]. Alumina is resistant to acidic slag and mechanical wear. Addition of alumina improves the resistance of the block to erosion and dissolution by the liquid metal [Tomala et al. 2007]. Addition of elemental silicon in the carbon block mixture leads to the formation of silicon carbide (SiC) by the reactions between silicon and carbon. SiC forms during the baking of the mixture. Formation of SiC reduces the pore diameter of the block thus improving the microporous structure of the block [Nitta et al. 2008, Tomala et al. 2007, Chen et al. 2010]. Reduction of pore diameter increases the resistance of the block to penetration by a liquid metal [Nitta et al. 2008].

A typical manufacturing process of the MPC refractory involves premixing, shaping and curing of the components at 200 °C for 10 hours. The cured sample is put in an alumina crucible and then embedded in graphite, the sample is baked at 1400 °C for 3 hours at an air atmosphere [Chen et al. 2010].

3.1.4 Refractory wear mechanisms

Compatibility of a refractory with a liquid is defined as an ability of a refractory to resist penetration or chemical attack/dissolution by a liquid [Lee et al. 2004]. The best refractory should have a low solubility in a liquid melt, a high resistance to chemical attack and a high resistance to penetration by the liquid melt it is exposed to. Wear of a refractory material by a liquid can proceed through chemical attack and mechanical or physical wear. Chemical wear involves a combination of different mechanisms, such as penetration, dissolution [Lee et al. 2004] and oxidation-reduction reactions [Rigaud 2011]. Mechanical or physical wear involves erosion [Lee et al. 2004, Mills 2011].

3.1.4.1 Refractory penetration

Any liquid can penetrate a refractory if the liquid is highly fluid and there are openings (pores or cracks) on the refractory surfaces. Penetration of a liquid is dependent on the amount and size of surface pores (apparent porosity) as well as the presence of cracks. The corrosive liquid can only penetrate through a pore or a crack if the size of the pore or crack is larger than that of the minimum droplet size of the slag or glass at temperature (consideration of surface energies). The higher the temperature, the lower the viscosity of the liquid and the lower will be the minimum size droplet. Therefore higher temperature increases the chance of penetration [Sarkar 2017].

Physical penetration occurs when a strictly non-wetting liquid is forced into the pores of a solid by external forces such as gravity. Physical penetration is affected by the hydrostatic pressure and the viscosity of the liquid [Rigaud 2011, Lee et al. 2004, Jansson et al. 2004].

Physical penetration of a liquid can be quantified by using the expression in Equation 2 [Lee et al. 2004, Jansson et al. 2004]. Chemical penetration is when there is dissolution and physical penetration taking place [Lee et al. 2004, Jansson et al. 2004].

$$l^2 = \frac{(\sigma d \cos\theta)}{2\eta} t \qquad \text{Equation 2}$$

where l = penetration depth (m), σ = surface tension of the liquid ($N.m^{-1}$), d = pore diameter (m), θ = contact angle (°), η = viscosity of the liquid (Pa.s), t = time (s) [Lee et al. 2004, Jansson et al. 2004]

3.1.4.1.1 Factors that affect the penetration of a liquid through the refractory

Penetration of a refractory by a liquid is affected by the porosity (pore size), wetting, viscosity, surface tension, contact time, temperature and the composition of the liquid [Lee et al. 1999, Jansson et al. 2004, Silva et al. 2005, Carniglia et al. 1992]. Factors affecting penetration are discussed in turn.

a) Porosity

Porosity is a measure of the effective pore volume in the refractory into which the liquid can penetrate. The porosity of a refractory is expressed as the average percentage of pore volume in the total refractory volume. The resistance of a refractory to penetration by liquids is improved by reducing the open porosity of the refractory [Carniglia et al. 1992]. If the microstructure of the refractory has open joints, cracks or gaps the liquid invasion can be very rapid and to the full extent of the refractory wall. If the refractory has connected pores the liquid invasion can be rapid but it occurs progressively. If the refractory is chemically bonded or has matrix, the liquid invasion is moderate and progressive, it leads to debonding of the refractory
[Carniglia et al. 1992]

b) Wetting

Wetting is characterized by a contact angle between a solid refractory and a liquid. A contact angle of <90° is regarded as wetting and a contact angle which is >90° is "non-wetting". In general an increase in temperature will increase wettability [Bhoi et al. 2008, Yuan et al. 2013].

Sundström et al. 2008 has studied the effect of matte composition on the wettability of refractories by matte. They concluded that the contact angle between a matte and a substrate (refractory) increases with an increase in Ni_3S_2 concentration, whereas high FeS decreases the wetting angle between the matte and the substrate. Therefore wetting is not favoured by high Ni_3S_2 while high FeS favours the wetting of the refractory by a matte [Sundström et al. 2008]. Effect of Cu_2S on wetting was not reported in literature. The effect of dissolved carbon on wettability of carbon by a melt was discussed by Nizhenko et al. 1974, the increase in dissolved carbon increases the wetting angle between the carbon and the melt.

Reactive wetting is where there are reactions at the solid–liquid interface, dissolution of the solid into the liquid or formation of a new compound. The contact angle in such a system varies between two characteristic contact angles, the initial contact angle between the liquid and the unreacted substrate, as well as the final contact angle between the liquid and the reaction product [Eustathopoulos 2015].

For non-wetting liquids, infiltration is achieved by applying a sufficiently high pressure to overcome the capillary pressure. Equation 3 is the expression to calculate the capillary pressure for non-wetting liquids. In Equation 4 is the expression for differential pressure between the

capillary pressure and the applied pressure. If the liquid infiltration is limited by viscous friction an expression in Equation 5 is used to calculate the infiltration distance [Eustathopoulos 2015].

$$P_C = -(2\sigma_{LV}/r_{eff})\cos\theta \quad \text{Equation 3}$$

$$\Delta P = P_0 - P_C \quad \text{Equation 4}$$

$$h^2 = r^2_{eff}(\Delta P/4\eta)t \quad \text{Equation 5}$$

Where P_c is capillary pressure (Pa), P_o is applied pressure (Pa), r_{eff} is an effective pore radius (m), θ is the contact angle (°), σ is the surface tension of a liquid ($N.m^{-1}$), η is the viscosity of a liquid (Pa.s), t is contact time (s) and h is the infiltration distance (m). The infiltration distance (h) increases parabolically with both time (t) and excess pressure [Eustathopoulos 2015].

c) Viscosity

Viscosity is the measure of the fluid's resistance to flow; it is the ability of a liquid to resist movement of one layer of molecules over another when stress is applied [Mills 2011, Atkinson 2006].

The presence of solids in a melt increases its viscosity [Muller et al. 2011]. In a semi-solid melt, the fraction solid decreases with an increase in temperature [Atkinson 2006]; the increase in temperature decreases the viscosity [Muller et al. 2011].

Sundström et al. 2008 has studied the effect of composition and temperature on the viscosity of a sulfide melt. They observed that viscosity is highly dependent on temperature and the composition of the fluid. Viscosity increases with decreasing temperature [Sundström et al. 2008]. For the Cu_2S-Ni_3S_2 system, viscosity decreases with an increase in Ni_3S_2 up to 90 mass percent. The viscosity of the FeS-Cu_2S decreases with an increase in FeS till ~70 mass percent FeS. From 1190 °C to 1250 °C the viscosity of this system decreases with increasing temperature [Sundström et al. 2008].

The viscosity of the FeS-Ni_3S_2 system is an anomaly, at temperatures below 1190 °C it decreases with an increase in temperature, from 1190 °C to 1210 °C the viscosity of the FeS-Ni_3S_2

increases. From 1250 °C to 1500 °C the viscosity of FeS-Ni_3S_2 decreases from 2.8 x 10^{-3} to 2.2 x 10^{-3} Pa.s [Sundström et al. 2008].

The viscosity of the slag depends on the basicity of the slag and the temperature [Eric 2004]. The viscosity of Slag-A and Slag-L was estimated to be 0.4 Pa.s, the estimation is based on the work of Eric [Eric 2004]. Viscosity and surface tension are useful in the estimation of the penetration depth of the liquid.

d) Surface tension

Surface tension is the measure of the energy required to break the intermolecular cohesion forces acting on the surface of the fluid [Yuan et al. 2013]. Surface tension is referred concerning forces action on a gas/liquid interface. Interfacial tension is referred when the forces are acting in the interface between immiscible liquids or a liquid and a solid interface [Ip et al. 1992].

Surface tension in the Cu_2S-FeS-Ni_3S_2 system is sensitive to composition [Sundström et al. 2008]. Increase in sulfur content decreases the surface tension of a sulfide melt; sulfur has been shown to have the greatest influence on the surface tension of the nickel-iron matte [Sundström et al. 2008]. Addition of Cu and Ni to the FeS melt leads to an increase in the surface tension of the melt, increasing the iron content of a melt decreases surface tension. The addition of up to 3.9 mass percent oxygen has no effect on the surface tension of the FeS melt. Increase in metallization of a sulfide melt increases its surface tension [Sundström et al. 2008].

The dependency of the surface tension of sulfides on the temperature has been reported by Sundström et al. 2008. The surface tension of Cu_2S and that of FeS have a negligible dependence on temperature, while that of Ni_3S_2 decreases linearly with increasing temperature from 1100 °C to 1300 °C [Sundström et al. 2008, Hamuyuni et al. 2012].

At 1200 °C, the surface tension of Cu_2S, FeS and Ni_3S_2 is respectively 0.39, 0.326 and 0.494 $N.m^{-1}$ [Yan et al. 2000]. Surface tension affects the corrosive interaction of matte or slag with the refractory [Sundström et al. 2008].

Interfacial tension is a parameter that affects the interaction between immiscible liquids and liquid-solid interaction. Interfacial tension greatly affects the phenomenon such as entrainment of matte in slag and flotation of minerals with gas. If interfacial tension between a slag and a matte is low, slag can be entrained in matte, if the interfacial tension is high bubbles may become

entrapped in the metal phase resulting in defects in solidification such as pores [Sundström et al. 2008].

There is a lack of data on interfacial tensions pertinent to the slag-matte systems produced in the electric furnace, an indirect approach was adopted where interfacial tension was calculated using the available surface tensions [Eric 2004]. The surface tension of the slag was calculated from the expression in Equation 6, taken from Eric [Eric 2004]. The surface tension (σ) of Amplats slag (Slag-A) and Lonmin slag (Slag-L) is respectively 0.39 $N.m^{-1}$ and 0.4 $N.m^{-1}$.

$$\sigma = 570X_{FeO} + 285X_{SiO_2} + 640X_{Al_2O_3} + 614X_{CaO} + 512X_{MgO} \quad \text{Equation 6}$$

e) Contact time

The penetration of a liquid through a refractory increases with increasing contact time. As the penetration progresses the properties of the liquid may change, e.g. if there is a temperature gradient from the hot-face to the cold-face the penetrant may freeze when it gets to lower temperatures and the penetration will stop even if the contact time is increased. Therefore the penetration rate may change with an increase in contact time [Carniglia et al. 1992].

f) Temperature

Temperature affects the properties of the melt such as viscosity and surface tension amongst others, temperature has an indirect influence on wettability through its influence on the properties of the melt [Lee et al. 1999, Jansson et al. 2004, Silva et al. 2005, Carniglia et al. 1992]. The higher the temperature the lower the viscosity of the liquid and the higher the chances of penetration [Sarkar 2017, Lee et al. 1999]. Generally, corrosion of the refractories by a melt can be prevented if the temperatures are kept low [Duncanson et al. 2004].

g) Composition of the melt

According to Vollmann et al. 2013, a high composition-gradient between the melt and the refractory enhances mass transfer between the refractory and the melt that leads to the corrosion of the refractory. In the current work, the refractory used was graphite that is neutral; therefore the effect of the composition of liquid on its penetration through graphite should be negligible.

3.1.4.2 Refractory dissolution

The simplest case of pure dissolution is to consider the solid reacting with a liquid to form a product with new properties [Carniglia et al. 1992]. Dissolution of a refractory can lead to the consumption of the refractory [Jansson et al. 2004]. Dissolution of a refractory is a function of temperature, composition (refractory and liquid), flow conditions and liquid properties (viscosity, density, diffusivity) [Lee et al. 2004]. A refractory which is not readily wetted by a given process liquid also tends to resist dissolution by that liquid [Carniglia et al. 1992]. The effective liquid-solid wetting increases dissolution of the refractory by the wetting fluid [Rigaud 2011].

If the refractories have impurities or matrix phase they are more prone to chemical attack by a corrosive fluid. Chemical attack mainly proceeds through the matrix phase or grain boundary of the refractory microstructure [Sarkar 2017].

The factors affecting dissolution are similar to the factors affecting penetration, these have been discussed in the paragraphs above. Flow conditions can be ignored since dynamic tests were not done in the current work.

3.1.4.3 Erosion

Erosion of a refractory material by a liquid is associated with the motion of the liquid [Jansson et al. 2004]. It is caused by high-velocity liquids and gases [Jansson et al. 2004]. Refractories in industrial furnaces often exhibit an area of wear (deep groove) at the region between slag/metal and slag/gas interface, this is known as “slag line erosion”. Localised erosion at three-phase-contacts is often caused by an intense bath motion due to Marangoni effect [Mills 2011].

Marangoni convection is driven by the gradient in surface tensions [Mills 2011]. Marangoni effect induces a flow from low to high surface tension region, this flow results in a vortex. The upward flow is caused by the Marangoni effect, the backward–down flow happens when the gravity force is higher than the Marangoni flow. The vortex flow causes gradual erosion of the refractory at the slag-line [Mills 2011].

Vollmann et al. 2013 have done simulations to calculate the effect of Marangoni convections and forced convection on refractory corrosion of a dynamic system, they used computational fluid dynamics for their simulations. They reported that at low Reynolds numbers the Marangoni convections have a significant effect on the mass transfer between the refractory and the fluid, whereas at high Reynolds numbers the effect of the Marangoni convection is negligible [Vollmann et al. 2013].

Vollmann et al. 2013 compared the simulation data to the experimental work where silica-based slag was interacted with silica-based refractory. The silica content of the slag was varied such that the concentration gradient and surface tension gradient between slag and refractory existed. The rotation speed of the refractory rod was varied [Vollmann et al. 2013]. It was observed that there is a critical velocity below which Marangoni effect is ascertained, above this critical speed Marangoni convection does not have an effect on mass transfer between the melt and the refractory. The critical velocity increases with the decrease in concentration and surface tension gradients between the melt and the refractory. For dynamic systems, above critical velocity only forced convection (rotation) has an effect on mass transfer between refractory and melt.

Vollmann et al. 2013 concluded that Marangoni effect has the highest influence where high concentration and surface tension gradients exist. The groove at the three-phase contact indicates the contribution of Marangoni convection to corrosion. Forced convection is dominant at high rotational speeds; it is characterized by uniform corrosion [Vollmann et al. 2013].

In the current work, matte and slag were exposed to graphite simultaneously (in one crucible), there was a three-phase region slag/graphite/gas and slag/matte/graphite interface. As such, high concentration gradients and surface tension gradients were expected at these three-phase regions. Hence the discussion of possible refractory wear at three-phase regions.

3.1.5 Refractory-wear testing methods

Refractory wear testing methods have been discussed in literature [Dunkl 1994, Lee et al. 1999]. The description of the different methods and the methods used in this work are discussed in turn:

3.1.5.1 Dynamic methods

A dynamic testing method is where the fluid moves relative to the refractory [Lee et al. 1999, Dunkl 1994]. Types of dynamic testing methods are the following: rotating furnace test, rotating finger test [Dunkl 1994], and rotating slag test [Lee et al. 1999]. The advantage of dynamic tests is the ability to simulate flows of the melt relative to the refractory. It allows evaluation of refractory erosion. The draw back with the dynamic methods is that; it is relatively expensive, the evaluation of the geometric profile is difficult (wear profile changes with the depth of liquid) different flow velocities can be experienced with the depth of the specimen, as such dynamic tests have low reproducibility, [Tomala et al. 2007, Dunkl 1994].

3.1.5.2 Static methods

The static method is where the motion of the fluid is not simulated [Lee et al. 1999, Dunkl 1994]. Examples of static method tests are; crucible/cup/brick test, button or sessile drop, dipping/immersion/finger/plate test and induction furnace. Static methods are simple, economical and they have higher reproducibility than the dynamic tests. The draw back with the static method is that wear of the refractory due to the motion of the fluid cannot be evaluated [Lee et al. 1999, Dunkl 1994]. The static methods are discussed in turn:

3.1.5.2.1 Crucible/cup/brick test

A cored out refractory brick is filled with the test material and exposed at high temperature to promote interaction. Refractory wear is evaluated by measuring the change in the geometry of the cavity. Crucible test performed in the electrical furnace has the best reproducibility [Dunkl 1994]. The advantages of this method are the following:

- It is simple
- It has higher repeatability than other methods
- Chemical wear and structural spalling due to liquid penetration and densification can be evaluated [Lee et al. 1999, Dunkl 1994]

The draw back with the crucible test is the following:

- The temperature gradient through the refractory wall cannot be achieved, therefore, it does not fully resemble the typical industrial setup due to its isothermal nature.
- Rapid saturation of the refractory components in the melt is also a limitation [Lee et al. 1999, Dunkl 1994]

3.1.5.2.2 Button or sessile drop tests

Sessile drop method is the most used method for determination of wettability. A shaped material is placed on a refractory substrate and heated to its melting temperature [Eustathopoulos et al. 1999]. The interfacial contact angle between the solid and the molten droplet is an accepted measure of wettability [Siddiqi et al. 2000]. A schematic illustration of the sessile drop method and contact angle profiles are depicted in Figure 3-2 (a and b), where a contrast between the wetting system and the non-wetting system is illustrated (sketches taken from [Eustathopoulos et al. 1999]). By definition when the interfacial angle (between the solid and liquid) is <90°, the liquid wets the solid (Figure 3-2a) and when the interfacial angle is >90° the solid is non-wetted by the liquid (Figure 3-2b) [Eustathopoulos et al. 1999, Siddiqi et al. 2000].

For in-depth study of refractory-wear it is initially required to understand the mechanism of wetting when the refractory material is in contact with the liquid [Luz et al. 2008]. Wetting can be classified into physical wetting or chemical wetting [Bhoi et al. 2008]. In physical wetting, reversible physical forces, such as van der Waals and dispersion forces provide the attractive energy required to wet the surface. In chemical wetting, the reaction occurring at the solid-liquid interface is responsible for wetting [Bhoi et al. 2008].

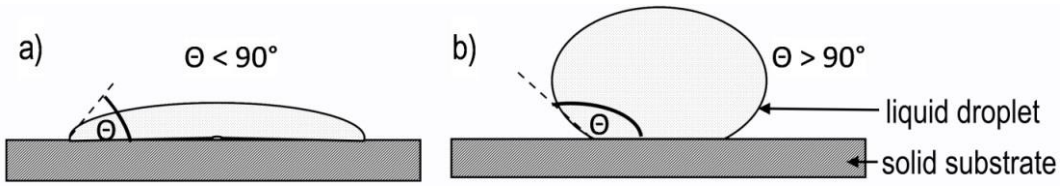

Figure 3-2: Schematic illustration of the solid-liquid profiles (a) contact angle <90° (wetting system), (b) contact angle >90° (non-wetting system) [Eustathopoulos et al. 1999]

The main factors which influence wetting behaviour are surface tension, operating temperature, liquid composition, roughness and surface heterogeneity of the substrate, contact time, test atmosphere as well as reactions between liquid and solid [Luz et al. 2008, Lee et al. 1999, Wu et al. 2000]. Surface tension is a function of temperature and composition of the liquid. A low surface tension enhances wetting [Lee et al. 1999, Wu et al. 2000].

The surface of the substrate should be smooth, flat, horizontal and chemically homogenous to prevent contact angle hysteresis (errors or variations in contact angle) [Luz et al. 2008].

Chemical reactions between the solid substrate and liquid can lead to the dissolution of the substrate into the droplet, or the formation of the reaction products at the interface [Luz et al. 2008]. Substrate dissolution and formation of interfacial product affect wettability and can change the value of the contact angle [Luz et al. 2008]. If the reaction product is soluble in the droplet, it will dissolve into the liquid melt [Lee et al. 2004].

With an increase in contact time, evaporation of material results in variations in contact angle and reduced droplet volume [Luz et al. 2008]. The fluctuation of the contact angle and the changes of the size of the droplet have been discussed by Shen and co-workers. They explained that the formation and evolution of the gas during the interaction causes the changes in the size of the droplet and the contact angle. When gas generation exceeds escaping rate, the gas could accumulate inside the droplet causing the droplet to inflate. Once the gas is released the droplet contracts [Shen et al. 2009].

Volatile or gaseous products result in mass loss due to the evaporation of gas [Lee et al. 2004]. Formation of gaseous products results in significant consumption of both the droplet and the substrate. This may result in the formation of a curvature at the droplet-substrate interface [Lee et al. 2004].

3.1.6 Prevention of refractory wear using cooling

Wear of refractories can be prevented if the temperature is kept low. If the hot-face temperature is kept below the solidus temperature of the process materials, the process materials freeze forming a protective layer. Refractories are cooled to facilitate the formation of the protective

layer at the hot-face. The protective layer prevents or retards the chemical attack of the refractory by the process material [Duncanson et al. 2004].

In the current work a test was done where a graphite crucible was cooled, this was to test whether a protective layer does form at the hot-face if the hot-face temperature is below the solidus temperature of the melt.

3.1.7 Summary

The literature review on refractories covered the description of the refractories, the manufacturing of the refractories used in this work, the wear mechanisms of refractories and the refractories testing methods. The refractories used in this work were SG graphite, HG graphite and MPC. These materials have not been used in contact with a PGM melt previously; hence the aim of this work is to determine their behavior when in contact with a PGM melt. As such there was virtually no data on the behavior of these refractories when in contact with PGM melt.

The wear mechanisms of refractories and the factors affecting the wear of refractories by the melt have been covered in the literature. Penetration, dissolution and erosion were the refractory wear mechanisms discussed. In the current work all these mechanisms were observed, the parameters deemed responsible for each mechanism are discussed under Section seven of this report.

According to the literature presented in this section factors affecting the refractory wear mechanisms are the following; the properties of the melt such as viscosity, surface tension and composition; the properties of the refractory such as porosity and the composition, the operating parameters such as contact time and temperature; as well as the wettability of the refractory by a melt. In the current work it is discovered that in physical penetration contact time and operating temperature have negligible effect on the penetration of liquid matte through the SG graphite, external pressure has the most effect on the extent of liquid matte penetration through the SG graphite. The three-phase region was the most eroded portion of the refractory when SG graphite was exposed to industrial matte; this means that gradient in surface tension has a significant impact on the erosion of graphite by a PGM melt.

Refractory wear testing methods have been discussed in literature. In the current work, crucible tests and wettability tests were the testing methods selected to determine the wear mechanisms of carbon-based refractories by a PGM melt. The porosity of the refractory, the operating temperature and the contact time were the parameters selected as variables in the current work. The current work confirms the effect of porosity, operating temperature and contact time on the wear of graphite by a PGM melt.

No work has been published on the effect of cooling graphite when it is exposed to a PGM melt. In this work it has been established that at static conditions a PGM matte can form a stable freeze lining.

The following section describes the previous work done where a graphite block was used at a tap-hole in a PGM smelter. This work was included in order to understand the important parameters when graphite is in contact with matte.

3.2 Factors affecting matte flow rate through a graphite block tap-hole

Snyders et al. 2006 has tested a graphite brick in a matte tap-hole. After a number of taps the brick had a crack. Where more than one bricks were lined in the tap-hole, the tap-hole was enlarged which necessitated replacement after few taps [Snyders et al. 2006]. On examination of the graphite brick, it was observed that matte penetrated the brick.

Snyders and co-workers modelled the tapping channel of a matte tap-hole using a graphite brick. They tested the effect of the matte tap-hole diameter, the temperature of the matte and the bath level on the matte flow rate through a tap-hole. The findings from the model are listed below, these findings were also tested in the plant and they corresponded to the model [Snyders et al. 2006].

- No relationship was observed between tap rate (ton/min) and matte temperature, the flowrate of matte out of a tap-hole did not vary with matte temperature.
- The hole diameter had a significant impact on the matte flow rate, the matte flow rate increased with the hole diameter.
- The matte-tapping rate increased with increasing bath levels (matte and slag levels) because of the increase in head pressure.

The findings from the work of Snyders and co-workers give basis for selecting the variables in the current work. Although their work was based on using graphite brick in a tap-hole, findings can still be applicable in this work in terms of the following:

The effect of matte temperature on the liquid penetration of matte through the graphite wall: Matte temperature should not affect the flow rate of liquid matte through the graphite wall. In their test work the matte penetrated the graphite brick, this means that the matte has the ability to penetrate the graphite under certain conditions.

3.3 Phase relations in the Cu-Fe-Ni-S system

PGMs associate with base metal sulfides such as chalcopyrite ($CuFeS_2$), millerite (NiS), pentlandite $(Fe, Ni)_9S_8$, pyrite (FeS_2) and pyrrhotite ($Fe_{1-x}S$) [Xiao et al. 2004, Jones 1999].

The components of these sulfides (Cu, Fe, Ni, S) can be described by two ternary systems, namely; Fe-Cu-S and Fe-Ni-S. These systems have to be considered in studying the phase transformations of the sulfides as a function of temperature.

The Cu-Fe-S and Fe-Ni-S ternary systems have been studied extensively [Starykh et al. 2012, Raghavan 2004]. Phase relations in each of the ternary systems are discussed in turn using phase diagrams. Phase diagrams typically depict the compositional information of condensed phases as a function of temperature.

3.3.1 Fe-Ni-S system

The condensed phases in the Fe-Ni-S system at 450 °C are presented in a phase diagram in Figure 3-3 [extracted from Vaughan et al. 1978]. At low temperatures (from 850 °C to 400 °C), this system is dominated by solid solutions namely; pentlandite solid solution, monosulfide solid solution and heazlewoodite solid solution [Starykh et al. 2012, Raghavan 2004]. For each solid solution the atomic fractions of Fe, Ni and S vary significantly [Sinyakova et al. 2001, Fabrichnaya et al. 2009].

A pentlandite is a Fe-Ni-S solid solution that takes a form $(Fe_zNi_{1-z})_{9+\delta}S_8$, its ideal composition is $(Fe_{4.5}Ni_{4.5})S_8$. There is a high pentlandite form and a low pentlandite form. High pentlandite is

stable between 865 °C and 584 °C [Fleet 2006]. The low pentlandite is stable from 615 °C to below 400 °C, its composition limits are as follows [Fleet 2006]:

$(Fe_{5.95}\ Ni_{3.07})S_8$ to $(Fe_{2.8}Ni_{6.55})S_8$ at 400 °C

$(Fe_{6.57}Ni_{2.82})S_8$ to $(Fe_{3.79}Ni_{5.45})S_8$ at 500 °C, including $(Fe_{4.5}Ni_{4.5})S_8$

Pentlandite is a metal-rich solid solution which is in equilibrium with a sulfur-rich monosulfide solid solution (mss) from 865 °C to 400 °C. Mss is a continuous solid solution at a sulfur atomic fraction of 50, it extends from pyrrhotite ($Fe_{1-x}S$) to $Ni_{1-x}S$ with a typical formula of $(Fe_zNi_{1-z})S_{1+\delta}$. Mss is stable from 1100 °C to below 400 °C [Fleet 2006, Starykh et al. 2012, Raghavan 2004].

Heazlewoodite (Ni_3S_2) is an end member of the heazlewoodite solid solution that is stable up to 565 °C. Heazlewoodite solid solution has a composition range of the form $(Fe_zNi_{1-z})_{3\pm\delta}S_2$ [Fleet 2006]. In the Ni-S system shown in Figure 3-4, Ni_3S_2 transforms to $Ni_{3\pm x}S_2$ solid solution at 565 °C [Kitakaze et al. 2011]. The $Ni_{3\pm x}S_2$ solid solution with 39.5 atomic percent of sulfur starts forming a liquid at 785 °C and is fully molten at 792 °C. A melting path for a typical Ni_3S_2 is highlighted with a dotted line in Figure 3-4.

The loss of sulfur by a sulfide drives the equilibrium to a metal Fe, Ni phase field in the Fe-Ni-S system [Vaughan et al. 1978]. In Figure 3-3 it can be seen that below 50 atom percent sulfur Fe,Ni is a stable phase. At 1200 °C Fe-Ni alloy is a stable phase at low sulfur partial pressure according to the Yazawa diagram presented by Willis and co-workers [Willis et al. 2009]. At temperature around 625 °C, pentlandite, monosulfide solid solution and iron-nickel alloy (taenite and kamacite) coexist [Kitakaze et al. 2011]. Therefore the Fe,Ni alloy is expected in the matte samples.

Pyrrhotite ($Fe_{1-x}S$) is a solid solution with sulfur varying from 50 to 55 atoms per 50 atoms of iron. In the ($Fe_{1-x}S$), x vary from 0 to 0.2 [Vaughan et al. 1978]. The Fe-S phase diagram is shown in Figure 3-5, from 950 °C to 1200 °C the $Fe_{(1-x)}S$ solid solution dominates. A typical melting path for a ($Fe_{1-x}S$) is highlighted in Figure 3-5.

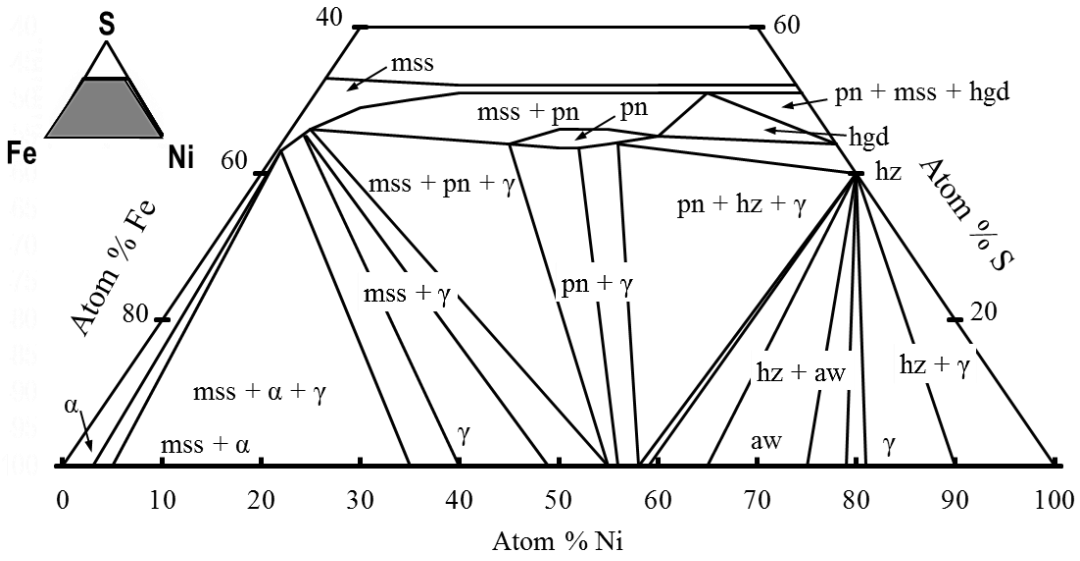

Figure 3-3: Phase relations in the central portion of the Ni-Fe-S system at 450 °C (atomic percent); aw-awaruite, mss_monosulfide solid solution, pn_pentlandite, hz_heazlewoodite, hgd_high pentlandite, γ_FeNi, α _Fe [Vaughan et al. 1978]

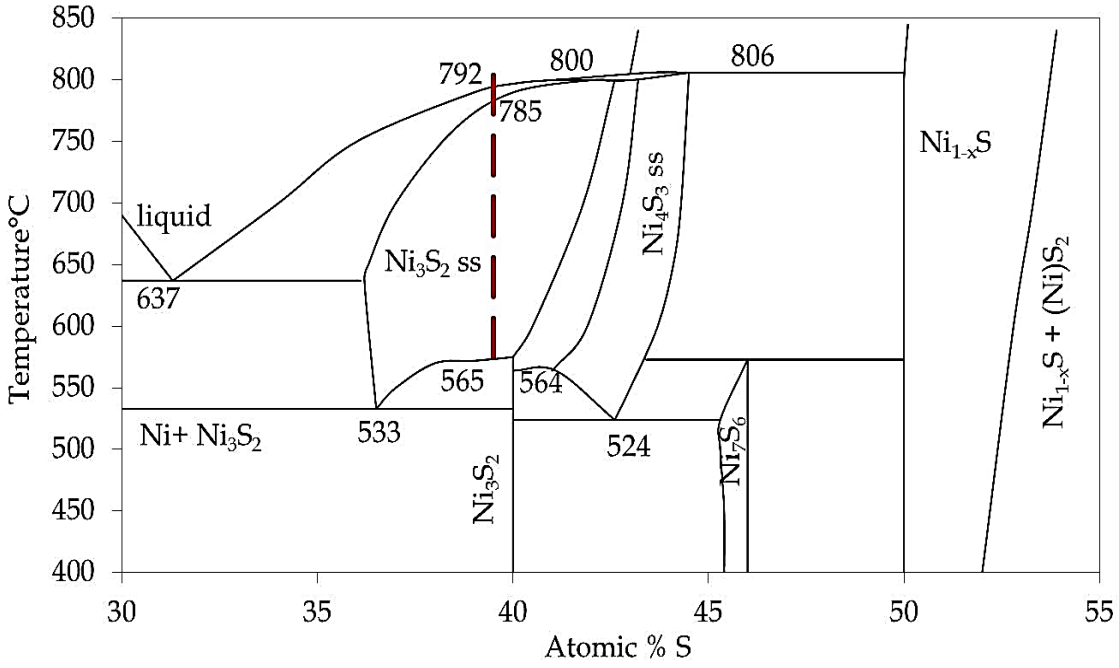

Figure 3-4: Phase relations among condensed phases in the Ni-S binary system (400 °C to 850 °C), (30 to 55) atomic percent S, a typical melting path of Ni_3S_2 is marked with a dotted line [Kitakaze et al. 2011]

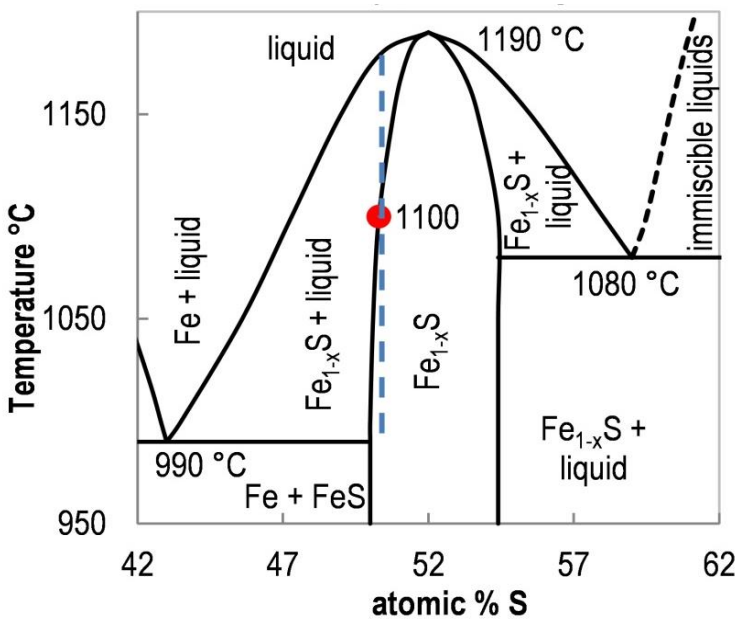

Figure 3-5: Phase relations among condensed phases in the binary system Fe-S, a melting path for $Fe_{1-x}S$ is highlighted with a dotted line [Vaughan et al. 1978]

3.3.2 Cu-Fe-S system

The Cu-Fe-S ternary system (Figure 3-6) has extensive fields of solid solutions including bornite (Cu_5FeS_4) solid solution at the Cu-S corner, chalcopyrite (intermediate solid solution) and pyrrhotite ($Fe_{(1-x)}S$) at the Fe-S end. Bornite is stable from 228 °C to 1100 °C, chalcopyrite ($CuFeS_2$) is stable up to 557 °C, and the intermediate solid solution (iss) extends from $CuFe_2S_3$ to $Cu_{1.1}Fe_{1.2}S_2$ [Fleet 2006].

Vaughan and co-workers have discussed the phase relations in the Cu-S system in Figure 3-7 [Vaughan et al. 1978]. In the Cu-S system, Cu_2S inverts to hexagonal chalcocite and high-digenite solid solution at 103.5 °C. A high-digenite solid solution has a composition ranging from Cu_2S to $Cu_{1.73}S$ [Vaughan et al. 1978]. From 813 °C to 1105 °C sulfur-rich high-digenite is in equilibrium with a sulfide melt, Cu_2S inverts to a sulfide melt at 1105 °C [Vaughan et al. 1978]. The dotted line highlights the melting path for a typical $Cu_{(2-x)}S$ such as used in the current work.

Iron metal and copper liquid are stable phases at the metal-rich portion of the Cu-Fe-S system at 1200 °C. Copper and iron are immiscible hence there is no Cu-Fe alloy in the Cu-Fe-S system [Willis et al. 2009].

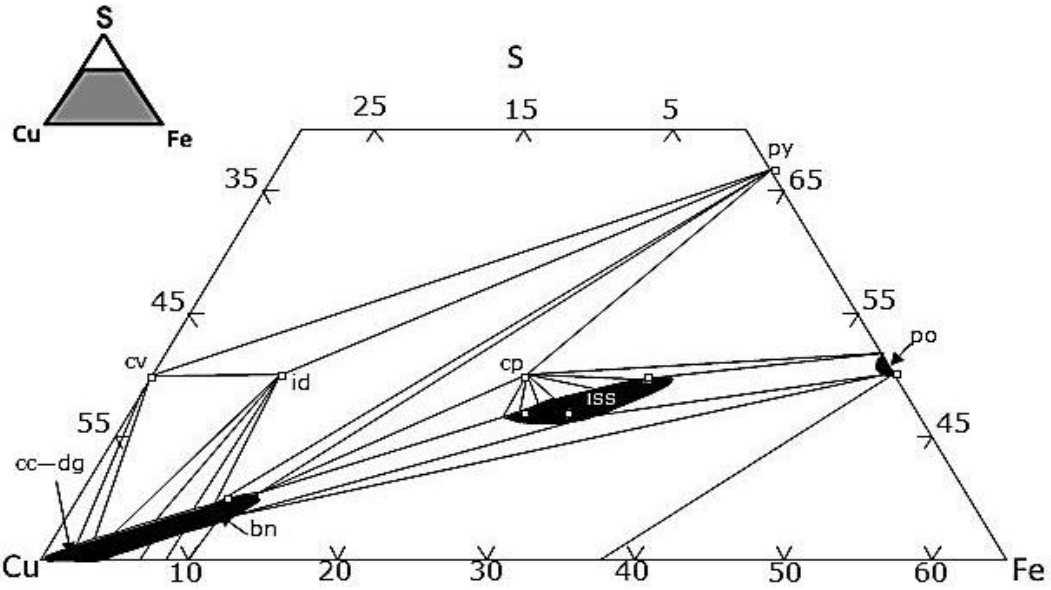

Figure 3-6: Phase relations in the central portion of the Cu-Fe-S system at 400 °C (atomic percent); [bornite_bn, chalcocite_cc, chalcopyrite_cp, covellite_cv, digenite_dg, idaite_id, pyrrhotite_po, pyrite_py, intermediate solid solution_iss]; [diagram extracted from Vaughan et al. 1978]

Extensive solid solutions that exist in the Fe-Ni-S and Cu-Fe-S systems cause the non-stoichiometry of phases in the sulfide sample. With an increase in temperature, the sulfide phases undergo phase transformations, therefore the sulfides in the PGM concentrate converts to their high-temperature form before they are molten. Koutsoyiannis 2012 discussed the relations between vapour pressure and temperature. He stated that for any substance vapour pressure increases with increasing temperature [Koutsoyiannis 2012]. As such, the vapour pressure of matte species is expected to increase as the operating temperature is increased above the melting point. Since our crucibles have appreciable porosity, the escape of the vaporised matte species is envisaged.

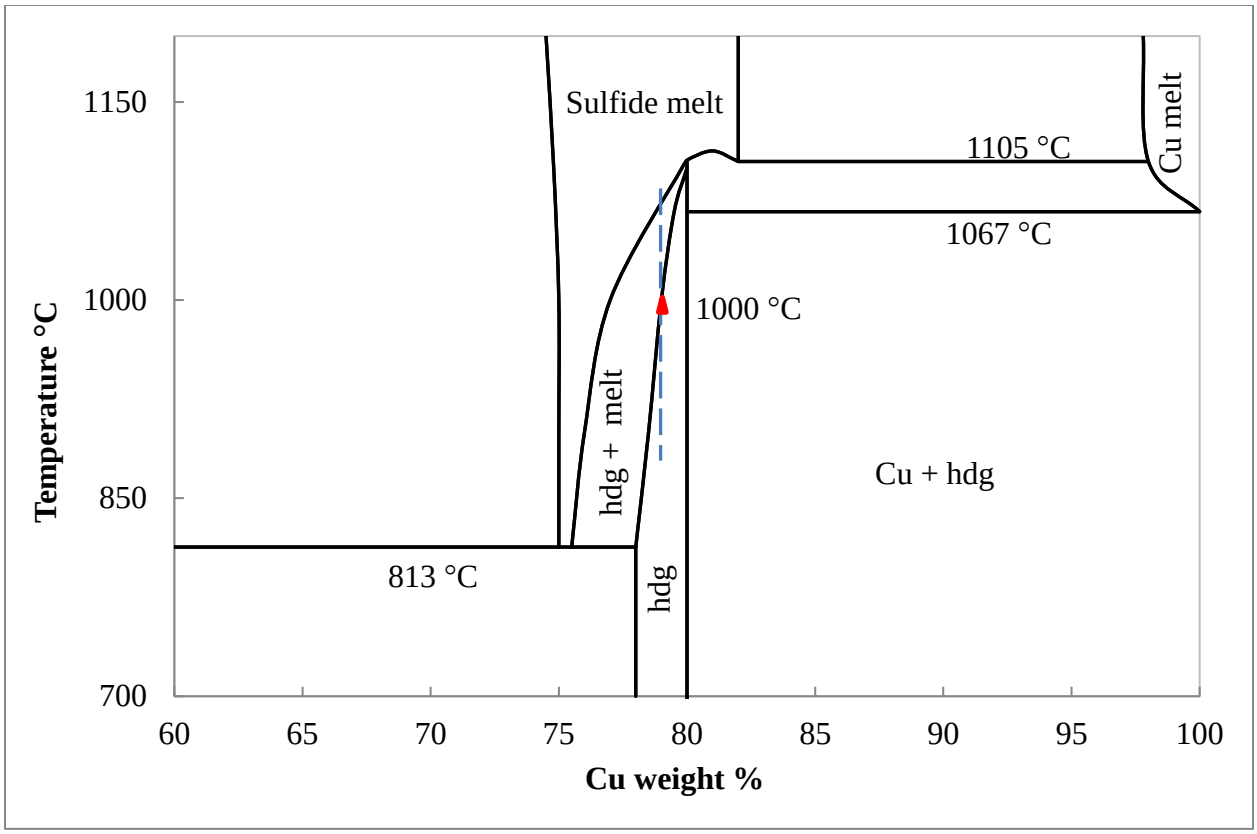

Figure 3-7: Phase relations among condensed phases in the Cu-S binary system, a typical melting path of a Cu_2S is highlighted with a dotted line [Vaughan et al. 1978]

3.3.3 FeS-FeO-Fe_2O_3 system

Dissolution of oxides in matte during smelting is a common occurrence; at high temperatures Fe_xO and Cr_xO have significant solubility in a PGM furnace-matte [Eksteen et al. 2011]. The presence of impurities (e.g. FeO) in matte has been shown to alter matte properties such as liquidus temperature. FeS-FeO-Fe_2O_3 phase diagram is shown in Figure 3-8 [extracted from McLennan et al. 2000]. FeS melts at 1190 °C as shown in the phase diagram. The melting temperature of a 60/40 FeS/FeO (by mass) is 910 °C. In the absence of impurities, FeS and FeO liquids are miscible.

This is an example of an oxide effect on the properties of the sulfide; this phase diagram does not describe the actual effect that the oxides will have in a particular matte sample.

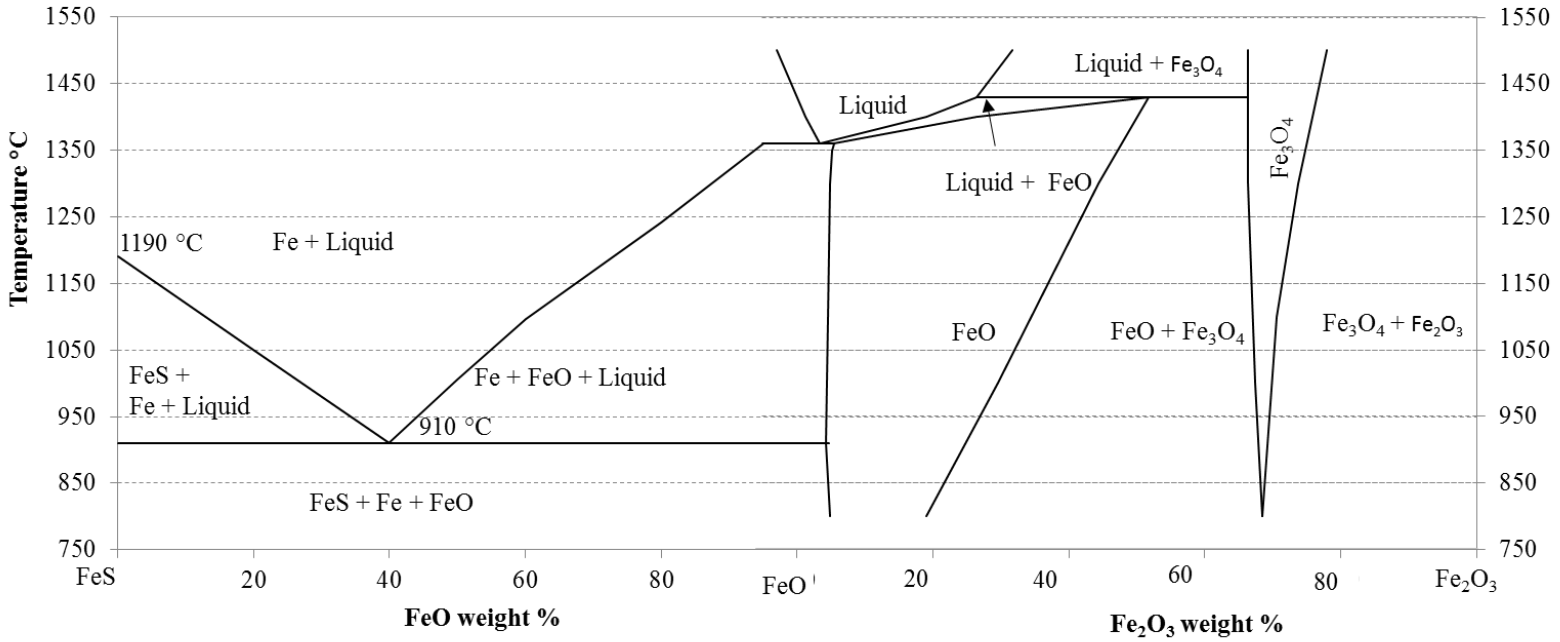

Figure 3-8: FeS-FeO-Fe_2O_3 equilibrium phase diagrams vs. temperature [McLennan et al. 2000]

3.4 Interaction of carbon with sulfides

Data on the interaction between carbon and sulfides is scarce in the open literature. Sulfides are not reduced by carbon, if any reduction happens; CS_2 is the product of the reduction [Habashi 2002]. Reduction reactions between sulfides and carbon are not favourable, $\Delta G°$ is greater than zero at temperatures up to 1550 °C [Bale et al. 2009].

Tsymbulov and co-workers studied the solubility of carbon in iron-nickel sulfide melt; they varied Fe to Ni ratio, metal to sulfide ratio and the operating temperature. The solubility of carbon as a function of the Ni content in the melt at 1673 K is shown in Figure 3-9. The solubility of carbon as a function of sulfur at 1673 K is shown in Figure 3-10, where Fe:Ni ratio is varied. These authors made the following observations: [Tsymbulov et al. 2001]

- Carbon dissolution in matte is dependent on the sulfur content of matte, metal content in a sulfide and temperature
- When the sulfur content of the melt is less than 20 mass percent the solubility of carbon in the melt decreases with increasing sulfur content, if the sulfur content of melt is above 20 mass percent it does not affect the solubility of carbon in the melt
- Carbon solubility decreases with nickel amount up to about 80 mass percent, iron dissolves a greater amount of carbon than nickel
- Melts of the system Fe-S separate into sulfide and metallic phases in the presence of carbon
- The Fe-S separation depends on the initial content of the sulfur in a sulfide, sulfur should be between 1.94 and 28.7 mass percent

Gabriel and co-workers have evaluated the C-Fe-Ni system. These authors reported that the solubility of carbon in the Fe-Ni system decreases with the increase of nickel up to about 80:20 Ni-Fe ratio [Gabriel et al. 1987]. This observation is in agreement with the work of Tsymbulov et al. 2001.

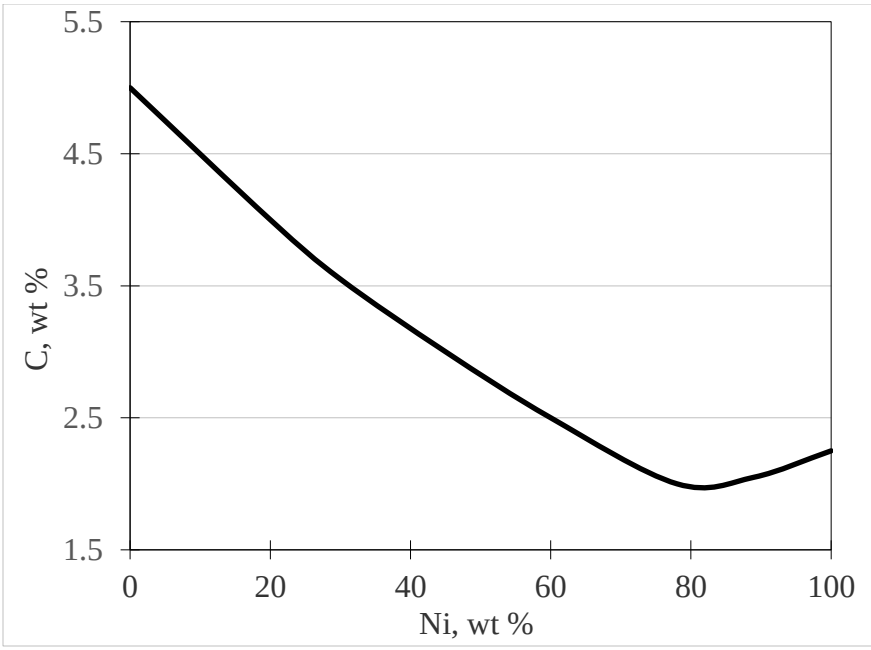

Figure 3-9: Solubility of carbon in Fe-Ni melts at 1673 K, according to Tysmbulov et al. 2001

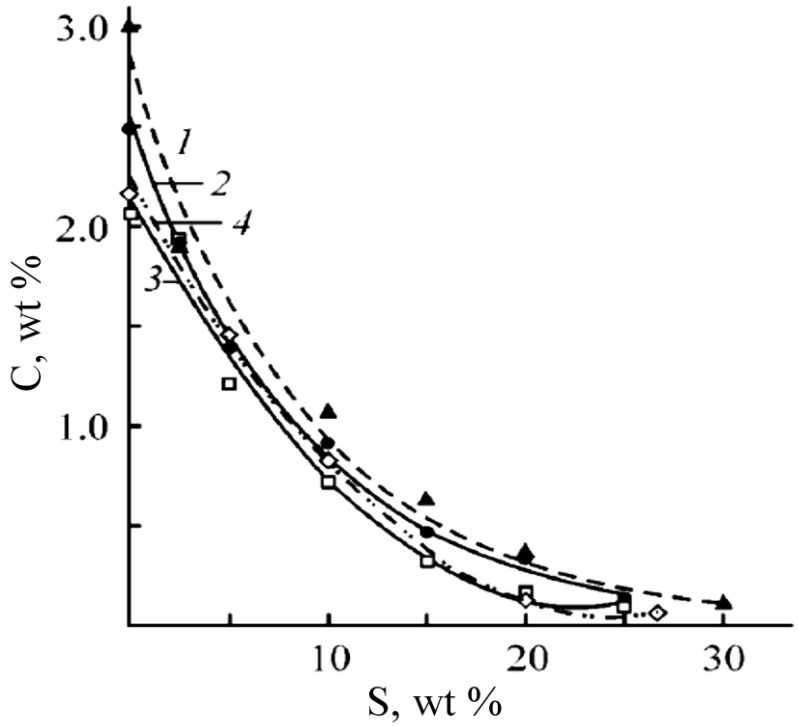

Figure 3-10: Solubility of carbon vs. the content of sulfur in melt, at 1673 K. Fe:Ni ratio: 1_50:50, 2_40:60, 3_10:90 and 4_0:100; according to Tysmbulov et al. 2001

The sulfur content in a typical PGM matte sample is an average of 27 mass percent according to the data in Table 2-3; therefore carbon solubility by matte is not envisaged to be a significant wear mechanism of graphite. It is envisaged that the solubility of carbon will be minimal if the sulfur content of the melt does not drop below 20 mass percent. However in industrial application it may be tricky to maintain the required amount of sulfur since there is constant tapping and gases given off during operation.

The average Fe:Ni ratio of a typical PGM matte is 55:45, at low sulfur contents the melt can dissolve up to 3 mass percent carbon according to the data in Figure 3-9.

No published work was found on Copper-Sulfur-Carbon system. However Nizhenko et al. 1974 studied the solubility of carbon in liquid iron and iron base melts as well as the effect of dissolved carbon in the wettability of carbon by the tested melts. It was observed that the carbon content of the melt affects the wetting angle of the carbon by the melt. From 0 mass percent to 3.7 mass percent carbon, the wetting angle increase from 40° to 100°. A carbon free Cu-Fe wets carbon while a carbon saturated Cu-Fe does not wet carbon in all proportions of Cu:Fe. Carbon is non-wetted by copper, if copper in increased in a Cu-Fe alloy the wetting angle between the alloy and the carbon increases [Nizhenko et al. 1974].

3.5 The solubility of carbon in the FeNi-Si

The formation of (Fe, Ni)Si has been reported by Schiepers and co-workers [Schiepers et al. 1993]; they studied the interaction of iron-nickel alloy with SiC at 850 °C. These authors observed that an iron-nickel alloy interacts with SiC to form $(FeNi)_xSi$ solid solution and a carbon precipitate.

In the current work, silica and silicon carbide were constituents of the MPC refractory. Therefore interactions between melt species and refractory material had to be understood.

Chen et al. 2015 has studied the solubility of carbon in the FeNi-Si alloy. It was shown that carbon solubility in the FeNi alloy decreases with an increase in Ni/Fe ratio at constant Si content. At variable Si contents the carbon solubility decrease with increase in Si content in the FeNi-Si alloy [Chen et al. 2015].

In the current work, the formation of a FeNi-Si in the matte may alter the dissolution of the carbon in the matte where matte is exposed to MPC refractory.

3.6 Interaction of silicates with sulfides in the presence of carbon

Carbon is used as a reductant in the treatment of many oxide compounds but not for sulfides. Carbon has a high affinity for oxygen, when an oxide is in contact with the carbon at suitable temperatures, the carbon will reduce the oxide to a lower oxidation state or to a metal [Habashi 2002]. Although the interaction of graphite with oxide compounds has been studied, no data is published on the interaction of graphite with a typical PGM furnace slag. The PGM furnace slag consists of silicates, iron and chrome oxide. The data available in open literature covers the interaction of silicates with the sulfides in the presence of a reductant.

The interaction between silicates and sulfides in reducing conditions has been studied by Lenher et al. 2013. Silicates such as $CaSiO_3$, $FeSiO_3$, $MgSiO_3$ and $MnSiO_3$ can be sulfidised in reducing and sulfurous environment [Lenher et al. 2013]. Sulfidation of silicates forms monosulfides (CaS, FeS, MgS and MnS) according to Equation 7 [Lenher et al. 2013, Fleet et al. 1987]. These monosulfides are soluble in each other; they form complex solid-solutions (Mg, Fe, Mn, Ca)S or (Fe, Mg, Mn, Ca)S [Fleet et al. 1987, Shimizu et al. 2002]. The solubility of each sulfide in the (Fe, Mg, Mn, Ca)S solid-solution increases with temperature (from 600 °C to 1000 °C) [Skinner et al. 1971, Vaughan et al. 1978]. The Mg-rich solid-solution is called niningerite, and the iron-rich solid-solution is called keilite, their average composition is shown in Table 3-1. The ideal formula for keilite is FeS, it has 63.53 mass percent Fe and 36.47 mass percent S [Shimizu et al. 2002].

Table 3-1: Average composition of niningerite and keilite

Phase	Composition	Reference
Niningerite	$(Fe_{0.19}, Mg_{0.66}, Mn_{0.14}, Ca_{0.007}, Cr_{0.002})S$	Skinner et al. 1971
Keilite	$(Fe_{0.55}, Mg_{0.32}, Mn_{0.05}, Ca_{0.04}, Cr_{0.03}, Zn_{0.003}, Ti_{0.001})S$	Shimizu et al. 2002

Fleet and co-workers [Fleet et al. 1987] investigated the formation of this monosulfide solid-solution (Fe, Mg, Mn, Ca)S. They reacted Mg_2SiO_4 with FeNi-monosulfide at 1200 °C in a

graphite crucible, the contact time was 6 days to 9 days; experiments were performed in an evacuated silica tube. The quenched reaction products had MgS, $MgSiO_3$, FeNi-Si, FeNi, and exsolved lamellae of $(Fe_{1-x})S$. They proposed the reaction in Equation 7 as the mechanism for the sulfidation of silicates, where M could be Ca, Fe, Mg or Mn.

$$MSiO_3(s) + ½S_2 + C \rightarrow SiO_2 + MS + CO \qquad \text{Equation 7}$$

Sulfidation of silicates is favoured by high temperature, high sulfur and low fugacity of oxygen and CO [Lenher et al. 2013, Fleet et al. 1987]. Sulfidation of silicates starts at 1200 °C [Fleet et al. 1987], the current experiments were done at 1450 °C, and therefore the operating temperature was favourable for the conversion of silicates to sulfides.

Monosulfides such as [(Fe, Ni)S] serve as a source of sulfur when sulfides are in contact with the silicates [Lenher et al. 2013, Fleet et al. 1987]. Sulfur is provided by the metallization of Fe-Ni-S to Fe, Ni according to Equation 8 [Lenher et al. 2013].

$$(FeNi)_9S_8(s) \rightarrow 9FeNi(s) + 4S_2(g) \qquad \text{Equation 8}$$

In the current work sulfides (matte) and silicates (slag) were exposed to carbon (graphite), therefore the reactions outlined in Equations 7 to 8 are envisaged.

3.7 Interaction of sulfides with gas bubbles

Evolution of process gases occurs during the melting of sulfides [Eksteen 2011], as such, it is vital to understand how molten sulfides behave in relation to the gas phase. Sulfides have been reported to attach themselves to the gas bubbles during smelting [Herman 2013]. The attachment of gas bubbles to the sulfides is attributed to the surface tension. When minerals are entirely wetted by the solution, there is no place for attachment of gas bubbles, but if compounds (such as sulfides) are poorly wetted by the solution there are spaces for the attachment of gas bubbles which cause them to rise to the surface [Herman 2013]. The ability of the gas bubbles to pick up matte droplets is dependent on the surface tension of the matte, slag and the matte-slag interfacial

tension. The matte droplet can either form a film around the gas bubble or an attachment on the gas bubble upon contact [Ip et al. 1992].

The morphology of the compound drop (sulfide and vapour) depends on the ratio of the surface tension between the immiscible fluids. Metal or matte film will be stable on a gas bubble and the slag phase only when the spreading and flotation coefficients are negative. Flotation takes place when the spreading and flotation coefficients are negative. When the spreading coefficient is negative and the flotation coefficient is higher than zero, dispersion of matte or metal droplets is expected. The expression for the spreading coefficient is in Equation 9, the expression for the flotation coefficient is in Equation 10 [Ip et al. 1992].

$$\Phi = \gamma_{\frac{s}{g}} - \gamma_{\frac{m}{g}} - \gamma_{\frac{m}{s}} \quad \text{Equation 9}$$

$$\Delta \approx \gamma_{\frac{s}{g}} - \gamma_{\frac{m}{g}} + \gamma_{\frac{m}{s}} \quad \text{Equation 10}$$

The terms in these equations are surface tensions, $\gamma_{s/g}$ is slag surface tension, $\gamma_{m/g}$ is matte surface tension and $\gamma_{m/s}$ is matte/slag interfacial tension.

Filming is when a film of melt forms around the gas bubble. Flotation is when melt droplets attach to the gas bubble. Dispersion is when a melt droplet detaches from the bubble [Ip et al. 1992].

In the current work a typical layout of an industrial smelter was simulated where matte and slag were filled in the same crucible. Since the matte had oxide impurities the reactions between the oxides and graphite would possibly form a gas. As discussed, matte has an affinity for gas therefore attachment of matte to gas bubbles was expected.

3.8 Melt foaming

The gases produced during the reduction reactions cause slag foaming. The reduction reaction initiated by direct contact of slag with the graphite surface produces CO gas, which spreads into the molten bath causing foaming [Bhoi et al. 2006]. When gas generation exceeds escaping rate, the gas could accumulate inside the liquid causing the liquid to inflate [Shen et al. 2009].

The low interfacial tension between slag and metal causes gas bubbles to be entrapped in the metal phase resulting in the formation of pores upon solidification [Sundström et al. 2008]. Körner et al. 2005 have also observed that when a melt is mixed with gas bubbles, the melt become highly porous when it solidifies [Körner et al. 2005].

The following enhances slag foaming: gas generation, high viscosity, high interfacial/surface tensions and the presence of solids [Bhoi et al. 2006, Körner et al. 2005]

In the current work, slag and matte were in contact with graphite; the chemical reaction between graphite and slag was envisaged where CO would form. The formation of CO could lead to melt foaming as discussed above.

3.9 Summary

In the literature review the discussed topics were the refractories, previous work done on a graphite block used in a matte tap-hole, Cu-Fe-S and Ni-Fe-S systems, interaction of graphite with selected sulfides, interaction of graphite with FeNi-Si and the interaction of a melt with gas bubbles. The data on the interaction of graphite with a CuFe-S system was not available in the open literature.

The refractory section included the description of the refractories, the manufacturing of the used refractories, wear mechanisms of refractories, factors affecting wear of refractories, and the refractory-wear testing methods.

The work done on a graphite-block used at a matte tap-hole highlighted the parameters that could affect matte interaction with graphite. The effect of the tap-whole diameter, bath levels and matte temperature was discussed. In the current work the effect of head pressure on matte penetration is estimated, the effect of temperature and contact time on liquid matte penetration is also studied.

The phase transformations on the Cu-Fe-S and Ni-Fe-S systems have been discussed in literature. This section brought understanding of the phases most likely to be detected on the matte samples after exposure if chemical interaction with graphite did not occur. The effect of carbon addition on the phase relations has not been reported in literature, as such the

sulfide-carbon phase diagrams are not discussed in this work. The effect of other impurities such as oxides (SiO_2, Cr_2O_3, etc.) on sulfide phase relations has not been reported in open literature. Due to a broad scope of the current work and limited resources, it was not possible study the effect of carbon and other impurities on the phase relations in the Cu-Fe-Ni-S system. It is however a consideration for future work to study the effect of impurities on sulfide phase relations.

The melting temperature of binary phases (Cu_xS, Ni_xS and Fe_xS) and the condensed phases (at low temperatures) were discussed. In the current work the melting temperatures and the change of composition of the sulfides with increase in temperature were confirmed to be similar to the properties reported in the literature.

The effect of FeO on the FeS was briefly discussed, FeO addition of up to 40 mass percent lowers the melting temperature of FeS from 1190 °C to 910 °C. In the current work, the matte samples used had minute amounts of oxide impurities, slightly lower melting temperatures were observed for contaminated matte.

Work done on the interaction of graphite with FeNi-S discussed the effect of sulfur and Fe:Ni ratio on the dissolution of graphite in this sulfide melt. At sulfur content less than 20 weight percent carbon solubility decrease with an increase in sulfur content. Carbon solubility decreases with increasing nickel content up to 80 mass percent. In the current work effect of sulfur content on the solubility of carbon in a sulfide melt is confirmed. The carbon content of a Cu-Fe alloy affects the wettability of a carbon by the alloy, the increase in copper increases the wetting angle when Cu-Fe is in contact with a carbon. The effects of dissolved carbon on the wetting behaviour of a melt is vital in understanding the changes in the contact angle with contact time or with exposure temperature. The effect of dissolved carbon implies that during the exposure the wettability of a refractory may change as the carbon content of the melt change even if other parameters (melt composition) remain constant.

Work reported on the interaction of FeNi-Si with graphite discussed the effect of Fe/Ni ratio on the solubility of graphite by this silicide. An increase in Ni decreases the solubility of carbon in a silicide at constant Si. At variable Si, carbon solubility decreases with an increase in Si content.

In the current work the FeNi-Si formed during the interaction of matte with the MPC refractory, the effect of melt composition on carbon solubility was not studied.

The interaction of silicates with sulfides in reducing conditions have been discussed in literature. In the presence of carbon silicates can be sulfidised to sulfides with SiO_2 and CO as the products of the reaction. In the current work the matte was contaminated with some oxide and silicate phases, the findings of this work confirms the sulfidation of silicates as discussed in the literature.

The review of the interaction of matte with gas highlighted the effect of interfacial tensions on the gas/matte interaction. The mechanical loss of matte through bubble entrainment was also discussed. In the current significant wear of the graphite was observed at the three-phase region that confirms the significance of surface tension gradient on the wear of a refractory by a melt. The surface tension of matte and slag are calculated using published equations. The interfacial tension between the melt and the graphite is not quantified in the current work.

The phenomenon of melt foaming has been discussed in literature. Melt foaming is affected by the amount of gas released during the reactions in the process, the interfacial tension between fluids and the properties of a melt (i.e. viscosity). In the current work melt foaming is observed during the melting stages of the ore, pure matte does not foam while matte with oxide and silicate impurities has high foamability in the presence of graphite.

The aim of the current work was to determine the compatibility between carbon-based refractories with a PGM melt. Using carbon-based refractories against a PGM melt is a recent development, hence the literature is scarce on this subject. The findings of the current work contains the possible wear mechanisms when selected carbon-based refractories are in contact with a typical PGM melt in static conditions. There are still gaps on the effect of carbon on the properties of matte species since this work focuses on the overall behaviour of matte and slag when in contact with graphite and a micropore carbon. Further work should concentrate on determining the effect of carbon on the phase relations in the Cu-Fe-Ni-S system, as well as the effect of different oxides and silicates on the properties of matte.

4 Materials and methods

This chapter describes the techniques and materials used to study the interaction of carbon-based refractories with a typical PGM matte and a PGM slag. The analytical techniques used in this work are described in the first section. The discussed techniques were used to determine the compositions and properties of materials prior to exposure and after the experiments. The properties and composition of the materials are discussed in the second section, the materials discussed are refractories (graphite and MPC), industrial PGM matte, synthetic matte and industrial PGM slag. The apparatus used to carry out the simulations and the experiments are discussed in the third section, the apparatus are these; FactSage, coal ash fusion furnace and a vertical tube furnace. The experimental design and procedures are described in the fourth section of this chapter. The following procedures are discussed; wettability tests, crucible tests performed to determine the prominent wear mechanism of graphite by a PGM matte and slag, as well as crucible tests performed to determine the prominent wear mechanism of MPC crucible by a PGM matte.

4.1 Characterization Techniques

Prior to analysis, a sample had to be prepared according to the specified preparation methods for the specific technique. For powder analysis the samples were milled to ~10 µm prior to analyses. For polished sections, samples were mounted in a resin and polished using SiC paper, for final polishing an MD-nap from size 3 µm to 1 µm was used. The analytical techniques used for characterization of materials are listed below, their description follows.

- Carbon and sulfur analyser
- Electron probe micro analyser (EPMA)
- Inductively Coupled Plasma Optical Emission Spectrometry (ICP-OES)
- Optical microscope (OM)
- Scanning Electron Microscope (SEM)
- X-Ray powder diffraction (XRD)

- X-Ray fluorescence (XRF)
- X-Ray Micro tomography (XRM)

4.1.1 Carbon and sulfur analyser

The amounts of carbon and sulfur in the samples were determined using LECO (CS-400 for carbon and SC-144DR for sulfur). The sample is finely ground to less than 10 µm before analysis. The powder sample is heated to 1350 °C in an oxygen environment, the resulting gas is analysed by an infrared detection system that gives the total sulfur or carbon in the gas [Kowalenko 2001].

4.1.2 Electron Probe Micro Analyser (EPMA)

The EPMA used for analyses in this work was a Cameca SX100. A typical EPMA is fitted with a Wavelength-dispersive spectroscopy (WDS) detector that measures the wavelengths of the X-rays emitted by the specimen. EPMA determines the elemental composition of the phases in the sample [Goldstein et al. 2003]. The polished sample was coated with carbon to ensure good conductivity. The microprobe used was calibrated and optimised to analyse slag and matte, specific databases were created for matte and for a slag. The microprobe could calculate the stoichiometric oxygen for a specific phase and therefore could detect differences in oxidation states of the oxide phases.

Two setups were created for the current work, one for sulfide analysis and another for the oxide analysis. The following calibration of elements were done: O on Al_2O_3, Na on jadeite, Mg on olivine, Al on almandine, Si on diopside, K on orthoclase, Ca on wollastonite and Co and Cu on pure elements, S and Fe were calibrated on pyrite, Cr, Mn and Ni were calibrated on pure elements. For oxides the calibrations were done as follows; S on Celestine, Cr on Cr_2O_3, Mn on rhodonite, Fe on hematite and Ni on NiO. The pure elements, Al_2O_3, Cr_2O_3 and NiO were synthetic, the other minerals were natural materials.

The oxygen analysis depends on the calibration of Al_2O_3. The oxygen content was calculated by stoichiometry based on the following assumptions: (Al was present as Al^{3+}, Ca as Ca^{2+}, Co as

Co^{2+}, Cr as Cr^{3+}, Cu as Cu^{+}, Fe as Fe^{2+}, K as K^{+}, Mg as Mg^{2+}, Mn as Mn^{2+}, Na as Na^{+}, Ni as Ni^{2+}, S as S^{6+} and Si as Si^{4+} (and O as O^{2-}); i.e., we assumed that the cations and S were present as Al_2O_3, CaO, CoO, Cr_2O_3, Cu_2O, FeO, K_2O, MgO, MnO, Na_2O, NiO, SO_3, and SiO_2.

4.1.3 Inductively coupled plasma-optical emission spectrometry (ICP-OES)

ICP-OES analyses specimen in a liquid state using ionized argon plasma to interact with the solute at high temperatures. The wavelength of the photons released by the analyte is used to identify the elements [Hou et al. 2000]. A finely ground powder (<10 µm) sample was submitted for ICP. ICP-OES was used to determine the quantitative elemental composition of the materials. Varian Vista Pro was the equipment used for the analysis; it is fitted with the ICP expert software.

4.1.4 Optical microscope (OM)

An optical microscope was used to acquire magnified images of the samples and to estimate the pore distribution in the graphite block. Olympus microscope was used for the analysis. It has stream essentials V1.3 software for image analysis. A camera is fitted into the microscope to allow image capturing.

4.1.5 Scanning Electron Microscope (SEM)

SEM (Jeol JSM6300 and SEM5800) was used for sample characterisation in this work. The basics of how SEM works are detailed in the work of Goldstein and co-workers [Goldstein et al. 2003]. The energy dispersive spectrometry (EDS), backscattered electron imaging (BSE) and X-ray mapping are the SEM detectors used to analyse materials. EDS measures the intensity or amount of energy of X-rays emitted by a specimen [Goldstein et al. 2003], EDS was used to determine the elemental composition of the samples. BSE was used for distinguishing different phases in a sample and obtaining high-resolution compositional maps of a sample.

X-ray mapping was used to determine the concentration of the sulfide phases in the refractory wall after exposure. The samples were mounted in a resin, and polished to an MD-nap size of 1 µm. The polished sample was coated with carbon to ensure good conductivity.

4.1.6 X-Ray powder diffraction (XRD)

XRD is primarily used for phase identification of crystalline material [Loubser et al. 2008]. The equipment used for XRD analysis was a PANalytical X'Pert Pro powder diffractometer that has an X'Celerator detector, variable divergence and receiving slits with Fe filtered Co-Kα radiation. The machine was operated at 35 kV, 50 mA and 25 °C. X'Pert Highscore plus software was used for phase identification. Quantification was done using the Autoquan software (BGMN® program). The quantitative analysis (mass percentage of phase) was estimated using the reference intensity method in the X'Pert Highscore plus software. XRD was used to determine the crystalline phases present in the materials used. A finely ground powder (<10 µm) sample was prepared for XRD analysis.

4.1.7 X-Ray fluorescence spectroscopy (XRF)

XRF was used to determine the bulk chemical composition of the samples. The XRF machine used was an ARL 9400XP Wavelength dispersive XRF spectrometer; it has a rhodium tube, a scintillation detector and the analysing crystal. Several crystals are used, (lithium fluoride, Ammonium dihydrogen phosphate, pentaerythritol, etc.) depending on the wavelength of the element to be analysed. A finely ground powder (<10 µm) was mixed with a binder and pressed into a briquette. The pressed briquettes were dried at 105 °C to remove moisture prior to analyses. WinXRF and UniQuant software were used for data reduction.

4.1.8 X-Ray computed micro tomography (XRM)

Tomography is an X-ray imaging technique that allows for a three dimensional image of the interior of a sample to be created [Ketcham et al. 2001, Holler et al. 2014]. During tomography

analysis, the sample is placed between the X-ray source and the detector. The sample is rotated and illuminated in different directions, for each direction a projection of the attenuation coefficients is measured. A computerized reconstruction of the sample is then carried out [Dhawan et al. 2012]. Tomography image is called a slice or a tomogram. The gray levels in a computed tomography slice correspond to X-ray attenuation [Ketcham et al. 2001]. X-Ray attenuation is primarily a function of X-ray energy, density and the atomic number of the material being analysed. Photoelectric adsorption and Crompton scattering are the dominant attenuation mechanisms. Photoelectric adsorption is dominant at low x-ray energies (50-100 keV), it is proportional to Z; Z is the atomic number of the atom in the attenuating material. Crompton scattering is dominant at high X-ray energies (50-100 MeV), it is proportional to Z (atomic number of the atom in the attenuating material) [Ketcham et al. 2001]. Imaging depends on the density and atomic composition of the imaged material [Ketcham et al. 2001]. Digital geometry processing is used to generate a three dimensional image of an object from a large series of two dimensional radiography images taken around a single axis of rotation [Holler et al. 2014]. While a 2D image only gives one plane of the specimen at a time, in a 3D image the full view of the specimen is attainable; this is the advantage of using the XRM technique. For XRM analysis the specimen was analysed as is, the parameters used were 100 kV photon energy and 7 W beam energy.

4.2 Materials

The properties of the materials are discussed in this section. Carbon-based refractories (graphite and MPC), carbon paste, industrial matte, synthetic matte and industrial slag are discussed in turn.

4.2.1 Carbon-based refractories

The carbon-based refractories tested in this work include synthetic graphite (extruded and isostatically pressed) and a micropore carbon (MPC). A criterion used to select these refractories was based on the performance of similar materials used in industry. SGL carbon was a supplier for all the refractory materials used.

4.2.1.1 Synthetic graphite

An isostatically pressed graphite (HG) and extruded graphite (SG) were the graphite materials tested in this work. Properties of these graphite specimens (HG and SG) are summarized in Table 4-1; the properties of MPC are also included in Table 4-1 for comparative reasons. HG graphite was of a higher quality than the SG graphite. HG graphite was a denser, isostatically pressed material characterized by high thermal conductivity, low porosity, low permeability and considerably higher cost. The reason for testing graphite materials with different qualities was to determine whether the quality of graphite affect its resistance towards wear by liquid PGM melt (matte and slag).

The manufacturing route for HG and SG graphite differs, the starting materials for producing HG graphite are finer in particle size and have low levels of impurities compared to the starting materials for the SG graphite. The HG graphite was isostatically pressed while the SG graphite was extruded. These differences affect the properties of the final product such as porosity, permeability and thermal conductivity. As such the porosities of HG and SG graphite were 15 percent and 24 percent respectively.

Apparent porosity and permeability of graphite specimen were measured by a refractory testing company called Cermalab; they used EN993-4 standard for porosity measurement and ISO5017 standard for permeability measurement. Pore-size distribution was determined by optical microscope. Other properties in Table 4-1 were extracted from the supplier's data sheets.

The microstructure of the graphite samples (HG and SG) is shown in the optical microscope images in Figure 4-1 a) and b). SG graphite is porous with an average pore diameter of 20 µm and minor cracks that are the artefacts of the production process. Due to high porosity, SG graphite has higher permeability compared to the HG graphite (Table 4-1). The microstructure of HG and SG graphite concur with the properties of these materials in Table 4-1, HG graphite seem dense and has finer pores compared to the SG graphite.

The chemical analyses of the graphite samples are shown in Table 4-2. The impurities in the SG graphite were mostly Ca and Fe compounds as shown in the chemical analysis in Table 4-2. According to the supplier's data sheet SG graphite has iron content of 0.8 mass percent, but the iron content detected by ICP (Table 4-2) in SG graphite was 0.5 mass percent. Impurities and additives detected in the HG graphite are listed in Table 4-2.

Table 4-1: Physical and thermal properties of HG and SG graphite

Property	**Units**	***HG**	***SG**	***MPC**
Apparent density	[$g.cm^{-3}$]	1.72	1.62	1.7
Apparent porosity	[%]	15	24	15
**Apparent porosity	[%]	15.4	19.9	12.2
**Permeability	[cm^2]	$3.7x10^{-12}$	$9.1x10^{-10}$	$1.4x10^{-12}$
Proportion of pores ≤10 µm	[%]	44	70	70
Proportion of pores ≥ 50 µm	[%]	1	5	4
$^{+}$Average pore size	[µm]	13	20	12
Thermal conductivity (30 °C)	[$W.K^{-1}.m^{-1}$]	180	150	17
Coefficient of linear thermal expansion (20-200 °C)	[$\mu m.K^{-1}.m^{-1}$]	$^{\#\#}2.9x10^{-6}$	$1.9x10^{-6}$	$2.6x10^{-6}$
Iron content	[%]	0.1	0.5	0.1
Production process	-	Isostatic press	Extrusion	Extrusion

**HG: Isostatically pressed high grade graphite; SG: extruded standard grade graphite, MPC: micropore carbon,*

***Performed by Cermalab using ISO5017 and EN993-4, $^{\#\#}$thermal expansion in K^{-1}*

$^{+}$Average pore size of the refractory determined using optical microscope

Table 4-2: Impurities in HG and SG graphite types, measured by ICP-OES and LECO

Mass percent	**C**	**S**	**Al**	**Si**	**Ca**	**Cr**	**Fe**	**Ni**	**Cu**	**Zn**
SG-graphite	98.3	0.05	0.1	0.1	0.5	<0.05	0.8	0.1	0.1	<0.05
HG-graphite	99.5	0.03	0.1	0.0	0.1	0.1	0.1	<0.05	0.1	0.1

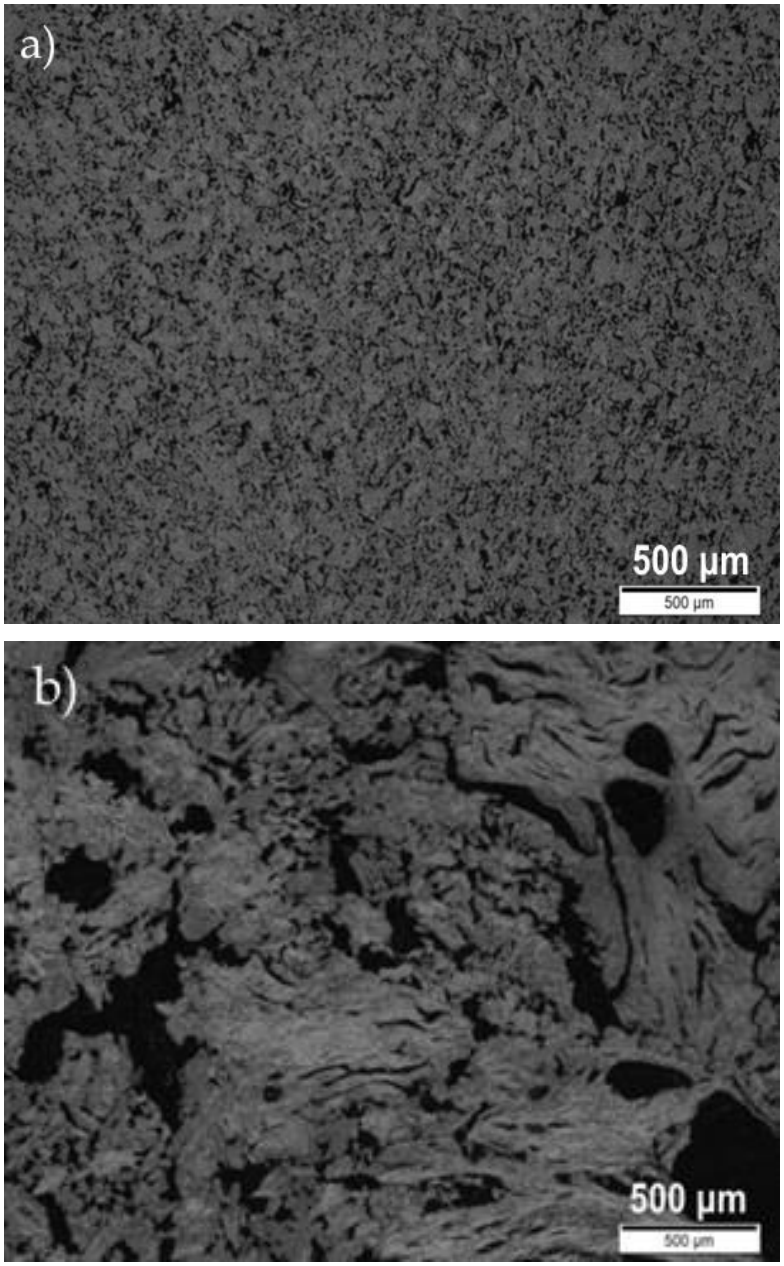

Figure 4-1: Microstructure of graphite samples: a) HG graphite, b) SG graphite; images by optical microscope

4.2.1.2 Micropore carbon (MPC)

MPC had similar properties to the HG graphite, it had lower porosity, high density, and low permeability, however MPC had the lowest thermal conductivity of 17 $W/K^{-1}.m^{-1}$. MPC was extruded during manufacturing. The properties of the micropore carbon sample are shown in Table 4-1. Cermalab performed the permeability and apparent porosity measurements using ISO standards ISO5017 and EN993-4. An optical microscope was used to determine the pore size distribution. All the other MPC properties in Table 4-1 were extracted from the supplier's data sheet.

The composition of the phases of the MPC was determined by XRD. The XRD detected the following phases in the MPC sample: carbon, alumina, silicon and silicon carbide. The XRD analysis is shown in Table 4-3.

The XRD analysis confirmed the presence of alumina and silicon based compounds in the micropore carbon. The data from the supplier indicated that the additives add up to 22 mass percent whereas the additives detected by XRD add up to 48 mass percent. The size of the MPC sample tested is relatively small when compared to the size of the industrial sample, this could be responsible for the discrepancy in the contents of the MPC sample analysed. Different methods used to determine the amount of additives in the sample content could also cause discrepancies.

Aluminosilicate compounds and silicon compounds were detected by the EPMA as the major components of the matrix in the MPC sample, the summary of the EPMA analysis is shown in Table 4-4.

Table 4-3: Micropore carbon, XRD quantitative analysis

	Phase	**Mass %**
Carbon	*C	52
Alumina	Al_2O_3	27
Silicon carbide	SiC	14
Silicon	Si	7

**The total carbon in the sample can be higher than the 52% detected by XRD, if carbon in the sample is not crystalline XRD would not be able to detect it. This would affect the fraction of the other compounds in the sample*

The microstructure of a micropore carbon sample was assessed using an optical microscope. The arrangement of the aggregate particles, matrix and pores in the MPC are seen in the MPC image in Figure 4-2. SEM elemental mapping was used to determine the elemental distribution of the materials in the MPC block. The BSE image and the X-ray maps are shown in Figure 4-3. Figure 4-3a is the BSE image, Figure 4-3b is the Al X-ray map and Figure 4-3c is the Si X-ray map.

Table 4-4: EPMA analysis of the materials in a micropore-carbon block (atom %)

	Si	**SiO_x**	**$(Si, Al)_xSiO_y$**
Si	100.0	35.7	11.9
Al	0.0	0.0	28.6
O	0.0	64.3	59.5

The micropore carbon consisted of carbon, elemental silicon plus Al and Si compounds based on the X-ray maps in Figure 4-3b and c. The bright phases in Figure 4-3a) mostly consisted of Si, while the grey phases consisted of an Al-Si compound. The unidentified dark grey phases are carbon that forms part of the aggregate and the matrix material of the MPC refractory. Cu, Fe, Ni and S were not detected in the MPC block. No other elements could be identified in the MPC refractory. The SEM used could not detect carbon and oxygen, Si and Al X-rays could originate from compounds containing SiC, SiO_2 or Al_3O_2. The SEM and the XRD analysis are in agreement, the MPC sample consisted of carbon as the aggregate material as well as Al and Si compounds as the matrix in the MPC structure.

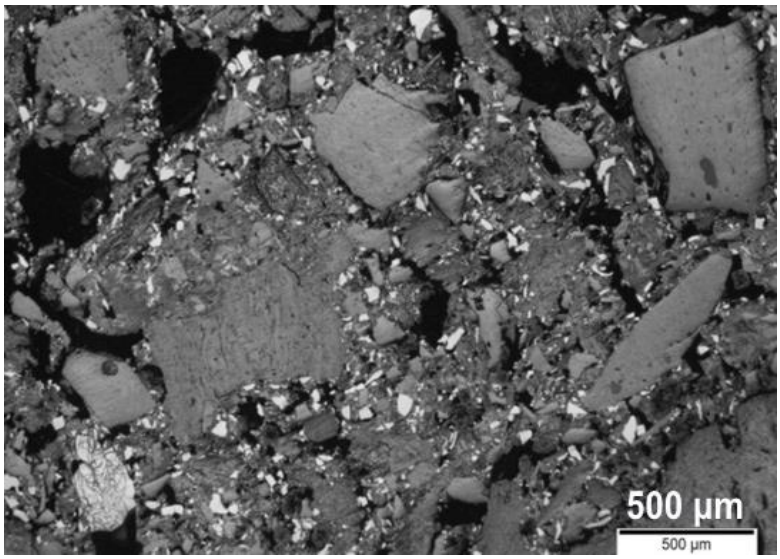

Figure 4-2: Micropore carbon sample (before exposure), optical microscope image

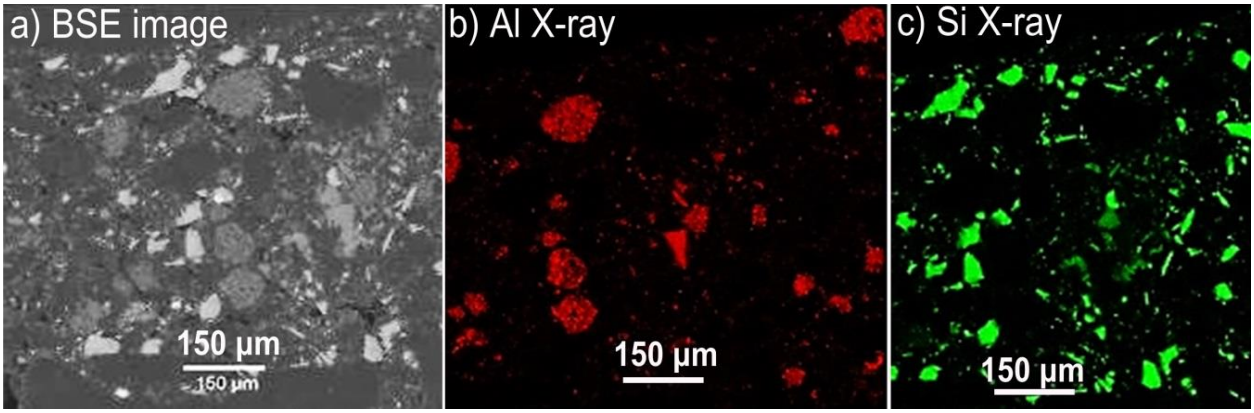

Figure 4-3: Micropore carbon sample (before exposure); a) BSE-image, b) Al x-ray map, c) Si x-ray map

4.2.1.3 Carbon paste

Carbon paste was used to seal the gap between the crucible and its lid. A C-34 carbon paste was acquired from Graftech South Africa. The contents of the paste were in a powder and a liquid form. The composition of the paste is shown in Table 4-5, this data was acquired from the supplier. To prepare the paste the powder and liquid was weighed in a ratio of 10:3 powder to liquid. The mixture was stirred for 45 minutes after which it was set-aside for 30 minutes, before

application the mixture was stirred for 30 minutes. After application the paste was cured first at 100 °C for 4 hours and then at 120 °C for 6 hours.

Table 4-5: Composition of the carbon paste

Contents	Mass %
Carbon black	25
Methenamine	2
Graphite	57
Phenolic resin	14
Petroleum	2

4.2.2 Industrial PGM matte

Amplats, Implats, and Lonmin are three major producers of PGMs in South Africa [Ryan 2014]. Amplats is the largest primary platinum producer in the world; it has three PGM smelters namely; Mortimer, Polokwane and Waterval [Hundermark et al. 2011]. The industrial matte samples studied in this work were acquired from Amplats and Lonmin, Implats sample was not acquired. Two samples were acquired from Amplats' Waterval smelter (Matte-A) and Polokwane smelter (Matte-P), the third sample was acquired from Lonmins' no.1 furnace (Matte-L).

The acquired matte samples were crushed and milled to less than 100 μm to ensure homogeneity of the sample. After milling the matte was split and sampled for chemical analysis. Purification was not done on the matte samples, they were tested as received.

Matte was subjected to EPMA, ICP, LECO, XRD, XRF and SEM to determine its chemical and phase composition. For EPMA and SEM analyses the matte samples were sectioned and polished as received.

4.2.2.1 Amplats-Waterval matte (Matte-A)

Amplats-Waterval smelter treats a blend of Merensky, UG2 and Platreef concentrate [Hundermark et al. 2011]. The matte from this smelter is granulated after tapping. Matte

granulation involves tapping a hot matte into cold running water such that the matte is quenched from tapping temperature to below 100 °C. Granulated matte therefore may have high temperature phases and fine crystal structures compared to a slow cooled matte. Matte-A sample was a composite of a number of taps; as such the tapping temperature could not be attained.

XRD quantitative analysis of Matte-A is shown in Table 4-6. Matte-A had pentlandite, pyrrhotite, troilite and an oxide phase (Fe_3O_4) of up to ten mass percent. A typical matte can dissolve between one and nine mass percent oxygen [Eksteen 2011], therefore the presence of an oxide in the matte is highly possible. The oxide phases in industrial furnace matte could result from slag entrainment in matte, poor separation between the slag and matte, high solubility of slag phases in matte, or the solubility of a refractory into the matte, these are typical phenomenon during the PGM-matte smelting process [Eksteen et al. 2011].

The composition of the phases of Matte-A was estimated from EPMA analysis; summary of analysis is shown in Table 4-7. Pyrrhotite solid solution, monosulfide solid solution, high pentlandite, haezlewoodite solid solution and an (Fe, Ni) alloy were major phases in Matte-A. It has been discussed in Section 3.3 that pentlandite and haezlewoodite are solid solutions see Figure 3-3 and Figure 3-4. The metal to sulfur ratio of a high pentlandite can vary from a metal rich $(FeNi)_9S_{6.93}$ to $(FeNi)_9S_8$ [Kitakaze et al. 2011]. Similarly heazlewoodite is a solid solution, its metal to sulfur ratio varies [Fleet 2006].

The Fe,Ni alloy coexist with pentlandite, haezlewoodite and monosulfide solid solution at low temperatures in a Fe-Ni-S system [Kitakaze et al. 2011]. Andrews et al. 2010 reported the presence of an alloy (Cu-Fe-Ni) in the PGM furnace matte, therefore the detection of an alloy in the matte is not an anomaly. Matte-A was granulated upon tapping, therefore the final matte may have high temperature phases since the matte was quenched and not slow cooled.

Copper sulfides were not detected in the sample, however copper was present in all the iron-nickel sulfide phases as seen in Table 4-7. The sulfide phases detected by XRD were confirmed by the EPMA analysis. Iron-chrome oxide and silicates of Al, Ca, Fe, Mg and Na were detected in the oxide impurities in Matte-A according to the EPMA analysis; summary of oxide analysis is shown in Table 4-8.

Oxide phases reported in Table 4-8 are typical crystalline phases, they possibly originated from refractory material that dissolved in the matte during operation. Typical PGM smelter refractory for hearth and lower sidewall is MgO-Fe_xO-Cr_2O_3 brick. Matte has an ability to sulfidise the chromite, solubility of a chromite in matte increases with increasing operating temperature. Due the ability of matte to dissolve oxides, matte can carry oxygen between refractory brick and slag [Eksteen 2011]. Oxidic chromium spinel is another impurity detected in the Matte-A sample. According to Kwatara 2006, some chromium dissolves in matte during smelting, it is generally present in matte as both dissolved CrS and as precipitated oxidic and sulfidic chromium spinel phases [Kwatara 2006]. Since the spinel in Table 4-8 does not have Mg and Al it is an indication that this spinel was formed due to the oxidation of CrS-FeS.

Matte has a significant solubility for oxygen at typical operating temperatures of a PGM smelter, [Eksteen 2011]. FeO is fully miscible in FeS in all proportions in the absence of other components [Eksteen 2011], therefore FeO (in slag) can dissolve in matte.

The dissolution of FeO in FeS significantly lowers the melting temperature of FeS from 1190 °C to 940 °C depending on the fraction of FeO in FeS (Figure 3-8) [Raghavan 2004]. As such, the behaviour of contaminated matte is expected to deviate from that of pure sulfides. It should be noted that the FeS-FeO phase diagram quoted is a mere example of the oxide effect on the sulfides, it does not represent the behaviour of all the sulfide compounds when contaminated by the oxide. The presence of oxides in the Matte-A sample made it difficult to accurately determine the amount of oxygen dissolved in matte (Table 4-8).

The silicates are typically amorphous material hence XRD could not detect the silicate phases, instead XRD only detected the Fe_3O_4 phase as an impurity in the matte. The layout of the oxides in the matte is shown in the optical microscope images in Figure 4-4 and BSE images in Figure 4-5. From these images it seemed that some of the oxide impurities were intertwined with matte phases while other oxides were liberated from the matte phases. Separation of oxides from matte would be a challenge because a simple density separation technique would not be ideal to separate the impurities from the matte. The possible purification for matte would be re-melting such that the oxides form a slag layer and matte settles below the slag. Purification of matte was not attempted in this work since the aim was to determine the behaviour of matte as is, re-melting matte would alter the properties and the behaviour of matte.

Matte-A had significant impurities in the form of oxides and silicates, as such it was envisaged that the behaviour of Matte-A would be affected by the impurities. It is a challenge to evaluate the behaviour of matte with these oxides since these oxides alter the properties of matte.

Table 4-6: XRD quantitative analyses of Matte-A (mass percent)

Phase	**Formula**	**Wt.%**	**3-σ error**
Magnetite	Fe_3O_4	9.76	0.69
Pentlandite	$(Fe, Ni)_{8.9}S_8$	56.33	1.11
Pyrrhotite	Fe_7S_8	15.25	1.29
Troilite	FeS	18.66	1.62

Table 4-7: EPMA analyses of the sulfide phases in Matte-A sample (mass percent)

Formula	**S**	**Cu**	**Fe**	**Ni**	**Co**
$(FeNi)_{9.7}S_8$	31.5	7.8	36.7	22.9	1.1
$(FeNiCu)_{2.6}S_2$	29.0	6.1	47.0	17.2	0.7
(Fe, Ni)S	35.9	2.7	48.5	12.5	0.4
FeNi	0.1	4.4	48.5	43.7	3.3
FeS	35.9	3.2	54.8	5.8	0.5
$(FeNiCu)_{0.8}S$	33.9	9.2	52.0	4.6	0.3

Table 4-8: EPMA analyses of the oxide phases in Matte-A (mass percent)

Wt.-%	**Si**	**O**	**Fe**	**Cr**	**Al**	**Ca**	**Mg**	**Na**	**Ni**
$(Fe, Mg, Ca, Al)Si_2O_5$	30.7	44.8	11.2	0.8	3.1	4	4.1	1.2	-
$(Al, Si)_{1.2}O_2$	26.1	49.5	-	-	24.4	-	-	-	-
$(Mg, Fe)SiO_3$	26.0	44.7	7.6	1.0	2.4	2.1	16.1	-	-
$(Ca, Na)(Si, Al)_4O_8$	23.4	45.5	0.5	-	17.3	11.3	-	2.0	-
Fe_2SiO_4	14.1	30.9	49	-	-	-	-	-	6
$FeCr_2O_4$	-	26.9	23.2	46.7	-	-	-	-	3.2

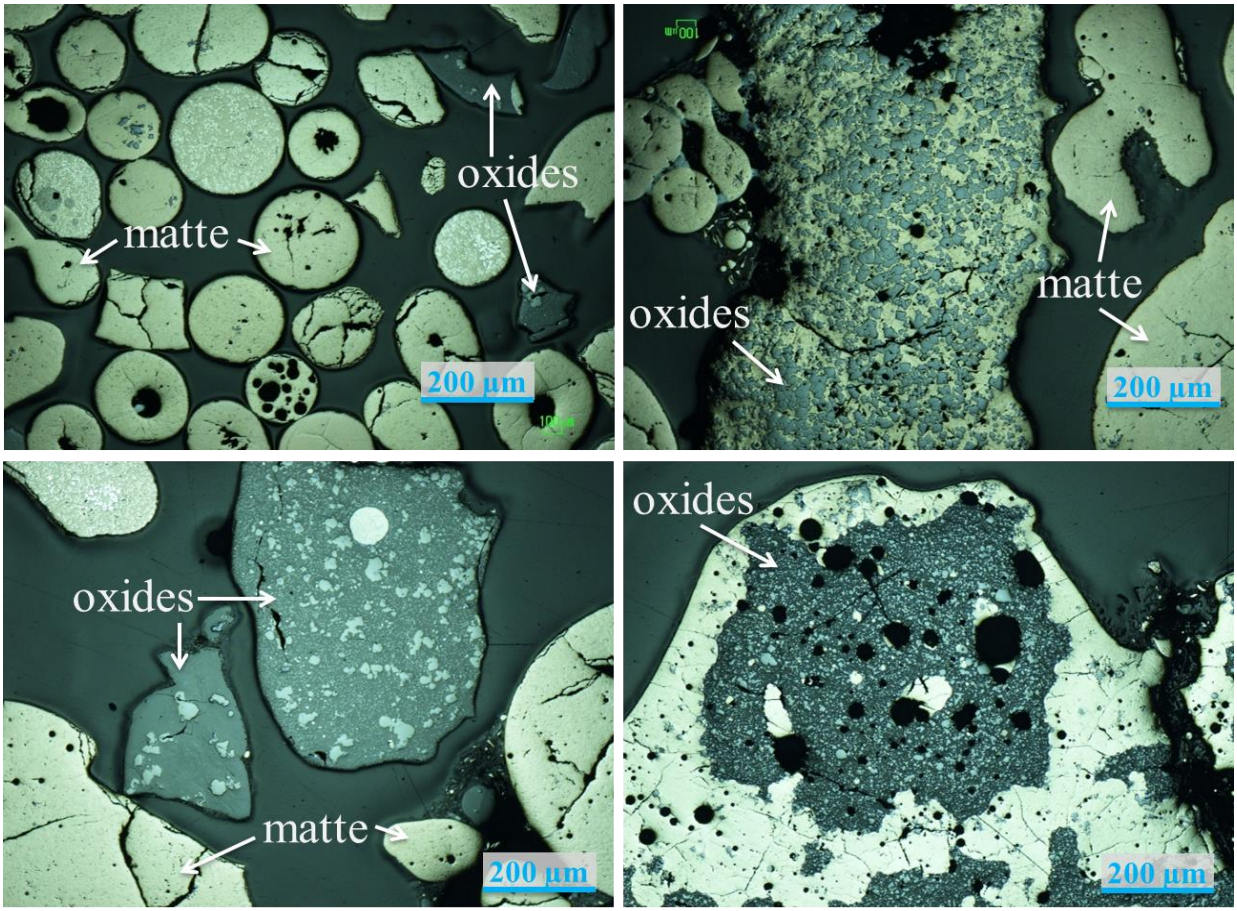

Figure 4-4: Oxide inclusions in the Matte-A sample, matte and oxides are annotated in the images, the background is the resin, optical microscope images

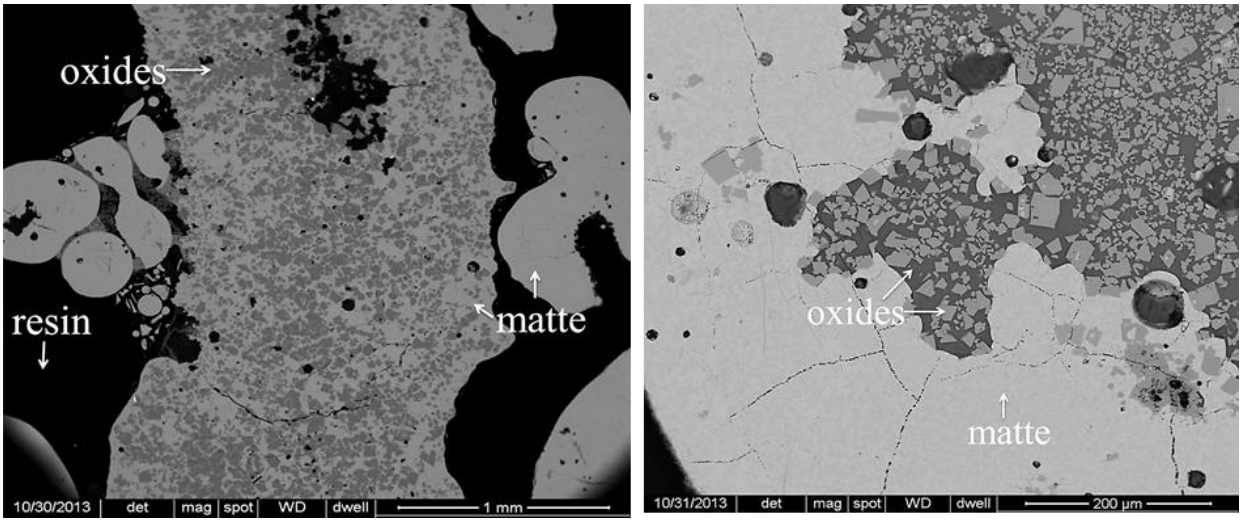

Figure 4-5: Oxide impurities in Matte-A sample, BSE images, matte and oxides are annotated in the images, light phases are matte, grey phases are oxides, the background is the resin

4.2.2.2 Amplats-Polokwane matte (Matte-P)

An industrial matte with undetectable amounts of oxides was acquired from Amplats-Polokwane smelter. Amplats-Polokwane smelter primarily treats Platreef concentrate, after tapping the Polokwane matte is cast and crushed. The major differences from Matte-A and Matte-P are the concentrate type and the treatment after tapping. The concentrate used to produce Matte-A was a blend of Merensky, UG2 and Platreef, while Matte-P was produced from a Platreef concentrate [Hundermark et al. 2011]. Matte-A was granulated while Matte-P was cast. Matte-P and Matte-A were subjected to XRF to determine their chemical composition, the XRF analysis are in Table 4-9.

Matte-P had minute amounts of Al and Si impurities when compared to Matte-A, Al was 0.6 mass percent and Si was 0.2 mass percent. The chrome content in Matte-A and Matte-P was 1.1 mass percent. The amount of chrome in Matte-P gave a clue that there might be a chromite in Matte-P such as detected in Matte-A. Matte-P was used as a purer form of industrial matte since it had minimal amounts of silicate impurities.

Table 4-9: XRF analysis of Matte-A and Matte-P (mass percent)

	Al	**Co**	**Cr**	**Cu**	**Fe**	**Mg**	**Ni**	**S**	**Si**	**Total**
Matte-A	0.8	0.7	1.1	10.7	44.7	1.6	16.5	20.9	3.0	100.0
Matte-P	0.6	0.7	1.1	12.3	42.0	0.0	17.5	25.7	0.2	100.0

4.2.2.3 Lonmin matte (Matte-L)

Matte-L was acquired from the Lonmins' No.1 furnace that uses a blend of UG2 and Merensky ore as a feed material. The tapping temperature of Matte-L varied from 1390 °C to 1450 °C. During operation the Lonmin matte is tapped into ladles and transported to the Pierce Smith converters for the conversion of matte. The received sample was a spoon sample that was taken during furnace tapping.

Matte-L was subjected to XRD to determine the composition of its phases; quantitative analyses are shown in Table 4-10. Pentlandite, troilite and bornite-digenite solid solution were major phases detected by XRD in Matte-L; Fe-Ni alloy was detected as a minor phase. Fe-Ni alloy is

expected in the slow cooled matte since at 450 °C Fe-Ni alloy is in equilibrium with pentlandite and monosulfide solid solution as seen in Figure 3-3 (Fe-Ni-S phase diagram).

Matte-L was subjected to EPMA to determine the chemical composition of the phases; summary of EPMA analysis is in Table 4-11. A metal-rich pentlandite, troilite and a bornite-digenite solid solution were detected as major phases constituting Matte-L. The metal to sulfur ratio of a high-form pentlandite can vary from a metal rich $(Fe,Ni)_9S_{6.93}$ to $(Fe,Ni)_9S_8$ [Kitakaze et al. 2011] hence the formulas calculated in Table 4-11 varies slightly from the ideal formulas. Bornite and digenite coexist as a solid solution in the Cu-S system as discussed by Vaughan et al. 1978, hence the formula in Table 4-11 deviates from the ideal formula, the Cu-S phase diagram is in Figure 3-7.

A metallic phase (Fe, Ni) was not detected by EPMA; this could be attributed to the low concentration of (Fe, Ni) alloy in the matte. An oxide phase ($FeCr_2O_4$) was detected by EPMA in Matte-L; this phase was not detected by the XRD. The sulfide phases detected by XRD and EPMA in Matte-L were comparable.

Table 4-10: XRD quantitative analyses of Matte-L (mass percent)

Phase	**Formula**	**Mass percent**	**3-σ error**
Awaruite	Ni, Fe	2.0	0.3
Bornite	Cu_5FeS_4	8.3	1.2
Pentlandite	$(FeNi)_9S_8$	55.7	1.1
Troilite	FeS	34.0	0.9

Table 4-11: EPMA analyses of the Matte-L sample (mass percent)

Phase	**Formula**	**S**	**Cu**	**Ni**	**Fe**	**Cr**	**O**
Bornite-digenite	$(Cu, Fe)_xS_y$	22.4	68.2	0.6	8.8	-	-
Pentlandite	$(FeNi)_xS_y$	32.7	4.1	21.0	42.2	-	-
Troilite	FeS	36.5	2.6	2.7	58.2	-	-
Chromite	$(FeCr)_xO$	-	-	-	25.0	43.0	26.0

4.2.3 Synthetic matte (Matte-S)

A synthetic matte was prepared in the laboratory using pure sulfide powders. It was necessary to test the behaviour of the synthetic matte since all the industrial matte samples had traces of slag

phases and other compounds that geologically associate with the PGMs. The starting mixture for preparing Matte-S was calculated based on the published composition of a typical industrial matte. Sulfide powders acquired from Sigma-Aldrich were used for making synthetic matte. The mass fractions of the starting mixture are shown in Table 4-12. Cobalt was not included in the Matte-S mixture since it's a minor phase in the PGM matte. The purity and XRD analysis of sulfide powders are shown in Table 4-13. The composition of the pure sulfides are discussed in turn:

4.2.3.1 Composition of the sulfide powders

The sulfide purity values given in Table 4-13 were extracted from the supplier's data sheet, the phases detected by the XRD analysis are also included in Table 4-13.

Copper sulfide powder consisted of a mixture of Cu-S phases with Cu:S ratio ranging from 1:1 to 2:1. Iron sulfide powder was of low purity (technical grade); the cost of acquiring the pure iron sulfide was uneconomical for this project. As such, the starting iron sulfide had 83 mass percent FeS, 9 mass percent Fe and 8 mass percent FeO. Nickel sulfide powder consisted of a mixture of Ni-S phases with varying phase compositions (Ni:S ratio varied from 1:1 to 3:2).

4.2.3.2 Synthesis of Matte-S

The sulfide powders were weighed according to the proportions in Table 4-12; the sulfide mixture was loaded into an alumina crucible. The alumina crucible was further enclosed in a sealable steel crucible to minimize loss of gases to the atmosphere. The specimen was heated for 1 hour at 1100 °C in a vertical-tube electric furnace. The molten matte was then slow cooled at 4 °C/min to 50 °C. Matte-S was subjected to XRD, ICP and LECO to determine the composition of the phases and elemental composition. XRD quantitative analysis is shown in Table 4-14, ICP and LECO analysis are given in Table 4-15.

4.2.3.3 Analysis of Matte-S

Matte-S had $(FeNi)_9S_8$, FeS, Cu_5FeS_4 and (Fe, Ni) alloy. Minor amounts of Fe_3O_4 were detected by XRD in Matte-S; the source of Fe_3O_4 was the technical-grade FeS that was used as a starting material. The elemental composition of Matte-S by ICP and LECO is given in Table 4-15.

Minute amount of carbon (0.03 mass percent) was detected in Matte-S (LECO analysis); carbon could originate from the impurities in the starting sulfide powders.

Oxygen was measured by the titration method, it gives an indication of the dissolved oxygen in a sample. The oxygen content in Matte-S was up to 3.3 mass percent, this can be attributed to the presence of iron oxide. Matte-S was not purified before use, it was tested as produced.

Table 4-12: Mass fractions of sulfide powders for Matte-S synthesize

Compound	**(mass percent)**
Cu_2S	12
Ni_3S_2	22
FeS	66

Table 4-13: Purity and XRD analysis of as received sulfide powders

Compound	***Purity (mass percent)**	**Phases detected by XRD**
Cu_2S	99.99	Cu_2S, CuS
Ni_3S_2	99.70	Ni_xS
FeS	85.00	FeS, Fe, FeO

*Supplier's specification

Table 4-14: XRD quantitative analyses of Matte-S

Phase	**Formula**	**Mass %**	**3-σ error**
Awaruite	Ni, Fe	3.65	0.26
Bornite	$Cu_{5.4}Fe_{1.1}S_4$	8.29	0.99
Magnetite	Fe_3O_4	6.59	0.63
Pentlandite	$(Fe, Ni)_9S_8$	56.52	1.02
Troilite	FeS	24.97	0.87

Table 4-15: ICP and LECO analysis of Matte-S

Mass percent	**S**	**Fe**	**Ni**	**Cu**	**C**	**O_2**
Synthetic matte	26.79	44.61	16.41	8.87	0.03	3.28

4.2.4 XRF analysis of industrial and synthetic matte

Matte-A, Matte-L, Matte-P and Matte-S were subjected to XRF to confirm the chemical composition of all the matte samples, summary of XRF analysis is in Table 4-16. The major elements constituting matte are Co, Cu, Fe, Ni, and S; the other elements in the matte are inclusions. The composition of industrial matte presented in Table 4-16 is comparable with the published composition (Table 2-3). Al, Cr, Mg and Si are not present in Table 2-3, since these are inclusions in industrial matte. The chemical compositions of the matte specimen are comparable in all matte samples, except the impurities in Matte-A.

Matte-L, Matte-P and Matte-S had average sulfur content of 26 mass percent while Matte-A had significantly lower sulfur content of 21 mass percent. Matte-A also had significant amounts of Al, Cr, Mg, and Si. The presence of these elements in Matte-A confirms the presence of the slag phases in Matte-A as detected by EPMA analysis. The sulfur content in Matte-A could be diluted by the presence of the impurities.

The Cr content of Matte-L is slightly higher than that of Matte-A and Matte-P. This confirms the presence of chromite in Matte-L as detected in the EPMA analysis (Table 4-11). Although the sulfide content of matte was comparable, the behaviour or properties of these matte types could differ due to the presence of impurities in matte.

Table 4-16: XRF analysis of industrial and synthetic matte samples (mass %)

	Al	**Co**	**Cr**	**Cu**	**Fe**	**Mg**	**Ni**	**S**	**Si**	**Total**
Matte-A	0.8	0.7	1.1	10.7	44.7	1.6	16.5	20.9	3.0	100.0
Matte-L	0.5	0.6	1.7	9.3	44.8	0.0	15.7	27.3	0.1	100.0
Matte-P	0.6	0.7	1.1	12.3	42.0	0.0	17.5	25.7	0.2	100.0
Matte-S	0.5	0.3	0.1	11.1	45.8	0.1	16.8	25.1	0.2	100.0

Matte-A has the highest amount of impurities based on its Si and Mg content. Cr in the industrial matte samples is higher than the published values. This confirms the presence of an oxidic chromite phase in the matte samples. Al content is below 1 mass percent for all matte types, in Matte-S Al could be inclusions from the alumina crucible used during the synthesis of Matte-S.

Matte-S has minute amounts of Al, Co, Cr, Mg and Si as impurities, these elements could originate from the technical grade FeS which was used in the starting mixture, and the total amount of these impurities is below ~1 mass percent.

The common impurity in industrial matte samples is Cr, Matte-A also has Mg and Si, Mg and Si were not detected in Matte-L and Matte-P. In this aspect Matte-A might behave slightly different from Matte-L and Matte-P.

Matte-S and industrial matte differs in that Matte-S has negligible amounts of Cr, in this aspect Matte-S might behave differently to industrial matte.

4.2.5 Industrial PGM slag

To study the interaction between graphite and the industrial slag, slag samples were acquired from Amplats-Waterval (slag-A) and Lonmin (slag-L). The slag samples were analysed using XRF to confirm the chemical composition of the samples, XRF analysis are presented in Table 4-17.

The published composition of industrial slag (Table 2-4) and the XRF analysis of the industrial slag are comparable. The major oxides in the slag are (in decreasing order) SiO_2, FeO/Fe_2O_3, MgO, CaO, Al_2O_3 and Cr_2O_3.

The compounds in these two slag samples are comparable; there is no significant difference in the composition.

Table 4-17: XRF analysis of Slag-A and Slag-L (mass %)

	Al_2O_3	**CaO**	**Cr_2O_3**	**CuO**	**Fe_2O_3**	**K_2O**	**MgO**	**SiO_2**	**SO_3**	**TiO_2**
Slag-A	3.8	6.5	2.5	0.1	22.7	0.3	9.3	51.9	1.3	0.7
Slag-L	3.0	8.9	2.7	0.2	25.2	0.3	8.7	47.9	1.9	0.2

4.3 Apparatus

To study the interaction between the carbon-based refractories and a liquid PGM melt (matte and slag), the specimen had to be heated to typical operating temperatures of a PGM smelter. A coal ash fusion furnace and a vertical tube furnace were used as a heating source in this work. The layout and the operating specifications of these furnaces are presented in this section. Thermodynamic simulations of the reactions were done using FactSage 7.0 software. The apparatus are discussed in turn.

4.3.1 FactSage

FactSage is a thermochemical software that has databases for pure compounds and for solutions; FactSage has been described by Bale et al. 2009. The Fact(PS) database contains the data for pure species. An FTmisc_miscellaneous database contains data for sulfides, metals and alloys. Equilib is a module available to calculate the concentrations of chemical species when species react to reach chemical equilibrium [Bale et al. 2009]. The mentioned databases were used during the simulations in this work. FactSage was used to predict the stable phases at given temperatures. The melting points of pure compounds were also determined using FactSage.

The challenge encountered with FactSage was that the databases available have limited data on PGM ores. There is also a limitation on the databases that can be used simultaneously e.g. some matte databases cannot be simultaneously used with the metal databases. But the matte databases do not have the alloys such as Fe-Ni although this phase is in equilibrium with the sulfides according to the phase diagrams. There is also no sulfide database that has dissolved carbon. Due to these challenges the use of FactSage was limited and accurate modelling of the element distribution when matte is in contact with carbon was not done. Although FactSage allows entry of elements and compound to the databases, addition of alloy phases (FeNi-Si) was avoided since the thermodynamic data for these phases is not known. It is recommended that a database be added on FactSage that includes the metal phases that are in equilibrium with the sulfide at the PGM operating temperatures. Such database will improve the accuracy of the simulations done in FactSage especially for PGM containing sulfides.

4.3.2 Coal Ash fusion furnace

Wettability tests were carried out in a Coal Ash Fusion (CAF) furnace using a sessile drop method. A CAF furnace is a horizontal tube furnace that is heated using silicon carbide heating elements. The furnace working tube is made of sintered alumina with an inside diameter of 80 mm. The work tube is fitted with stainless steel flanges at both ends. The gas inlet and outlet ports are fitted on the flanges. The furnace temperature is controlled and measured using a B-type thermocouple placed inside the furnace tube at the hot zone. The CAF furnace is rated at 1600 °C. It is fitted with a digital camera to enable image capturing; the camera is connected to a computer that stores the images that have been captured. A schematic diagram of the CAF experimental set-up is shown in Figure 4-6.

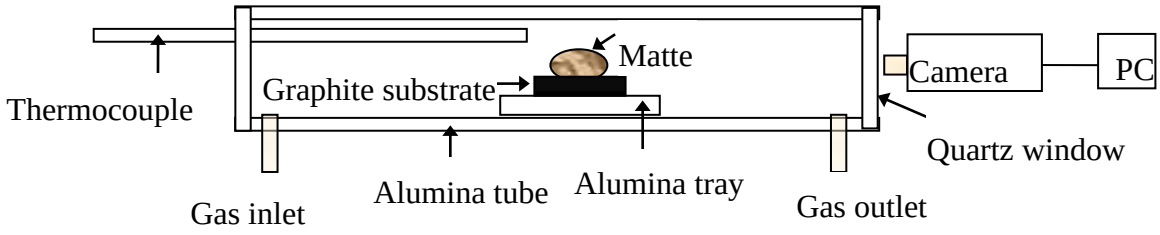

Figure 4-6: Schematic diagram of the Coal Ash fusion furnace setup

The CAF furnace was used because it was equipped to record wetting angle, melting point and softening point, the images captured were used to determine these properties. The interfacial contact angle between the molten droplet and the substrate was measured from the images; the contact angle was used to evaluate wettability.

4.3.3 Vertical tube furnace

Crucible tests were performed in an electrically heated vertical-tube furnace. A schematic diagram of the vertical-tube experimental set-up is shown in Figure 4-7. The furnace work tube was a sintered 99.5 percent Al_2O_3. It had a 65 mm ID and 100 mm hot-zone. This furnace was heated externally using $MoSi_2$ heating elements. A thermocouple was positioned on the outer

surface of the working tube approximately in the centre of the hot zone. This thermocouple was connected to the controller that regulates the temperature of the furnace. Another thermocouple (S-type [Pt-Rh10/Pt]) was inserted inside the work-tube; this thermocouple detected the temperature inside the furnace.

4.3.3.1 Temperature profile

To determine the temperature profile of the work tube the furnace was heated to 1000 °C and to 1600 °C. The temperature was measured from the top lid to below the hot zone. Measurements were taken every 10 cm with 0 cm being the top of the lid. The resulting temperature profile is shown in Figure 4-8a. The hot zone was from 60 cm to 70 cm from the lid. For a set point of 1000 °C the operating temperature read 964 °C to 966 °C, at a set point of 1600 °C the working temperature read 1555 °C to 1559 °C at the hot zone.

The hot zone temperature had an offset of about 4 percent; this was because the working temperature was measured at the centre of the work tube whereas the control thermocouple was situated next to the elements (outside the work tube). The sample stand was placed such that the bottom of the specimen was at 70 cm from the lid of the work tube.

4.3.3.2 Oxygen measurements

The work-tube was sealed with water-cooled brass caps on both ends. The top brass cap had a gas outlet port and a thermocouple port through which the working thermocouple and SIRO_C700+ oxygen probe fitted. The oxygen probe was occasionally used to determine the amount of oxygen in the furnace. Oxygen could potentially consume the graphite specimen at the operating temperatures since graphite is prone to oxidation. Oxygen was kept minimal by purging the furnace with purified argon gas. Argon was passed through zirconium turnings at 300 °C for purification. The gas inlet port was at the bottom brass-cap. Purified argon was continuously purged through the furnace to ensure inert working environment and to prevent the oxidation of the working crucible. A sample stand made of alumina was fitted inside the work tube, such that the sample level was at the furnace hot zone.

The oxygen partial pressure was measured inside the furnace work tube before the specimen was inserted. The graph with the measured oxygen is shown in Figure 4-8b.

It was observed that without argon purge the oxygen inside the worktube was 0.18 atmospheres around 850 °C. When the work tube was purged with argon the oxygen drops to 0.0009 atmospheres. It is envisaged that the amount of oxygen drops when the specimen is inserted to the worktube since the specimen contains graphite and was enclosed in a graphite crucible. Reducing conditions are envisaged when graphite is present since the available oxygen will react with carbon and form Co or CO_2 depending on the temperature.

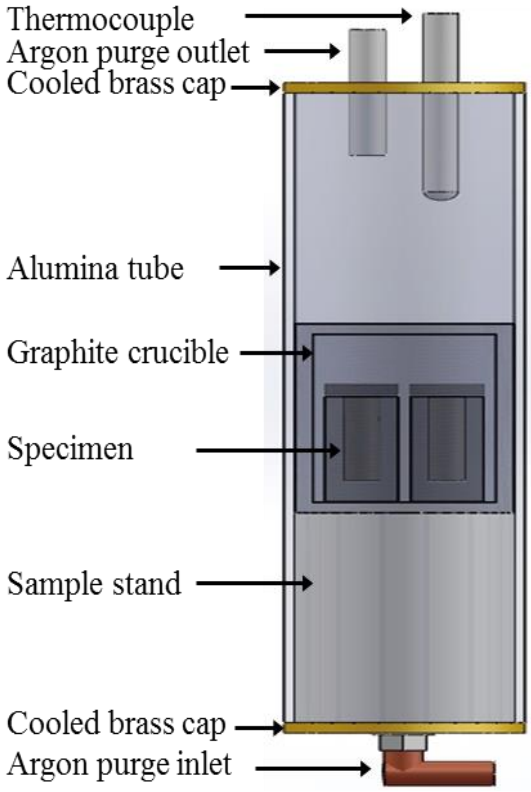

Figure 4-7: Schematic illustration of the static crucible test set-up (vertical tube furnace)

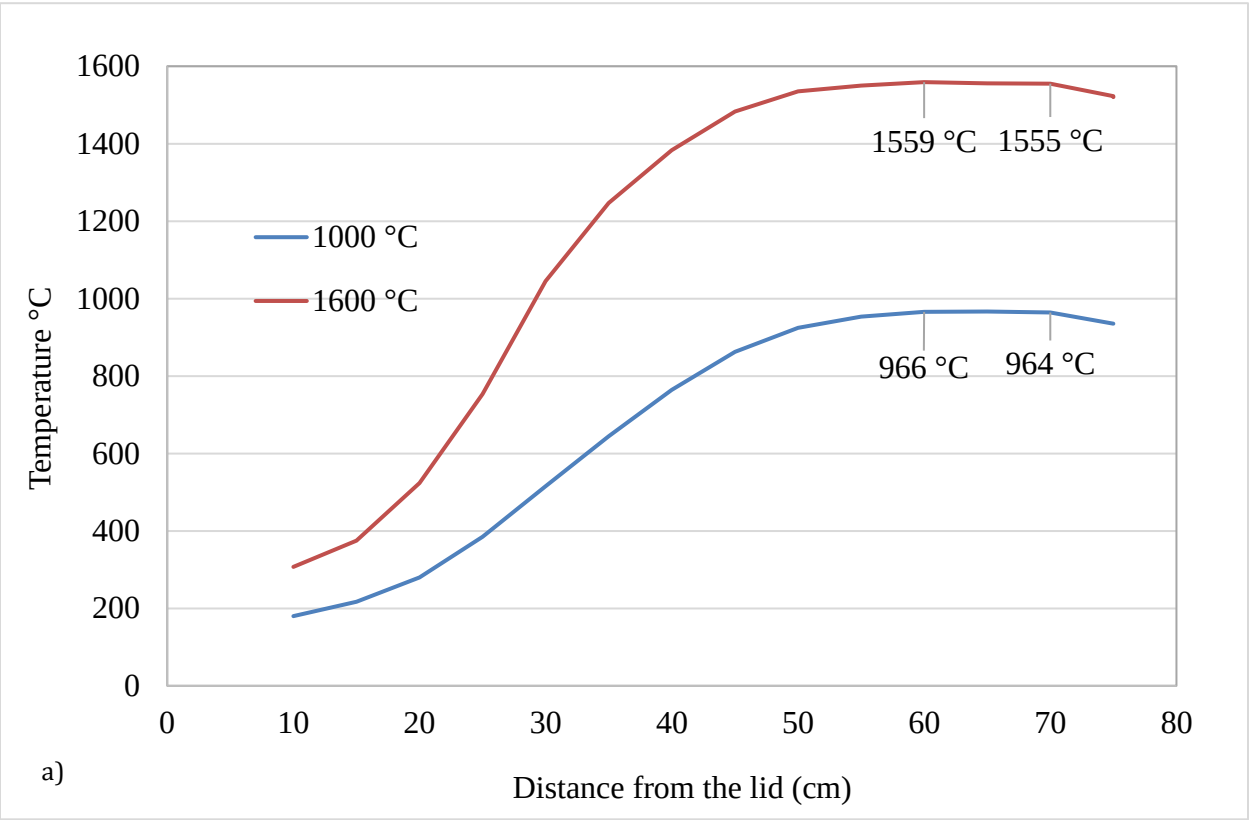

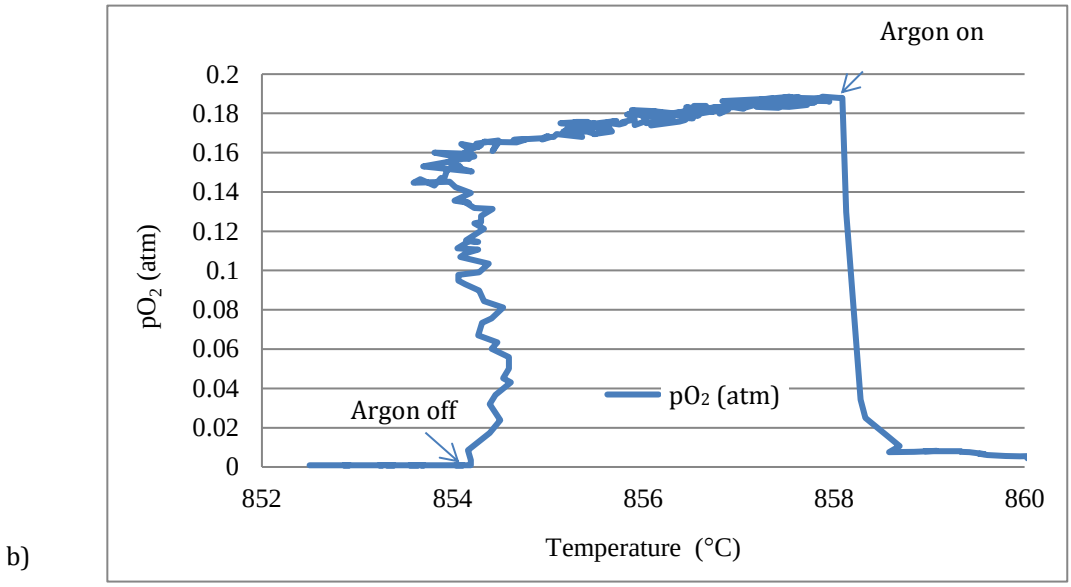

Figure 4-8: a) Temperature profile of a vertical tube furnace, b) oxygen measurement inside the worktube without the specimen, O_2 reading with argon and without argon is annotated

4.4 Experimental procedures

To study the wear mechanism of carbon-based refractories by a primary PGM matte and slag wettability tests and crucible tests were performed. This section entails the procedures used to prepare the specimen, the experimental designs and the procedures used to prepare the sample for analysis.

4.4.1 Wettability test measurements

The objective of the wetting tests was to determine the interfacial contact angle between the refractory (solid substrate) and the molten sulfide droplet. A sessile drop configuration was adopted for these tests. In a sessile drop method, the material is prepared into a pellet, a pellet is placed on the surface of the flat, smooth, solid substrate [Luz et al. 2008, Eustathopoulos et al. 1999, Lee et al. 2004]. The specimen is heated to the melting temperature and the interfacial contact angle between the molten droplet and the solid substrate is measured [Eustathopoulos et al. 1999].

When the pellet is heated the temperature at which the pellet starts deforming is called the deformation temperature. The hemisphere temperature is the temperature where the pellet is deformed to the point where it assumes a hemispherical shape. The fluid temperature is the temperature at which the pellet flattens out to a pancake shape [Raask 1985]. In this work the hemisphere temperature is taken as the fluid temperature since the pellets never got to a point where they flatten out.

4.4.1.1 Experimental procedure

Sulfide powder samples were formed into cylindrical pellets using a press and die. During pelletizing a powder sample was weighed into the mould and a hydraulic press was used to compress the powder unto a pellet. A typical pellet was 10 mm diameter and ± 5 mm in height. A typical specimen setup is depicted in Figure 4-9; a pellet was placed on a graphite block with these dimensions (20 mm x 20 mm x 5 mm). The specimen was placed in an alumina tray for containment.

A CAF furnace was used for the wettability tests (Figure 4-6). The specimen was pushed into the hot zone of the furnace at the beginning of the test. The furnace temperature was then raised to 1350 °C at 7 °C/minute. The furnace was continuously purged with high purity argon in order to maintain inert atmosphere inside the furnace. The furnace camera was set to capture an image of the specimen every 2 °C starting from 650 °C, the last image was taken at 1350 °C, when possible. A video of the specimen was recorded continuously during the experiments. The deformation and hemispherical temperatures of the pellet were recorded manually using the video and captured images. The melting temperature, volume and shape of the droplet were used to assess the melting behaviour of the matte and the pure sulfides.

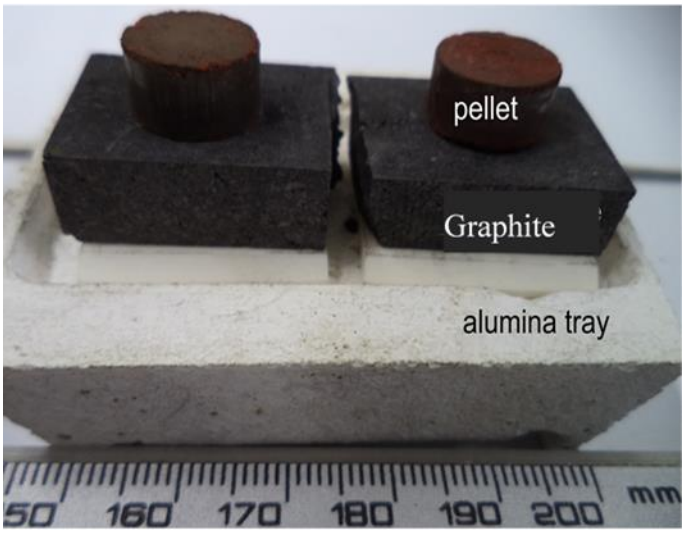

Figure 4-9: Wettability specimen layout showing a pressed pellet, a graphite substrate and the alumina tray

Graphite wettability was determined by direct measurement of the interfacial contact angle between the molten material and the graphite block. Contact angles between graphite and the molten droplet were determined from images captured by the camera during the experiments. The contact angle considered was the angle formed immediately after the droplet was fully molten, this was done to minimise errors associated with long contact time. The contact angle between the substrate and the droplet was measured manually on printed images using a protractor. For each image the contact angle was measured on both sides, the contact angles

reported were the average of the angles from both ends of the droplet. After melting, the specimen was cooled under argon after which it was subjected to SEM for analysis.

4.4.1.2 Experimental design

The wettability test conditions are summarized in Table 4-18. All the tested materials (pure sulfides, matte and slag) were heated to 1350 °C. The initial tests were done to observe the melting behaviour, wetting angle and the behaviour of the molten droplet with increasing temperature. All the tests were repeated twice to confirm the melting behaviour. Other tests were repeated at lower final temperature for two reasons; to study the mechanism of droplet inflation and to heat the droplet such that it does not fall off the substrate. Matte-A was repeated at 915 °C and at 1000 °C. Matte-P was repeated at 940 °C. Matte-L was repeated at 1030 °C.

Table 4-18: Wettability tests conditions

	Final temperature (°C)	**Repeat 1 (°C)**	**Repeat 2 (°C)**
Ni_3S_2	1350	-	-
Cu_2S	1350	-	-
FeS	1350	-	-
Matte-S	1350	-	-
Matte-L	1350	1030	-
Matte-A	1350	915	1000
Matte-P	1350	940	-
Slag A	1350	-	-
Slag L	1350	-	-

4.4.2 Prominent wear mechanism of graphite by a PGM melt (matte and slag)

A vertical tube furnace was used for static crucible tests (refractory exposure to synthetic and industrial matte as well as industrial slag) and for melting the synthetic matte. Crucible tests were performed to assess the resistance of carbon-based refractories to chemical attack (penetration and dissolution) by a PGM matte. Refractories were received as rectangular blocks of 20 mm x 20 mm x 80 mm. To create a crucible, these blocks were cored out using a 10 mm drill bit. The

dimensions of the crucible were the following, 10 mm inside diameter, 60 mm depth and 5 mm thickness.

The matte samples were milled to fine powder and weighed into the crucible. The matte was filled to the top edge of the crucible; the mass of the matte would vary slightly from one crucible to the next. A typical mass of matte in a filled crucible was between seven grams and nine grams. The matte-filled crucible was closed with a lid of the same grade material as the crucible.

A carbon paste was applied between the crucible and the lid to ensure a tight seal. The paste was applied at the area where the lid contacts the crucible; the lid and the crucible were pressed together for a tight seal, to ensure that there are no spaces between the lid and the crucible. The estimated final thickness of the paste (between the lid and the crucible) was less than 1 mm. The paste was cured at 120 °C before the specimen was exposed.

The graphite-matte specimen was enclosed in a graphite crucible to prevent contamination of the specimen and to capture any material that might penetrate through the inner crucible. A typical crucible specimen is shown in Figure 4-10. Figure 4-10a) shows the specimen layout for the experiments used for refractory exposure to matte. The specimen layout for graphite exposure to PGM melt (matte and slag) is shown in Figure 4-10b), the matte occupied the bottom of the crucible and the slag was filled from the centre to the top of the crucible.

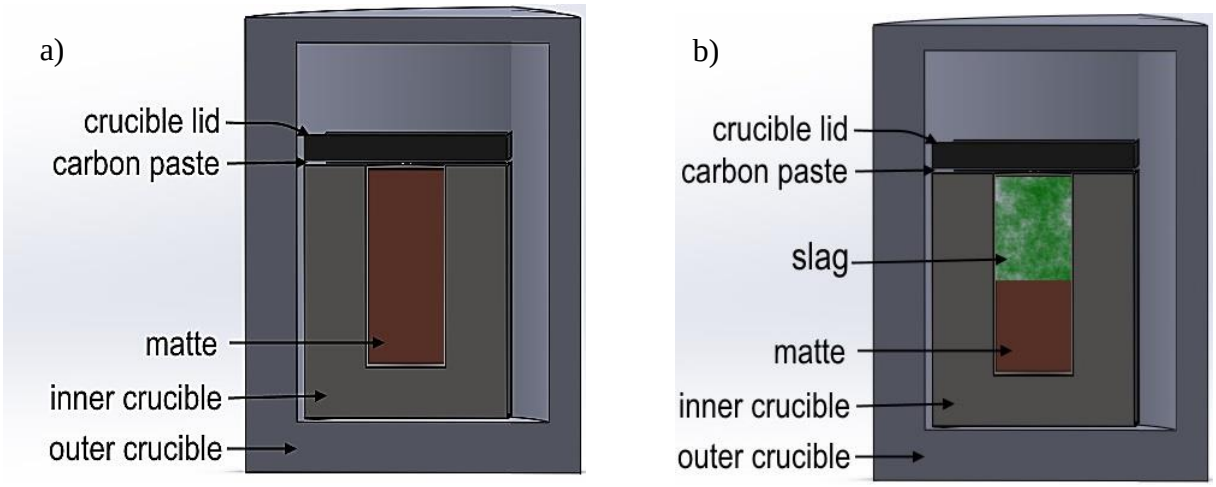

Figure 4-10: Refractory-matte specimen before exposure, a) a matte only set-up; b) graphite-slag/matte specimen, the layout of inner and outer crucible is shown, the filling level and a layout of matte and slag is shown

The specimen was loaded into the furnace (Figure 4-7) and placed on top of the sample stand (hot-zone), a steel wire was used to drop the sample to the sample stand. The furnace was heated to temperature at 4 °C/minute. The furnace was held at operating temperature for a specified duration. When the contact time had lapsed the furnace was slow cooled to below 50 °C at 4 °C/minute. The specimen was removed from the furnace using the steel wire. Each specimen was weighed before and after the experiment. The cooled samples were cut axially, mounted in resin and polished for analysis. A portion of the solidified sample (matte) was milled for ICP, LECO and XRD analysis to determine the elemental composition and composition of the phases in the samples. Samples were analysed using ICP for elemental composition, LECO for carbon and sulfur and XRD for crystalline phases.

4.4.2.1 Graphite dissolution by Matte-S

Matte-S was exposed to graphite to study the solubility of graphite in Matte-S. The variables were operating temperature and contact time. The solubility of graphite in matte was studied by determining the change in the carbon content of the matte after exposure. Matte residue was analysed using LECO to determine the amount of carbon in matte. The loss of matte was also monitored since the loss of matte affected the composition of the residual matte. The operating parameters are summarised in Table 4-19.

4.4.2.1.1 Effect of temperature

The operating temperature was varied from 1150 °C, 1350 °C to 1550 °C, this temperature range was selected based on the liquidus temperature of matte (875 °C) and typical matte tapping temperature which ranges from 1380 ºC to 1600 ºC [Eksteen 2011]. From Matte-S synthesis, it was observed that Matte-S was only molten above 1100 °C hence the low operating temperature for Matte-S was 1150 °C. The operating temperature was limited to 1550 °C to prolong the service life of the furnace work tube and the thermocouples. The mid-temperature (1350 °C) experiments were repeated five times to determine repeatability of the experiments.

Table 4-19: Effect of temperature and contact time on the dissolution of carbon by Matte-S

Matte type	Variable	Levels	Response 1	Response 2
Matte-S	Temperature (°C)	1150, 1350, 1550	%C in matte	% matte loss
Matte-S	Contact time (days)	1, 3, 5	%C in matte	% matte loss

4.4.2.1.2 Effect of contact time

The specimens were heated to 1550 °C, and reacted for either 1, 3 or 5 days. In industrial applications the refractory is expected to last for years but running laboratory experiments for extended periods is not economical since the operating equipment is not designed to be in operation for long periods of time. Varying contact time from 1 to 5 days gave an indication of the effect of time whether the interaction between the refractory and melt is enhanced with time or if the interaction is not a function of contact time. The mid-contact time (3 days) experiments were repeated 5 times to determine the repeatability of the experiments.

4.4.2.2 Penetration of Matte-S through graphite

The degree of penetration of Matte-S through the SG graphite was studied by monitoring the loss of matte (comparing the starting mass of matte with the mass of the residual matte). The variables were the operating temperature and the contact time. The summary of operating conditions is shown in Table 4-20.

4.4.2.2.1 Effect of temperature and contact time

The operating temperature was 1150 °C, 1350 °C and 1550 °C. The selection of the low temperature 1150 °C was based on the melting temperature of Matte-S which was 1100 °C. The temperature was varied in order to determine the effect of increasing temperature on the penetration of Matte-S through graphite. Tests run at 1150 °C and 1550 °C were repeated 3 times, the tests run at 1350 °C were repeated 5 times.

The contact time was varied from 1, 3 to 5 days; the contact time was varied in order to determine the effect of exposure time on the penetration of Matte-S through graphite. The tests

run at 1 day and at 5 days were repeated 3 times, the tests run for 3 days were repeated 5 times to determine repeatability.

Table 4-20: Effect of temperature and contact time on Matte-S penetration through graphite

Matte type	Variable	Levels	Repeats	Response
Matte-S	Temperature (°C)	1150, *1350, 1550	3	% matte loss
Matte-S	Contact time (days)	1, *3, 5	3	% matte loss
**The mid points (1350 °C and 3 days) were repeated 5 times*				

4.4.2.3 Penetration of liquid industrial matte through graphite

Degree of penetration of liquid industrial matte through graphite was studied by determining the amount of liquid matte that was collected outside the crucible after exposure. The variables were the grade of graphite, the operating temperature and the contact time. The tested matte types were Matte-A, Matte-L and Matte-P.

4.4.2.3.1 Effect of graphite grade

Matte-A, Matte-L and Matte-P were exposed to SG and HG graphite at 1000 °C for a contact time of 12 hours. Each test was repeated 3 times. The summary of operating parameters is shown in Table 4-21.

4.4.2.3.2 Effect of temperature

Matte-A, Matte-L and Matte-P were exposed to SG graphite at a temperature range from 800 °C to 1450 °C for a contact time of 1 hour. Each test was repeated 3 times. The summary of operating conditions is shown in Table 4-22. The response was the amount of liquid matte that was collected outside the crucible after exposure.

4.4.2.3.3 Effect of contact time

Matte-A and Matte-L were exposed to SG graphite at 1450 °C for 1, 3, 6, 9 and 12 hours. Each test was repeated 3 times. The summary of operating conditions is shown in Table 4-23. The response was the amount of liquid matte that was collected outside the crucible after exposure.

Table 4-21: Effect of graphite grade on the degree of penetration of liquid industrial matte through graphite

Matte type	Variable (graphite type)	Temperature (°C)	Contact time (hours)	Repeats
Matte-A Matte-L Matte-P	HG SG	1000	12	3

Table 4-22: Effect of temperature on penetration of liquid industrial matte through SG graphite

Matte type	Variable Temperature (°C)	Contact time (hours)	Repeats	Responses
Matte-A Matte-L Matte-P	800 900 1000 1250 1450	1	3	Liquid matte penetration

Table 4-23: Effect of contact time on penetration of liquid industrial matte through SG graphite

Matte type	Variable Contact time (hours)	Temperature (°C)	Repeats	Responses
Matte-A Matte-L	1 3 6 9 12	1450	3	Liquid matte penetration

4.4.2.3.4 Effect of matte level

The industrial matte was exposed to SG graphite at 1150 °C for 1 hour to determine the influence of the level of matte on the penetration of liquid matte through graphite. In one crucible, matte was filled to half-volume capacity, while another crucible was filled to capacity (to the top edge) with matte. The response was the amount of matte collected outside the crucible after exposure.

4.4.2.3.5 Collection of a gas condensate for verification of gas composition

During the current experiments, a gas condensate accumulated in the cooled portion of the furnace work-tube. The work-tube used was sealed with water-cooled brass caps as shown in Figure 4-7.

The off-gas pipe was connected to the top brass cap. During the exposure of the industrial matte to graphite an accretion accumulated at the top 15 cm of the work tube and around the cooled brass cap. The temperature of the work tube at the top was estimated to be 100 °C. The temperature of the cooled brass was ~25 °C. The off gas duct was cooled to ~0 °C using ice, this was done to trap the gaseous species that could condense at 0 °C.

Samples of gas condensate were collected after each run where industrial matte was exposed to SG graphite. A composite gas condensate (for a number of runs) was analysed using SEM-EDS to determine the elemental composition of the gas condensate. A condensate at 100 °C was collected on the work-tube, a condensate at 25 °C was collected on the cooled brass, and a condensate at 0 °C was collected on the cooled off-gas duct.

4.4.2.4 Graphite dissolution by industrial matte

Industrial matte was exposed to graphite to determine the degree of dissolution of graphite by a liquid matte. The variables were the graphite grade; the response was the carbon content in matte.

4.4.2.4.1 Effect of graphite grade

Matte-A, Matte-L and Matte-P were exposed to SG and HG graphite at 1000 °C for a contact time of 12 hours. The amount of carbon in the matte residue was determined. Each test was repeated 3 times. The summary of conditions is in Table 4-24.

Table 4-24: Effect of graphite grade on the dissolution of graphite

Matte type	Variable (graphite type)	Temperature (°C)	Contact time (hours)	Repeats	Responses
Matte-A Matte-L Matte-P	HG SG	1000	12	3	% C in matte

4.4.2.5 Interaction of industrial melt (slag/matte) with graphite

The industrial matte and slag were exposed to graphite simultaneously (in one crucible) to study the behaviour of these materials towards graphite. The operating temperature was 1450 °C and the contact time was 12 hours, this test was repeated 3 times. The response was the depth of penetration of the melt and the erosion of graphite. The summary of conditions is in Table 4-25.

Table 4-25: Interaction of industrial melt (slag/matte) with graphite

Melt	Contact time (hours)	Temperature (°C)	Repeats	Response
Slag-A/ Matte-A	12	1450	3	Graphite wear

4.4.2.6 The effect of cooling the graphite on the behaviour of liquid industrial matte

A test was done where the graphite crucible was cooled on one side to simulate the layout of a cooled refractory in industry. This was done to determine if cooling graphite will improve its resistance to penetration by a melt and to determine if the matte can form a frozen skull if the temperature of the refractory is below the solidus temperature of the matte.

A crucible test was designed such that the top portion of the crucible is water cooled while the bottom part of the crucible was at the operating temperature. A vertical tube furnace was used as a source of heat; the hot zone of the furnace was at the middle of the work tube about 70 cm from the top lid. The hot-zone of the furnace was 10 cm long, the bottom 10 cm of the crucible was within the hot zone. A water-cooled copper-cooling finger was attached to the lid of the crucible, to maintain the top portion of the crucible cold.

The graphite crucible had 60 mm outside diameter, 20 mm inside diameter and a depth of 250 mm. The matte was filled to 230 mm to avoid the penetration of matte during melting.

A graphite crucible with Matte-A was heated to 1350 °C, its lid was maintained at ~700 °C using a copper cooling finger. A thermocouple was positioned at the lid of the crucible to measure the lid temperature. A temperature gradient was established between the bottom of the crucible and the cooled lid (top of the crucible). The temperature of the crucible (from the lid to the bottom) was estimated using the temperature profile of the furnace as projected in Figure 4-8.

The estimated average temperature of the hot zone of the furnace was 1203 °C.

After 1-hour exposure the specimen was cooled and sectioned axially. Samples were taken every 10 cm from the top to the bottom of the crucible. Polished sections were analysed using the SEM. The operating conditions are summarised in Table 4-26.

Table 4-26: The effect of cooling graphite on the behaviour of industrial matte

Melt	Contact time (hours)	Temperature (°C)	Repeats	Response
Matte-A	1	1350	1	Skull formation

4.4.3 Prominent wear mechanism of a micropore carbon by a PGM matte

To determine the wear mechanism of MPC by matte, synthetic and industrial matte were exposed to MPC. The temperature was varied from 1350 °C to 1450 °C at a contact time of 12 hours. Each test was repeated 3 times. The responses were the change in the composition of the melt and the change in the structure of the refractory (chemical composition and layout). The summary of the operating parameters is shown in Table 4-27.

Table 4-27: Wear mechanism of micropore carbon by a PGM matte

Melt	Contact time (hours)	Temperature (°C)	Repeats	Response
Matte-S, Matte-A	12	1350	3	Change in chemical composition of the melt and the refractory
Matte-S, Matte-A	12	1450	3	Change in chemical composition of the melt and the refractory

4.5 Summary: Materials and methods

In this section the description of the analytical techniques, materials and apparatus was discussed. The analytical techniques included the carbon and sulfur analyser, EPMA, ICP-OES,

OM, SEM, XRD, XRF and XRM. The properties of the refractories were discussed, the refractories used were the HG graphite, SG graphite, carbon paste and the MPC.

The composition and the process history of the following matte samples were discussed, Matte-A, Matte-L, Matte-P and Matte-S. The composition of Slag-A and Slag-L was also given.

The apparatus discussed were FactSage, CAF furnace and a vertical tube furnace. The experimental procedures and experimental design for wettability tests and crucible tests were discussed in this section.

5 Results-A: Wear of graphite by a PGM melt (matte and slag)

The main objective of this work was to determine the most prominent wear mechanism when carbon-based refractories are in contact with a liquid PGM matte and a PGM slag. To achieve this objective wettability tests and crucible tests were performed. The materials, apparatus, experimental procedures and experimental designs for the experiments have been discussed in Chapter 4. This chapter has part A of the results that are wettability tests and crucible tests for graphite exposure to matte and slag. The results for the interaction of matte with MPC are reported in the following chapter that is part B of the results.

Results-A reports the outcome of the wettability test and crucible tests of graphite exposure to matte and slag.

- Wettability of graphite by pure sulfides (Cu_2S, FeS and Ni_3S_2), industrial matte, industrial slag and synthetic matte;

Wettability was the initial step in understanding the possible wear mechanism of SG graphite when it is exposed to sulfides, synthetic matte, industrial PGM matte and industrial PGM slag. The response was the contact angle between the graphite substrate and the molten droplet. Wettability tests addressed the first research question that was concerned with determining the wettability of SG graphite by the selected materials.

- Wear mechanisms of graphite by (synthetic matte, industrial matte and industrial slag);

Crucible tests were performed to further understand the interaction between graphite and a PGM matte (industrial and synthetic matte). The interaction between graphite and a PGM matte was investigated to determine the compatibility of graphite with the PGM matte. The responses were depth of liquid penetration and the degree of dissolution of graphite (carbon) in the melt as well as the erosion of graphite at the slag/matte interface. The effect of operating temperature and the contact time on graphite-melt interaction is presented.

The findings from the crucible tests addressed the second research question that was concerned with determining the prominent wear mechanism of graphite by a PGM melt (matte and slag).

- Effect of cooling the graphite on the behaviour of liquid industrial matte;

Graphite crucible was cooled on one side to determine whether matte could form a frozen protective layer if it is sufficiently cooled. This test addressed the third research question that dealt with prevention of liquid matte penetration.

5.1 Wettability of SG graphite

Wetting behaviour of pure sulfides (Cu_2S, Ni_3S_2 and FeS), industrial matte, industrial slag and synthetic matte is presented in this section. The contact angle between the graphite and the molten droplet of the tested materials is reported.

5.1.1 Wettability of graphite by pure sulfides

The recorded wetting angle, deformation temperature and the melting temperature of the pure sulfides are shown in Table 5-1. The melting temperatures determined by FactSage (FactPS) [Bale et al. 2009] and those published in the literature are shown in Table 5-1 for comparison.

Table 5-1: Contact angle, deforming and melting temperatures of sulfides

Material	Contact angle θ (°)	Melting temperature (°C)			
		Deforming	Melting	FactSage (FactPS)	**Published data
Ni_3S_2	107 ± 5	790	800	789	781
Cu_2S	108 ± 2	1000	1110	1130	1125
FeS	*130 ± 3	1100	1180	1190	1195

*this is the contact angle between the bulk droplet and the material adsorbed at the surface of the graphite
**Habashi 2002

The recorded contact angles between graphite and pure sulfides (Cu_2S and Ni_3S_2) were greater than 90°. The variation of the contact angle between graphite and each sulfide droplet was less than five percent.

The interfacial contact angle greater than 90° indicates non-wetting behaviour; therefore graphite was poorly wetted by pure sulfides (Cu_2S and Ni_3S_2).

FeS droplet was adsorbed on the graphite surface however the bulk droplet formed an angle with the adsorbed material. The angle between FeS and the adsorbed material was also greater than 90°.

A cross-section of the graphite-FeS specimen (BSE image) is shown in Figure 5-1. The profile of the specimen at the graphite-FeS interface is distinct, the FeS droplet is not in direct contact with the graphite, and the bulk material (FeS droplet) makes contact with the penetrated material. The elemental composition of the FeS droplet is shown in Table 5-2. The composition of the FeS droplet and the adsorbed material is similar therefore it is not conclusive whether the adsorbed sulfide is the same compound as the $Fe_{(1-x)}S$, in the bulk droplet.

Reactive wetting occurred between FeS and graphite based on the profile of the final wetting angle. The droplet intersects the penetrated material at an angle of 130°; this indicates non-wetting behaviour between penetrated material and the bulk droplet. Based on this contact angle it is plausible that the composition of the adsorbed material is different from that of the bulk droplet otherwise these materials would wet each other.

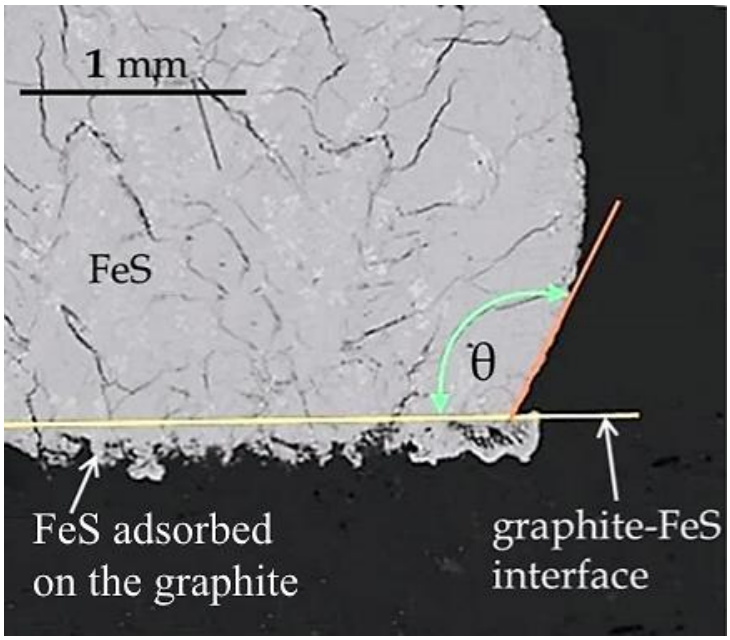

Figure 5-1: FeS droplet on the SG-graphite substrate after wettability test at 1180 °C, BSE image (θ is a contact angle), the adsorbed FeS and the initial graphite-droplet interface is annotated

It is not conclusive whether FeS wets graphite or not, a different method of wettability testing should be used to verify the wettability of graphite by FeS. A high purity FeS powder must be used for wetting tests, the FeS powder used for these tests was a technical grade which had a purity of 85 mass percent. The presence of the impurities might have played a role in the behaviour of the FeS droplet.

Quantitative analysis of the FeS droplet were not performed since some material was adsorbed on the graphite surface, it was not possible to remove the droplet off the graphite. Therefore the amount of metallic iron and oxide was not quantified.

Table 5-2: EDS analysis of the FeS droplet in Figure 5-1 (mass percent)

Element	bulk	bright
Fe	62	99.6
Cu	0	0.2
S	37.9	0
Ni	0.1	0.2

5.1.2 The melting behaviour of pure sulfides

The deformation and melting temperatures for tested sulfide pellets were recorded during wettability tests, the results are reported in this section.

5.1.2.1 Cu_2S

The deformation and melting stages of a Cu_2S pellet are shown in the images in Figure 5-2. Cu_2S started deforming at 1000 °C, the droplet seemed molten at 1110 °C. The melting of Cu_2S was very sluggish, the deformation and melting temperatures were 110 °C apart.

The Cu_2S droplet was analysed using SEM, EDS analysis are in Table 5-3. Two phases were identified by SEM on the Cu_2S residue, both phases were Cu_xS, one phase has about one mass percent Fe while another phase had no Fe. No metallic Cu or reduced phases were detected at the interface of the Cu_2S residue and the graphite. It seemed that there were no reactions between graphite and the Cu_2S droplet.

a)

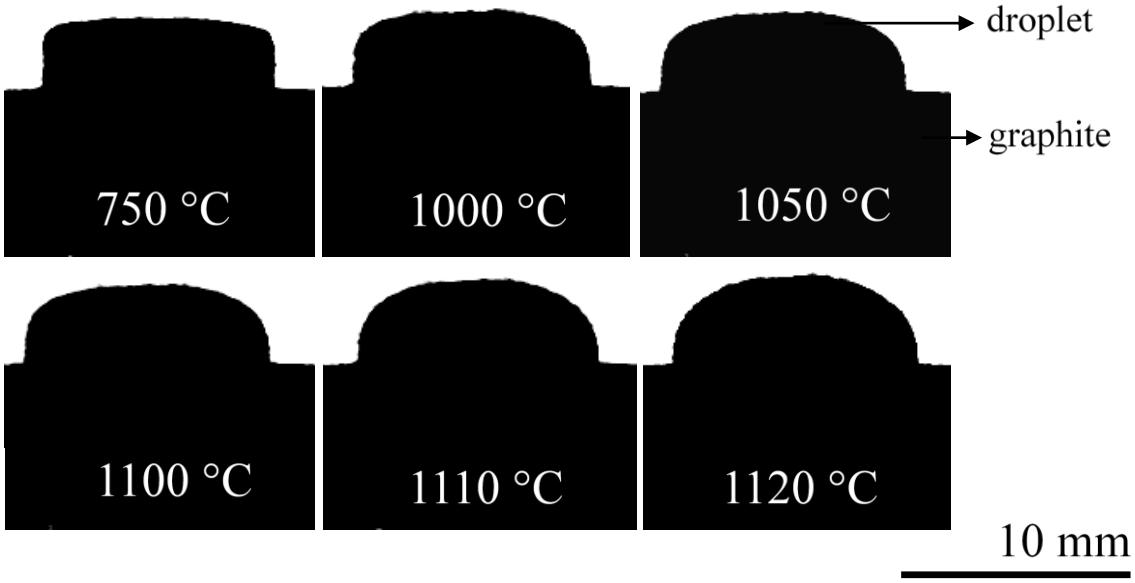

b)

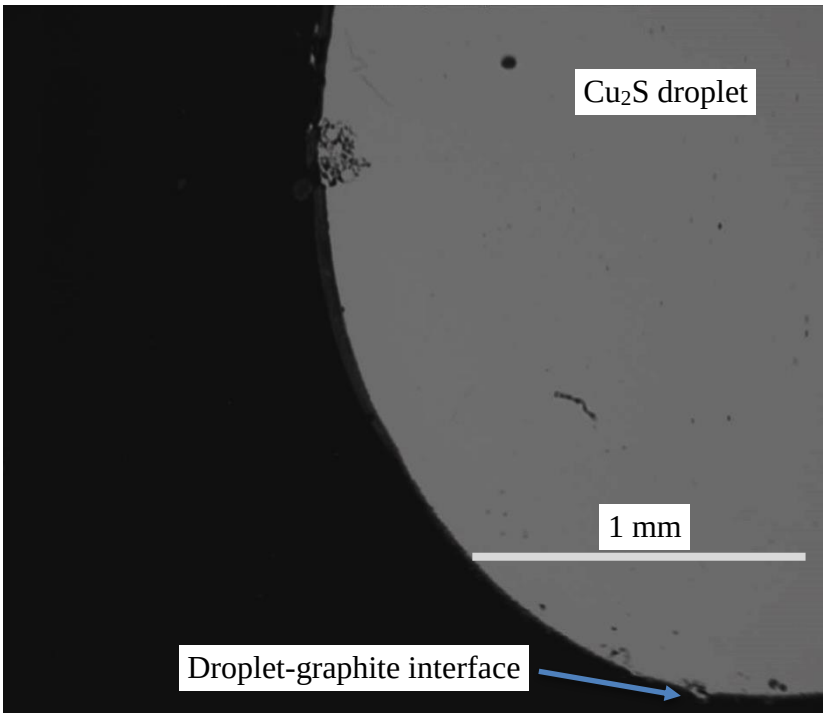

Figure 5-2: a) Cu_2S pellet on a graphite substrate, CAF furnace images from 750 °C to 1120 °C, b) BSE image of the Cu_2S droplet after exposure

Table 5-3: EDS analysis of the Cu_2S droplet after exposure to graphite at 1120 °C (mass percent)

Elements	Phase 1	Phase 2
Fe	1.4	0.2
Cu	75.9	78.0
S	22.7	21.9
Ni	0.0	0.0

5.1.2.2 FeS

The FeS pellet started deforming at 1000 °C, it seemed molten at 1180 °C, images of the FeS pellet during melting are shown in Figure 5-3. The FeS-pellet melted gradually; the softening and melting temperature (1000 °C to 1180 °C) was 180 °C apart.

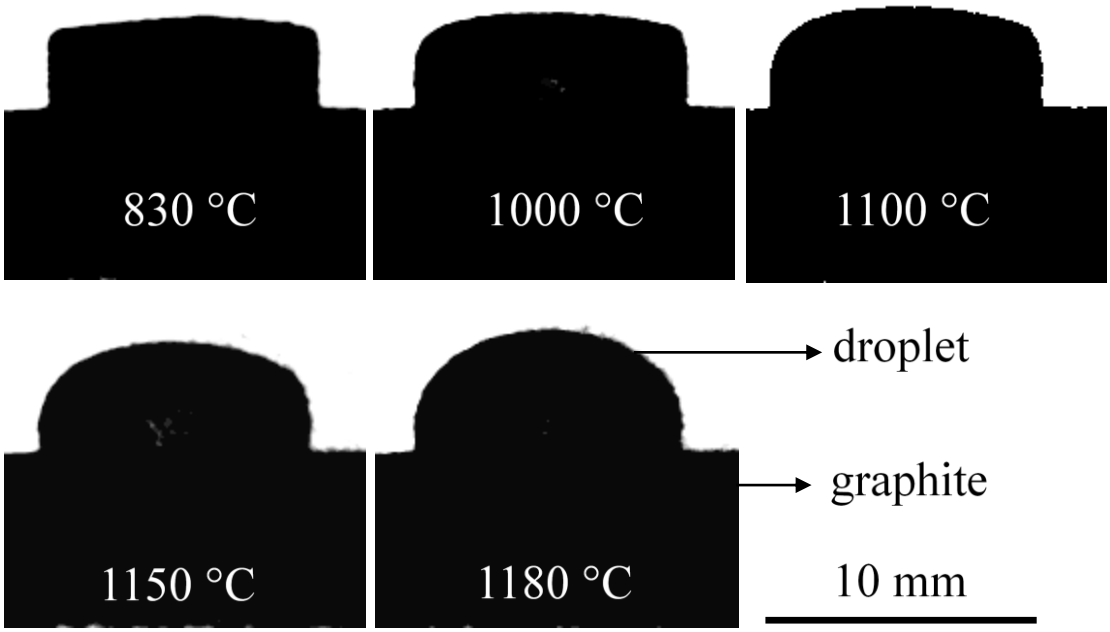

Figure 5-3: FeS pellet on a graphite substrate, CAF furnace images from 830 °C to 1180 °C

5.1.2.3 Ni_3S_2

Ni_3S_2 started deforming at 785 °C and the droplet appeared fully molten at 792 °C, the deformation and melting temperatures were 7 °C apart. Ni_3S_2 progressive melting stages are shown in the images in Figure 5-4.

No interfacial product was detected between graphite and the Ni_3S_2 droplet. The absence of any interfacial product indicated that there was no significant reaction between graphite and the droplet. Three phases were identified using the SEM, the phases varied in Ni:S ratio. The droplet residue had a composition corresponding to heazlewoodite (Ni_3S_2) and milllerite (NiS); the EDS analysis is in Table 5-4. No metallic phase was detected in the residue, this was an indication that sulfur losses by Ni_3S_2 were minimal and reactions between Ni_3S_2 and graphite were negligible.

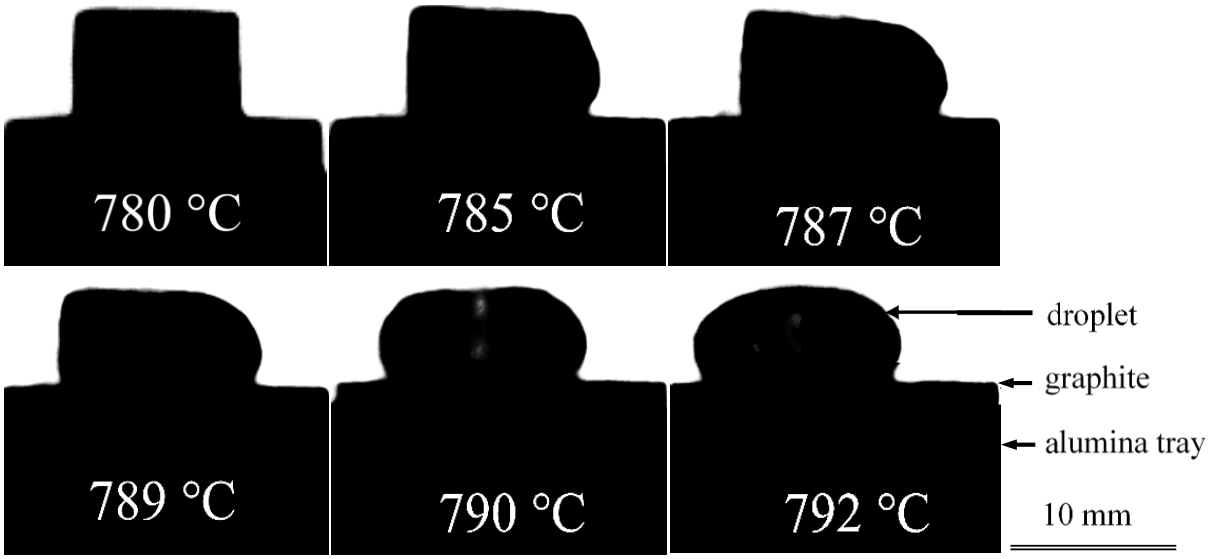

Figure 5-4: Melting of Ni_3S_2, CAF furnace images from 780 °C to 792 °C

Table 5-4: EDS analysis of Ni_3S_2 droplet after exposure to graphite at 792 °C (mass percent)

Element	Phase 1	Phase 2	Phase 3
Fe	0.1	0	0.4
S	25.7	21.1	13.6
Ni	74.2	78.9	86

5.1.3 Wettability of graphite by a synthetic and an industrial PGM matte

The recorded wetting angle, deformation temperature and melting temperature for Matte-A, Matte-L, Matte-P and Matte-S are shown in Table 5-5. Graphite was poorly wetted by all the tested matte samples, this was determined by a contact angle which was greater than 90°.

The Matte-A pellet rolled off the substrate before it was fully molten. A residue remained on the substrate after the bulk of Matte-A had fallen off the substrate, this material was named Matte-A residue. The Matte-A residue did not wet the graphite, the contact angle between graphite and the molten Matte-A residue was 120°.

Matte-A wettability test was repeated, the pellet size was decreased to 0.5 g to avoid the falling of the pellet before it is fully molten. The Matte-A wetting angle of a repeat test was 147 °C, therefore graphite was poorly wetted by Matte-A.

Table 5-5: Contact angle, deforming and melting temperatures of matte droplets on an SG-graphite substrate

Material	**Contact angle θ (°)**	**Temperature (°C)**	
		Deformation	Melting
Matte-S	113 ± 3	920	1070
Matte-L	126 ± 7	950	1020
Matte P	135 ± 5	850	950
Matte-A	147 ± 7	850	955
Matte-A residue	120 ± 5	1260	1350

5.1.4 Melting behaviour of synthetic and industrial matte

The deformation and melting temperatures of the matte pellets were recorded during the exposure. Matte-S, Matte-L, Matte-P and Matte-A were the matte samples tested for graphite wettability. The layout of the pellets and the composition of the residue are reported in turn.

5.1.4.1 Matte-S

Matte-S started deforming at 920 °C and was molten at 1070 °C; the images from deforming to melting are depicted in Figure 5-5. Matte-S initially spread on the graphite surface before the spherical droplet was formed. The volume of Matte-S remained constant during and after melting. The residue of Matte-S was analysed using SEM, BSE image is shown in Figure 5-6.

The Matte-S droplet had no apparent pores. Slight penetration of Matte-S into the graphite was observed. The contact angle was greater than 90° in both the CAF images and the SEM-BSE

images. The composition of Matte-S did not change during the contact with graphite, however; an oxy-sulfide phase was observed at the periphery of the Matte-S droplet, EPMA analysis is in Table 5-6.

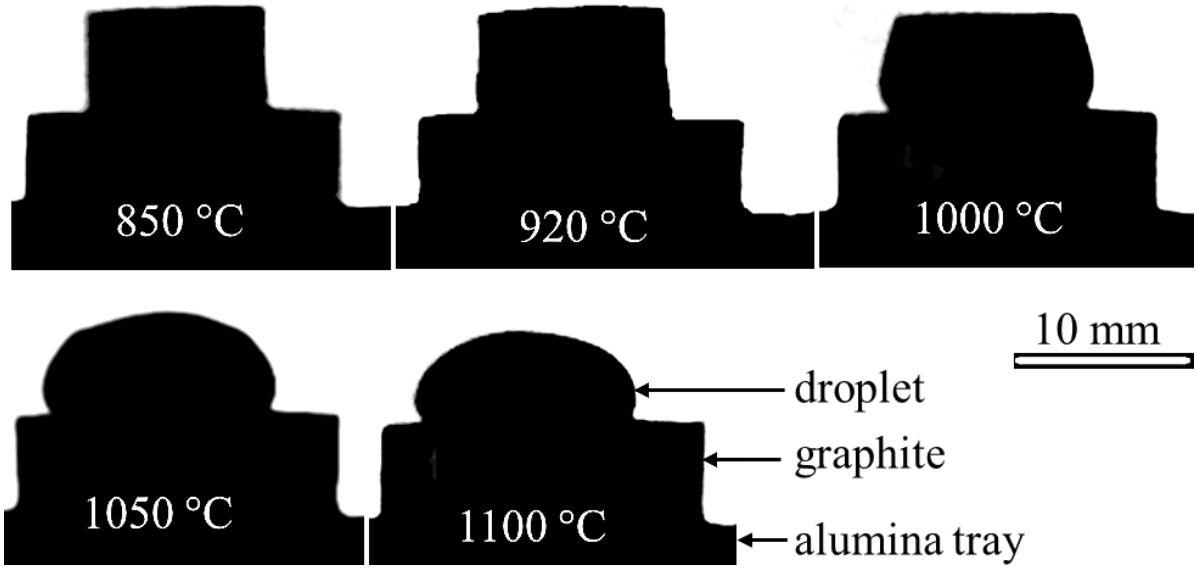

Figure 5-5: Matte-S droplet on the SG-graphite substrate (850 °C to 1100 °C)

Table 5-6: EPMA analysis of an oxy-sulfide at the periphery of the Matte-S droplet after exposure to SG-graphite substrate at 1100 °C (atomic percent)

Elements	S	Fe	Cu	O
Atomic percent	19.9	41.51	31.82	6.77

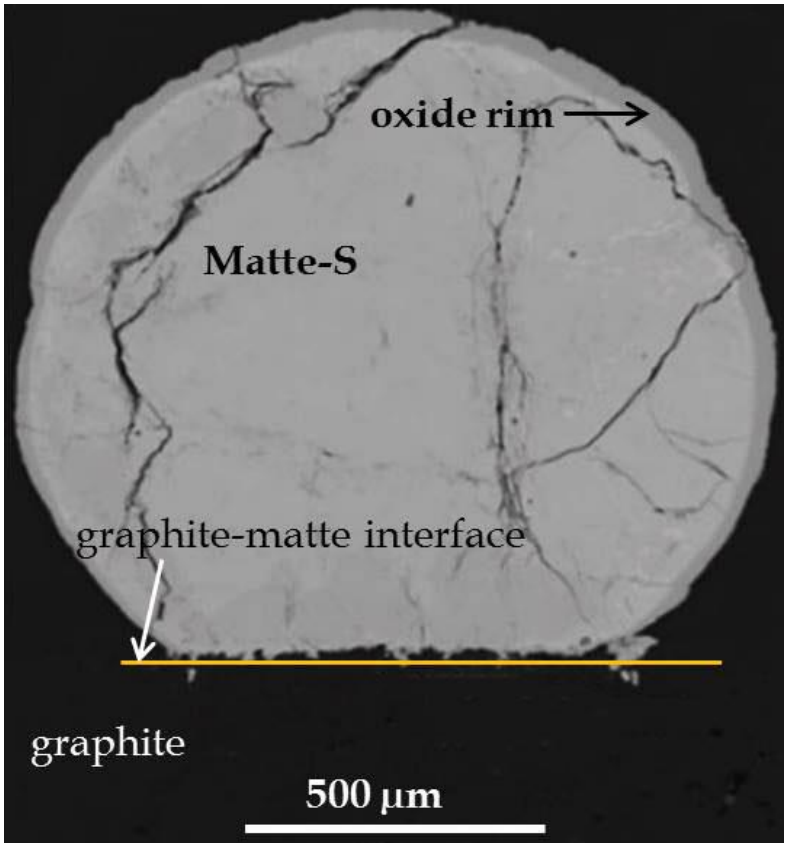

Figure 5-6: Matte-S droplet on the SG-graphite substrate, BSE image after exposure to 1100 °C

5.1.4.2 Matte-L

Matte-L started deforming at 950 °C and it appeared molten at 1020 °C, the images of a Matte-L pellet during melting are depicted in Figure 5-7. The volume of the droplet remained constant during melting, after melting the size of the pellet started decreasing with increasing temperature. The graphite substrate was analysed with SEM-BSE, matte species were not observed at the surface of the graphite substrate, BSE image is shown in Figure 5-8.

The Matte-L droplet in Figure 5-8 was heated to 1030 °C to study the state of the droplet just after melting. The droplet was porous and slightly inflated, the pores are annotated in Figure 5-8.

Matte-L droplet was analysed with EPMA to determine the interaction between the droplet and the graphite. No detectable changes were observed on the composition of the droplet. Interfacial

products were not observed between the graphite and the Matte-L droplet. Some oxide phases were detected in the Matte-L droplet, the EPMA analysis is in Table 5-7.

The abundant oxide phase was ($FeCr_2O_4$), other phases in Table 5-7 were in minute amounts. $FeCr_2O_4$ was also the most abundant impurity in the Matte-L sample (Table 4-10). The detection of $FeCr_2O_4$ in matte after exposure to graphite at 1030 °C indicates that at this temperature the oxide was not yet reduced by graphite. A BSE image of Matte-L droplet is shown in Figure 5-9, $FeCr_2O_4$ phase is observed scattered amongst the sulfide phases.

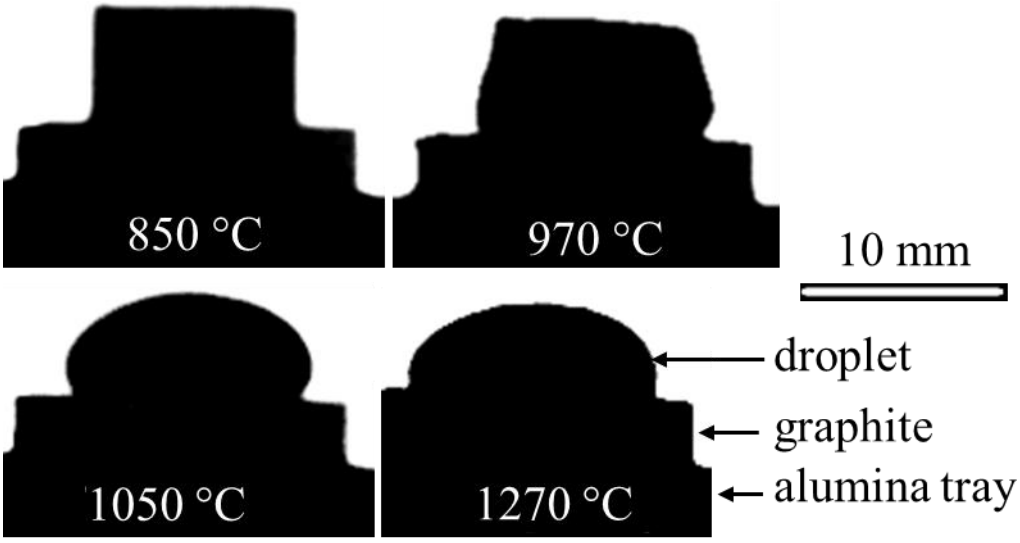

Figure 5-7: Matte-L droplet on the SG-graphite substrate (850 °C to 1270 °C)

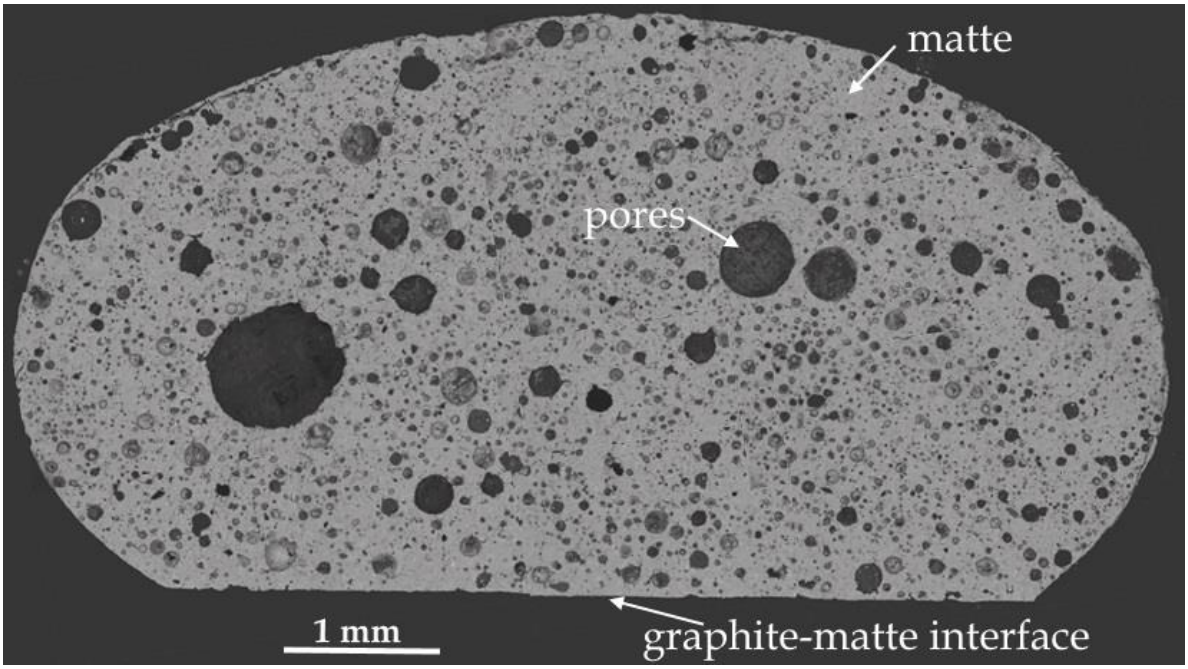

Figure 5-8: Matte-L droplet after exposure to 1030 °C on the SG-graphite substrate, BSE image

Table 5-7: EPMA analysis of the oxide phases in the Matte-L droplet residue exposed to SG-graphite at 1030 °C (atomic percent)

Al	Ca	Co	Cr	Cu	Fe	Mg	Na	Ni	O	Si
-	-	-	43.3	0.2	21.7	2.7	-	0.8	25.8	0.1
0.5	-	0.5	25.2	-	35.8	0.1	-	6.1	25.0	0.1
2.4	2.1	-	1.0	0.1	7.5	15.9	0.2	0.1	44.2	25.7
17.1	11.2	-	-	-	0.5	-	1.9	0.1	44.8	23.0
0.5	0.2	0.6	0.2	1.3	45.1	0.3	0.1	3.9	29.7	14.6

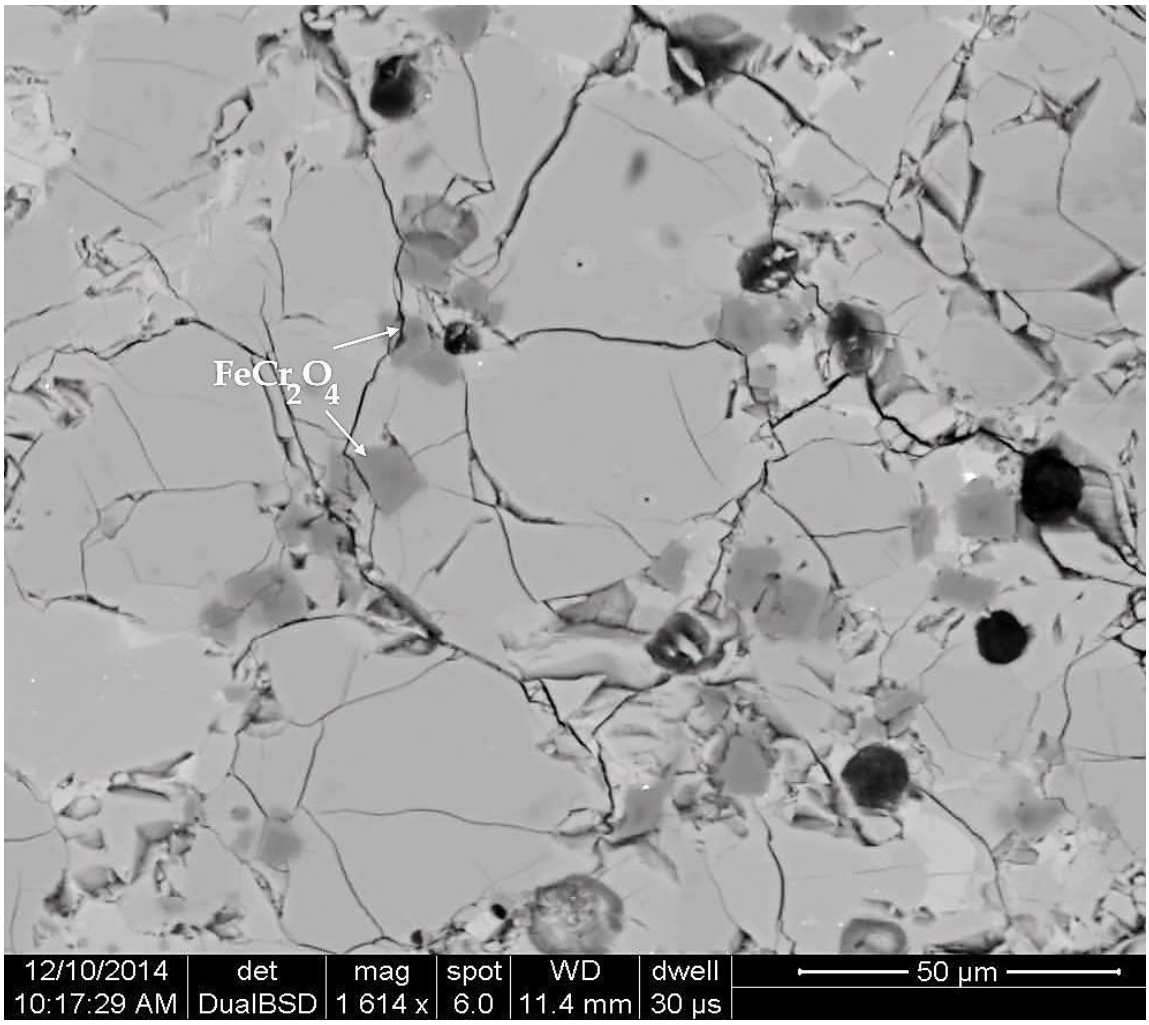

Figure 5-9: Matte-L BSE image after exposure to SG-graphite substrate at 1030 °C, oxide phases in matte are annotated

5.1.4.3 Matte P

Matte-P started deforming at 880 °C, it seemed fully molten at 950 °C. Inflation of the droplet was observed during melting. The exposure of the Matte-P droplet was repeated to determine the possible causes of the inflation of the pellet. The pellet was heated to 940 °C, BSE image of the droplet is shown in Figure 5-10.

Matte-P appeared porous after exposure to graphite at 940 °C. Matte-P droplet was analysed using SEM and EPMA to determine changes in the composition of Matte-P during melting, the detailed BSE image is shown in Figure 5-11. $(FeCr)_xO$ was the oxide phase detected by EPMA

in the Matte-P droplet, the EPMA analysis is in Table 5-8. Silicate phases were not detected in the Matte-P droplet.

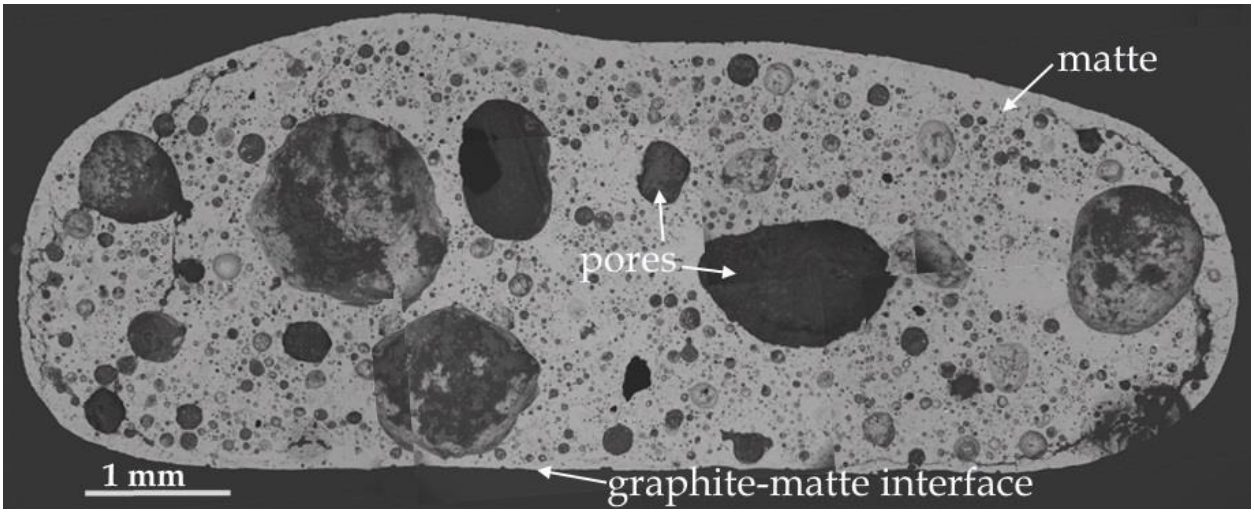

Figure 5-10: Matte-P droplet after exposure to SG-graphite substrate at 940 °C, BSE image

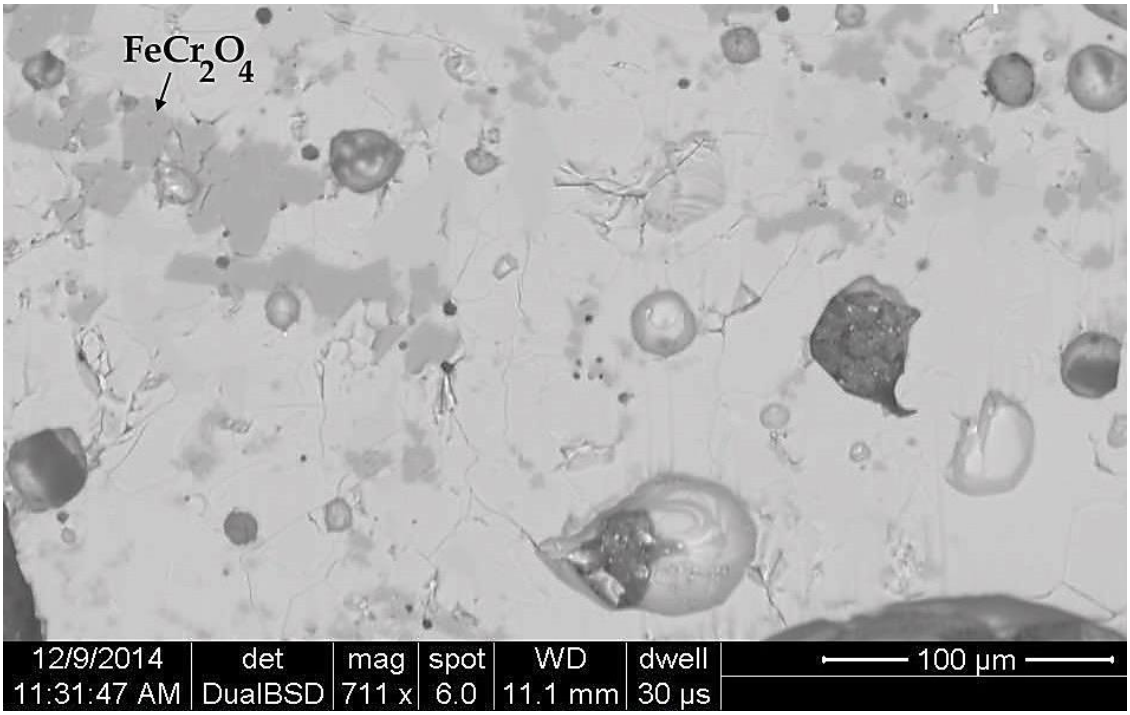

Figure 5-11: Matte-P BSE image; after exposure to SG-graphite substrate at 940 °C, BSE image

Table 5-8: EPMA analysis of the oxide phase in Matte-P droplet residue exposed to 940 °C (mass percent)

Co	Cr	Fe	Mg	Ni	O	Si
0.4	12.4	49.2	0.1	10.7	26.9	0.3
0.4	45.5	24.5	1.1	1.0	27.4	0.1

5.1.4.4 Matte-A

The deformation and melting images of Matte-A are shown in Figure 5-12. Matte-A started deforming at 850 °C. Significant increase in the volume of the droplet was observed during deformation. ImageJ software was used to measure the change in volume of Matte-A droplet, the volume of the droplet increased by 25 percent.

The Matte-A pellet rolled off the graphite block at 1100 °C, before it was fully molten. The droplet falling was gradual and the material seemed very sticky.

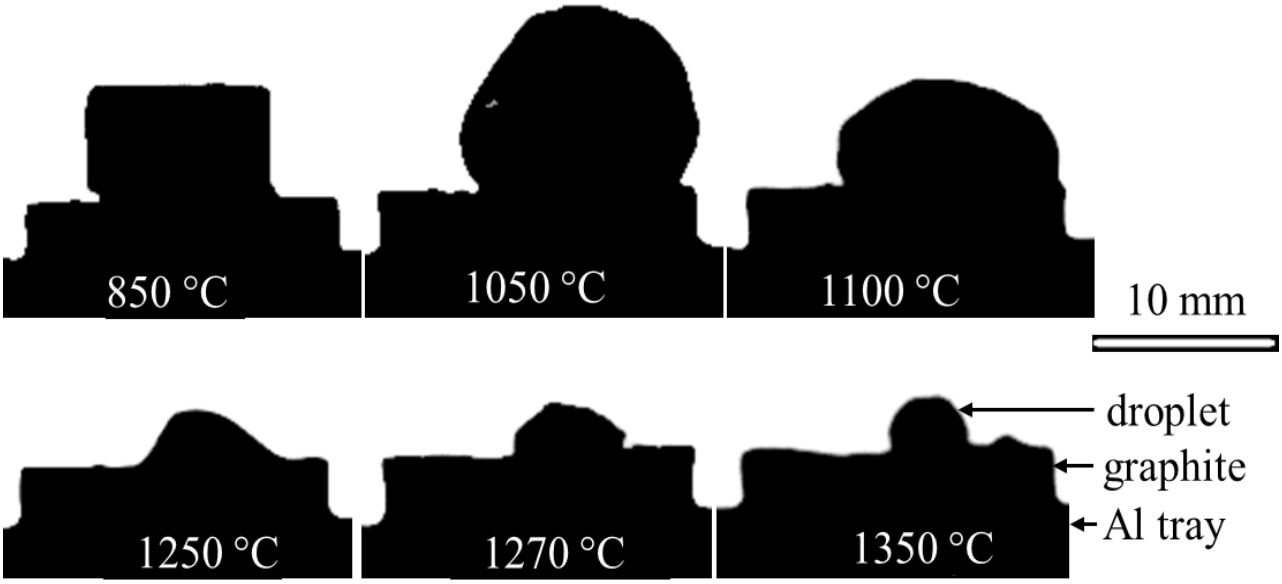

Figure 5-12: Matte-A droplet on graphite substrate (850 °C_droplet deforming, 1050 °C_an inflated droplet during melting, 1100 °C_a droplet during falling, 1250 °C_residue before melting, 1270 °C_residue during melting, 1350 °C_a molten residue)

A small amount of material remained on top of the graphite after the bulk of the matte had fallen off (Figure 5-12, Matte-A 1250 °C). Matte-A residue appeared molten at 1350 °C; it formed a contact angle of 120° with graphite. The Matte-A residue was analysed using SEM and EPMA.

A cross-section of the Matte-A residue is shown in Figure 5-13 (BSE image), the composition of the annotated phases is in Table 5-9. The major phases in the Matte-A residue were silicates of Fe-Ca, Fe-Mg and the oxides of Cr and Fe; these phases were similar to the slag-impurities detected in the Matte-A sample (Table 4-8). Minor amounts of sulfide phases were detected in the Matte-A residue, this indicated that when the matte-droplet fell off the substrate, some matte was trapped in the slag-impurities.

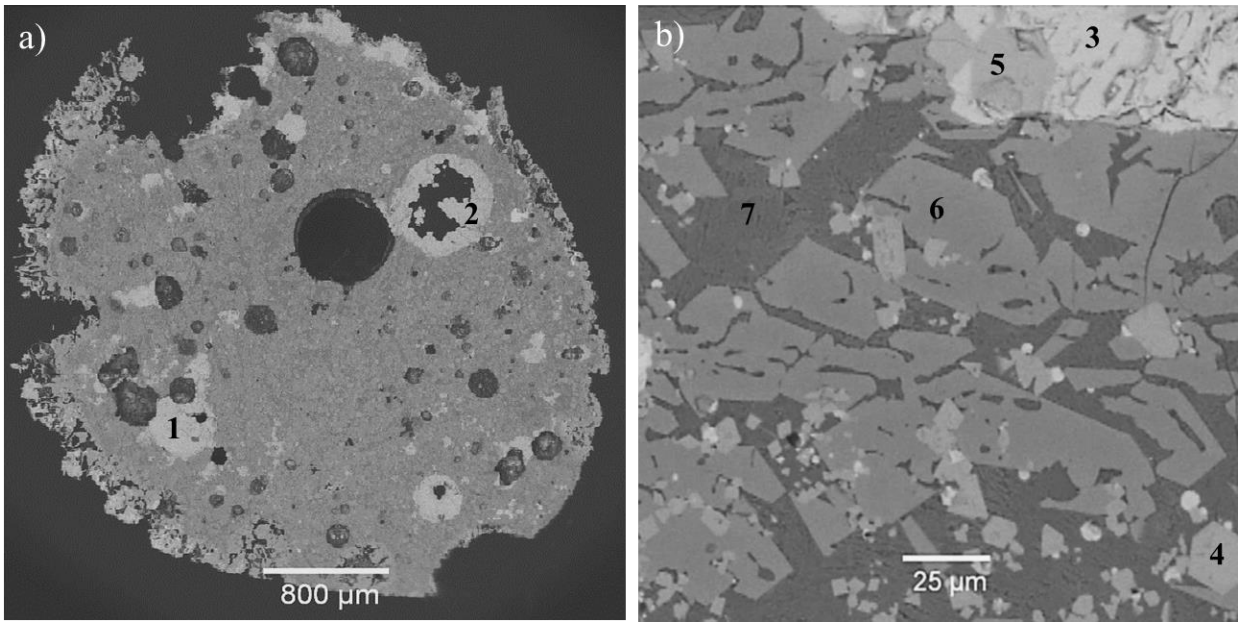

Figure 5-13: Matte-A residue BSE image after exposure to SG-graphite substrate at 1350°C; a) cross-section, b) detail of the phases, composition of the annotated phases (1-7) is in Table 5-9

Table 5-9: Composition of the Matte-A droplet residue (mass percent) by EPMA

Phase no.	Al	Ca	Cr	Cu	Fe	Mg	Mn	Ni	Si	S	O
1	-	-	0.5	77.8	1.2	-	-	0.2	-	20.0	-
2	-	-	-	28.8	34.9	-	-	2.1	-	34.0	0.6
3	-	-	-	2.4	51.7	-	-	7.8	-	37.0	0.6
4	-	-	48.2	-	24.5	1.0	0.3	-	0.1	-	25.9
5	-	-	-	-	73.0	-	-	-	0.3	-	26.7
6	-	0.4	1.0	-	45.7	5.6	0.6	-	15.3	-	31.4
7	2.0	14.3	0.6	-	23.4	0.7	0.5	-	21.8	-	36.9

Matte-A exposure was repeated in order to determine the mechanism for the expansion of the matte during melting. Two tests were done, one pellet was heated to 915 °C and another pellet was heated to 1000 °C. Droplets were analysed by SEM. Matte-A droplet at 915 °C is shown in Figure 5-14, the Matte-A droplet at 1000 °C is shown in Figure 5-15.

At 915 °C, Matte-A had evenly dispersed pores. The morphology of the droplet at 915 °C and 1000 °C shows that with increase in temperature the size of the pores increases. The droplet became inflated with the increase in temperature.

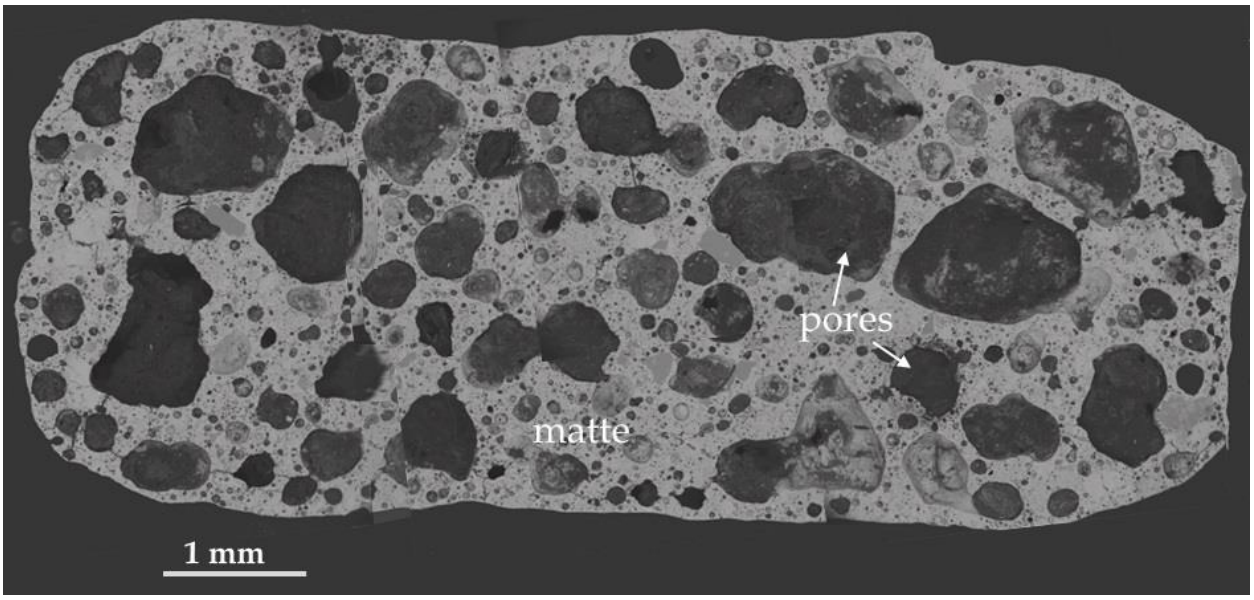

Figure 5-14: Matte-A after exposure to SG-graphite substrate at 915 °C, BSE image

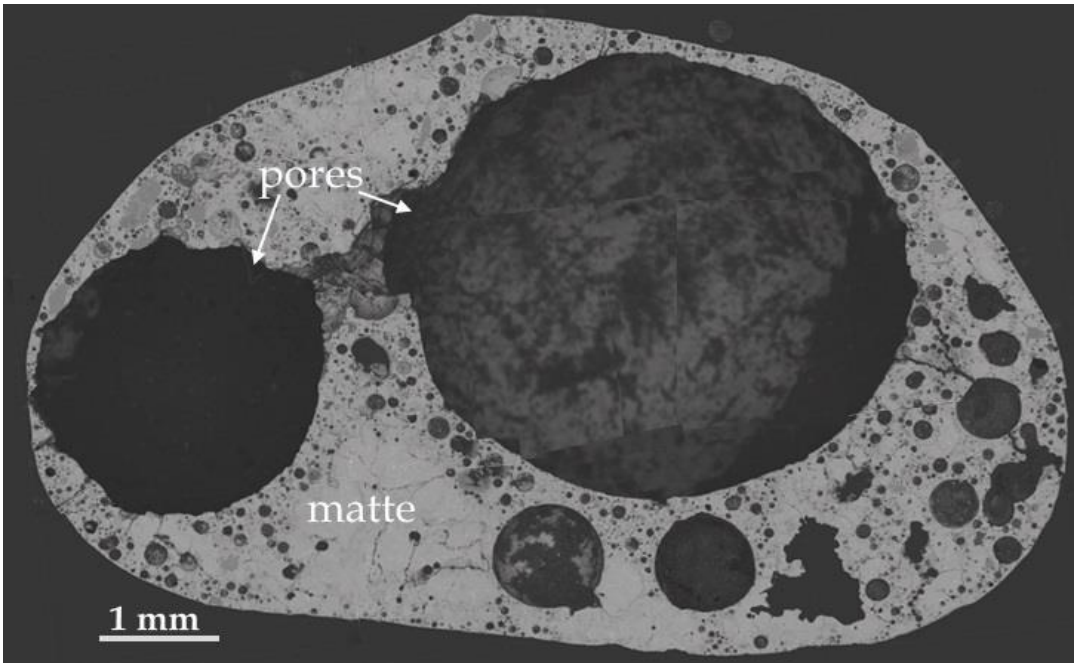

Figure 5-15: Matte-A droplet after exposure to SG-graphite substrate at 1000 °C

A detail of Matte-A droplet at 1000 °C is shown in a BSE image in Figure 5-16. The oxide phases (slag) are observed in the matte, the oxides have not reacted with the sulfides at this temperature.

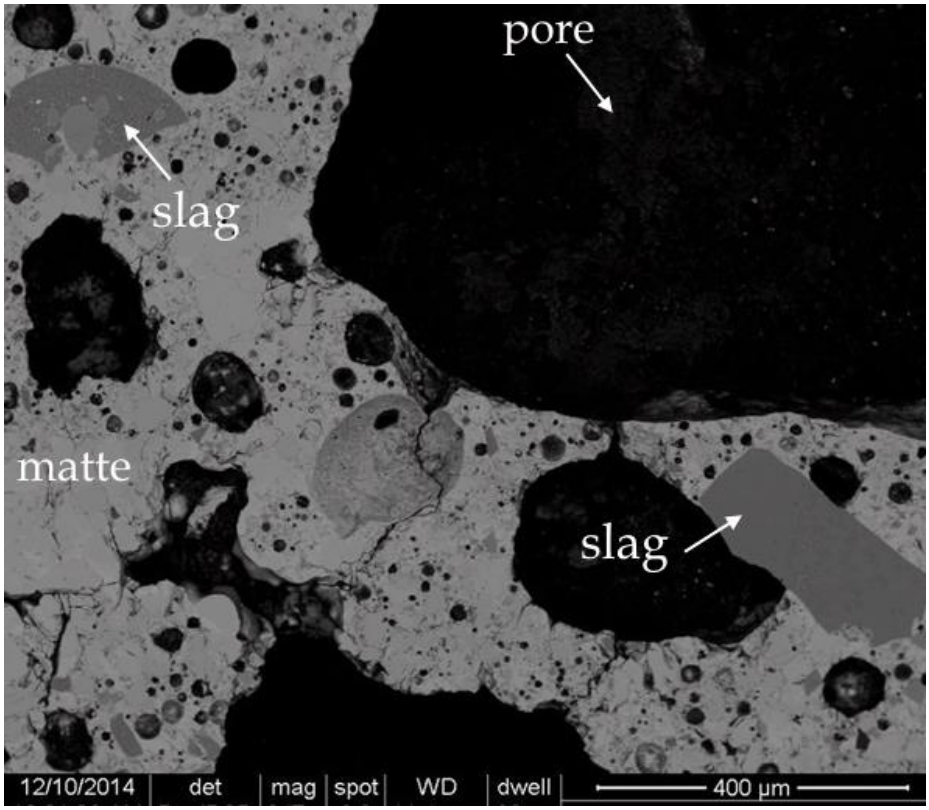

Figure 5-16: Matte-A detail after exposure to SG-graphite at 1000 °C, BSE image

5.1.5 Wettability of graphite by industrial PGM-slag

Amplats slag (Slag-A) and Lonmin slag (Slag-L) were each made into a pellet and exposed to a graphite substrate. The slag specimens were heated to 1350 °C. The recorded wetting angles and the melting temperatures are shown in Table 5-10.

5.1.5.1 Wettability of graphite by Slag-A

Slag-A melted at 1340 °C, the interfacial contact angle between Slag-A and graphite was 145°, this signified non-wetting. BSE image of the Slag-A droplet is shown in Figure 5-17; only the interface of graphite and slag is shown in Figure 5-17.

There was no interfacial product between the graphite and the Slag-A droplet; this signified that the graphite did not react with the slag at the interface. The composition of the slag phases did not change during the exposure to graphite. The bright phases observed at the periphery of the

droplet are sulfide phases that were minor impurities present in the slag sample. Slag-A did not penetrate through the graphite; no slag was detected in the graphite substrate after exposure.

5.1.5.2 Wettability of graphite by Slag-L

Slag-L melted at 1320 °**C**, the interfacial angle between Slag-L and graphite was 138°, this signified non-wettability. The droplet was analysed using SEM, BSE image is shown in Figure 5-18. Penetration of Slag-L was not observed at the graphite surface, no interfacial products were observed at the graphite-slag interface. The composition of Slag-L remained unchanged after exposure.

Table 5-10: Melting temperature and wetting angle of Slag-A and Slag-L

	Melting temperature (°C)	**Wetting angle (°)**
Slag - A	1340	145
Slag - L	1320	138

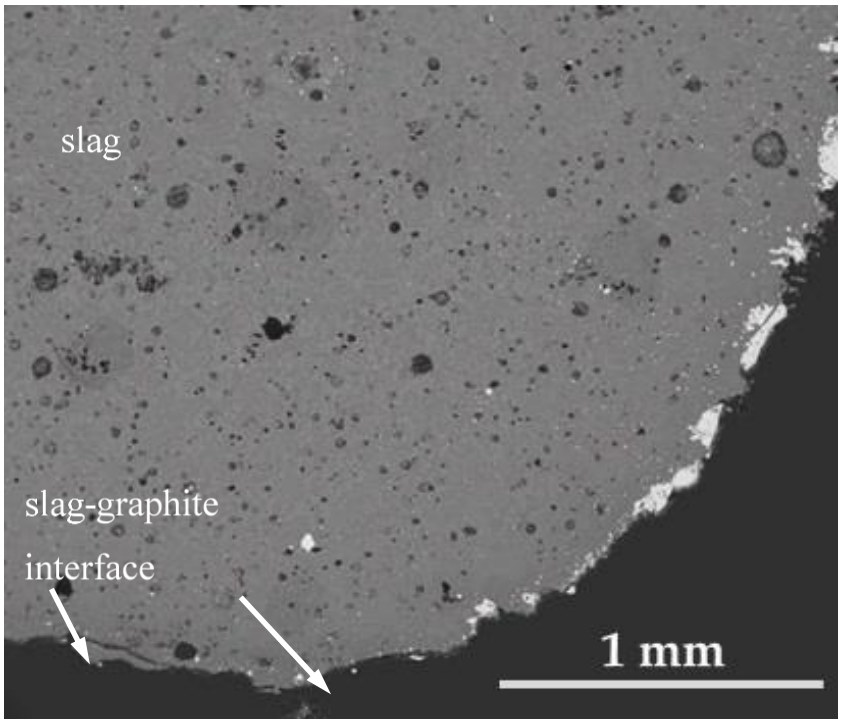

Figure 5-17: Slag-A droplet after exposure to SG-graphite substrate at 1350 °C, BSE image

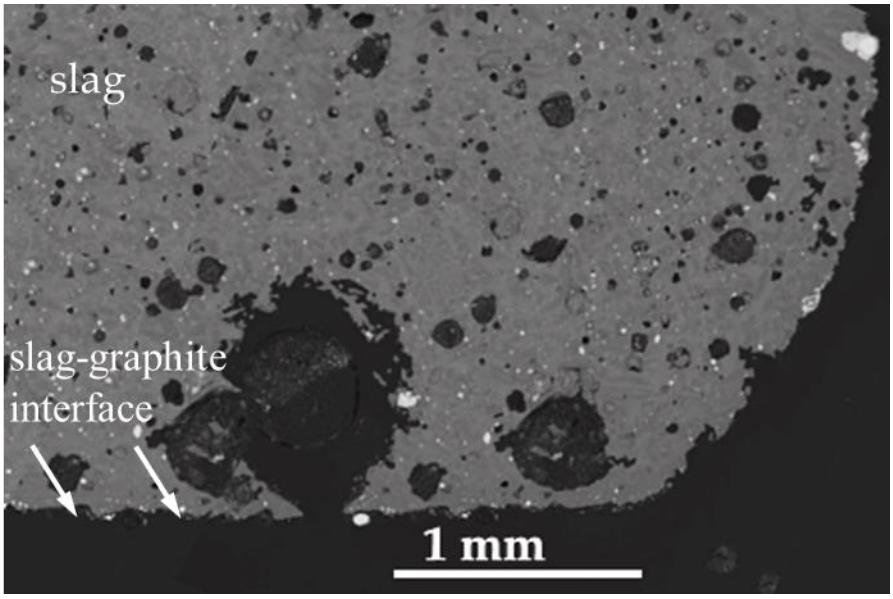

Figure 5-18: Slag-L droplet after exposure to SG-graphite substrate at 1350 °C, BSE image

5.2 Graphite wear by Matte-S

Matte-S was exposed to graphite to study the interactions between the graphite and a liquid Matte-S. Crucible tests were performed where temperature and contact time were varied. The responses were the dissolution of graphite in Matte-S and the penetration of Matte-S through the graphite. Carbon content in matte indicated the extent of graphite dissolution. Matte-S penetration was measured by the matte loss and the detection of matte prills in the graphite wall.

5.2.1 Graphite dissolution by Matte-S

Dissolution of graphite in Matte-S was determined as a function of operating temperature and contact time. The carbon content in matte was used as a measure of carbon dissolution. The operating temperature was 1150 °C, 1350 °C and 1550 °C at a constant time of 1 day. For the effect of contact time the tests were done at 1550 °C for 1 day, 3 days and 5 days.

5.2.1.1 Effect of temperature

Carbon content in matte, elemental composition of matte residue and total matte loss is shown in Table 5-11 as a function of temperature, the contact time was 1 day. Carbon content in the matte residue was constant at 0.1 mass percent from 1150 °C to 1350 °C, at 1550 °C carbon content in matte increased to 0.33 mass percent. There was no linear correlation between exposure temperature and graphite dissolution by Matte-S.

The amount of matte loss increased by 0.6 mass percent from 1150 °C to 1350 °C, at 1550 °C the matte loss increased to 11.3 mass percent. Similar to carbon dissolution, the loss of matte was not directly correlated to the exposure temperature. The sulfur content in matte decreased with increasing temperature.

Table 5-11: Matte loss and elemental composition of Matte-S as a function of temperature after exposure to SG-graphite for 1 day

Temperature °C	% C in matte	Matte loss (%)	% Cu	% Fe	% Ni	% S
0	0.03	0.0	8.9	44.6	16.4	30.1
1150	0.10	5.1	8.8	43.8	18.3	29.1
1350	0.10	5.7	10.6	44.3	17.8	27.3
1550	0.33	11.3	9.5	47.2	17.5	25.5

In Figure 5-19 there is data for the composition of the Matte-S residue after exposure to SG-graphite. The mass percent of elements, the carbon content of matte and the total matte-loss is presented in the graph as a function of temperature after 3 days exposure. Carbon dissolution in matte seems to be correlated to matte loss. Sulfur and copper are the elements that affect the matte loss the most. From 1150 °C to 1350 °C carbon solubility is almost constant at 0.08 mass percent, between 1350 °C and 1550 °C days there is significant increase in the rate of carbon dissolution in matte from 0.08 mass percent to 0.31 mass percent. The increase of carbon solubility in matte between 1350 °C and 1550 °C can be attributed to the following:

1) The decrease of sulfur in the residual matte
2) The decrease of copper in the residual matte
3) The concentration of iron in the residual matte (the matte residue became enriched in iron due to the loss of sulfur and copper in matte)

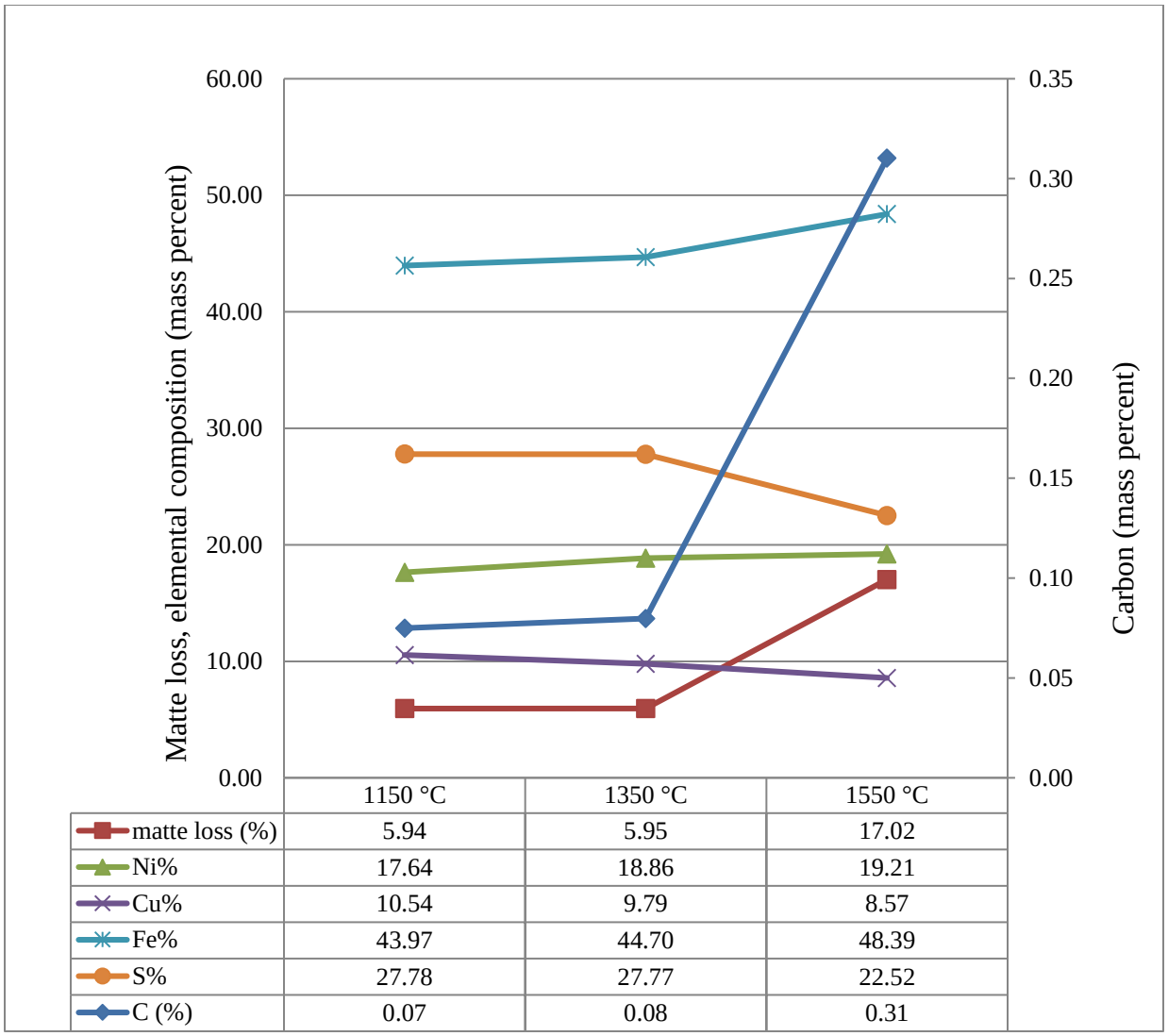

	1150 °C	1350 °C	1550 °C
matte loss (%)	5.94	5.95	17.02
Ni%	17.64	18.86	19.21
Cu%	10.54	9.79	8.57
Fe%	43.97	44.70	48.39
S%	27.78	27.77	22.52
C (%)	0.07	0.08	0.31

Figure 5-19: Matte loss, elemental composition and carbon content of Matte-S residue after exposure to SG-graphite at 1150°C, 1350°C, and 1550°C for 3 days

5.2.1.2 Effect of contact time

Carbon content in matte increased with contact time, from 1 day to 5 days the carbon content increased from 0.33 to 0.43 mass percent. There was no linear correlation between the graphite dissolution and contact time. The matte composition and total matte loss as a function of contact time are shown in Table 5-12.

Significant matte loss was observed, increasing from 11 to 20 mass percent after 1 and 5 days exposure respectively. The elemental composition of the residual matte (by ICP) and its carbon

content (by LECO) is shown in Table 5-12. Significant amount of sulfur and copper were lost during the exposure of Matte-S to graphite according to the composition of the matte residue in Table 5-12.

The composition of the Matte-S sample and the composition of the Matte-S residue (in Table 5-12) were used to calculate the elemental fraction of matte loss. The values in Table 5-13 includes the mass of elements retained in the Matte-S residue and the calculated mass of the elements that supposedly reported to the off-gas. Equations 11, 12 and 13 have the expressions used to calculate the elemental account of matte-S reported in Table 5-13.

$$E_i = M_s \, x \, \%E_i \; (in \; Matte - S) \qquad \text{Equation 11}$$

$$E_f = M_{res} \, x \, \%E_f \; (in \; Matte - S \; residue) \qquad \text{Equation 12}$$

$$\frac{E_i - E_f}{E_i} = \%E \; (in \; off - gas \; or \; elemental \; diffusion \; through \; graphite) \qquad \text{Equation 13}$$

Where E_i is the initial mass (grams) of the element in Matte-S, E_f is the final mass (grams) of the element retained in the Matte-S residue, $\%E_i$ is the mass percent of the element in Matte-S, $\%E_f$ is the mass percent of the element in Matte-S residue.

Copper and sulfur were the most prone to losses as seen in Table 5-13. Owing to high losses of sulfur and copper, the iron and nickel in the residue were concentrated as seen in Table 5-12. Copper losses increased from ~ 5 to ~30 mass percent after respectively 1 and 5 days exposure. Sulfur loss was ~25 mass percent after 1 day exposure, it increased to ~42 mass percent after 5 days exposure. This translates to a sulfur loss rate of 25 mass percent per day to 8 mass percent per day after 5 days exposure. The loss rate of sulfur decreased with exposure time, this could be attributed to the decreasing sulfur concentration in the residual Matte-S.

Carbon dissolution is correlated to the sulfur loss by Matte-S according to the data in Figure 5-23. Figure 5-23 is a plot of sulfur loss rate and carbon dissolution in Matte-S as a function of contact time, at 1550 °C. Data in Figure 5-23 was calculated based on the data in Table 5-12 and Table 5-13. The dissolution rate of carbon decreased from 0.33 (mass percent) per day to 0.09 (mass percent) per day from respectively 1 day exposure to 5 days exposure at

1550 °C. Sulfur-loss rate per day decreased from 25 mass percent to 8 mass percent after respectively 1 day and 5 days exposure at 1550 °C.

Table 5-12: Composition of Matte-S after exposure to SG-graphite at 1550 °C for 1 day, 3 days and 5 days

Mass percent	**Matte loss (%)**	**Cu (%)**	**Fe (%)**	**Ni (%)**	**S (%)**	**C (%)**
Matte-S	-	8.9	44.6	16.4	30.1	0.03
1 day	11.3	9.5	47.2	17.5	25.5	0.33
3 days	17.0	9.6	48.4	19.2	22.4	0.38
5 days	20.1	7.7	51.1	19.3	21.5	0.43

Table 5-13: Elemental accounting for Matte-S exposed to SG-graphite at 1550 °C

		Cu	**Fe**	**Ni**	**S**	**Total**
Matte-S sample (g)		0.89	4.46	1.64	3.01	10
Matte retained in grams	Exposure					
	1 day	0.84	4.21	1.55	2.26	8.87
	3 days	0.80	4.09	1.55	1.86	8.3
	5 days	0.62	4.08	1.54	1.74	7.99
Matte loss in grams						
	1 day	0.05	0.25	0.09	0.75	1.13
	3 days	0.09	0.37	0.09	1.15	1.70
	5 days	0.27	0.38	0.10	1.27	2.01
Element loss in mass percent						
	1 day	5.32	5.53	5.35	24.86	
	3 days	10.47	8.25	5.36	38.23	
	5 days	29.98	8.46	5.97	42.13	

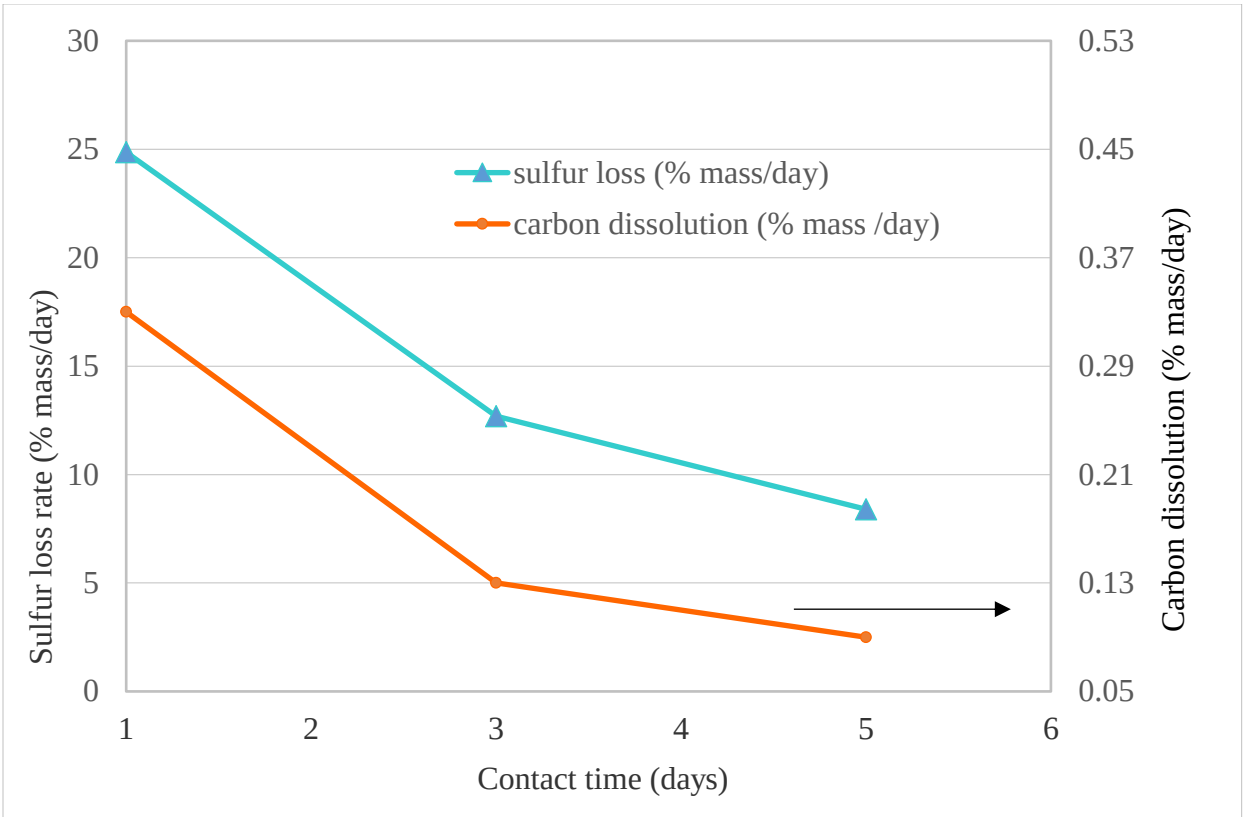

Figure 5-20: Dissolution rate of carbon in Matte-S and loss rate of sulfur by Matte-S as a function of contact time at 1550 °C

5.2.2 Penetration of Matte-S through SG graphite

The interface between Matte-S and graphite was analysed using XRM and an optical microscope. The specimen shown in the images in Figure 5-21 were exposed to 1550 ºC for 5 days. Figure 5-21a is an XRM tomogram and Figure 5-21b is an optical microscope image. The crucible in Figure 5-21a had a 10 mm inside diameter while a crucible in Figure 5-21b had a 5 mm inside diameter; a smaller crucible was used to allow detailed analysis with an optical microscope.

Matte-S formed a convex meniscus with graphite as seen in Figure 5-21. Convex meniscus signifies a non-wetting behaviour [Eustathopoulos et al. 1999]. This observation confirms the finding from the wettability tests in which it was deduced that graphite is non-wetted by Matte-S.

5.2.2.1 Effect of temperature and contact time

Liquid Matte-S did not penetrate through the SG-graphite at all tested conditions. Increasing the exposure time (from 1 to 5 days) and operating temperature (from 1150 °C to 1550 °C) did not affect the interaction between liquid Matte-S and the SG-graphite. A thin sulfur deficient iron-copper oxy-sulfide layer was observed at the interface between the graphite and the Matte-S. This was an indication that there could be interaction between liquid Matte-S and the graphite. The composition of the oxy-sulfide layer is included in Table 5-14.

The specimens exposed at 1150 °C, 1350 °C and 1550 °C looked similar; therefore operating temperature did not have an effect on the penetration of liquid Matte-S through graphite. The example of the specimen after exposure is shown in (Figure 5-21); this specimen was exposed to 1550 °C for 5 days.

The Matte-S residue appears dense, no apparent porosity is observed in the Matte-S residue. A detailed cross-section of a graphite-matte interface is shown in a BSE image in Figure 5-22. Figure 5-22a is the graphite-matte interface that also shows a matte infiltrate embedded in a graphite wall, b) is the detail of the Matte-S infiltrate. Globules of matte were observed in the graphite-wall up to 2 mm from the graphite-matte interface. The EPMA analysis of the infiltrated Matte-S is in Table 5-14.

The infiltrated matte consisted of stoichiometric sulfide phases and a sulfur deficient iron-copper oxy-sulfide layer in contact with graphite.

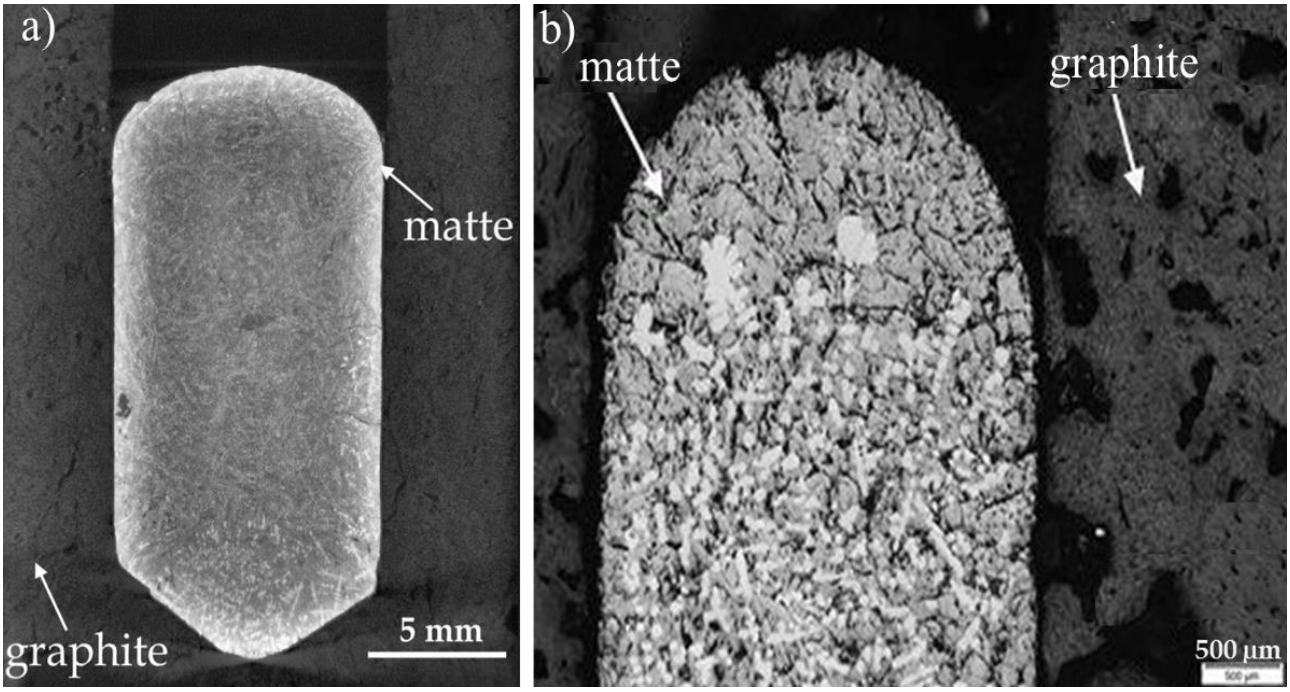

Figure 5-21: Cross section of the SG-graphite crucible with solidified Matte-S after reaction at 1550 °C for 5 days, a) XRM image, b) OM image

Table 5-14: Analysis of Matte-S embedded in SG-graphite after exposure to 1550 °C for 5 days (EPMA atomic percent)

	a	b	c, d	e
S	42.6	34.58	20.0	50.6
Fe	34.3	8.97	40.5	42.8
Cu	1.3	56.45	32.8	4.2
O			6.8	
Ni	21.8			2.4

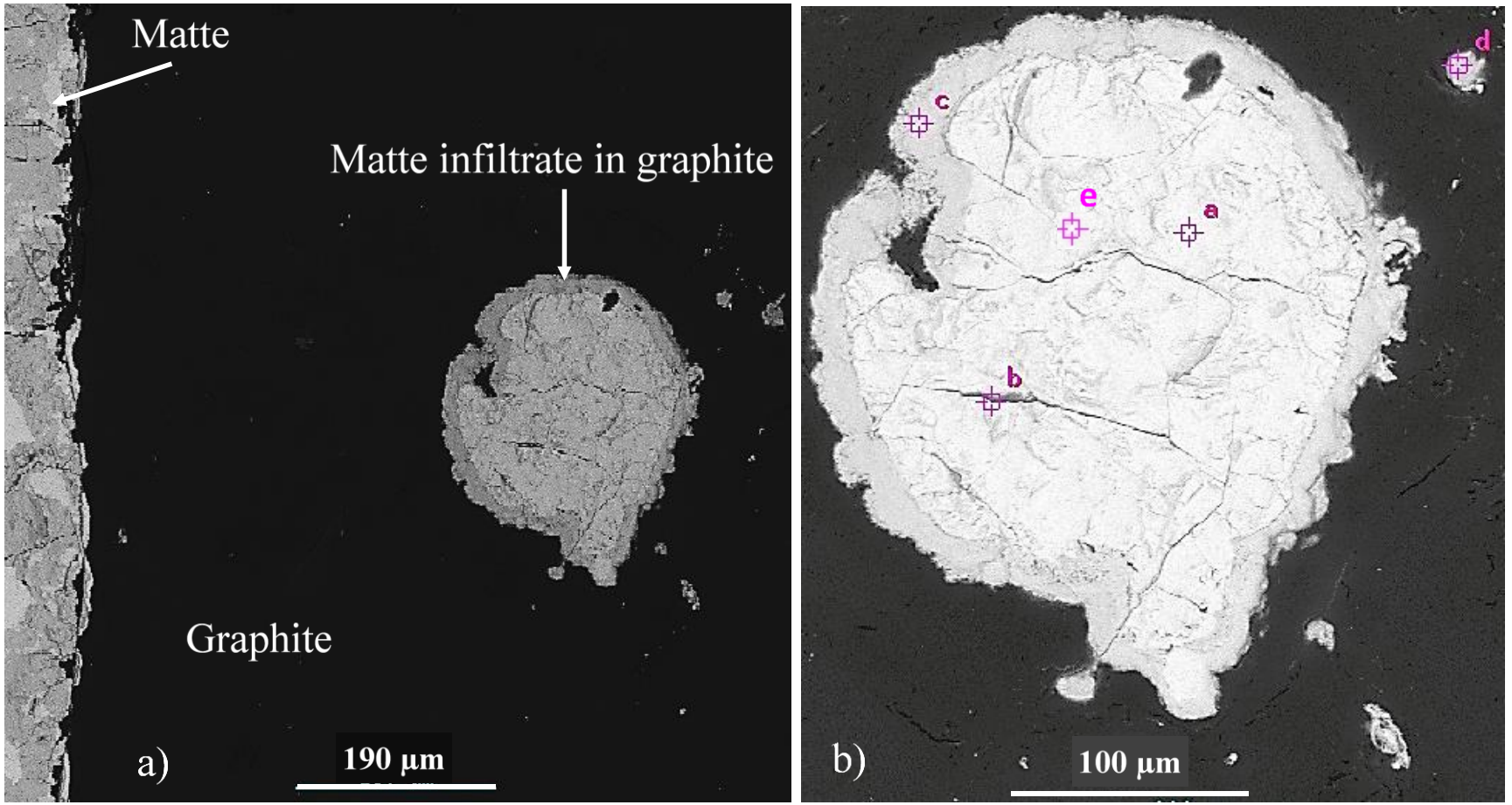

Figure 5-22: Matte-S infiltration into the SG-graphite at 1550 °C for 5 days: a) Matte-S_ graphite interface with matte infiltrate in graphite; b) detail of matte infiltrate (composition of annotated phases is in Table 5-14)

5.2.2.2 Analysis of Matte-S residue after exposure to graphite at 1550 °C

BSE image of Matte-S residue is in Figure 5-23, EDS analysis of the phases is in Table 5-15. Three major phases were identified in the Matte-S residue, these are annotated as 1, 2, 3 Figure 5-23 and in Table 5-15, solid solutions of these phases were also identified (annotated with asterisk Table 5-15. FeNi, $(CuFe)_x$ S and $(FeNi)_xS$ were the phases detected in the Matte-S residue. The oxide impurities were not observed on the Matte-S residue.

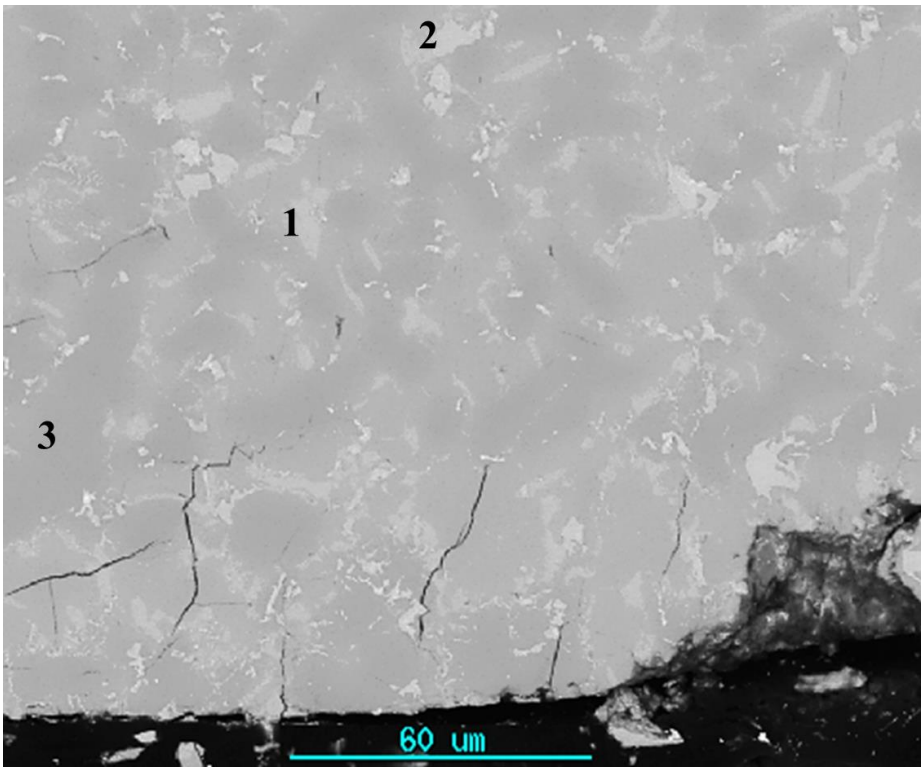

Figure 5-23: Matte-S residue after exposure to SG-graphite at 1550 °C for 1 day, BSE image, the compositions of the annotated phases are in Table 5-15

Table 5-15: EDS analysis of Matte-S residue after exposure to SG-graphite at 1550 °C for 1 day (atomic percent)

Element	**1**	**2**	**3**	***1**	***2**	***2**	***3**	***3**
Fe	13.0	73.2	38.9	38.7	35.8	60.3	40.4	43.1
S	31.9	0.0	38.2	30.7	4.3	2.6	38.8	13.9
Ni	1.2	24.6	19.8	4.9	57.2	35.1	15	38.2
Cu	53.9	2.2	3.1	25.7	2.7	2	5.8	4.8

**these phases are solid solutions of phases denoted as 1, 2 and 3 on the BSE image Figure 5-23*

5.2.3 Mechanism of Matte-S loss through SG graphite

Significant amount of Matte-S could not be accounted for after exposure. The loss of Matte-S increased with exposure temperature and contact time (matte loss in Table 5-11 and Table 5-12). The total matte loss was calculated based on the initial and final mass of Matte-S. There are two possible mechanisms by which Matte-S could be lost during exposure to graphite; deposition of matte prills in the graphite wall and evaporation of matte species due to high temperatures. The total matte loss in Table 5-11 and Table 5-12 includes the mass of matte prills in the graphite wall and evaporated matte species. Mechanisms for Matte-S loss are expounded in turn;

5.2.3.1 Matte-S infiltration into the graphite wall

It is evident from Figure 5-22 that liquid Matte-S was transported from the bulk matte to the graphite wall. This is one mechanism by which Matte-S could be lost from the bulk matte. Matte prills in the graphite wall could not be accurately quantified since it was not possible to mechanically separate graphite from the Matte-S embedded in the graphite wall.

5.2.3.2 Evaporation of Matte-S species

In the current study, gaseous species from the off-gas precipitated on the top water-cooled brass end cap (Figure 4-7). The temperature of the brass cap was estimated to 25 °C, although this condensate give an idea of the gas composition, it does not account for the gases that condense

below 25 °C. The gas condensate was analysed using XRD to determine the composition of the phases, XRD quantitative analysis is shown in Table 5-16.

The accretion consisted of a mixture of copper-iron sulfide phases. The composition of the gas condensate is in agreement with the analysis of the matte residue (Table 5-12 and Table 5-13), which indicated that sulfur and copper are the elements that contribute the most to matte loss.

Table 5-16: XRD quantitative analysis of the gas condensate produced during the exposure of Matte-S to SG-graphite

Condensate	**mass percent**	**3 σ error**
Bornite (Cu_5FeS_4)	25.6	1.1
Chalcocite (Cu_2S)	21.7	1.8
Mooihoekite ($Cu_9Fe_9S_{16}$)	20.6	1.7
Covellite (CuS)	18.3	1.2
Chalcopyrite ($CuFeS_2$)	13.8	1.4

5.2.3.3 FactSage simulation of gas released during sulfide smelting

The Matte-S sample consisted of the sulfides of copper, iron and nickel i.e. Cu_5FeS_4, FeS and $(Fe, Ni)_9S_8$, as reported in Table 4-14. The phase relations in these sulfides are complex and are constituted by extensive solid solutions as discussed in Section 3.3. FactSage was used to estimate the amount and composition of gas that is released when each of these sulfides is exposed to the operating temperatures with and without carbon. Equilib (FTmisc) database was used for all the calculations.

The XRD analyses of Matte-S in Table 4-14 were used as basis for FactSage calculations. The $(Fe, Ni)_9S_8$ content in the Matte-S sample was 57 mass percent which made it the most abundant phase, it was followed by FeS at 25 mass percent and copper containing sulfide was only about eight mass percent. The dissociation of $(Fe, Ni)_9S_8$ was the only phase considered since it was the abundant phase and based on the composition of the residue, FeNi alloy formed during the exposure. The dissociation of other sulfide phases was not considered at this stage because the most contributor to matte loss was sulfur and it is presumed that $(Fe, Ni)_9S_8$ released sulfur

during exposure. This is evinced by the formation of an alloy. Therefore the study of the dissociation of the (Fe, Ni)$_9$S$_8$ phase was deemed relevant to give estimated amount of sulfur that the matte released during the exposure to graphite. The presence of the oxide impurities should also be noted but oxides were not included in these calculations.

The FactSage used did not have data for (Fe, Ni)$_9$S$_8$, instead it had Ni$_9$S$_8$ and Fe$_9$S$_8$. Ni$_9$S$_8$ was used as a substitute for (Fe, Ni)$_9$S$_8$. The heating temperature ranged from 100 °C to 1500 °C. The simulation was done for a closed system where it is assumed that the gas is not escaping the system, therefore the gas accumulates as the temperature is increased. The FactSage simulation results for the dissociation of Ni$_9$S$_8$ as a function of temperature are shown in Table 5-17. The FactSage simulation is discussed in turn:

a) FactSage simulation for a 10 gram Ni$_9$S$_8$ from 100 °C to 1500 °C

Ni$_9$S$_8$ dissociated to Ni$_7$S$_6$ and NiS as the temperature was increased to 517 °C. The initial liquid phase and gas phase formed at 1000 °C, the liquid had Ni$_3$S$_2$ and the gas had S$_2$. S$_2$ was the abundant gas and the S$_2$ fraction in the gas phase increased with increasing temperature. The gas quantity as a function of temperature is summarised in Table 5-17. The gas stream increased by an average of ~0.2 litres per 100 °C from 1000 °C to 1300 °C, from 1300 °C to 1500 °C the gas volume increased by 0.23 litres per 100 °C. The dissociation of Ni$_9$S$_8$ is summarised in Equation 14.

$$Ni_9S_8(s) \xrightarrow{517\,^{\circ}C} Ni_7S_6(s) + 2NiS(s) \xrightarrow{1000\,^{\circ}C} 3Ni_3S_2(l) + S_2(g) \qquad \text{Equation 14}$$

Table 5-17: Gas quantities as a function of temperature for the melting of 10 g of Ni$_9$S$_8$ (FactSage simulation)

Temperature (°C)	**S$_2$ gas (grams)**	**Gas volume (litres)**
1000	0.03	0.05
1100	0.13	0.23
1200	0.22	0.42
1300	0.30	0.62
1400	0.39	0.83
1500	0.47	1.06

b) FactSage simulation for a 10 gram Ni_9S_8 + 10 gram carbon from 100 °C to 1500 °C

The dissociation of Ni_9S_8 in the presence of carbon was also simulated in FactSage. The aim was to determine the effect of carbon on the amount of gas released by a sulfide.

Adding carbon to the Ni_9S_8 decreased the temperature at which the gas and the liquid formed. Without carbon, a gas and a liquid started forming at 1000 °C. With carbon, a liquid, S_2 and CS_2 gas started forming at 811 °C. This indicated that carbon reduces the solidus temperature of Ni_9S_8. This meant that melting of pentlandite contributes towards the penetration of matte because matte penetrates around 900 °C and in the presence of carbon a pentlandite liquid and gas formed below 900 °C. The reactions predicted by FactSage are summarised in Equation 15. Summary of gas quantities predicted by FactSage simulation is shown in Table 5-18.

$$Ni_9S_8(s) + 0.5\,C \xrightarrow{517\,^{\circ}C} Ni_7S_6(s) + 2NiS(s) + 0.5\,C \xrightarrow{811\,^{\circ}C} 3Ni_3S_2(l) + 0.5\,CS_2(g) + 0.5S_2(g) \quad \text{Equation 15}$$

The addition of carbon increased the volume amount of the gas stream. The gas volume in Table 5-17 and the gas volume in Table 5-18 were compared, the calculated increment amount of the gas volume (in percentage) is Table 5-18. The gas volume increment is a percentage increase in volume comparing the volume without carbon (in Table 5-17) and the gas volume with carbon (Table 5-18). The gas increase is higher at lower temperatures (1000 °C), it decreases from 1200 percent to 168 percent from respectively 1000 °C to 1500 °C. From 1000 °C to 1100 °C the percentage increment dropped from respectively 1200 percent to 343 percent, this is a significant drop which can cause drastic changes to the gas pressure. Based on this calculation the effect of carbon on the gas volume is enormous, and it has the highest impact at melting temperatures.

The rate increase of the gas volume as a function of temperature was ~0.2 litres per 100 °C between respectively 1000 °C and 1300 °C. From 1300 °C to 1500 °C this rate increased to 0.23 litres per 100 °C. This is a significant observation since it is similar to a trend observed on the values of Matte-S loss between 1300 °C and 1550 °C (Table 5-11).

Table 5-18: Gas quantities for the 10-gram Ni_9S_8 + 10 gram C (FactSage simulation), S_2 and CS_2 are in grams; gas volume increment is a percentage of gas volume increase comparing the gas volume without carbon and with carbon

Temperature (°C)	S_2 (g)	CS_2 (g)	Gas volume (litres)	Gas volume increment (percent)
839	0.03	0.25	0.34	-
900	0.04	0.30	0.43	-
1000	0.05	0.38	0.60	1200
1100	0.06	0.46	0.79	343
1200	0.08	0.53	1.00	238
1300	0.10	0.61	1.23	198
1400	0.11	0.69	1.49	179
1500	0.14	0.77	1.78	168

5.2.3.4 Gas pressure calculation based on the gas quantity estimated with FactSage

The pressure build-up inside the crucible due to the expansion of process gas was calculated using the volume of the crucible and the universal gas law. The formation of high volumes of gas is envisaged during melting of base metal sulfides [Eksteen 2011]. The vaporisation of matte species results to losses of matte to a gas phase. The increase of the volume of the gas inside the crucible creates pressure that drives the gas to escape the crucible.

Dimensions of the crucible used for the experiments were the following; 5 mm radius, 60 mm depth and 5 mm thickness. The volume of the empty crucible was calculated using Equation 16.

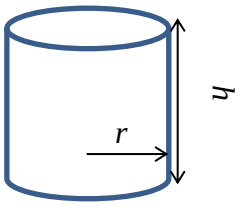

$$V = \pi r^2 h \qquad \text{Equation 16}$$

$= 3.142 \times 5^2 \times 60\ mm$

$= 4713\ mm^3$ $= 0.004713$ litres

The volume of the empty crucible was calculated to be 0.004713 litres. According to the volume of the gas estimated in Table 5-17, a 10 gram matte sample produces 0.01 litres of gas at 1000 °C. The estimation of volume was based on the following assumptions:

- The gas was only produced by the Ni_9S_8 compound
- Matte had 22 mass percent Ni_9S_8

The estimated gas volume exceeded the crucible volume by 233 percent. Therefore pressure build-up is inevitable inside the specimen during the dissociation of sulfides. The calculated gas pressure is summarised in Table 5-19. The amount of gas used in the calculation is the number of moles of sulfur which are released when Ni_9S_8 is heated from 1000 °C to 1500 °C (FactSage simulation data in Table 5-17). The universal gas law was used for the pressure calculations, the expression is in Equation 17. The volume used in calculations is the crucible volume that was calculated and found to be 0.004713 litres.

$$PV = n \times R \times T \qquad \text{Equation 17}$$

where P is the pressure exerted by the gas on the vessel in Pascal, V is the volume of the vessel in m^3, n is the amount of gas in moles, R is the gas constant in Joule/(mole. Kelvin), T is the temperature in Kelvin,

The effect of gases produced by side reactions has not been considered in the pressure calculation, only the amount of S_2 released during the melting of Ni_9S_8 was considered. The oxide impurities present in the matte could react with carbon and form CO, such reactions would increase the amount of gas inside the crucible that would increase the pressure exerted by gas on the crucible.

Table 5-19: Calculated pressure of S_2 gas as a function of temperature for melting 10 gram of Ni_9S_8 (simulation by FactSage)

T (°K)	**S_2 amount (mol)**	**Pressure (Pa)**	**Pressure (atm)**
1273	0.0005	1122822	11.08
1373	0.0020	4844100	47.81
1473	0.0034	8834750	87.19
1573	0.0047	13041849	128.71
1673	0.0061	18002730	177.67
1773	0.0073	22832012	225.33

R =	8.314 J/mol.K
Mm S_2 =	64.132 g/mol
P =	n R T/V

5.3 Graphite wear by industrial matte

The compatibility of graphite with industrial matte was investigated to determine the prominent wear mechanism of graphite by industrial matte using crucible tests. The variables were graphite grade, operating temperature and contact time. The responses were the depth of liquid matte penetration, the dissolution of graphite and the chemical interaction between graphite and each matte type. Industrial matte samples tested were Matte-A, Matte-P and Matte-L, all these matte types behaved similarly when exposed to graphite as such; the results presented here are representative of all the matte samples unless specified.

5.3.1 Penetration of liquid industrial matte through graphite

The industrial matte was exposed to HG and SG graphite to determine which graphite has high resistance to penetration by liquid industrial matte. The effect of temperature and contact time was only tested on the SG graphite. The penetration path of the liquid matte was verified with OM analysis and CAF tests. The gas condensate was analysed to confirm that matte species are lost to the off-gas during the interaction. The effect of the crucible volume was tested to determine the mechanism behind liquid matte penetration.

5.3.1.1 Effect of graphite grade

Comparative interaction tests were performed on HG and SG graphite crucibles. HG was a denser graphite (12 percent porosity) and SG was a porous graphite (24 percent porosity). The specimens were exposed to 1000 °C for 12 hours.

The liquid industrial matte penetrated the entire width of the SG graphite. The graphite-matte specimen after exposure is shown in Figure 5-24. A portion of the matte was collected outside the crucible in a solid form (matte-outside-crucible in Figure 5-24), another portion of the matte remained inside the SG crucible after exposure (matte-residue in Figure 5-24). The presence of the solid matte outside the crucible indicated that at temperature the liquid industrial matte penetrated through the SG crucible.

HG graphite was not penetrated by liquid industrial matte, matte was not observed outside HG crucible after exposure.

The matte loss of ~5 mass percent was observed in both SG and HG specimens. This matte loss was attributed to the evaporation of matte species similar to the matte loss observed when Matte-S was exposed to SG graphite (Section 5.2.3).

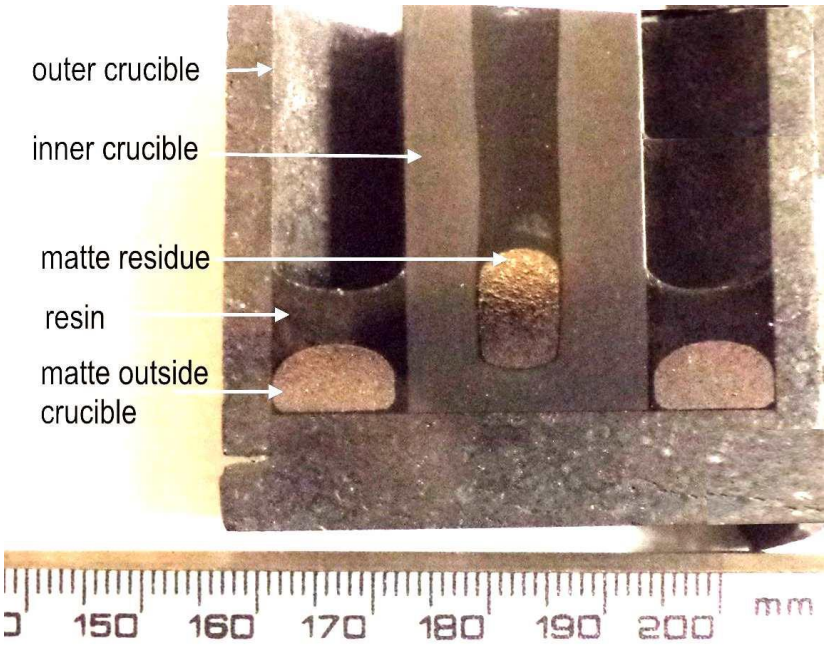

Figure 5-24: SG-graphite industrial-matte specimen after exposure at 1000 °C, a picture showing the cross-section of specimen, a layout of the outer crucible, inner crucible and matte residue after exposure

XRM was used to examine the wall of the HG and SG graphite after exposure, cross-section (top view) of the specimen is shown in Figure 5-25. Figure 5-25a is the HG graphite specimen, Figure 5-25b is the SG graphite specimen after exposure to 1000 °C. Traces of matte were observed in the SG graphite wall, matte traces confirmed the penetration path of the liquid matte. The HG graphite wall had no matte prills after exposure, this also confirmed that liquid matte penetration did not occur through the walls of the HG graphite crucible.

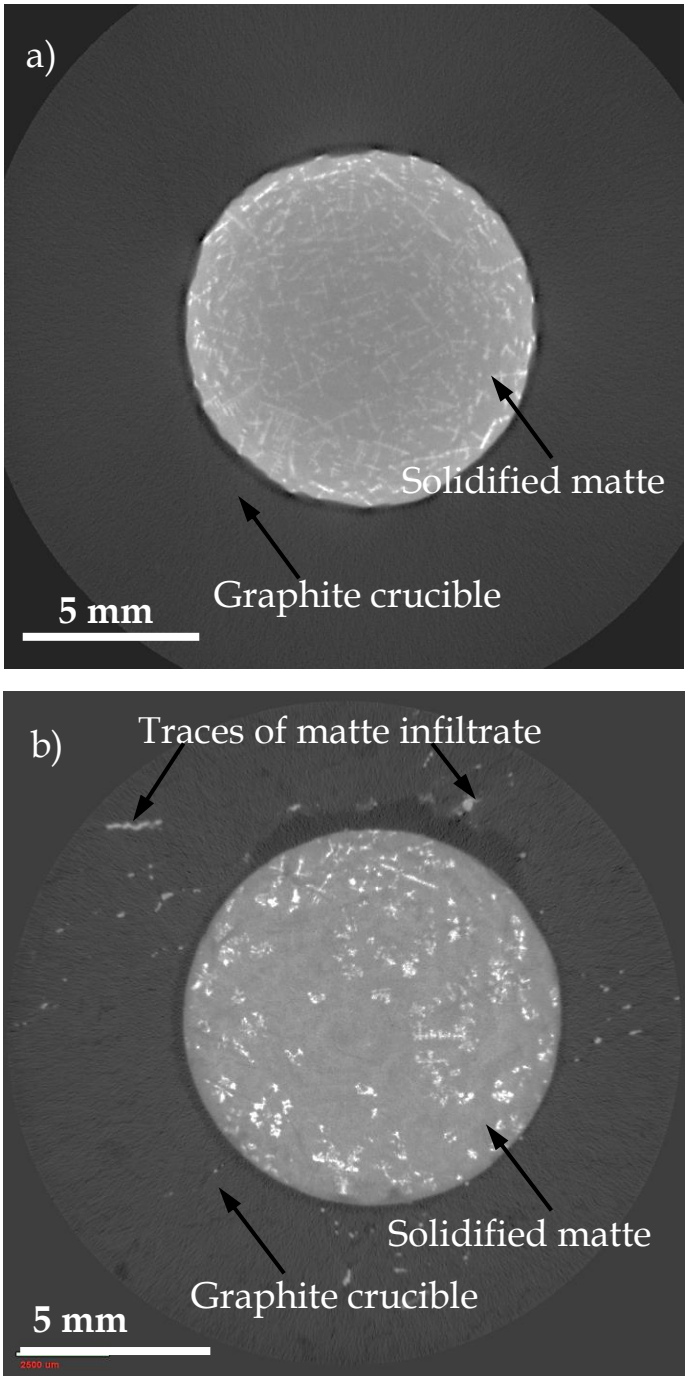

Figure 5-25: Top view (cross-section) of a post-mortem graphite crucible with solidified industrial matte a) HG crucible, b) SG crucible, after exposure at 1000 °C

5.3.1.2 Effect of temperature

Tests were conducted to determine the minimum temperature at which matte start penetrating through the SG graphite as well as to determine the effect of temperature on the interaction of matte with graphite. Matte loss as a function of temperature for Matte-A, Matte-L and Matte-P is summarised in Table 5-20. Matte-A, Matte-L and Matte-P were exposed to SG graphite for 1 hour.

At 800 ºC the matte had sintered into solid lumps. The measured matte loss was ~1 mass percent, this matte loss was attributed to gas formation during heating.

Matte was molten at 900 ºC, a portion of liquid matte penetrated through the crucible at 900 °C, this was observed for all matte types. The penetration of liquid matte was evinced by the collection of solid matte outside the crucible after exposure at 900 °C. The slight difference in average matte loss for Matte-A, Matte-L and Matte-P was attributed to the slight difference in the composition of the inclusions in these matte samples.

At 900 °C the total matte loss by all matte types was ~50 mass percent. As the temperature increased to 1450 °C the total matte loss increased by about 7 mass percent. It seemed that increasing temperature above 900 °C did not have a significant effect on the amount of total matte loss. Total matte lost refers to the mass difference between the starting matte and the matte remaining inside the crucible after exposure.

A proportion of matte was collected outside the crucible after exposure, this matte is reported as (MOC) in Table 5-21. The values of MOC in Table 5-21 are the actual weighed masses, these values are for Matte-A, similar fractions were observed for Matte-L and Matte-P.

MOC was an average of 50 mass percent from 900 °C to 1450 °C for all matte types. The matte that reported to the off-gas increased with exposure temperature from 1.5 to 6.2 mass percent from respectively 900 °C to 1450 °C. Matte loss to the off-gas was calculated based on the starting mass and the mass of the residual matte (inside and outside the crucible).

The rate of off-gas formation did not increase with temperature, the highest off-gas formation rate was between 900 °C and 1000 °C where 2 mass percent off-gas was reported. From 1000 °C to 1450 °C this rate dropped to less than 2 mass percent per 100 °C. The off-gas formation rate is

in agreement with the FactSage simulation in Table 5-17 the exception is that the FactSage rate (gas volume) increased with temperature. In the presence of carbon the gas volume increment was higher at melting temperatures and it dropped with increasing temperature.

Table 5-20: Total matte loss as a function of temperature for Matte-A, Matte-L and Matte-P that was exposed to SG-graphite for 1 hour

Temp (°C)	Matte-L (%)	Matte-A (%)	Matte-P (%)
800	0.72	1.3	1.2
900	50.7	50.5	49.7
1000	53.5	52.7	50.2
1250	57.3	55.0	52.0
1450	58.9	55.9	55.5

Table 5-21: Total matte loss, MOC and off-gas (mass percent) for Matte-A after 1-hour exposure

Temp (°C)	Matte loss (%)	MOC (%)	Off-gas (%)
800	1.3	-	1.3
900	50.5	49.1	1.4
1000	52.7	49.4	3.3
1250	55.0	50.8	4.2
1450	55.9	49.7	6.2

5.3.1.3 Penetration path of liquid Matte-A through SG graphite

Graphite-Matte-A specimen was examined using XRM, SEM-BSE and OM to determine the penetration path of the matte through SG graphite wall. The layout of the matte was also studied after exposure to 900 °C, 1250 °C and 1450 °C.

5.3.1.3.1 Matte-A specimen exposed to SG graphite at 900 °C

The micrographs of the specimen exposed to 900 °C are shown in Figure 5-26. Figure 5-26a) is a 2D side view, b) is a 3D and c) is a top view. The matte seems molten and highly porous at 900 ºC. The matte seems suspended on the pores.

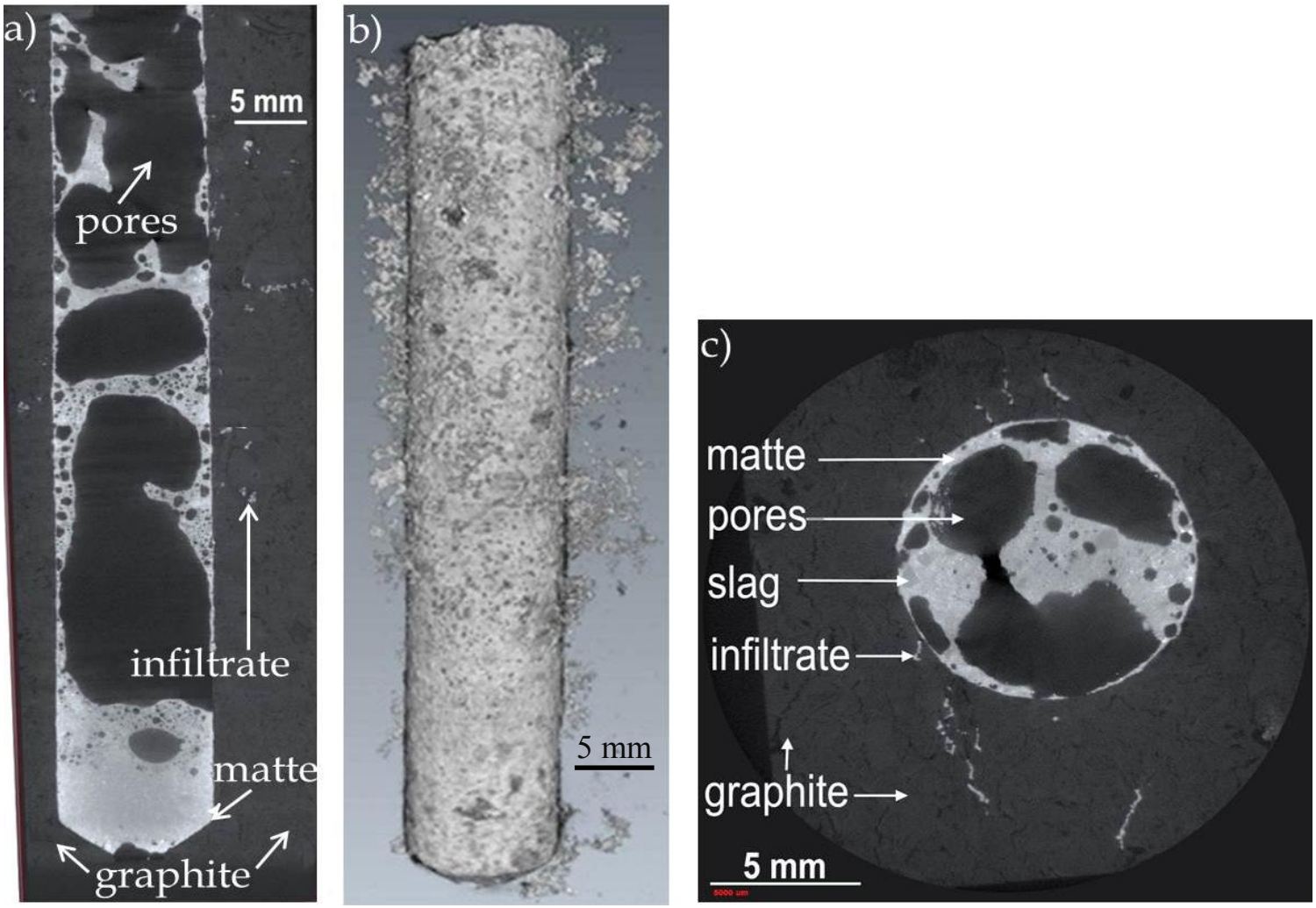

Figure 5-26: Matte-A specimen after exposure to SG-Graphite at 900 °C for 1 hour, XRM images a) side view, b) 3D image, c) top view

Matte adherence to the graphite surface is apparent. Slag phases can be seen dispersed in the matte. Traces of matte can be seen in the graphite wall in Figure 5-26a. The traces of matte are dispersed throughout the depth of the crucible (from the top of the crucible to the bottom) as seen in Figure 5-26b. This indicates that matte penetration was not localised to certain areas in a crucible.

In Figure 5-26c traces of matte can be observed in the connected pores of the graphite wall, traces of matte are annotated as infiltrate. Based on the appearance of the traces of solidified-matte in the walls of the crucible, it seem that connected pores present in the walls of the graphite is where the matte penetrated through the graphite.

The cross-section of the crucible post-mortem is in Figure 5-27 (optical microscope). The traces of matte are prevalent on the graphite wall. The image in Figure 5-27 confirms that matte penetrated through cracks and joined pores in the wall of the SG-graphite

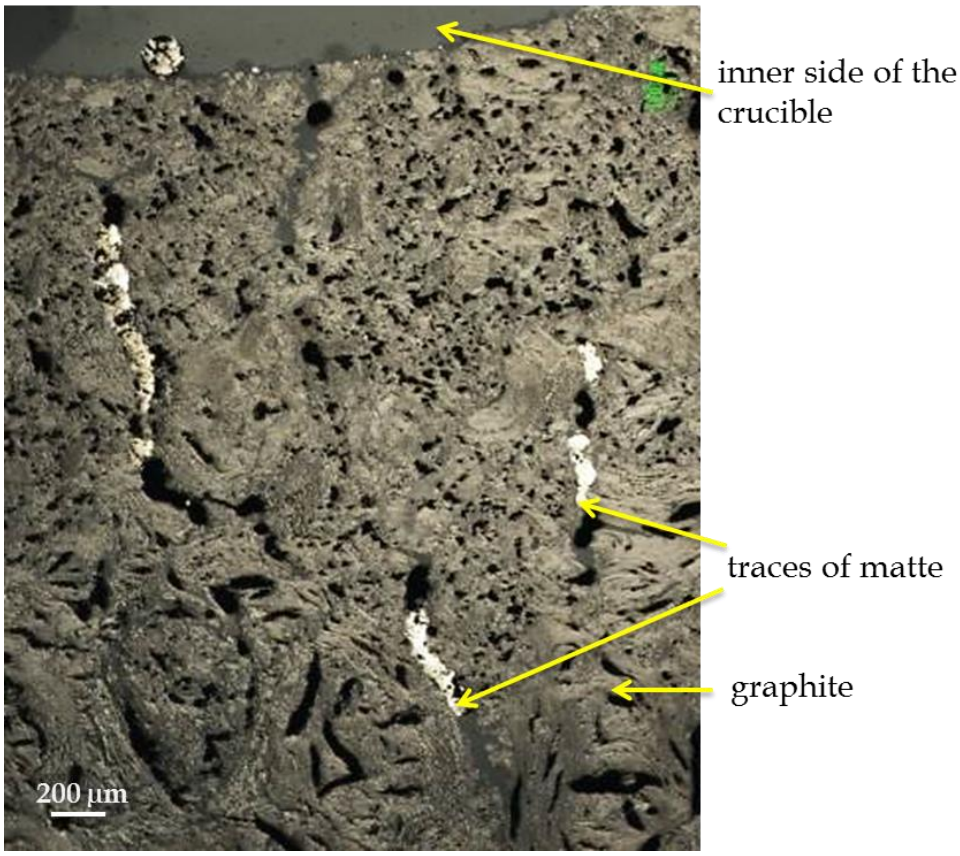

Figure 5-27: SG-graphite crucible wall after exposure to Matte-A at 900 °C for 1 hour, OM image

5.3.1.3.2 SG graphite-Matte-A specimen exposed to 1250 °C

The micrograph of a specimen after exposure at 1250 ºC is shown in Figure 5-28 (Figure 5-28a is a 3D image and Figure 5-28b is a 2D image). In a 3D image it can be seen that matte penetration in the graphite occurred throughout the height of the crucible (from the lid to the bottom). This observation highlights that the penetration of matte was not localised to a certain area (depth of a crucible). In a 2D image a few spots of matte traces in the wall of the graphite are observed, as such if the analysis were based on Figure 5-28b only, one might have concluded that the matte penetrates through those two channels where the traces of matte can be seen. A 3D image has more detail of the specimen and allows accurate examination of the specimen.

Traces of matte are observed in the walls of the graphite from the inner surface to the outer surface of the crucible. Matte residue is observed on the outer surface of the crucible as indicated in Figure 5-28 (annotated as MOC). The matte-penetration path can be traced back to the inside of the crucible when following the matte traces from the matte-residue in the wall of the crucible. This is a classic example of how the matte gets out of the graphite crucible.

Carbon-paste was applied between the lid and the crucible before exposure. In this area (between the lid and the crucible), no penetration of matte is observed. In contrast, traces of matte are observed to penetrate through the lid. This indicates that application of the carbon paste was able to inhibit the penetration of matte between the crucible and the lid. The paste is cured before the experiment to ensure that it is set before exposure, the paste appeared dense when compared to the crucible.

At 1250 °C a dense-matte layer has collected at the bottom of the crucible. This indicates that with temperature the fluidity of matte increased. A thin layer of a slag phase could be observed on top of the matte layer. This indicates that with temperature the immiscible phases segregated, at 900 °C the slag phases were observed scattered throughout the matte as annotated in Figure 5-26. It is difficult to comment whether slag was fully molten or not at 900 °C but at 1250 °C the slag seem molten. At 1250 °C a thin layer of matte is attached to the graphite surface from the crucible lid to the matte layer at the bottom. The adherence of matte to the graphite surface indicates some degree of wetting, attachment of matte to the graphite surface

was also observed at 900 °C. The shape of the matte at the bottom of the crucible (Figure 5-28) was caused by a drilling error, it was impossible to use an alternative image for analysis since the access to XRM was limited.

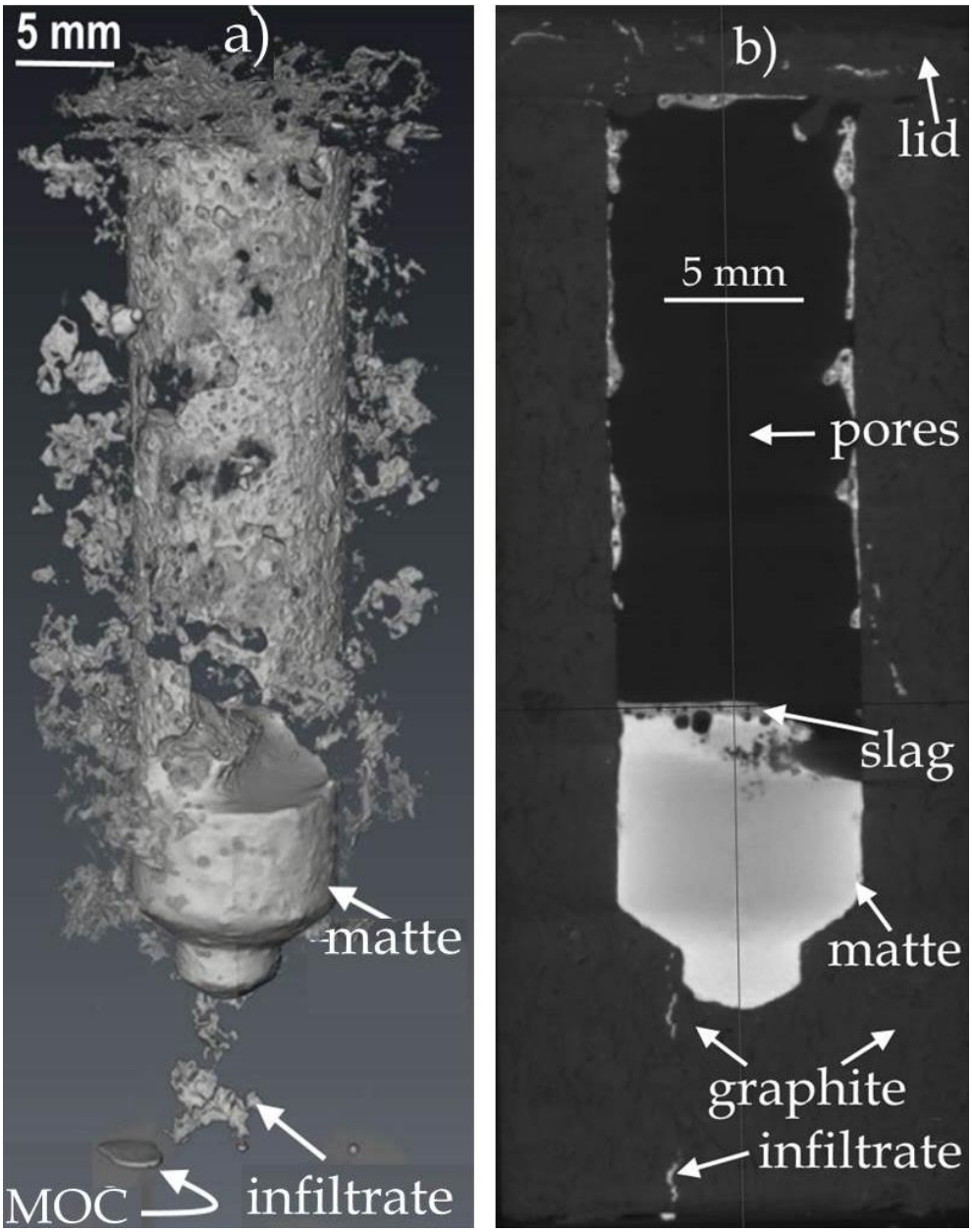

Figure 5-28: SG-Graphite Matte-A specimen after exposure at 1250 °C for 1 hour, images by XRM, a) 3D image of the specimen showing the matte residue, matte infiltrate and MOC [MOC is matte that penetrated through the graphite], b) 2D side view of the specimen showing the matte residue, matte infiltrate, slag layer, graphite and the graphite lid

5.3.1.3.3 Matte-A specimen exposed to SG graphite at 1450 °C

At 1450 ºC matte is fully molten as seen in the specimen in Figure 5-29. Matte is detached from the graphite surface and the top part of the crucible has no matte attached to the surface such as observed at 900 ºC and 1250 ºC. The pores observed in matte at low exposure temperatures are significantly decreased at 1450 ºC. Matte infiltrate is observed in the crucible wall as annotated in Figure 5-29. A metal phase appeared below the matte layer at 1450 °C, at lower temperatures metal was not observed.

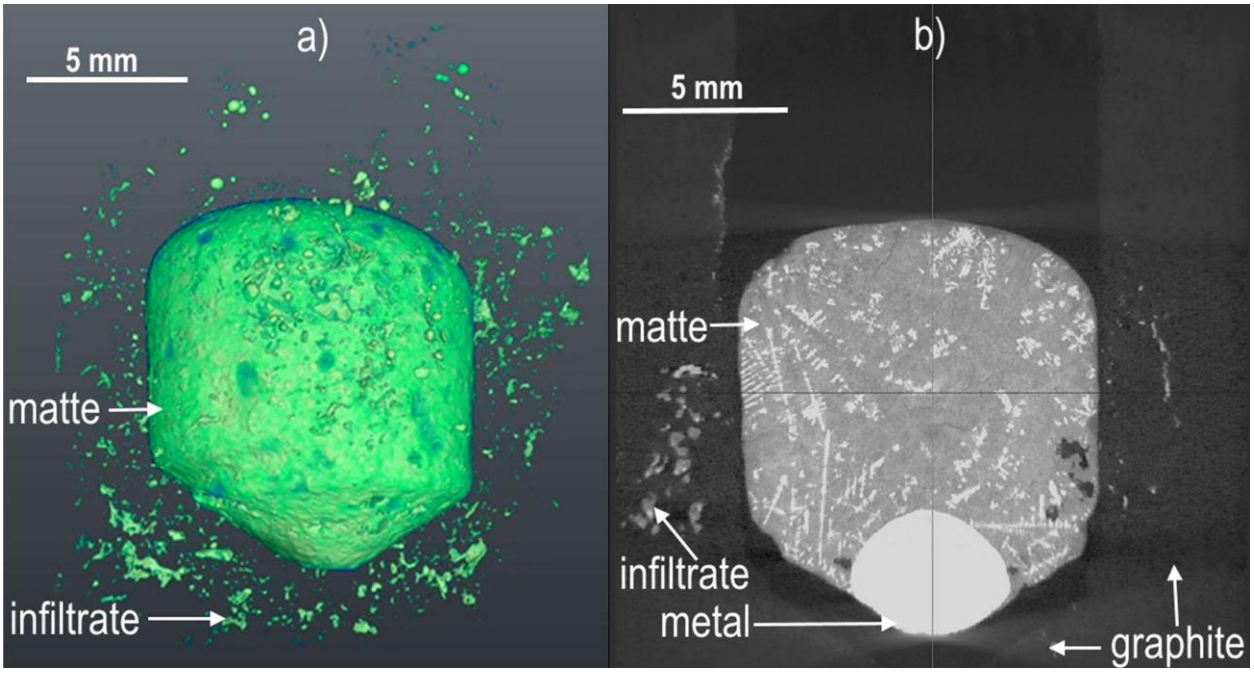

Figure 5-29: Matte-A specimen after exposure to SG-graphite at 1450 °C for 1 hour, a) XRM 3D image, b) XRM 2D image

5.3.1.4 Validation of penetration path of liquid Matte-A through SG graphite _ analyses by CAF images

CAF tests were conducted to confirm the penetration trend of liquid industrial matte through graphite. The SG graphite-industrial matte specimen was heated from 800 °C to 1060 °C. The

detailed images of the CAF tests are reported in Appendix C. The CAF tests confirmed the following:

- The penetration of industrial matte commenced at ~900 °C,
- The matte leakage was through the side wall and lid of the crucible, matte did not leak through the graphite paste seal (between the lid and the crucible),
- The hydrostatic pressure did not have significant effect on the penetration of matte, matte penetration was observed throughout the depth of the crucible,
- Liquid matte penetration did not increase with increasing operating temperature,
- Liquid matte penetration was driven by an internal gas pressure, when this pressure subsided the penetration ceased,

5.3.1.5 The effect of contact time on Matte-A penetration through SG-graphite

Matte-A was exposed to SG-graphite to determine the effect of contact time on the penetration of liquid industrial matte through SG-graphite. The operating temperature was 1450 °C, the contact time was varied from 1, 3, 6, 9 and 12 hours. The data in Figure 5-30 contains the total matte loss, matte outside crucible (MOC) and the matte reporting to the off-gas, all in mass percent. Total matte loss was calculated based on the initial mass and the final mass of the specimen. The mass of MOC is the actual weighed mass of the matte that was collected outside the crucible after exposure, this matte penetrated through the crucible in a liquid form during exposure. The matte that could not be accounted for after exposure was taken as the off-gas. The standard deviation was less than 2 mass percent for the values reported in Figure 5-30.

From 1 hour to 12 hours the total amount of matte loss increased by ~3 mass percent. Increasing the contact time did not enhance matte penetration.

Liquid matte penetration through the graphite was also not affected by contact time. MOC was 46 mass percent after 1 hour and 44 mass percent after 12 hours. There was a slight decrease on the mass of MOC with increase in exposure time; this may be attributed to the evaporation of MOC to the off-gas.

The evaporation of matte species to off-gas was enhanced by the increase in contact time, the proportion of the off-gas increased from 5 mass percent after 1 hour to 12 mass percent after 12 hours exposure.

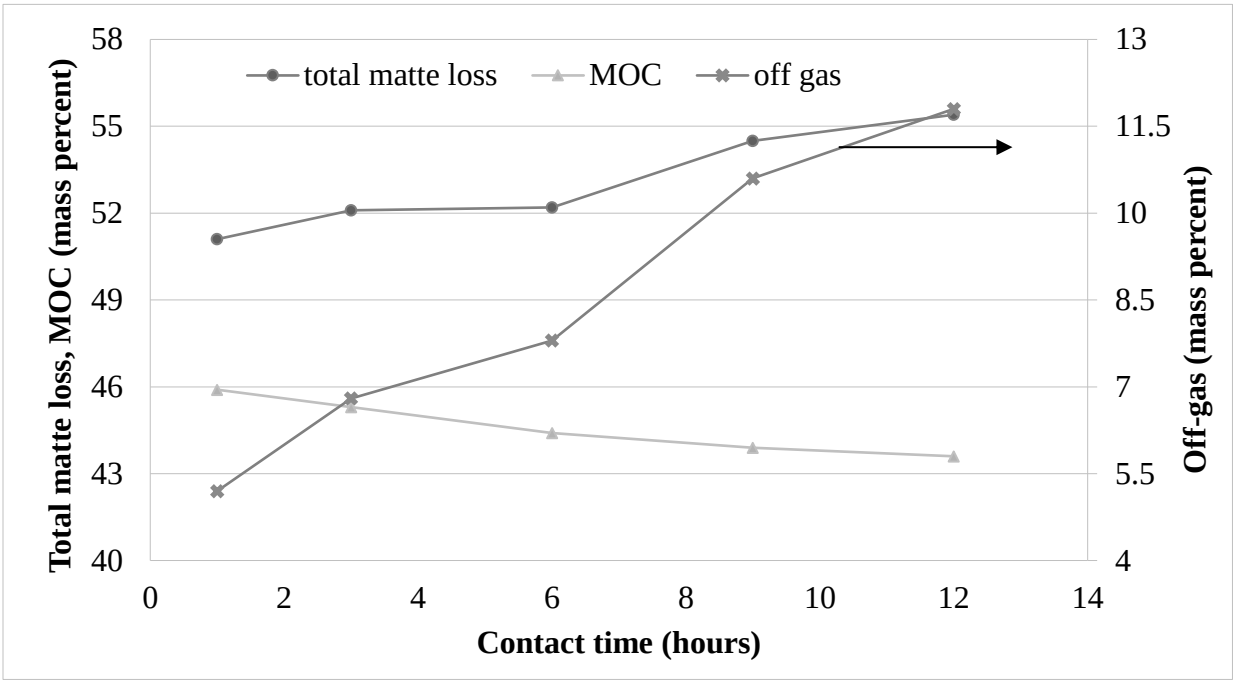

Figure 5-30: Total matte loss, MOC and off-gas as a function of contact time at 1450 °C, for Matte-A exposure to SG-graphite

5.3.1.6 Analysis of the gas condensate produced during the experiments: Verification of the FactSage simulations

The gas condensate was collected during the exposure of SG-graphite to industrial matte. It was analysed to confirm that matte species are lost to the off-gas. The off-gas produced during the experiments was trapped at 100 °C, 25 °C and 0 °C. For each temperature one sample was collected over a number of experiments because a very small amount of condensate was collected for each experiment, a composite of a number of tests was used for the analysis.

Analyses of the gas condensate are shown in Table 5-22, Table 5-23 and Table 5-24, for the condensate sample at respectively 100 °C, 25 °C and 0 °C.

Three phases could be identified by the SEM in a 100 °C condensate sample, the annotation in Table 5-22 (phase 1 to 3) refers to the three phases. The condensate at 100 °C consisted of the copper-iron based sulfide compounds which had Al, Mg and Si elements, one compound had up to 20 atomic percent Si, 13 atomic percent Al and 7 atomic percent Mg.

The condensate at 25 °C had three identifiable phases annotated phase 1, phase 2 and phase 3. This condensate mostly consisted of elemental sulfur and a copper iron sulfide compound (with Al, Mg and Si) similar to a phase detected at the gas condensed at 100 °C.

At 0 °C the condensate mostly consisted of elemental sulfur and the aluminium, magnesium and copper based sulfide compounds. Five phases could be identified, they are annotated phase 1 to 5 Table 5-24.

It should be noted that the species that are in a gaseous state below 0 °C were not captured in the gas condensate since the lowest temperature of the off-gas duct was 0 °C. Therefore the analyses of the gas condensate presented in Table 5-22 to Table 5-24 are merely an indication of the species that reported to the off-gas. As such it was a challenge to accurately estimate the mass balance of species after the exposure of industrial matte to graphite.

The quantification of the process gas was not possible owing to a lack of online-gas analysis. Some matte was embedded in graphite as such accurate mass balance around the system could not be attained. The chemical analysis of the graphite crucible post mortem was not helpful due to the concentration effect. Due to the minute fraction of matte inclusions compared to the volume of graphite, accurate detection of matte species in graphite was not possible.

Table 5-22: The analysis of the condensate collected at ~100 °C (SEM-EDS atomic percent), composite sample collected during exposure of industrial matte to SG-graphite

Atom%	Phase 1	Phase 2	Phase 3
Al	13.1	19.0	7.7
Cu	9.9	11.2	32.4
Fe	6.9	7.8	20.7
K	1.0	0.9	1.1
Mg	7.4	6.7	3.3
Ni	0.3	0.1	0.7
S	41.5	47.4	29.2
Si	20.3	6.8	4.8

Table 5-23: The analysis of the condensate collected at ~25 °C (SEM-EDS atomic percent), composite sample collected during exposure of industrial matte to SG-graphite

Atom (%)	Phase 1	Phase 2	Phase 3
Al	16.2	9.1	0.5
Cl	0.4	0.1	0.1
Cu	12.0	3.3	2.0
Fe	7.6	2.6	1.3
K	1.4	0.8	0.3
Mg	7.4	2.9	0.7
Ni	0.2	0.1	0.1
S	39.2	71.3	91.2
Si	15.6	9.6	3.6

Table 5-24: The analysis of the condensate collected at ~0 °C, (SEM-EDS atomic percent), composite sample collected during exposure of industrial matte to SG-graphite

Atomic percent	Phase 1	Phase 2	Phase 3	Phase 4	Phase 5
Al	2.4	0.2	2.4	17.9	3.7
Cl	-	-	3.9	1.7	0.5
Cu	2.0	0.8	33.0	0.9	14.9
Fe	1.3	0.6	1.2	6.4	7.1
K	-	-	1.5	3.3	0.5
Mg	1.0	20.3	1.6	0	1.7
Ni	0.0	0.3	0.0	0.2	0.1
S	87.6	76.8	54.2	65.7	63.5
Si	5.7	1.1	2.2	3.9	7.9

5.3.1.7 Effect of crucible volume on Matte-A penetration through SG graphite

To determine the effect of the matte foaming on the matte penetration through the SG graphite, tests were conducted in which the level or volume of the matte in the graphite crucible was varied. In one crucible, the industrial matte was filled to capacity (to the top edge), as in Figure 4-10a; the other crucible was half-filled with matte. Matte-A, Matte-L and Matte-P were exposed to SG graphite. The specimen (filled and half-filled crucibles) were heated to 1150 ºC and held for 1 hour.

The crucibles that were half-filled with matte were not penetrated by liquid matte (no matte was observed outside the crucible after exposure). The crucibles that were filled to full capacity were penetrated by liquid matte. The penetrated matte was around 50 mass percent, as observed in crucible tests performed at temperatures from 900 ºC to 1450 °C.

5.3.1.8 Summary

The industrial matte penetrated through the SG graphite, but the HG graphite was not penetrated by the industrial matte. The industrial matte was molten at 900 °C, below this temperature total matte loss was 1 mass percent. At 900 °C liquid matte started penetrating through the SG crucible. Temperature and contact time did not have an effect on the liquid matte penetration. The average amount of liquid matte penetration was 50 mass percent at all the tested conditions. An increase in temperature and contact time enhanced the matte loss to the off-gas. The gas condensate consisted of the species of matte such as copper, iron and sulfur. Other elements (Al, Si, and Mg) from the oxide impurities reported to the off-gas.

Liquid matte penetration was not observed where the matte occupied half the volume of the crucible. Therefore the level to which the matte fills the crucible was the parameter that affected the penetration of matte. The penetration of industrial matte was observed when the matte was filled to the top-edge of the crucible, the penetration of industrial matte was not observed when the matte was filled to half the volume of the crucible.

5.3.2 Chemical interaction between SG graphite and Matte-A

Wear of graphite was not observed after exposure to industrial matte at 900 °C and 1250 °C. Increasing the temperature to 1450 °C resulted in chemical reactions between the graphite, matte and the impurities in the industrial matte. Matte segregated into three layers, a metallic phase at the bottom, a sulfide phase and a slag globule that attached to the surface of the graphite. The specimen shown in Figure 5-31 was exposed to 1450 °C for 1 hour to study the chemical interaction between graphite and industrial matte. Similar behaviour was observed for Matte-A, Matte-L and Matte-P. The slight difference was the composition of the slag-globule, Matte-L and Matte-P had less impurities and they had $FeCr_2O_4$ as the abundant phase in the slag-globule. The results in this section are specific to Matte-A.

The oxide phases (impurities) that were present in the Matte-A sample reacted with the matte, forming a sulfide phase enriched in Al, Ca, Cr, Mg, and Si. The sulfide phase is annotated as matte in Figure 5-31a. The residual oxide-phases (slag in Figure 5-31 a) collected on top of the sulfide layer.

The detailed layout of the slag-graphite interface is shown inFigure 5-31. In Figure 5-31a is a 2D tomogram, b is a BSE image and c is a detail of graphite-slag interface (OM image). A metal layer segregated below the sulfide phase and settled at the base of the crucible (metal in Figure 5-31a).

The specimen was subjected to EPMA to determine the chemical composition of the species in the matte residue, metal and the oxides. BSE image of the matte residue is shown in Figure 5-32, the composition of the annotated phases is summarised in Table 5-25.

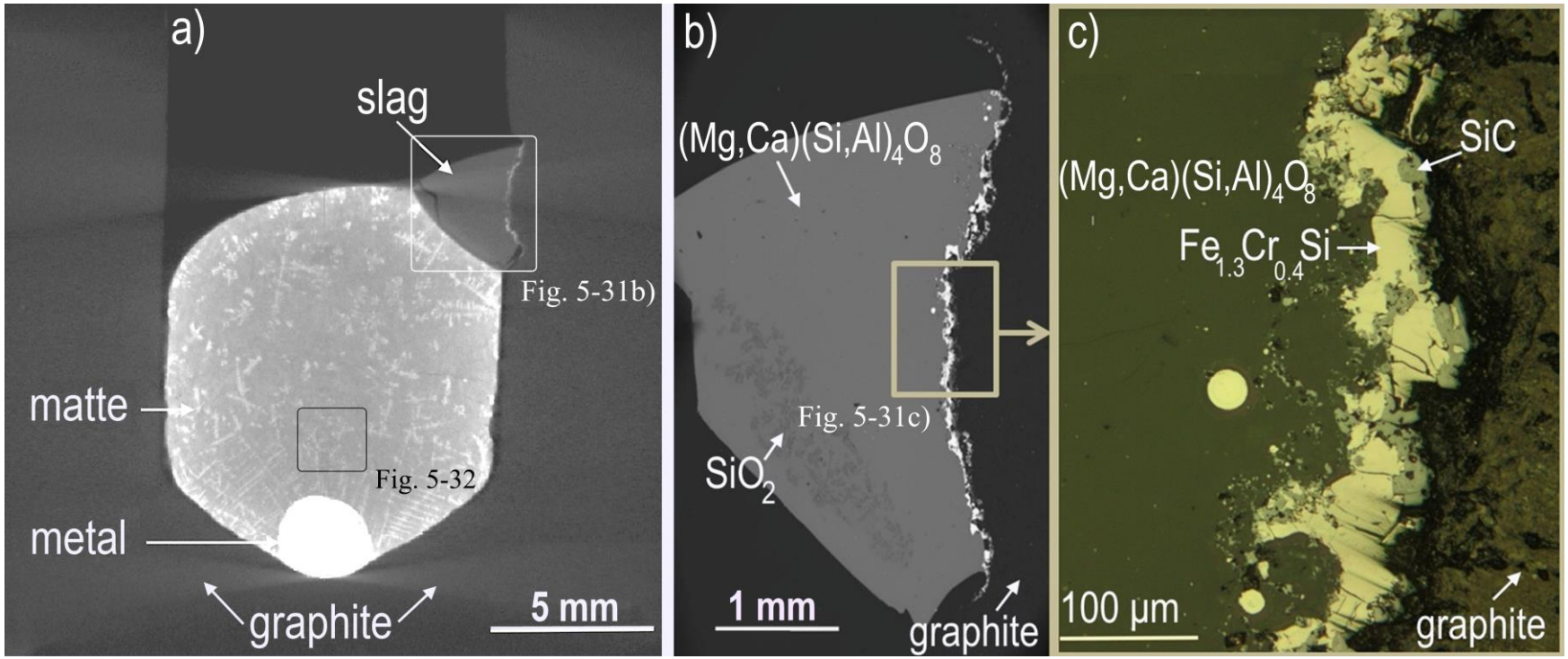

Figure 5-31: SG Graphite-Matte A specimen after 1 hour exposure at 1450 °C; a) graphite with solidified matte (XRM image), b) slag-graphite interface (BSE image), c) detailed slag-graphite interface (OM image)

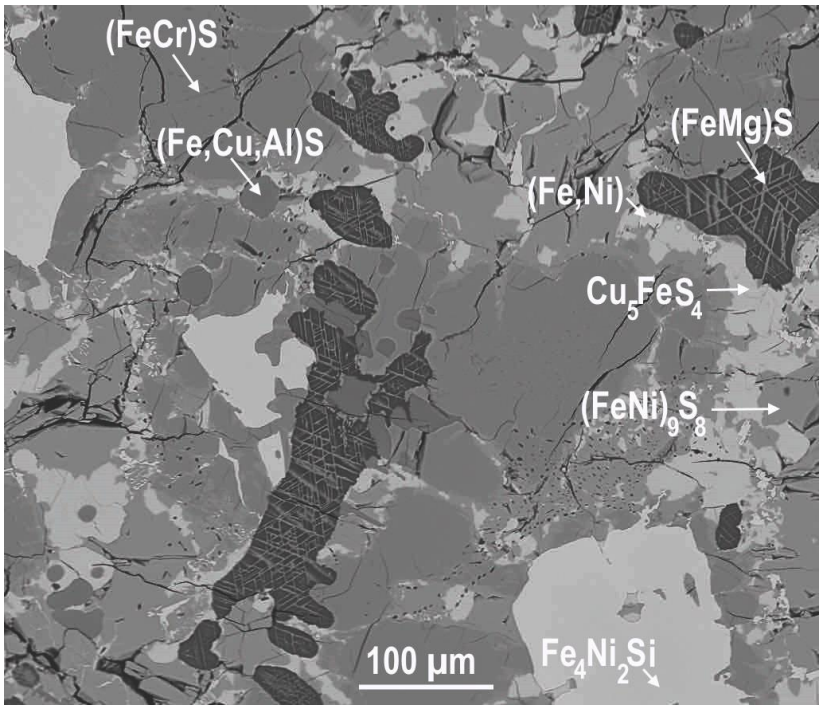

Figure 5-32: Matte-A after 1-hour exposure to SG-graphite at 1450 °C; BSE image, phases detected by EPMA are annotated

Table 5-25: EPMA Analysis of the Matte-A after exposure to SG-graphite for 1 hour at 1450 °C (mass percent)

	Al	Ca	Co	Cr	Cu	Fe	Mg	Mn	Ni	S	Si
*$(FeMg)_{0.95}S$	-	1.8	-	1.9	3.6	29.9	14.7	2.1	3.2	42.7	-
**$(FeMg)_{1.1}S$	-	1.4	-	4.2	7.0	47.7	2.1	0.3	1.4	36.0	-
CaS	-	50.9	-	-	3.7	2.2	0.9	-	-	42.3	-
$(CuFeAl)_1S$	6.4	-	-	-	20.8	31.0	1.0	0.9	0.3	37.3	-
$(FeCr)_1S$	-	1.5	0.2	4.2	4.9	49.2	2.0	0.3	2.4	35.4	-
$(FeNi)_9S_8$	-	-	0.3	-	3.5	40.3	-	-	22.9	33.0	-
Cu_5FeS_4	-	-	-	-	68.6	7.8	-	0.1	0.1	23.3	-
Fe_4Ni_2Si	-	-	1.6	-	1.2	57.9	-	-	32.1	-	7.2
$FeNi_2$	-	-	-	-	-	32.6	-	-	67.4	-	-

*In Figure 5-32 this is the dark phase labelled (FeMg)S,
**lamellae (lines_light phase) in the phase labelled (FeMg)S

5.3.2.1 Analysis of a sulfide residue (matte)

Troilite (FeS), pentlandite solid solution ($(FeNi)_9S_8$) and bornite solid solution (Cu_5FeS_4) were major phases in the Matte-A sample, these phases are still detected in the sulfide residue after

1 hour exposure at 1450 °C as seen in Figure 5-32 (SEM-BSE image of the matte residue). Other sulfides in a matte residue are the products of the interaction between the graphite, matte and the oxide-impurities. These are; (FeMg)S, CuFe(Al)S, (CuFeCr)S, Fe_4Ni_2Si, $FeNi_2$ and minor amounts of CaS. Elements such as; Al, Ca, Cr, Mg and Si were in an oxide form in the matte sample (Table 4-8). After exposure, these elements are in a sulfide phase. This indicates that; sulfidation of silicates occurred during the exposure of industrial matte to graphite at 1450 °C.

5.3.2.2 Analysis of a metal

The silicide (FeNi-Si) detected in the matte residue formed the bulk of the metal phase in Figure 5-31a. The metal consisted of Fe_4Ni_2Si and $FeNi_2$ alloy, similar to the metal phases detected in a matte residue (Table 5-25). The metal phase formed as a product of chemical reactions between the graphite, matte and oxide-impurities. This statement is qualified by the presence of silicon in the metal phase. The $FeNi_2$ alloy formed according to Equation 8 due to the metallization of (Fe, Ni)S that results from the loss of sulfur. The average density of an alloy (Fe, Ni) is 7400 $kg.m^{-3}$ [Tesfaye et al. 2010], while that of the matte varies from 4800 $kg.m^{-3}$ to 5200 $kg.m^{-3}$ [Eksteen 2011], this is why the metal settled below the sulfide layer.

5.3.2.3 Analysis of the slag globule

Oxide-impurities segregated from the sulfide residue and formed a globule of slag on top of the sulfide layer (annotated as slag in Figure 5-31a). The slag-globule consisted of $(Mg, Ca)(Si, Al)_xO_y$ and SiO_2 (annotated in Figure 5-31b). The EPMA analysis of the slag globule is in Table 5-26. A metallic layer formed at the interface of the graphite and the slag-globule. The metallic layer consisted of SiC that is attached to the graphite and the $Fe_{1.4}Cr_{0.4}Si$ adjacent to the SiC (annotated in Figure 5-31c).

The slag-globule is depleted in Al, Cr, Fe, Mg, and Si when compared to the composition of the oxide phases in the matte samples (Table 4-8). These elements were converted from silicates to sulfides as per the reaction in Equation 7. These sulfides (CaS, CrS, FeS and MgS) formed a sulfide solid solution as discussed in Section 3.3.

Table 5-26: EPMA analysis of Matte-A slag globule after 1 hour exposure at 1450 °C (mass percent)

Al	C	Ca	Cr	Fe	Mg	Ni	O	Si
-	-	-	14.8	59.5	-	3.1	-	22.6
8.3	-	3.8	-	0.1	6.1	-	50.2	31.7
-	-	-	-	-	-	-	53.3	46.7
-	28	-	-	-	-	-	-	72.0

5.3.2.4 Effect of contact time on the interaction between graphite and the slag-globule

The Matte-A was exposed to SG-graphite at 1450 °C for 12 hours to determine the effect of contact time on the interaction of graphite with industrial matte. The composition of the phases in the matte residue after 12 hours exposure at 1450 °C is shown in Table 5-27.

Metallization of (Fe, Ni)S in the bulk matte increased with exposure time. As such, the proportion of metal (FeNi-Si) in the matte increased. The compositions of the phases constituting the matte residue did not change with exposure time, the phases detected after 1 hour exposure (Table 5-25) were still present in a matte residue after 12 hours exposure.

Graphite wear around the slag globule increased with exposure time. The layout of the graphite-slag interface is shown in Figure 5-33, Figure 5-33a is the layout after 1 hour exposure, Figure 5-33b is the layout after 12 hours exposure. In Figure 5-33 the erosion depth is given by P-*i* and P-*f*, P-*i* marks the original periphery of the graphite wall, P-*f* marks the periphery of the graphite wall after exposure.

The consumption of graphite at the gas/slag and metal/slag interface was ≤0.5 mm after 1 hour exposure and it increased to >2 mm after 12 hours exposure. This indicated that with exposure time the consumption of graphite increased.

The size of the slag-globule decreased significantly with exposure time as seen in Figure 5-33b. The metal layer (SiC/FeCr-Si) disappeared with exposure time, this metal was observed at the slag-graphite interface after 1-hour exposure (annotated in Figure 5-31c). After 12 hours exposure the metal layer is not observed at the surface of the graphite (Figure 5-33b). The metal layer could react with the process gases such as sulfur; this could lead to losses of elements to the

off-gas since the sulfides are typically more volatile than the metal, the exception would be nickel sulfide that seem to be less prone to evaporation.

In the bulk matte residue the metallization of matte species continued with exposure time, this is evinced by the increase in the metal (Fe, Ni alloy) phase in the matte with exposure time.

Table 5-27: SEM-EDS analysis of the matte-residue after exposure of Matte-A to SG-graphite at 1450 °C for 12 hours (mass percent)

Formula	**Al**	**Ca**	**Cr**	**Cu**	**Fe**	**Mg**	**Mn**	**Ni**	**S**	**Si**
$(FeMg)_{0.95}S$	-	2.15	2.6	2.9	35.7	11.6	2	0.9	42.8	-
$(CuFeAl)_1S$	5.3	-	-	21.8	33.9	0.6	1.8	-	36.5	-
$(FeCr)_1S$	-	-	5.2	2.1	54.7	-	-	3.2	34.8	-
$(FeNi)_9S_8$	-	-	-	2.5	43.1	-	-	23.3	31.1	-
Cu_5FeS_4	-	-	-	67.8	10.5	-	-	-	21.7	-
Fe_4Ni_2Si	-	-	-	-	58.7	-	-	35	-	6.3
$FeNi_2$	-	-	-	2.9	32.5	-	-	64.5	-	-
(Fe, Ni)	-	-	-	2.6	63	-	-	35.8	-	-

5.3.2.5 Summary

The interaction between graphite and industrial matte resulted to the formation of three products, an alloy, a sulfide and a slag-globule. The alloy consisted of a FeNi-Si and FeNi. The sulfide had the sulfide phases that were present in the matte samples as well other sulfides that formed due to the sulfidation of silicate species that were in the oxide impurities. The slag segregated to the top of a sulfide layer. The slag-globule reacted with the graphite and formed metallic phases at the interface of the slag-globule and the graphite. The reactions between graphite and slag-globule were enhanced with exposure time. The volume of the slag-globule decreased with exposure time.

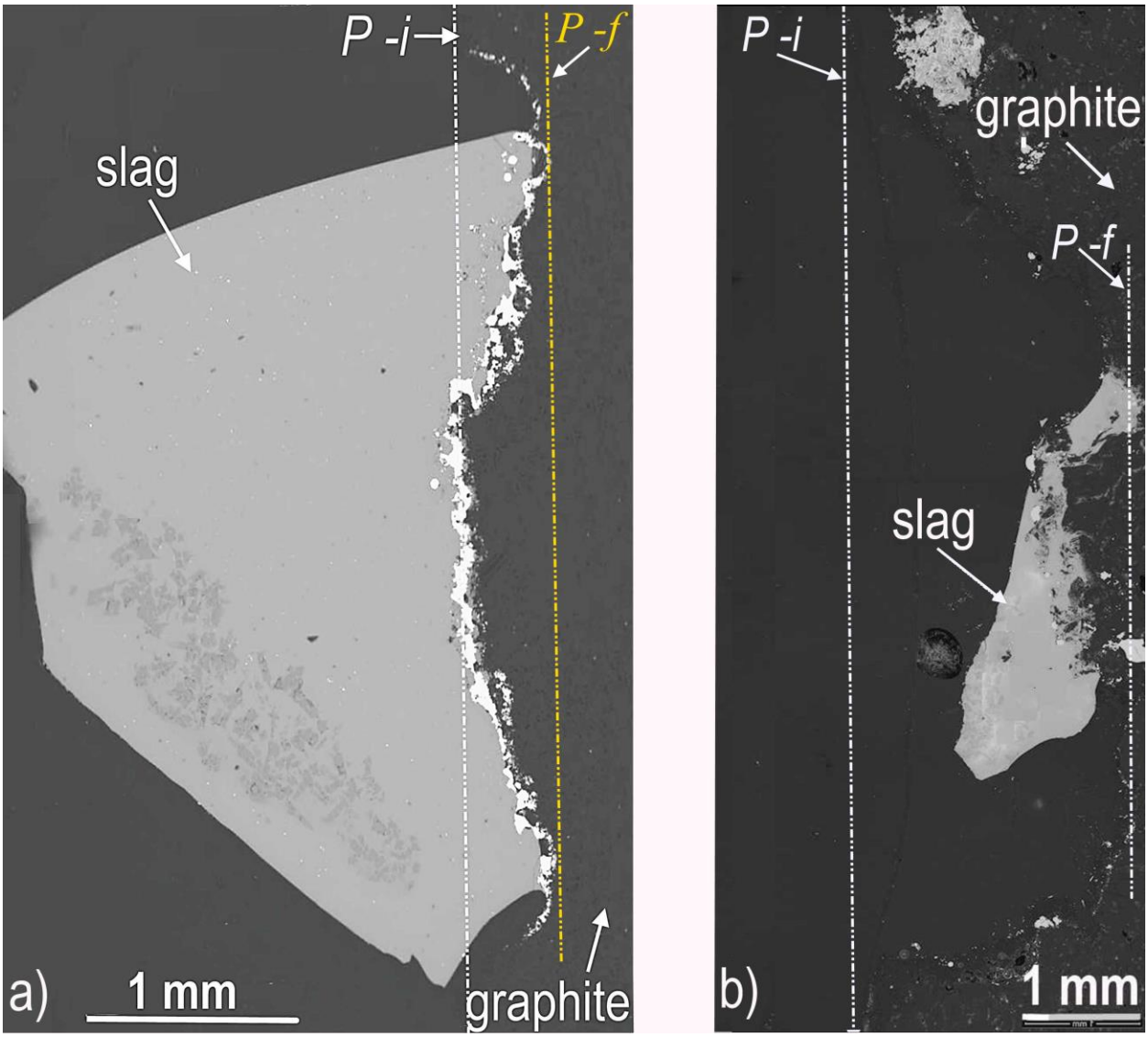

Figure 5-33: SG-graphite and slag-globule interface BSE-images a) 1 hour; b) 12 hours exposure, of Matte-A to SG-graphite, P–*i* = initial periphery of the crucible; P–*f* = final periphery of the crucible;

5.3.3 Dissolution of graphite by industrial matte

Industrial matte samples were exposed to SG-graphite to determine the dissolution of graphite by industrial matte, specimens were reacted for 1 hour at 1450 °C. The amount of carbon in the matte-residue was used as a measure of dissolution. The effect of graphite grade on the

dissolution of graphite by industrial matte was determined. HG and SG graphite was exposed to Matte-A at 1000 °C for 1 hour.

5.3.3.1 Dissolution of SG-graphite by Matte-A

Industrial matte samples were exposed to SG-graphite. The residual products were analysed for carbon. Three products formed, a metal/alloy, a sulfide and a slag-globule. The carbon content in the alloy (metal in Figure 5-31a) was 0.3 mass percent, whereas the sulfide phase (matte inFigure 5-31a) had 0.03 mass percent of carbon. This indicated that carbon has a higher solubility in a metal compared to the corresponding sulfide, a sulfide phase seemed to dissolve minimal amounts of carbon. The carbon content in the slag globule was not determined since the slag-globule adhered to graphite; acquiring representative powder sample was a challenge. The interaction between the slag-globule and the graphite resulted to the formation of CO gas according to the reaction proposed in Section 5.3.2.4. As such the slag globule possibly caused significant wear of graphite compared to graphite dissolution in a sulfide or a metal.

5.3.3.2 Effect of graphite grade on graphite dissolution by Matte-A

The matte residue exposed to HG and SG graphite was analysed for carbon content. Carbon content in the bulk matte was 0.38 and 0.33 mass percent for SG and HG graphite respectively. This is equivalent to 0.6 mm and 0.5 mm erosion depth (loss in diameter) for the SG and HG graphite crucibles respectively. Dissolution of SG and HG graphite by matte did not vary significantly since the difference in diameter loss was 0.1 mm. The estimated values of the erosion depth were calculated from the mass of carbon detected in matte, density of graphite and the calculated volume of the crucible.

There was no evidence of graphite erosion at the graphite-matte interface. The change in the thickness of the graphite wall could not be accurately measured with the SEM or optical microscope. The inner-surface finish of the crucible (graphite-matte interface) was not smooth therefore there was no clear point of reference. At higher magnification such as in SEM the surface seemed uneven therefore measuring the wall thickness before and after exposure poised challenges.

5.4 Graphite wear by industrial melt (matte and slag)

Graphite was exposed to both matte and slag as per the set-up in Figure 4-10b. Exposing matte and slag simultaneously was done to simulate the layout of the melt in an industrial set-up. The interaction of graphite with slag and with matte was directly compared. The slag-line erosion at the matte-slag interface was also assessed. The layout of the specimen after exposure is shown in Figure 5-34.

5.4.1 Overview-specimen layout

Traces of melt (annotated as infiltrate in Figure 5-34) were observed randomly dispersed in the graphite wall from the graphite-melt interface to the outer surface of the graphite. The melt prills were more prominent against the slag layer; these prills are bright phases annotated as infiltrate in Figure 5-34. The tiny prills were only observed microscopically, there was no evidence of melt dripping out of the crucible. The composition of the melt prills in the graphite wall was FeNi-Si; a summary of analysis is in Table 5-28.

5.4.2 Slag interaction with graphite

The slag is porous when compared to matte; pores in the slag can form as a result of foaming and gas formation during melting. The interface of the graphite and slag was examined with SEM-BSE; the image is shown in Figure 5-35. The analysis of the melt residue is shown in Table 5-28. The slag-residue is depleted in Cr, Fe, Mg and Si when compared to the initial composition of the slag (Table 4-17). The abundant phase in the slag layer is $(Mg, Ca)(Si, Al)_xO_y$, this phase is similar to the phase observed in a slag-globule that segregated from the matte (Figure 5-31b). The slag analyses before and after exposure are shown in Table 5-29.

Amongst the slag are sulfide phases and a metal phase as annotated in Figure 5-35. The sulfides consist of (Fe, Cr)S, (Fe, Mg)S, (Mg, Cr, Ca)S and (Mg, Ca)S and the bright metal phases consist of (FeNi)Si. Sulfides and metal were not detected in the original slag sample as seen in

(Table 4-17); the sulfides and metal are the products of the interaction between matte phases and slag.

Table 5-28: EPMA analysis of the sulfide and metal phases in slag after exposure of Matte-A and Slag-A to SG-graphite at 1450 °C for 12 hours (mass percent)

	Ca	**Co**	**Cr**	**Cu**	**Fe**	**Mg**	**Mn**	**Ni**	**S**	**Si**
$(FeCr)_xS$	-	-	13.0	0.7	46.9	-	-	-	39.5	-
(FeMg)xS	4.1	-	5.3	4.7	21.9	16.0	2.3	-	45.4	-
(MgCrCa)xS	7.5	-	16.0	0.7	3.3	23.0	0.5	-	48.7	-
(MgCa)xS	8.6	-	5.0	0.8	4.8	29.0	0.6	-	51.5	-
(Fe, Ni)xSi	-	0.2	1.0	0.1	77.6	-	-	6.3	0.8	14.0
$(FeNi)_xSi$	-	0.6	0.5	0.7	73.5	-	-	16.0	0.1	8.6

Table 5-29: EPMA analysis of Slag-A before and after exposure to SG-graphite at 1450 °C for 12 hours (mass percent)

Before exposure

Formula	**Al**	**Ca**	**Cr**	**Fe**	**Mg**	**Na**	**Ni**	**O**	**Si**
$FeCr_xO_y$	-	-	47	23	-	-	3	27	0
$^{\#}(FeSi)_xO_y$	-	-		49	-	-	6	31	14
$^{**}(Mg,Fe)_xSiO_y$	2	2	1	8	16	-	-	45	26
$^{*}(Fe, Mg, Ca, Al)Si_xO_y$	3	4	0.8	11	4	1.2	-	45	31
$^{\&}(Ca, Na)(Si, Al)_xO_y$	17	11	-	0.5	-	2	-	46	23
$^{*}(Al, Si)_xO_y$	24	-	-	-	-	-	-	50	26

After exposure

Formula	**Al**	**Ca**	**Cr**	**Fe**	**Mg**	**Na**	**Ni**	**O**	**Si**
$FeCr_xO_y$	-	-	48	25	-	-	-	26	-
$^{\#}(Mg, Fe)_xSiO_y$	-	-	1	46	7	-	-	31	15
$^{*}(Ca, Fe)_xSiO_y$	2	14	1	23	1	-	-	37	22
$^{\&**}(Mg, Ca)(Si, Al)_xO_y$	5	6	-	-	16	-	-	43	30
$^{*}(Al, Mg)Si_xO_y$	21	-	-	-	8	-	-	30	40

$^{\#}$Fe spinel has Mg after exposure, **abundant phase (no Fe after exposure), *reduced after exposure, $^{\&}$has Mg after exposure,

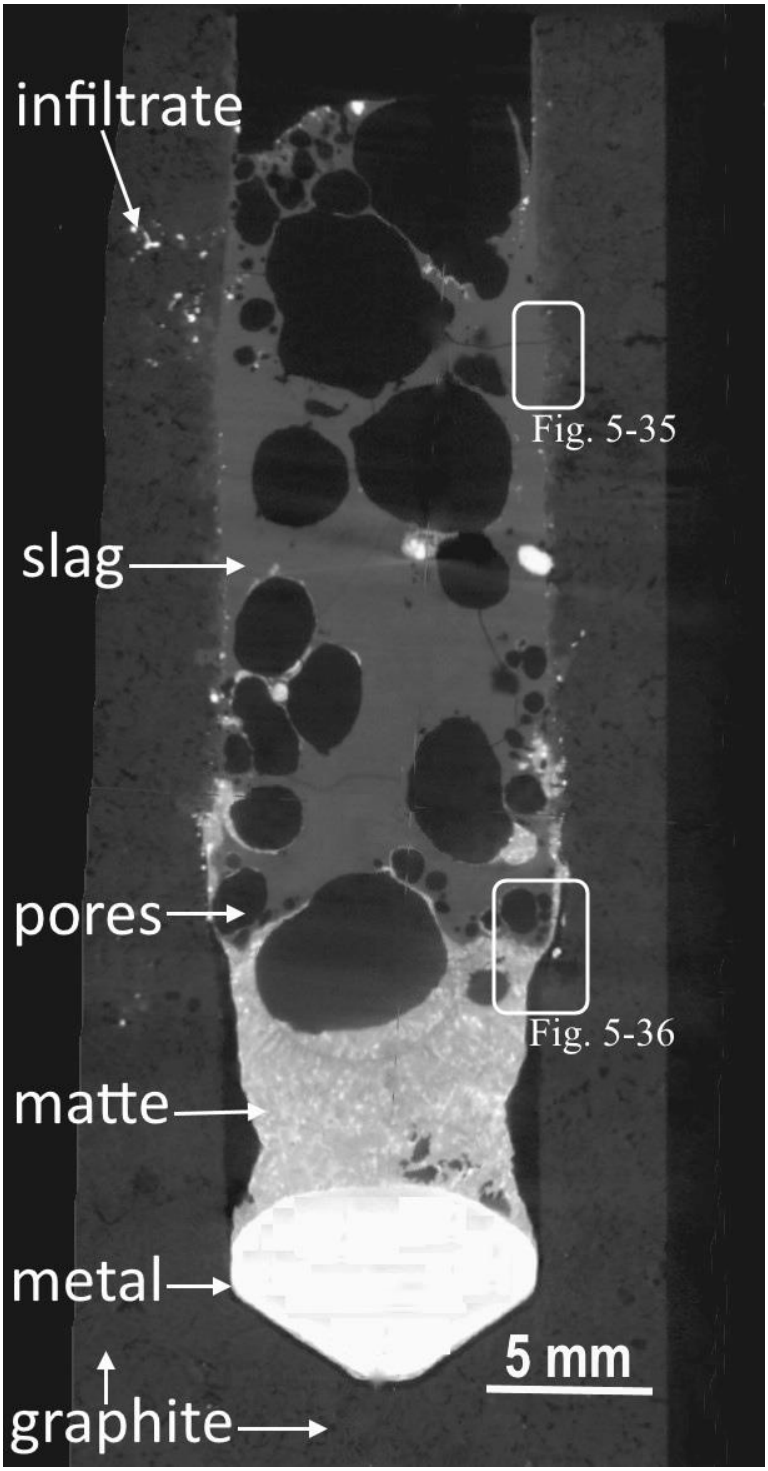

Figure 5-34: SG-graphite exposed to Slag-A and Matte-A at 1450 °C for 12 h, XRM image, the annotated positions are where Fig. 5-35 and Fig. 5-36 were taken

5.4.3 Penetration of slag through graphite

Slag penetration into the graphite wall was up to 1 mm after 12 hours exposure. The oxidation state of the infiltrate changed with depth of infiltration. Phases at the tip of the infiltrate had a lower oxidation state than the phases in the bulk slag. Phases such as SiO_x, SiC and $(AlMg)_x$ SiO_y were detected in the infiltrate (phases in-contact with the graphite). The EPMA analyses of these phases are highlighted in Table 5-29.

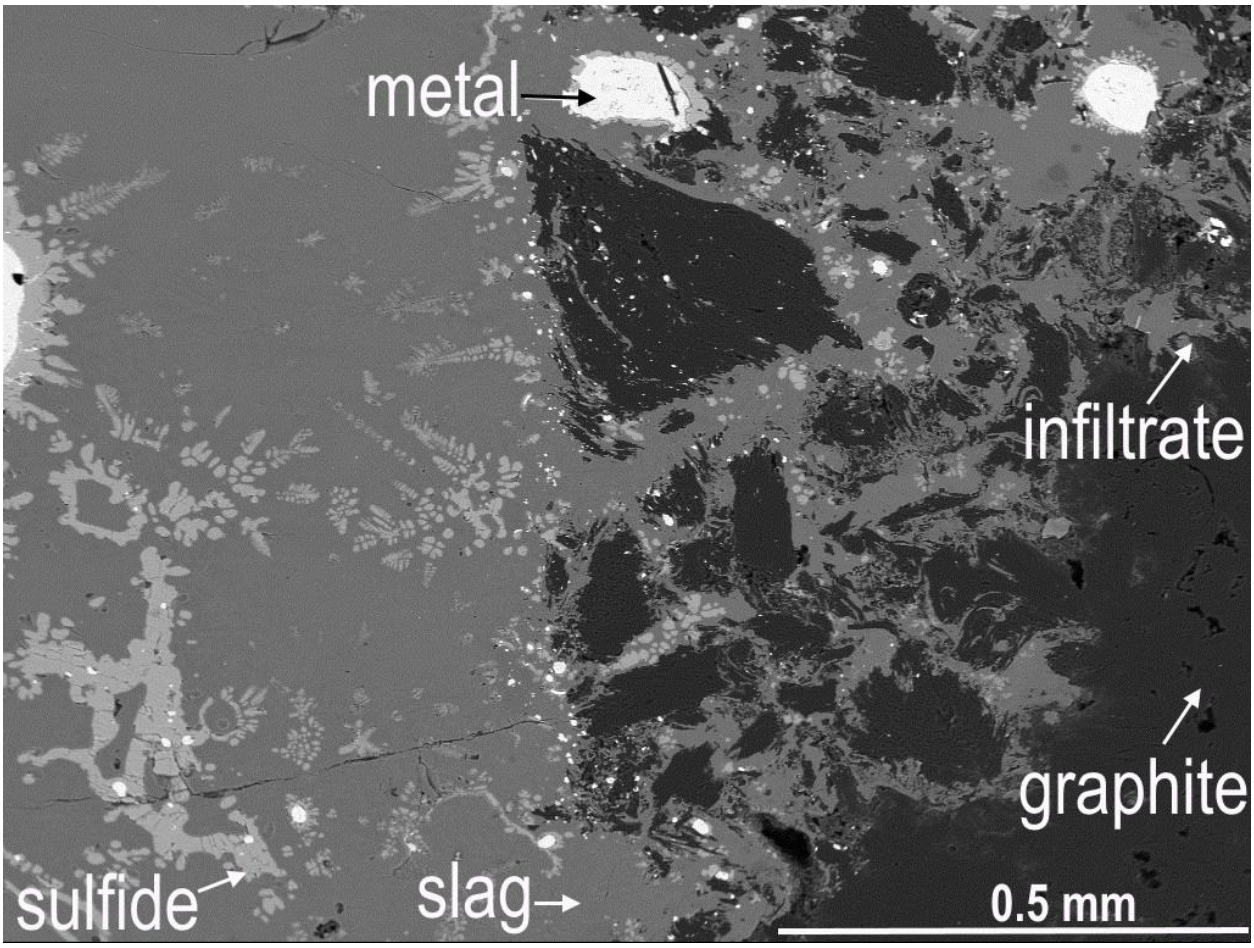

Figure 5-35: Graphite-slag interface for Slag-A exposed to SG-graphite at 1450 °C for 12 h, BSE image

5.4.4 Interaction of graphite with matte

The interaction between industrial matte and graphite has been discussed in Section 5.3.2. The silicate impurities in matte reacted to form sulfides and a metal phase. The oxide-impurities in matte were reduced by graphite such that a metallic phase formed at the interface of the graphite and the slag-globule (Figure 5-31). In the slag-matte set-up, the matte interacted with graphite similar to the behaviour discussed in Section 5.3.2. The composition of the matte residue is the same as reported in Table 5-28. A metal layer was observed at the bottom of the matte (Figure 5-34), this metal formed as a result of the metallization of sulfides such as $(FeNi)_xS$ as discussed in Section 5.3.2. FeNi-Si and FeNi alloy were major components of the metal phase in Figure 5-34.

The matte detached from the graphite as seen in Figure 5-34, there was a gap between the matte and the graphite after exposure. The matte pulled away from graphite due to non-wettability and shrinking during cooling and solidification.

5.4.5 Graphite erosion

Where graphite was exposed to both matte and slag simultaneously, localized wear of graphite was observed at the matte-slag interface. The profile of graphite at the matte-slag interface is shown in a BSE image in Figure 5-36, Figure 5-36 is a cross-section of a slag/matte setup after exposure to SG graphite at 1450 °C for 12 hours. Matte is a bright phase at the bottom, the slag is the grey phase on top of matte. Graphite is adjacent to the slag and matte from the bottom to the top. A vertical dotted line (annotated v) marks the original periphery of the graphite wall, a horizontal dotted line (annotated h) marks the height to which a matte layer appears between the graphite and slag at the interface.

A layer of matte appears parallel to the slag layer at the three-phase region (slag/matte/graphite interface). The height of this matte is ~5 mm above the slag-matte interface. Although this matte layer does not penetrate through the graphite wall, there is a minor erosion of the graphite where the matte layer appears. Above the marked height (h) it is mostly the slag that has penetrated the

graphite wall, the matte prills are scattered they do not form a continuous layer between the slag and the graphite.

It seem that erosion of graphite at the three-phase region does occur. To confirm the significance of Marangoni effect on the corrosion of graphite at the slag/matte/graphite interface the similar tests has to be run at longer interaction times and higher operating temperatures.

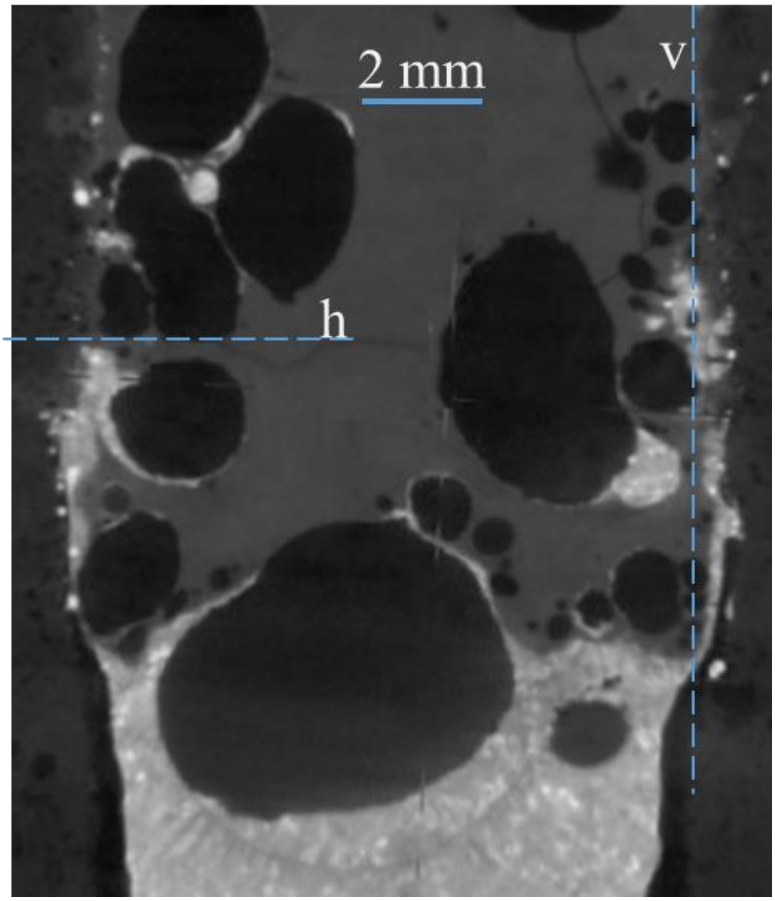

Figure 5-36: A BSE image of a three phase region of a specimen where SG-graphite was exposed to matte and slag at 1450 °C for 12 hours, matte is a bright phase at the bottom, slag is a grey phase on top of the matte, and graphite is adjacent to matte and slag from bottom to the top, a vertical line marked v indicates the initial periphery of the graphite inner surface, a horizontal line marked h indicates the height to which a matte layer appears between the slag and graphite interface

5.5 The effect of cooling graphite on the behaviour of liquid industrial matte

The forth research question was concerned with determining whether a frozen skull would form if graphite is cooled. To address this question a test was done to simulate the layout of a cooled PGM furnace refractory. The specimen was heated from the bottom and cooled from the top to create a temperature gradient. The sectioned specimen is shown in Figure 5-37, the temperature projections in Figure 5-37 were estimated using the temperature profile in Figure 4-8.

Sample 1 is shown in Figure 5-38 (BSE image). Matte is observed at the inner surface of the graphite. The estimated temperature around this area was ~902 °C. Sample 1 was cut 10 mm above the initial level of matte as annotated in Figure 5-37. The presence of matte above the initial level of matte indicate that during the exposure the matte foamed and its volume increased above its initial volume. The graphite wall against the frozen skull was not penetrated by matte, traces of matte were not observed on the graphite wall. From this sample it is observed that molten matte is able to form a frozen skull on the graphite surface when the temperature of the graphite is below the solidus temperature of the matte.

Sample 2 was cut 50 mm below Sample 1, BSE image of Sample 2 is shown in Figure 5-39. The frozen skull (solidified matte) was not observed on the inner edge of the graphite surface. Traces of matte were observed embedded in the graphite wall as seen in Figure 5-39. The presence of matte traces on the graphite wall indicates that liquid matte penetration occurred. The estimated crucible temperature at this area was ~1108 °C. It seem that as the temperature of the graphite surface increases the frozen skull at the graphite surface melts.

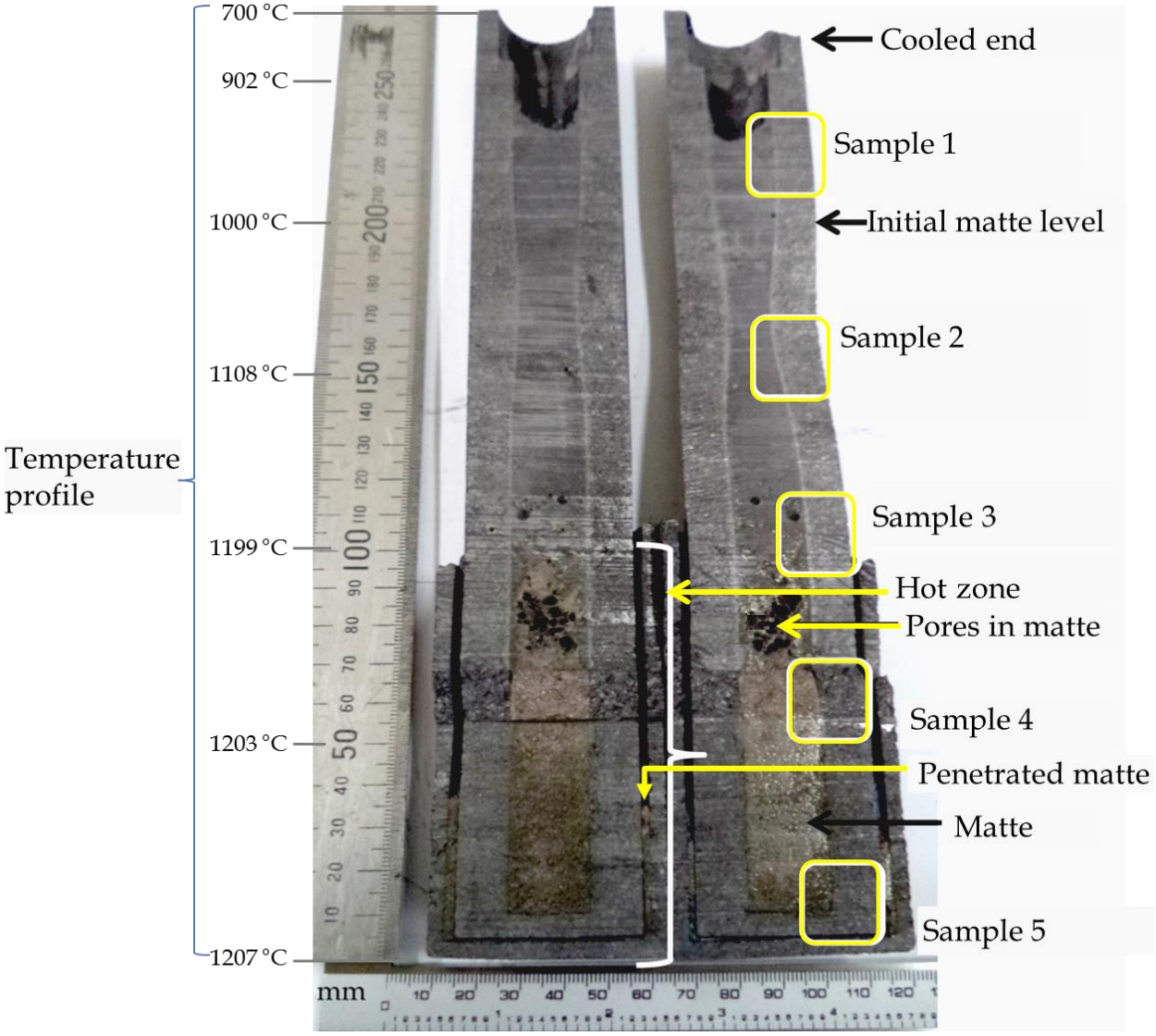

Figure 5-37: Cross-section of a cooled SG-graphite specimen after exposure to Matte-A at 1350 °C for 1 h, the temperature profile projections are on the right hand side, the scale is at the bottom of the image, the positions where the sample were taken are marked

Sample 3 was collected 100 mm below Sample 1, its BSE image is in Figure 5-40. The estimated temperature at this area is ~1199 °C, this marked the beginning of the hot zone. At this level the matte was porous, dark spots (annotated as pores in Figure 5-39) can be observed on the matte in Sample 3. A gap is observed between the matte and the graphite. The detachment of matte from the graphite surface may occur due to shrinkage during solidification.

Liquid matte penetration occurred at this level, this was evinced by the traces of matte in the wall of the graphite. Traces of matte were observed through the wall of the graphite, some matte

leaked to the outside of the crucible, this matte is annotated as penetrated matte in Figure 5-37. Due to the nature of the set-up, it is difficult to associate the liquid penetration of matte to a specific temperature zone. It is possible that matte penetrated during melting (before the temperature reached 1199 °C). The crucible was colder at the top while it was hotter at the bottom, therefore the liquid matte might have penetrated before the temperature reached 1199 °C as observed for the isothermal tests where liquid matte penetration occurred at melting temperatures which are below 1199 °C. At the hot-zone of the furnace (bottom of the crucible) the liquid matte penetration depth was greater than 10 mm, which was the thickness of the crucible.

Sample 4 was collected 150 mm below Sample 1; the BSE image of Sample 4 is shown in Figure 5-41. At this level the matte appears dense. The estimated temperature is 1203 °C. Liquid matte penetration occurred in this area, this is evinced by the traces of matte on the graphite wall.

Sample 5 was collected 200 mm below Sample 1; it was at the bottom of the crucible. BSE image of Sample 5 is in Figure 5-42. The estimated temperature is 1207 °C. The matte has no apparent pores. Matte penetration through the graphite wall was significant at the bottom of the crucible. Some matte penetrated through the entire width of the crucible and settled at the outer crucible (annotated as penetrated matte in Figure 5-37).

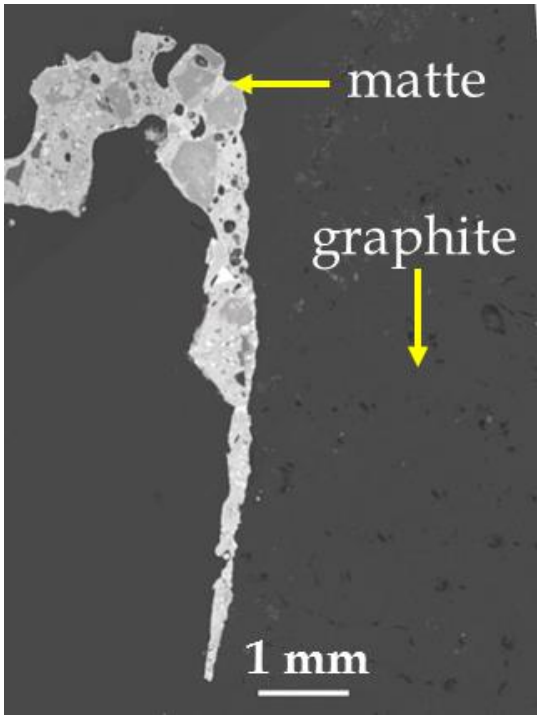

Figure 5-38: Sample 1 at ~902 °C; inner edge of the cooled-graphite, top cooled-end (side view), Matte-A exposure to cooled SG-graphite formed a frozen skull

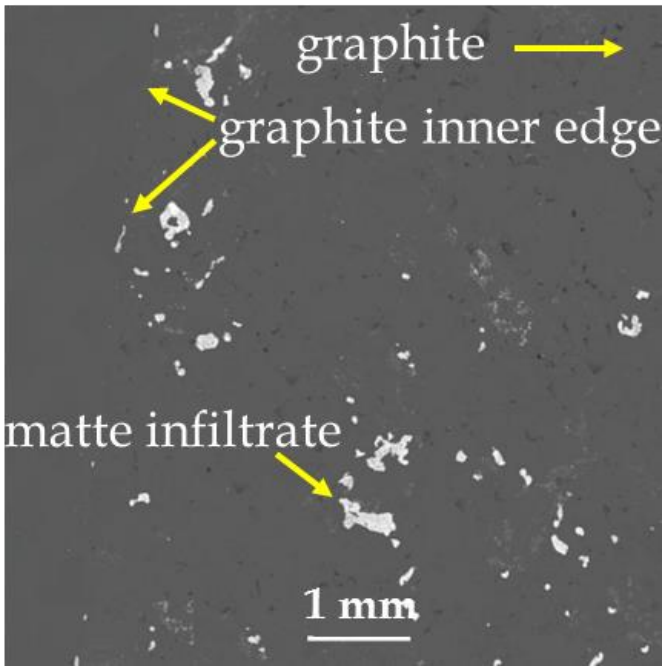

Figure 5-39: Sample 2 at ~1108 °C; inner edge of the cooled-graphite 50 mm below Sample 1 (side view), graphite wall infiltrated by matte

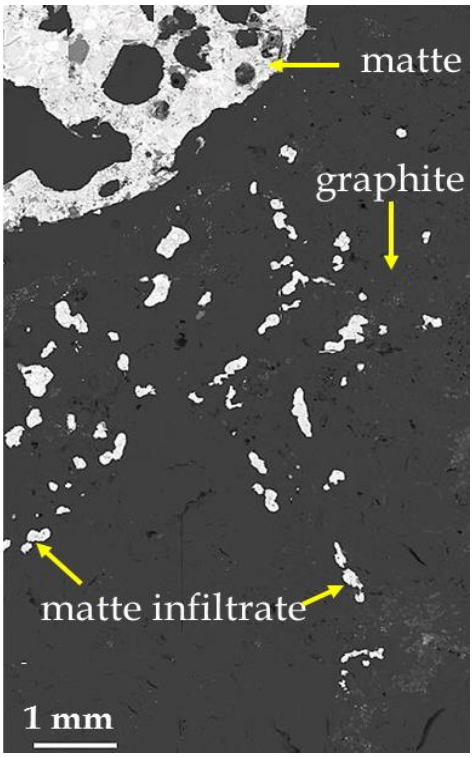

Figure 5-40: Sample 3 at ~1199 °C; inner edge of the cooled-graphite 100 mm from Sample 1 (top view), Matte-A residue and SG-graphite wall infiltrated by matte

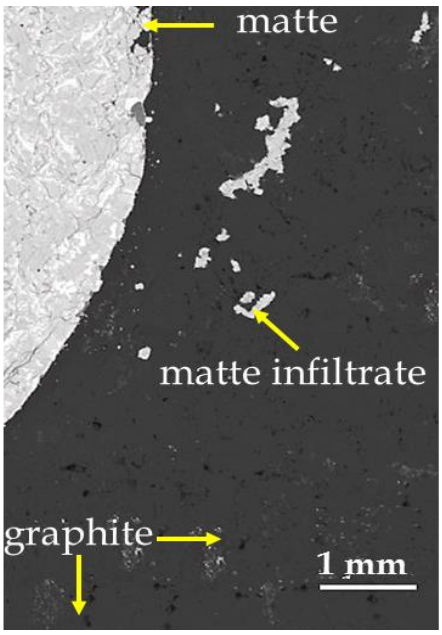

Figure 5-41: Sample 4 at ~1203 °C; inner edge of the cooled-graphite 150 mm from Sample 1 (top view), Matte-A residue, SG-graphite wall infiltrated by matte

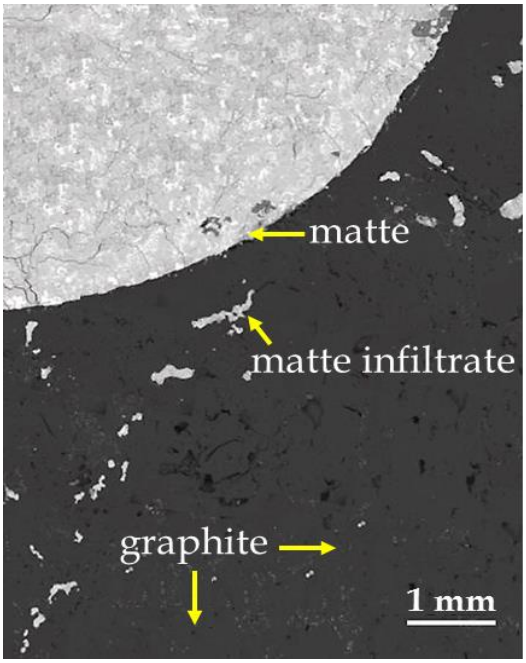

Figure 5-42: Sample 5 at ~1207 °C; inner edge of the cooled-graphite 200 mm from Sample 1 (side view), solidified Matte-A residue, SG-graphite wall with matte infiltrate

6 Results B: Wear of micropore carbon by a PGM matte

The compatibility of micropore-carbon with a PGM matte was assessed through crucible tests. These tests were done for comparative reasons to determine whether MPC could outperform graphite as a refractory against a primary PGM matte. These tests addressed research question 4: can MPC perform better than graphite?

MPC was exposed to a synthetic and an industrial PGM matte. Refractory wear was assessed by determining the chemical attack of the crucible using the following methods [Tomala et al. 2007]:

- Change in the composition and the microstructure of the refractory
- Change in the composition of the matte

Comparative static crucible tests were performed at 1350 °C and 1450 °C for 12 hours. The crucibles were filled to ¾ capacity to prevent penetration of liquid matte during melting which was observed with the SG graphite tests.

The mechanism of the dissolution of the refractory material was similar for synthetic and industrial matte. As such, the results reported apply to both synthetic and industrial matte.

6.1 Wear mechanism of the MPC refractory wall

The specimens were analysed with SEM to study the interaction between the MPC and the matte. Figure 6-1 has the BSE images of the MPC refractory wall, Figure 6-1a is the MPC sample (before exposure) and Figure 6-1b is the MPC refractory wall after exposure.

6.1.1 The microstructure of the MPC wall

The micropore-carbon sample consisted of carbon, Al and Si compounds, as annotated in Figure 6-1a. After exposure the structure of the micropore-carbon in Figure 6-1b appears disintegrated when compared to the original sample (Figure 6-1a).

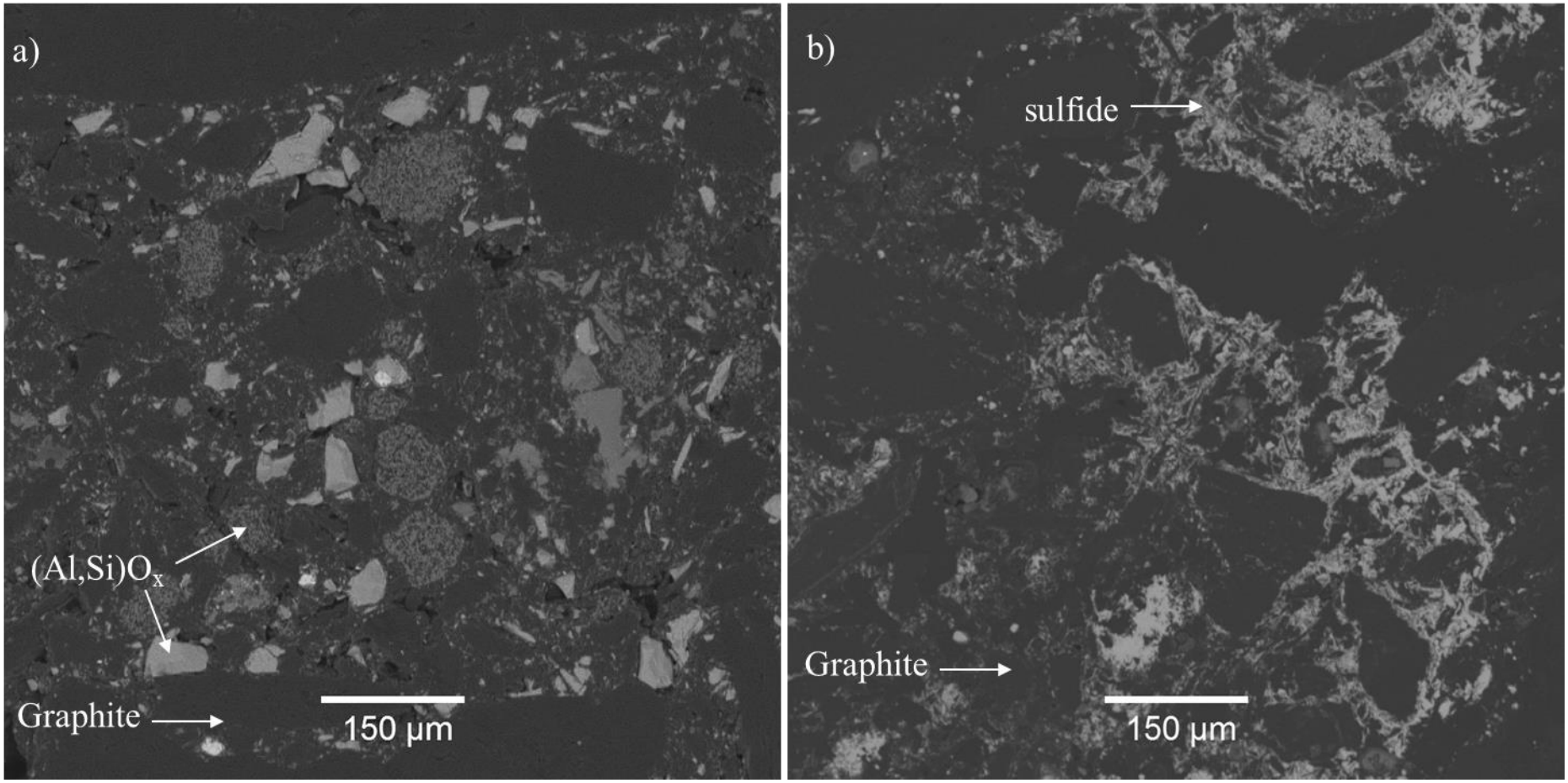

Figure 6-1: MPC refractory wall layout BSE-images (a) before exposure, b) after exposure to Matte-S at 1350 °C for 12 h

High infiltration of the matte constituents was observed at the interface of the refractory and the matte. The infiltrate in the MPC was analysed using SEM to determine its structure and its composition. Elemental composition of the infiltrate in the MPC refractory is shown in Table 6-1. Copper iron sulfide with up to 21 atomic percent Al was detected in the wall of the MPC refractory adjacent to the matte, Si was not detected in this sulfide phase. This sulfide phase seemed to have replaced the Si and Al compounds originally present as the matrix in the MPC refractory (Figure 6-1). The sulfide phase had a web like pattern, its concentration decreased towards the outer surface of the refractory. The infiltrated refractory appeared denser due to the web like structure of the sulfide phase, apparent pores were not observed in the infiltrated MPC wall (Figure 6-1b); in contrast the received block had open pores and minor cracks (Figure 6-1a).

Table 6-1: EDS analysis of the sulfide product in the MPC wall after exposure (atomic percent)

Elements	**S**	**Si**	**Al**	**Fe**	**Ni**	**Cu**
Atomic percent	50	0	21	11	0	18

6.1.2 Disintegration of the MPC wall

The wear mechanism of MPC wall was examined using SEM X-Ray mapping. The micropore carbon refractory wall was examined at the surface in contact with the matte (refractory-matte interface). The X-ray maps of the refractory-matte interface are shown in Figure 6-2.

The concentration of Si (Figure 6-2b) decreased significantly when compared to the starting material (Figure 6-1a). Al is still detected in the sulfide phase as seen in Figure 6-2c. In contrast, high concentrations of Cu, Fe and S are observed in the MPC wall (Figure 6-2 d to f), the MPC sample did not have Cu, Fe and S. The concentrations of Cu, Fe and S decreased towards the outer wall of the refractory. Based on the disintegration of the refractory wall and the detection of a sulfide compound in the MPC wall, it was evident that chemical reactions occurred between matte and the MPC.

The graphite specimen was not examined with X-ray mapping since the synthetic graphite was mainly carbon, no matrix was added. There was no interaction between the penetrated matte and the graphite therefore it was not necessary to use X-ray mapping to examine graphite.

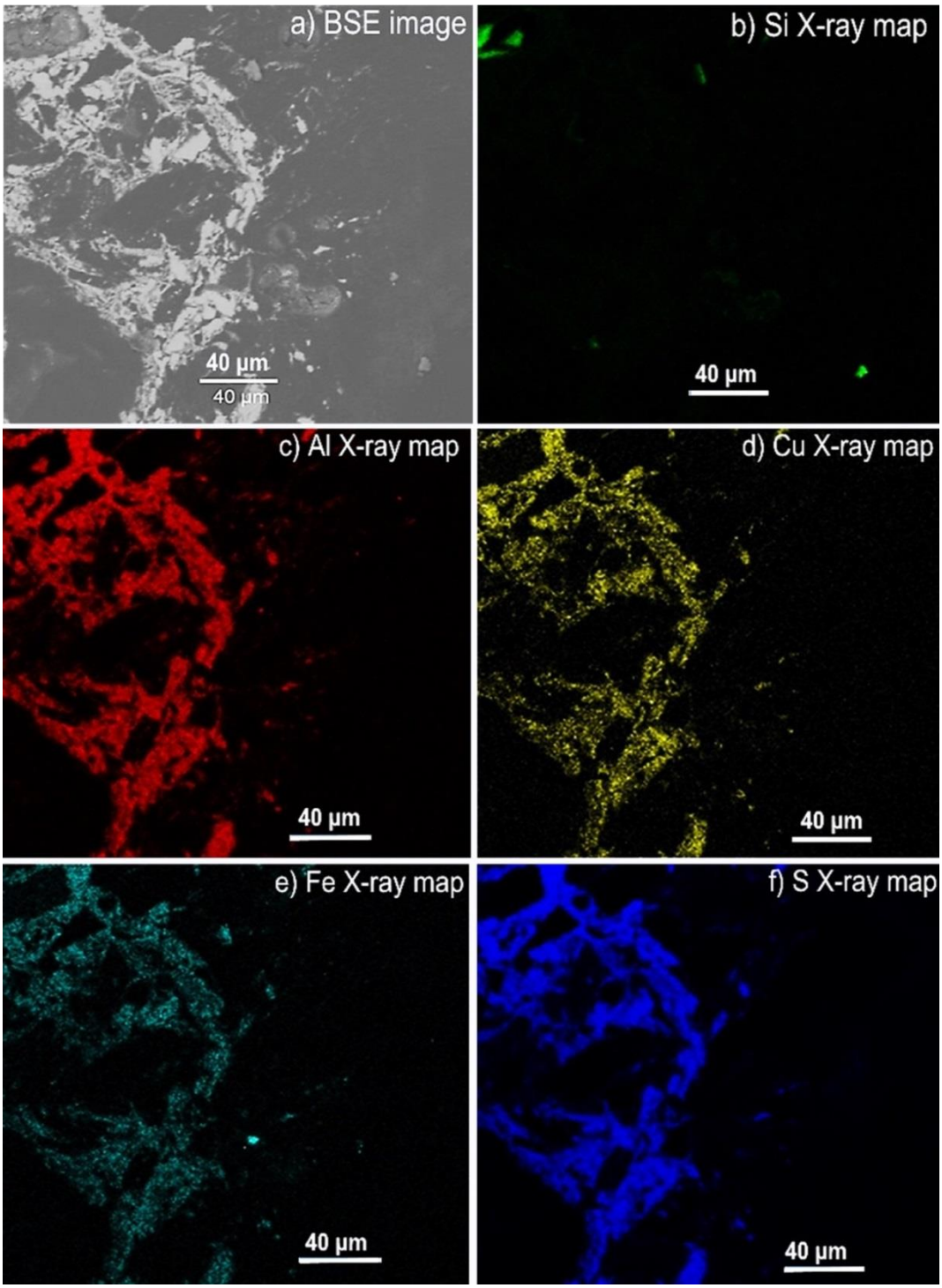

Figure 6-2: Micropore-carbon crucible wall after exposure, (a) BSE-image, (b) Si X-ray map, (c) Al X-ray map, (d) Cu X-ray map, (e) Fe x-ray map, (f) S X-ray map

6.2 The interaction of MPC with a PGM matte

MPC was exposed to Matte-S and industrial matte at 1350 °C and 1450 °C. After exposure the matte residue was studied using OM and XRM; images are shown in Figure 6-3. Matte segregated into three distinct layers during exposure, a top layer at the gas-matte interface, middle layer below the top layer and the bottom layer at the base of the crucible (as annotated in Figure 6-3). The segregation of reaction products indicated that these products are immiscible and have different densities. The composition of the interaction products was determined using EPMA and SEM-EDS. The analysis of the Matte-S residue and the industrial matte-residue are discussed in turn.

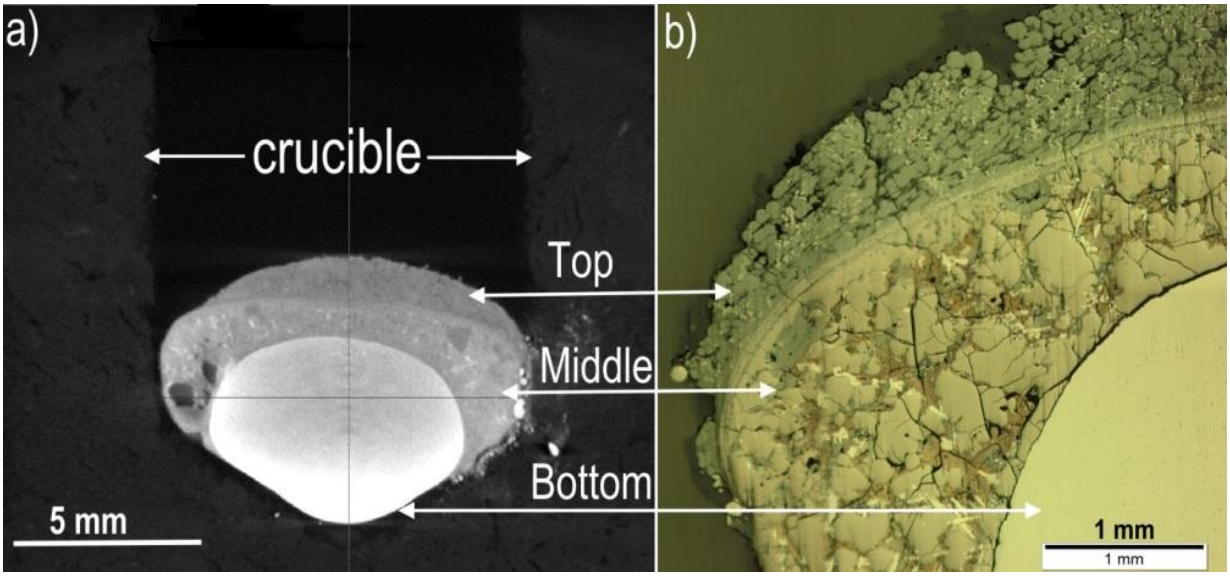

Figure 6-3: Micropore-carbon with solidified matte after exposure at 1450 °C for 12 hours, a) XRM image, b) OM image

6.2.1 Interaction of MPC with Matte-S

EPMA analysis of the phases constituting the Matte-S residue is shown in Table 6-2. The analysis are categorised according to the product layers, top layer, middle layer and the bottom layer.

6.2.1.1 The top layer (gas-matte interface)

The abundant phase in the top layer (gas-matte interface) was a CuFe-S phase with up to 11 mass percent Al, minor phases were FeNi and CuFeNi-S. The CuFe-S with Al is a product of the interaction between the matte and the Al_2O_3 in the refractory. This compound has the same composition as the infiltrate in the refractory wall (Figure 6-2). This phase was also observed in the matte residue exposed to SG graphite, discussed in Section 5.3.2. There is however no published data on a compound with this composition. Based on the experiments performed in this work, a copper-iron-aluminium sulfide forms as a result of the reactions between the aluminium and the matte. Attempts were made to reproduce this phase in the lab, the details of the synthesis are in the Appendix A.

6.2.1.2 The middle layer

The middle layer (Figure 6-3, Table 6-2) consisted of copper iron sulfide phases as well as the aluminium containing sulfide phase that was the abundant phase in the top layer. The middle layer mostly has the sulfide phases that were present in the starting matte except that this layer is deficient in nickel and enriched in aluminium.

6.2.1.3 The bottom layer

The metal layer at the bottom of the crucible (Figure 6-3) consists of (Fe, Ni)Si alloy with up to 12.9 mass percent Si, EDS analysis are in Table 6-2. This metal phase was also observed in the industrial matte residue exposed to graphite (Section 5.3.2).

Based on the composition of the matte residue in Table 6-2, significant amounts of Si and Al compounds reacted with the Matte-S during exposure. This led to the dissolution of the refractory material (Al_2O_3 and SiO_2/SiC) into the matte. Dissolution of the Al_2O_3 and SiO_2/SiC lead to the disintegration of the refractory material as evidenced in Figure 6-2.

Table 6-2: EPMA analysis of Matte-S after 12 hours exposure to MPC at 1450 °C (mass percent)

	Fe	Ni	Cu	Si	S	Al	Phase
Top	23.8	0.1	20.4	0.8	44.0	11.1	(CuFe)S, Al
	12.5	0.4	52.1	1.2	33.8	0.0	$(CuFe)_xS$
	55.0	42.8	2.1	0.1	0.0	0.0	FeNi
	25.9	6.3	28.5	0.4	38.9	0.0	$(CuFeNi)_xS$
	40.6	18.8	2.0	0.7	37.9	0.0	FeNi-S
Middle	21.0	0.1	33.7	0.2	38.9	6.1	$(CuFe)_xS$, Al
	12.4	0.0	55.0	0.6	31.9	0.1	$(CuFe)_xS$
	54.1	4.4	1.5	0.2	39.8	0.0	Fe_xS
	30.2	0.3	22.9	0.3	39.9	6.4	$(CuFe)_xS$, Al
Bottom	62.3	26.6	1.0	9.8	0.0	0.2	FeNi-Si
	54.1	28.0	3.3	12.9	1.7	0.0	FeNi-Si

6.2.2 The interaction of MPC with industrial matte

Similar to the synthetic matte, the industrial matte reacted with the MPC refractory wall. Reactions resulted to the following;

- Dissolution of the refractory materials (Al_2O_3 and SiO_2/SiC) into the matte
- Formation of a sulfide phase in the refractory
- The disintegration of the refractory and
- The formation of three distinct layers of the interaction products

Since the industrial matte had impurities, the composition of the residual industrial matte differed from that of the residual synthetic matte. Analyses of the industrial matte residue are divided into the three layers; top, middle and bottom layer.

6.2.2.1 The top layer (gas-matte interface)

Analyses of the top layer are shown in Table 6-3 and Figure 6-4 is the BSE image of the top layer. The phase numbers in Table 6-3 correspond to the annotations in Figure 6-4.

Three phases were detected in the top layer, intermediate solid solution (phase no. 1); iron-chrome sulfide (lamella-phase no. 2) and iron-copper-chrome sulfide (phase no. 3). Chemical formula of phase no. 1 is $(CuFe)_xS$ with up to 9 mass percent Al and 2 mass percent Mg; this is the abundant phase in the top layer. This aluminium-containing sulfide formed as a result of the interaction between matte and the alumina in the refractory.

Table 6-3: Elemental composition of the top layer of industrial matte residue after exposure to MPC at 1450 °C, phase numbers are annotated in Figure 6-4 (EPMA, mass percent)

number	phase	S	Fe	Cu	Ni	Cr	Mg	Al	Mn	Metal/Sulfur
1	Intermediate solid solution	41.2	20.3	27.0	-	-	1.8	8.9	0.7	1.2
2	Pyrrhotite (lamella)	40.1	37.4	1.5	1.4	19.5	-	-	0.3	0.9
3	Intermediate solid solution	33.7	38.4	14	1.3	7.2	0.6	3.6	-	1.2

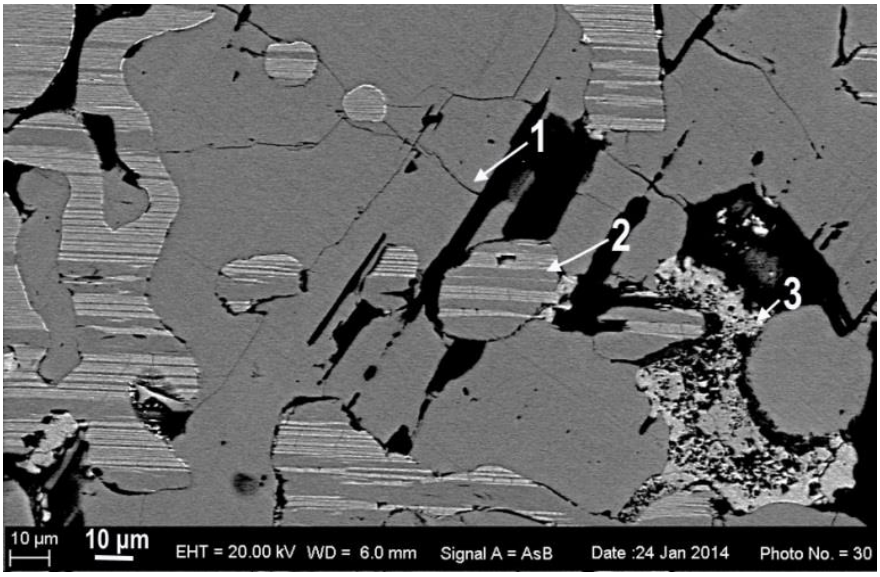

Figure 6-4: BSE image of the industrial matte residue (top layer) after exposure to MPC at 1450 °C. 1= [$(CuFe)_xS$, with 9 mass percent Al and 2 mass percent Mg], 2 = $(FeCr)_xS$, 3 = $(FeCuCr)_xS$

Lamella $(FeCr)_xS$ had a metal to sulfur ratio close to that of the stoichiometric pyrrhotite ($Fe_{(1-x)}S$) although it had a significant amount of chrome. The metal to sulfur ratio of a copper iron chrome sulfide ($(FeCuCr)_xS$) in phase no. 3 was close to that of an intermediate solid solution, this phase could be a mixture of chrome sulfide and intermediate solid solution.

6.2.2.2 The middle layer

The middle layer of the industrial matte residue consisted of $(CuFe)_xS$, (FeS) and $(CuFe)_xS$-Al, these are similar to the phases in the middle layer of Matte-S residue reported in Table 6-2. Nickel containing sulfides were not observed in the middle layer. The middle layer seemed to be a nickel-deficient matte-residue, which resulted from matte reactions with the refractory material.

6.2.2.3 The bottom layer

Iron nickel silicide $(FeNi)_3Si$ was a major phase constituting the bottom layer. The silicon content of this phase varied from 10 atomic percent to 13 atomic percent. The bottom layer was a product of the reactions between iron nickel sulfide (in matte) and silicon compound in the refractory. Conversion of silicates to sulfides and formation of an iron nickel sulfide has been discussed in Section 3.3.

6.2.2.4 XRD analysis of the matte residue

The matte residue after exposure to MPC was analysed with the XRD to confirm the phases detected by the EPMA in Table 6-3, the XRD analysis are in Table 6-4, and Figure 6-5. Sulfides were detected by the XRD as the abundant phases of the matte residue, no silicates or oxides were detected by the XRD, however there was spinel phase that was detected. The absence of silicates and oxides on the XRD analysis may be due to the amorphous structure of the silicates as well as the concentration effect since the silicate and oxide phases were impurities in matte but the abundant phases were the sulfides as detected by the EPMA.

Table 6-4: XRD analysis of industrial matte residue after exposure to MPC at 1450 °C, (mass percent)

		weight%	3 σ error
Awaruite	- Ni_3Fe	3.12	0.29
Bornite	- $Cu_{5.4}Fe_{1.1}S_4$	8.17	0.96
Covellite	- CuS	1.81	0.54
Mooihoekite	- $Cu_9Fe_9S_{16}$	15.98	1.02
Pentlandite	- $Ni_{17}Fe_{19}S_{32}$	30.1	1.26
Pyrrhotite	- $Fe_{28}S_{32}$	7.91	0.66
Spinel		2.63	0.81
Troilite	- FeS	30.28	1.05

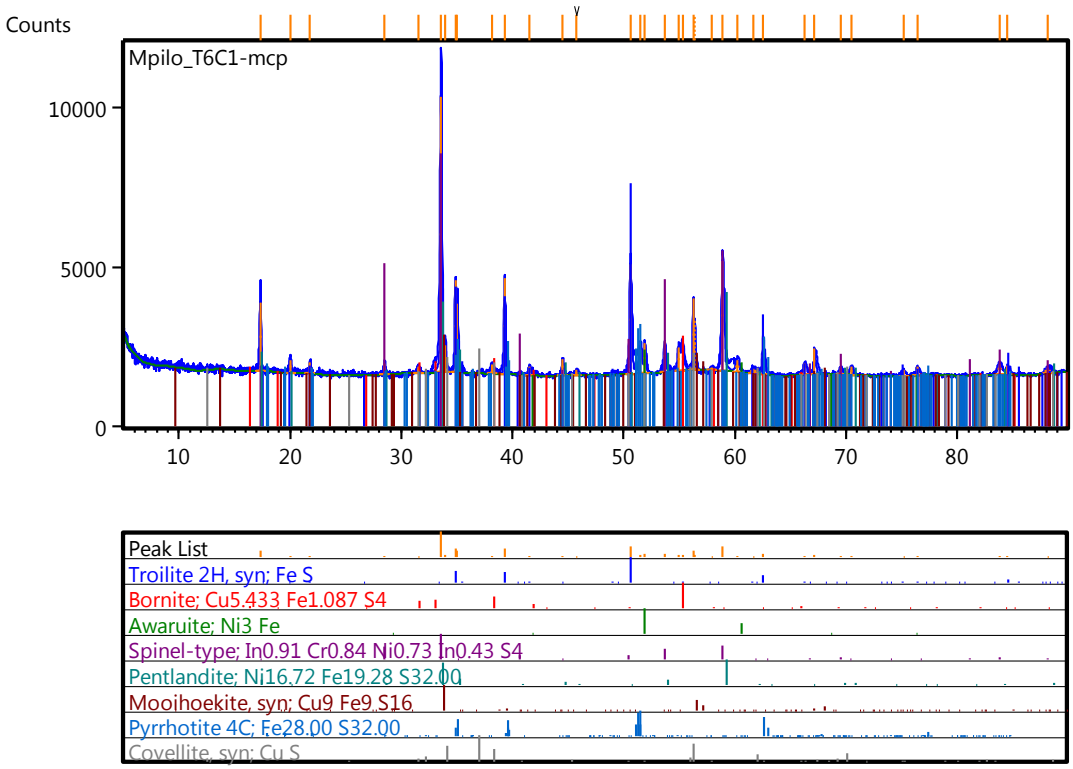

Figure 6-5: XRD pattern for the matte residue exposed to a MPC crucible at 1450 °C

6.3 The effect of temperature on the interaction of MPC with a PGM matte

Matte was weighed before and after exposure, total matte loss is the difference between the initial mass of matte and the mass of the residual matte. The total matte loss includes the matte that is in the refractory wall and the matte that reports to the off-gas.

6.3.1 Matte loss _ Matte-S

Significant matte loss was observed during the exposure of Matte-S to MPC, matte loss increased with the operating temperature. At 1350 °C Matte-S lost 9.1 mass percent and at 1450 °C Matte-S lost 13.4 mass percent. Total matte loss and chemical composition of the Matte-S residue is shown in Table 6-5. Sulfur is the most depleted in the matte residue, sulfur loss from the matte increased with temperature. Sulfur was 28 mass percent in the Matte-S sample, Matte-S residue has a sulfur amount of 24 and 21 mass percent after exposure to MPC at 1350 °C and 1450 °C respectively.

The amount of Si and Al in Matte-S increased with exposure temperature. This indicated that increasing temperature increases the dissolution of the MPC refractory into Matte-S. Matte-S sample (before exposure) did not have detectable amounts of Al and Si.

Table 6-5: Matte loss and chemical composition of Matte-S residue after exposure to MPC at 1350 °C and 1450 °C (mass percent)

	Matte loss (%)	**% C**	**% S**	**% Si**	**% Al**	**% Fe**	**% Ni**	**% Cu**
Matte	-	0.03 ± 0.005	27.7	<0.05	<0.05	46.1	16.9	9.2
MPC 1350°C	9.1 ± 0.2	0.14 ± 0.03	23.9	1.43	0.46	44.9	18.1	10.7
MPC 1450°C	13.4 ± 1.78	0.30 ± 0.05	20.6	1.81	0.56	46.7	19.5	10.2

6.3.2 Matte loss_Matte-A

Industrial matte lost up to 20 mass percent at 1450 °C. The increase in industrial matte loss compared to Matte-S can be attributed to high reactivity of the melt due to the presence of the silicate and oxide impurities in industrial matte.

6.3.3 Carbon dissolution

The average carbon content in the bulk matte residue increased with exposure temperature from 0.14 to 0.3 mass percent after exposure to 1350 °C and 1450 °C respectively (Table 6-5). The matte residue was separated into two products i.e. sulfides (top and bottom layers) and a metal (bottom layer), each product was analysed for carbon.

The carbon content in the sulfides was 0.03 mass percent, the metal (bottom layer) had up to 0.5 mass percent of carbon. Carbon dissolution in a sulfide proved to be minimal when compared to carbon dissolution in the alloy/metal. A similar observation was made when the matte was exposed to graphite, the sulfide residue had minimal amount of carbon (0.03 mass percent) whereas the metal had up to 0.3 mass percent carbon.

6.4 Mechanism for matte loss - analysis of the gas condensate

The analysis of the off-gas condensate and the chemical composition of the matte residue indicated that the interaction between MPC and matte results to significant vaporization of matte species and the species of the refractory material. The EDS analyses of the gas condensate (at 0 °C) are shown in Table 6-6, this gas condensate was collected at the ice-cooled gas-trap-pipe. The SEM analysis identified four phases; these phases are annotated 1, 2, 3 and 4 in Table 6-6. The condensate sample was a composite of a number of runs since not enough condensate could be collected in one experiment. Al, S and Si were major components of the condensed gas; Cu and Fe were in minor amounts.

Increase in matte loss with temperature could be attributed to the formation of the gaseous products during the interaction. Reactions of a micropore-carbon with the matte were accompanied by evolution of volatile phases.

The composition of the gas condensate for industrial matte exposure had Mg in addition to the species reported in Table 6-6.

Table 6-6: EDS analysis of the gas condensate trapped at 0°C for Matte-S exposure to MPC at 1450 °C

Element	1	2	3	4
Fe	7.6	2.6	1.3	6.4
Si	24.8	13.4	4.4	8.9
Ni	0.2	0.1	0.1	0.2
Cu	12.0	3.3	2.0	0.9
Al	16.2	9.2	0.5	17.9
S	39.2	71.3	91.8	65.7

7 Discussion

The aim of this work was to determine the compatibility of carbon-based refractories with a PGM matte and slag. The research questions were concerned with determining the wettability of graphite by matte and slag, the wear mechanisms of graphite when exposed to matte and slag, the effect of cooling graphite (whether a frozen skull forms when graphite is cooled), and the interaction of MPC with matte (whether MPC would perform better than a graphite when exposed to matte). The results have been presented in Sections 5 and 6.

The discussion of the results is entailed in this section. The wettability of SG graphite by matte and slag samples as well as the melting behaviour of the samples are discussed in the first section. Wear mechanisms of graphite by synthetic matte and industrial matte are discussed in the second section. The effect of cooling graphite is discussed on the third section. The interaction between liquid matte and MPC is discussed in the final section.

7.1 Wettability of SG graphite

Graphite was poorly wetted by the tested materials (pure sulfides, synthetic PGM matte, industrial PGM matte and industrial PGM slag) in an inert atmosphere, except for FeS. Since chemical penetration of a refractory by a liquid is enhanced by good wetting [Rigaud 2011], graphite was expected to have high resistance towards chemical penetration by the tested materials.

The tested sulfides were not reactive towards graphite, no reduced phases were observed after the exposure of individual sulfides to graphite. A refractory which is not readily wetted by a given process liquid also tends to resist the dissolution by that liquid [Carniglia et al. 1992]. The effective liquid-solid wetting increases dissolution of the refractory by the wetting fluid [Rigaud 2011]. Based on the non-wettability of the tested sample towards graphite, the reaction between the droplet and the graphite were not favoured.

Wettability of graphite by FeS was not conclusive since the bulk FeS droplet did not intersect with graphite; the FeS droplet made a contact angle with the penetrated material. FeS penetrated

into the graphite surface, the penetration depth of FeS into the graphite was up to ~0.2 mm. The penetrated material consisted of $Fe_{(1-x)}S$ (analysis in Table 5-2); metal (Fe) was not detected in the penetrated material.

Reactive wetting has been discussed by Eustathopoulos 2015, it is characterised by the initial contact angle between the liquid and the unreacted substrate, as well as the final contact angle between the liquid and the reaction product [Eustathopoulos 2015]. This phenomenon is a plausible mechanism for the formation of an adsorbed layer of FeS on the graphite surface. Since no new compound was observed, it was concluded that the adsorbed FeS was possibly the solid solution of FeS.

Carbon can dissolve in sulfides, carbon dissolution is a function of temperature, sulfur content and metal component of the sulfide melt [Tsymbulov et al. 2001]. There is a mutual repulsion of sulfur and carbon in the melt, as the sulfur content of the sulfide melt is decreased, the melt becomes more metallized and the solubility of carbon increases [Tsymbulov et al. 2001]. When carbon dissolve in a melt the content of carbon in the melt affects the wetting angle of a carbon substrate by the melt, therefore the carbon content of the melt affects the melt's wetting properties towards the carbon [Nizhenko et al. 1974]. The wetting angle between a carbon substrate and a melt can increase from 40° to >100° as the carbon content of a melt is changed from 0 to 3.73 mass percent carbon for iron and iron base melts [Nizhenko et al. 1974].

It is plausible that during the exposure of the FeS droplet to graphite, some graphite dissolved into the molten droplet. As the carbon dissolved the composition gradient is envisaged between the material in contact with the graphite and the bulk droplet. If the material adsorbed in graphite had higher carbon content than the bulk droplet, interfacial tension could exist which will then cause the bulk droplet to have unique wetting properties towards the adsorbed material.

The carbon content of the droplet and the adsorbed material was not determined for the following reasons: it was a challenge to mechanically separate the droplet from the graphite substrate without contaminating the droplet with the graphite pieces which were stuck on the droplet; on the polished section it was a challenge to determine the carbon content since the SEM used was not equipped for measuring carbon. It is recommended that extra work be done on the wettability of graphite by FeS where the composition of the residue could be determined for all the elements in the droplet.

Matte and slag droplets did not wet graphite, the contact angles between these droplets and graphite were greater than 90°. Therefore the penetration of graphite by matte and slag was not expected since these materials were non-wetting towards graphite.

7.1.1 Melting behaviour of sulfides

Melting behaviour of pure sulfides (Cu_2S, FeS and Ni_3S_2) compared well with the phase relations in the published temperature-composition phase diagrams discussed in Section 3.3.

The gradual melting of a Cu_2S pellet was observed in this work, it could be explained by the formation of a sulfide melt from 1000 °C to 1105 °C (the melting path is highlighted by a dotted line in Figure 3-7). The melting temperature of Cu_2S (1110 °C) is within the published range of values which are 1105 °C [Vaughan et al. 1978] and 1125 °C [Habashi 2002]. Cu_2S is a solid solution above 813 °C hence it melts over a range of temperatures.

7.1.2 Melting behaviour of a Matte-S

The Matte-S droplet was molten at 1020 °C. Since this mixture was prepared in the laboratory there was no reference melting temperature that could be used to verify the accuracy of the melting temperature. The Matte-S sample had oxide-impurities of up to 6.6 mass percent (Table 4-14). FeO has been shown to have high solubility in FeS [Eksteen 2011]. FeO could also alter the melting temperature of the sulfide mixture as discussed in Section 3.3, Figure 3-8. It is plausible that the oxy-sulfide layer at the periphery of the Matte-S droplet formed as a result of matte interaction with the oxide impurities. The work tube was constantly purged with argon, the ingress of oxygen was minimised during operation, and the oxide layer could not have formed due to excess oxygen in the system.

7.1.3 Melting behaviour of industrial matte

The liquidus temperature of a typical PGM-furnace matte is 850 °C to 875 °C, whereas that of the slag is 1350 °C [Eksteen 2011]. This explains why the slag-impurities in the Matte-A pellet

melted at 1350 °C whereas the matte started deforming at 850 °C. Impurities in matte can either increase or decrease the liquidus temperature of the matte. FeO decreases the solidus temperature of FeS [McLennan et al. 2000], while chromite ($FeCr_2O_4$) increases the liquidus temperature of the matte. Chromite was detected in Matte-A, Matte-L and Matte P, these matte samples melted above the published typical liquidus temperature (875 °C) of the matte.

7.1.4 The change of the volume of the droplet

Wettability tests reported in Section 5 revealed that the volume of the industrial matte expanded by up to 25 percent of the original volume. Substantial increase in porosity of the matte droplets was observed during melting at temperatures between 900 ºC and 1000 ºC.

Table 7-1 entails the FactSage simulation data for the melting of the Ni_9S_8 with and without carbon, only the total gas volume is reported in Table 7-1. Pentlandite was the abundant phase in the melt (about 60 mass percent) hence its dissociation will have the highest contribution to the gas phase, hence the simulation for gas formation was only done for the pentlandite represented by the Ni_9S_8 ($(FeNi)_9S_8$) is not available in the FactSage reaction database hence the use of the Ni_9S_8. In the Table above it can be seen that in the absence of carbon the gas starts forming at 1000 °C. In the presence of carbon the gas starts forming at 839 °C.

From 839 °C to 1200 °C the volume of the gas increased from 0.34 litres to 1 litre respectively, this amounts to a volume increase of 200 percent. If the volume of the gas is increased by 200 percent and this gas is retained inside a melt the gas will cause inflammation of the melt. The gases given off are S_2 and CS_2 when the Ni_9S_8 is heated in the presence of carbon.

The FactSage simulation is in agreement with the observation of the industrial matte melting behavior. A Matte-A pellet exposed to a graphite substrate was heated in an argon atmosphere. The pellet started deforming at 850 °C, this temperature is close enough to the 839 °C suggested by the FactSage. The images of the inflated matte pellet are presented in Section 5.1.4.4 of this report. The droplet started deforming at 850 °C, at 1050 °C the droplet volume was increasing as shown in Figure 5-15. Based on the residue of the matte droplet exposed to 1000 °C (Figure 5-15) and the matte residue exposed to 900 °C (Figure 5-25) and the cooled graphite-matte residue (Figure 5-36) matte retains pores after melting, at temperatures below

1100 °C. At higher temperatures (>1200 °C) the matte foam collapses, the pores are not observed on the matte residue exposed to lower temperature as seen in a matte residue exposed to 1250 °C in Figure 5-27.

Table 7-1: Total gas volume for the heating of a 10-gram Ni_9S_8 with and without carbon (FactSage simulation- Equilib), gas volume is in litres

	gas volume (litres)	**gas volume (litres)**
°C	without carbon	with carbon
839	_	0.34
900	_	0.43
1000	0.05	0.60
1100	0.23	0.79
1200	0.42	1.00
1300	0.62	1.23
1400	0.83	1.49
1500	1.06	1.78

Based on the FactSage simulation and the appearance of matte residue, it seem that during the melting stages of matte, a gas form from temperatures of ~840 °C. This gas forms due to the dissociation of sulfides as the temperature is increased. The matte appears viscous at melting temperature <~900 °C, as such the gas is trapped inside the semi-molten matte. As the temperature is increased >1100 °C all the matte is molten and the viscosity of the melt decreases. Due to low viscosity of the melt the gas easily escapes the molten matte and the matte becomes dense and all the pores collapses. The Figure 7-1 is a FactSage simulation of the formation of a liquid matte in the presence of carbon. This simulation confirms that the matte is fully liquid at 1100 °C. Above 1100 °C the rate of gas formation increases significantly as shown by the S_2 curve.

At the matte melting temperatures (~900 °C) the oxides and the silicates are still solid as seen in the Matte-A residue which melted at 1350 °C (Figure 5-12), therefore the effect of the impurities on the change of volume of the matte was not simulated.

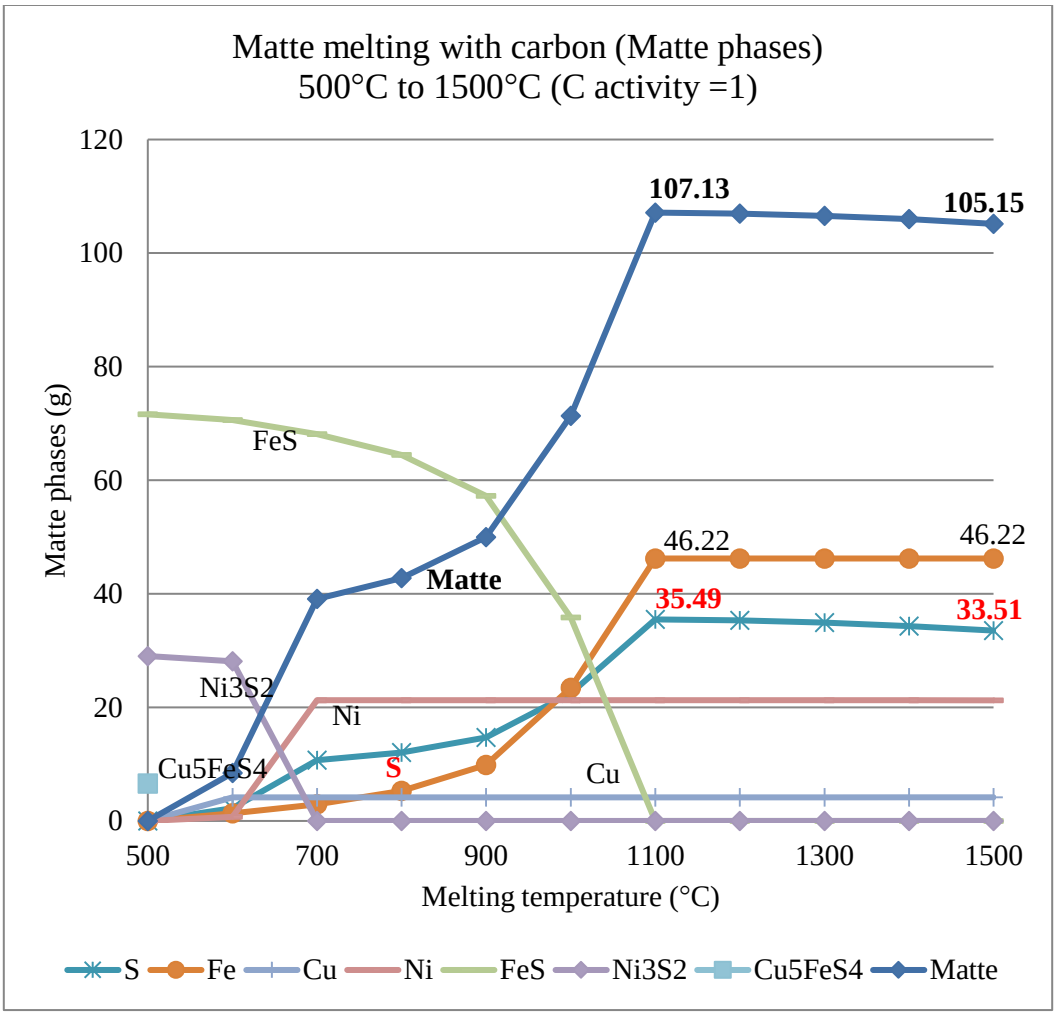

Figure 7-1: Equilib FactSage simulation of the equilibrium phases when a typical synthetic matte is heated from 500 °C to 1500 °C in the presence of carbon. The phases are annotated in the graph, the plot is matte phases in grams vs. temperature °C

The gas stream predicted by the FactSage simulation is entailed in the Figure 7-2. The gas stream graph has data (total amounts in grams) of Cu, Fe, Ni and S, the other gas components with oxygen and carbon are excluded in the graph below. Based on the gas stream components, the sulfur gas starts forming at 800 °C, sulfur remain the abundant specie in the gas phase as the temperature is increased to 1500 °C. Copper is the second most abundant gas specie, copper start forming at 1100 °C, a significant increase in copper gas is seen between 1400 °C and 1500 °C. Nickel gas and an iron gas start forming at 1300 °C, the amount of these gases increases with increasing temperature. Based on the FactSage simulation it is evident that from 1100 °C to 1500 °C matte species such as sulfur, copper, nickel and iron vaporize to the gas phase. This is shown by a significant decrease in the amount of the liquid stream and an increase in the gas stream from

1100 °C to 1500 °C. The FactSage simulation confirm the observation suggested by the gas condensate analysis that matte species vaporize to the gas phase during the exposure of matte to graphite at temperatures above the melting temperature of matte.

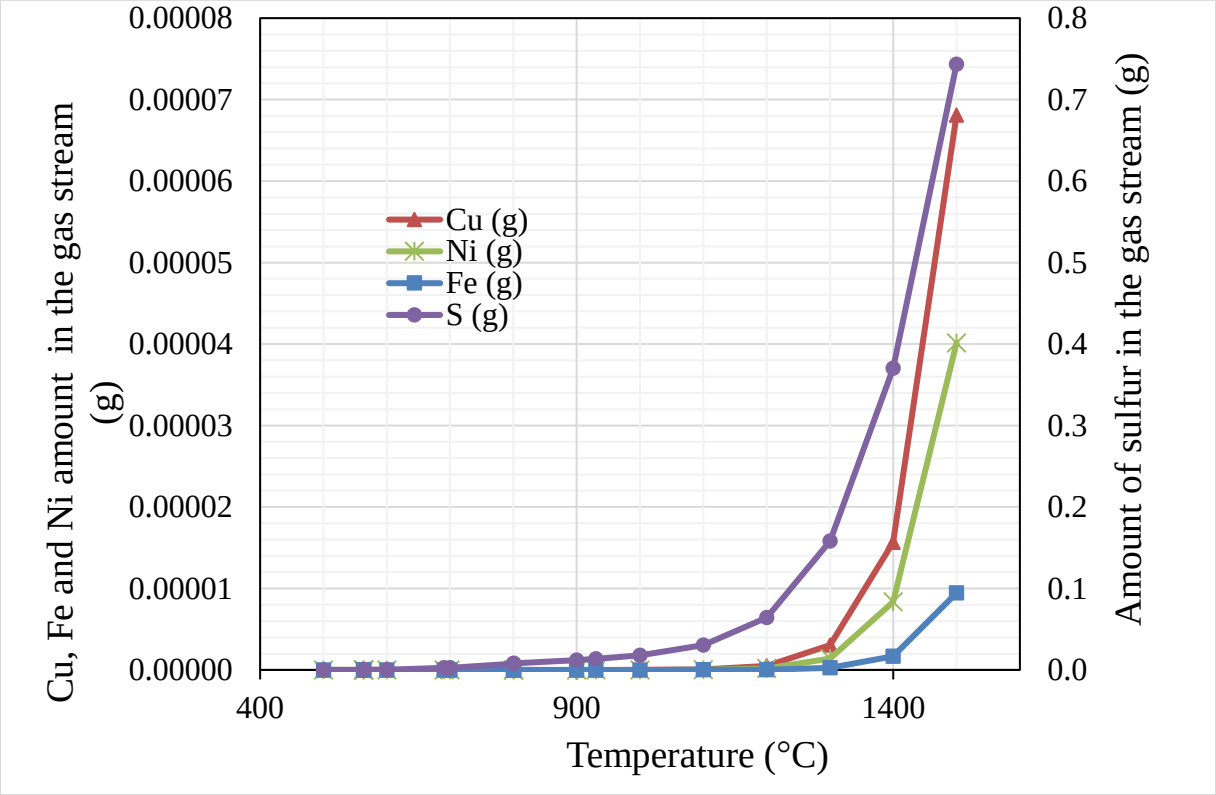

Figure 7-2: Equilib FactSage simulation of the equilibrium gaseous stream when a typical synthetic matte is heated from 500 °C to 1500 °C in the presence of carbon, carbon gases are excluded in this graph. The phases are annotated in the graph, the plot is gas phases in grams vs. temperature °C

Slag foaming has been discussed by Bhoi et al. 2006 and Körner et al. 2005. Slag foaming is enhanced by the following factors: gas generation, high viscosity, high interfacial/surface tensions and the presence of solids [Bhoi et al. 2006, Körner et al. 2005]. The foaming phenomenon was assumed to be applicable to the current experiments in order to explain how the melt inflation occurred.

In the presence of carbon, the volume of gas that is generated by a melting sulfide is increased by 1200 % at 1000 °C (FactSage simulations). The analysis of the gas condensate also confirmed that matte species dissociated during the melting of matte.

The Matte-A droplet was highly viscous, this was evidenced by the sluggish manner in which the droplet fell (Figure 5-12). There were solids in the Matte-A droplet during the melting stage. A small heap of material remained on the substrate after the bulk of the droplet had fallen. This residue was only molten at 1350 °C (Figure 5-12). Therefore the properties of the Matte-A droplet were conducive for the foaming phenomenon to occur. Gas formation, high viscosity and the presence of solids were all existent during the melting of a Matte-A droplet. The formation of pores upon cooling is a property of a melt that had foamed, pores were observed on the Matte-A specimen at 915 °C (Figure 5-14) and at 1000 °C (Figure 5-15).

The inflation of the droplets during wetting tests has been discussed by Bhoi et al. 2008 and Siddiqi et al. 2000. Siddiqi and co-workers studied graphite-slag wetting, they observed that the inflation of the droplet during wetting tests is caused by the formation of gaseous products. In their work they observed that when the gas is generated it inflates the volume of the droplet, the inflated volume is retained until the gas escapes the droplet [Siddiqi et al. 2000]. The gas accumulation inside the liquid occurs when gas generation exceeds the escaping rate. Gas accumulation inside the liquid causes the liquid to inflate [Shen et al. 2009].

Trapped gas forms pores in the droplet, which increases the volume of the droplet. When sulfides are being melted, gases such as sulfur are released due to phase transformations [Eksteen 2011]. Thermal expansion and phase transformation that occur in matte with increase in temperature could contribute to the change in matte volume. Since the Cu-Fe-S and Fe-Ni-S systems are dominated by solid solutions, detection of minor changes in the composition of the matte is a challenge. It is envisaged that significant amount of sulfur was released during the melting of sulfides.

The increase in the volume of the Matte-A droplet (Figure 5-14 and Figure 5-15) could therefore be attributed to the expansion of the gaseous species associated with the increase in temperature. This statement can be supported by the presence of pores in the molten droplet, at 915 °C (Figure 5-14) the pores are ~1 mm in diameter, at 1000 °C the pores are ~5 mm (Figure 5-15).

No metallic phases or reduced phases were observed in the analysis of the Matte-A residue in Table 5-9; only sulfides and oxides were observed. Oxy-sulfides were also not observed in the Matte-A residue. Based on the analysis of the Matte-A residue, there were no significant reduction reactions between graphite and oxide impurities in the matte at the melting temperature (~900 °C).

With an increasing in temperature the gases trapped inside a droplet are released to the off-gas and the size of the droplet decreases [Luz et al. 2008]. The decrease of the droplet after melting was observed for Matte-L, the decrease of Matte-L droplet could therefore be attributed to the escape of gaseous species from the droplet owing to an increase in temperature as explained by Luz and co-workers [Luz et al. 2008].

Absorption of the species of the droplet into the surface of the substrate is another factor that can cause a decrease in the volume of the droplet as discussed by Bruce and co-workers [Bruce et al. 2005]. The adsorption of Matte-L droplet into the graphite substrate was not the mechanism responsible for the decrease in the volume of the droplet since no matte was observed on the graphite substrate after exposure.

7.1.5 Deductions

- The melting patterns of the tested sulfides (FeS, Cu_2S and Ni_3S_2) closely narrated the melting behaviour discussed in the literature.
- With an exception of FeS, all the tested materials poorly wets graphite.
- Reactive wetting occurred between the FeS and the graphite substrate.
- Melting behaviour of matte samples differed although matte samples had comparable amounts of base metal sulfides. As such, the melting behaviour of matte cannot be generalized especially if there are impurities in the matte sample. Process history and impurities in matte seem to have major effect on the melting and wetting behaviour of matte.
- The instability of the droplet was observed with an increase in temperature (except the FeS droplet). All the droplets rolled off the graphite-substrate after melting except the FeS droplet. The droplets could roll off the graphite if there is no wetting, and at low viscosities,

the surface of the specimen could also contribute if it is not horizontal. From the wetting experiments we know that matte does not wet the graphite. We would expect the viscosity of the matte to be relatively low when the operating temperature is well above the liquidus and from the composition we do not expect a high viscosity melt.

- Graphite consumption by matte could not be quantified because the process gas could not be analysed. However, no measurable change was observed on the dimensions of the graphite-substrate (at the graphite-droplet interface) after exposure.
- The FactSage simulations suggest that when graphite in exposed to a typical matte gas starts forming at 840 °C, the amount of gas volume increases with an increase in temperature. Matte species such as sulfur, copper iron and nickel are vaporised at temperatures above 1100 °C, with sulfur vaporising before melting temperatures.

7.2 Wear of SG-graphite by a PGM matte

Wear of the SG graphite by a primary PGM matte was studied where operating temperature and contact time were varied. The wear mechanisms observed were the dissolution of carbon, penetration of liquid matte and minor erosion of the graphite at the slag-line where matte and slag were exposed simultaneously. The observed wear mechanisms are discussed in turn:

7.2.1 Graphite dissolution

Carbon has a higher solubility in a metal than in a sulfide [Tysmbulov et al. 2001]. The solubility of carbon in a sulfide is a function of the sulfur content [Tsymbulov et al. 2001]. When the sulfur content of matte is <20 mass percent the carbon dissolution in matte increases with the decrease in sulfur. When a sulfur content of matte is >20 mass percent sulfur has no effect on the solubility of carbon in the matte [Tsymbulov et al. 2001].

7.2.1.1 Graphite dissolution as a function of the sulfur content in matte

In the current work the following was observed:

- The content of carbon in matte increased with exposure temperature and contact time.
- Sulfur content in matte decreased with increasing temperature and exposure time due to gas evaporation.
- The loss of sulfur by matte resulted to the increase of the proportion of a metal (FeNi alloy) in the matte residue.
- The carbon content in matte increased with a decrease in sulfur.

The matte residue and its alloy component were separated and analysed for carbon and sulfur content. The carbon content in the metal (FeNi alloy) was up to 0.3 mass percent, the sulfur content in the metal (FeNi alloy) was undetectable by SEM-EDS. The corresponding matte residue had a carbon content of 0.03 mass percent and a sulfur content of up to 23 mass percent (Table 5-25).

In Figure 7-3 it seem that the solubility of carbon in the Matte-S is directly correlated with the sulfur content in the liquid matte. The amount of sulfur in matte depends on the dissociation of sulfides mostly $(FeNi)_9S_8$, dissociation of sulfides leads to the vaporization of sulfur, this phenomenon is enhanced with an increase in temperature and contact time. It is evident from this work that a significant amount of sulfur vaporizes and is evaporated to the off-gas based on the composition of the off-gas condensate that was rich in sulfur.

Therefore the saturation point of carbon in matte cannot be solely dependent on the exposure temperature or contact time, the amount of sulfur in the liquid matte has a significant role in carbon solubility in matte. The correlation observed between carbon dissolution in matte and sulfur content in matte was in line with the findings of Tsymbulov et al. 2001 (Figure 3-9 and Figure 3-10) The increase in carbon content in matte can be attributed to the increase of the Fe, Ni alloy in the matte. Since the sulfur content of matte was >20 mass percent carbon content on a sulfide was minimal (0.03 mass percent).

The solubility of carbon in the Fe-Ni-S system has been studied by Zhang et al. 2018 at high temperature and pressure. They varied their temperature from 920 °C to 1700 °C, the pressure was varied from 100 kPa to 20 GPa. They came up with the relation in Equation 18 to estimate the effect of sulfur and nickel in the solubility of carbon in the sulfide melt.

$$C_{Fe-Ni-S} = a(0.5 - X_S)^2\, X\, (b - Y_{Ni}) + 0.2 \quad (0 < X_S \leq 0.5) \text{ at } \mathrm{T} = 920\ °\mathrm{C} - 1700°\mathrm{C}, \mathrm{P} = 100\mathrm{kPa} - 20\mathrm{GPa};\ \text{where a} = 8.2 \text{ and b} = 2.8 \qquad \text{Equation 18}$$

Carbon dissolution in a sulfide can range from 0.1 mass percent to 6 mass percent for a sulfide melt with variable sulfur content. The report of Zhang et al. 2018 is in agreement with the work of Tsymbulov et al. 2001, the solubility of carbon in a melt is a factor of three variables, temperature, sulfur content and metal content.

This indicates that to minimize carbon dissolution in an industrial application the metallization of sulfides or the loss of sulfur by the sulfides should be minimized.

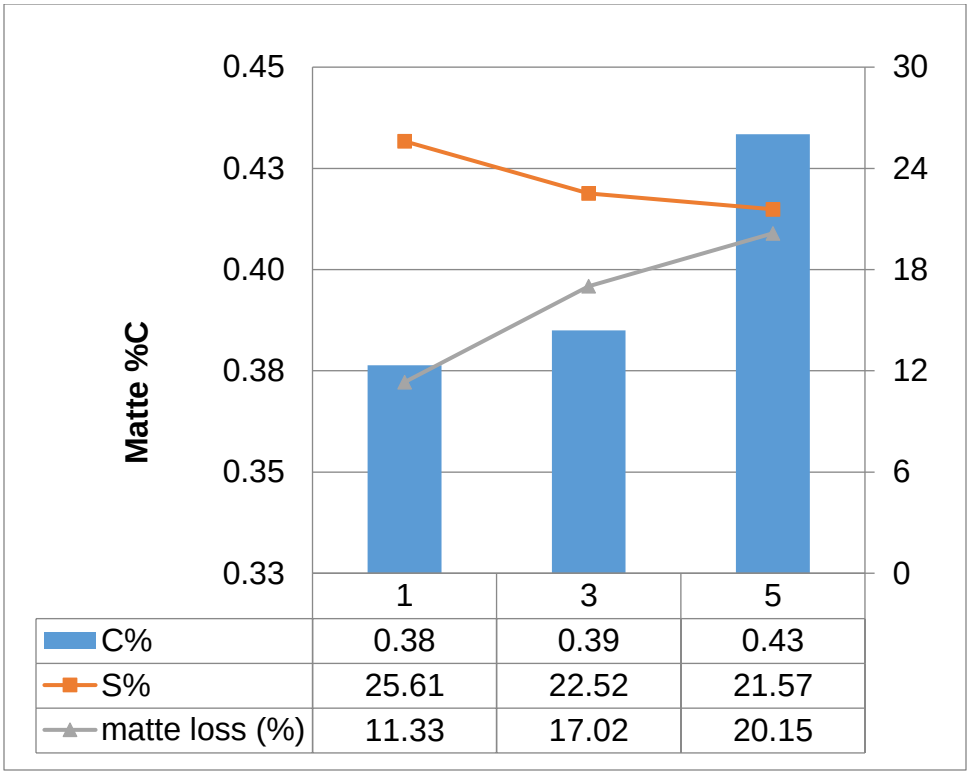

Figure 7-3: Total matte loss, carbon and sulfur content in matte residue (all in mass percent) vs. exposure time after exposure of matte to graphite at 1550 °C for 1, 3 and 5 days

7.2.1.2 Graphite dissolution as a function of graphite grade

An un-cooled graphite crucible can lose ~1 mm thickness per day through dissolution of carbon by matte. The difference between the thickness loss by SG graphite and HG graphite was 0.1 mm. Therefore, the HG graphite did not exhibit high resistance to carbon dissolution when compared to the SG graphite. Based on carbon dissolution HG graphite has no advantage over the SG graphite. Where carbon saturation is not reached or where the matte has low sulfur content (due to sulfur evaporation and formation of metal) carbon dissolution can become a significant wear mechanism of graphite.

Carbon dissolution can be significant in industrial application where matte is tapped out of the furnace frequently; due to frequent tapping carbon saturation in matte is not envisaged.

The solubility of carbon in a sulfide melt is a function of the melt composition and the temperature as discussed by Tsymbulov et al. 2001. The dissolution of carbon in a melt depends on a sulfur content in a melt, the Fe:Ni ratio and the temperature. Iron dissolves more carbon than nickel, this is due to the

ion-covalent bonds that are formed by the iron. At low sulfur concentrations (<20 mass percent) carbon dissolution decreases with an increase in the sulfur content. In the current work, the lowest average sulfur content of the melt was ~ 21 mass percent, therefore carbon solubility in the bulk melt could not be directly affected by the sulfur content in the melt. However, as discussed by Zhang et al. 2018 and Tsymbulov et al. 2001, in the presence of carbon the sulfide melt separates into a sulfide and a metal rich phase. Carbon has a higher solubility in a metal rich phase due to the metal-metal bond whereas there is mutual repulsion between the carbon and the sulfur in a sulfide. The solubility of carbon in a sulfide is minimal whereas the solubility of carbon in a metal can be as high as 6 mass percent depending on the Fe:Ni ratio [Zhang et al. 2018 and Tsymbulov et al. 2001].

7.2.2 Mechanical loss of matte during exposure to graphite

Some constituents of matte were lost during the exposure of matte to graphite. Three mechanisms of matte loss were observed during this work, i.e.:

- Penetration of gaseous species of matte
- Penetration of liquid matte prills into the graphite wall and
- Penetration of liquid matte through the graphite wall

Mechanisms of matte loss are discussed in turn:

7.2.2.1 Penetration of gaseous species of matte

Based on the composition of the gas condensate and the composition of the residual matte it was evident that vaporisation of the matte species occurred during the exposure of matte to graphite. Both Matte-S and industrial matte experienced matte loss to the gas phase. Matte loss to off-gas was observed on both the SG and the HG graphite. The current work was carried out in an isothermal system; there was no temperature gradient through the wall of the crucible. Therefore if the matte species escape the crucible in a gaseous form due to evaporation at high temperatures, the matte species should remain a gas throughout the crucible wall. However if

there is a temperature gradient, the matte species will evaporate at temperature and condense to a liquid or solid where the temperature drops below its solidus temperature.

Due to the temperature gradient from the work tube hot-zone to the cooled end of the work tube (around the brass cap) the process gases that were vaporised in the specimen hot-zone condensed when they reached the cooled end of the work tube. A condensate accumulated around the lid of the work tube (the cooled top end of the work tube).

Vaporised matte species were carried by the purge gas and when the gas reached the cooled end of the work tube some gaseous species condensed and formed the accretion.

Copper and sulfur were the most prone to vaporisation. Vaporization of copper from a copper concentrate has been discussed by Jorgensen and co-workers [Jorgensen et al. 1985]. They observed that at 1400 °C up to 41 mass percent copper vaporises from a complex copper concentrate in a nitrogen atmosphere with 1 mass percent oxygen [Jorgensen et al. 1985]. In the current work up to 30 mass percent copper was lost by matte when the matte was exposed to graphite at 1550 °C.

Sulfide phases dissociate to monosulfides as the matte is heated [Eksteen 2011]. Sulfur gas is given off during phase transformations of sulfides [Eksteen 2011]. It is plausible that sulfur detected in the off-gas condensate vaporised during the melting of the sulfides. The rate of evaporation of sulfur depends on the concentration of the sulfur in the melt, as the melt becomes deficient in sulfur (with increase in exposure time and operating temperature) the rate of sulfur evaporation decreases.

The loss of sulfur by a sulfide drives the equilibrium to a metal Fe-Ni phase field in the Fe-Ni-S system [Vaughan et al. 1978]. At low sulfur partial pressure Fe-Ni alloy is a stable phase at 1200 °C [Willis et al. 2009]. This alloy was detected in the matte residue in the current work, the fraction of FeNi increased with increasing temperature.

FeNi is a solid solution, at the Fe:Ni ratio of ~1:1 its melting temperature is ~1440 °C [Fabrichnaya et al. 2009, Raghavan 2004]. Considering the melting point of the matte species (790 °C for Ni_3S_2, 1105 °C for Cu_2S and 1190 °C for FeS) [Kitakaze et al. 2011, Vaughan et al. 1978], FeNi would be the last specie to melt. This is a plausible reason for the Fe and Ni to be the least to evaporate since these elements are in equilibrium with a liquid matte till

the FeNi melts at 1440 °C. The Fe-Ni binary phase diagram is in Figure 7-4 and the liquidus projection at 1350 °C is in Figure 7-5. These phase diagrams were extracted from Fabrichnaya et al. 2009. From the diagrams it is seen that Fe-Ni alloy is the last compound to melt in the Fe-Ni-S system.

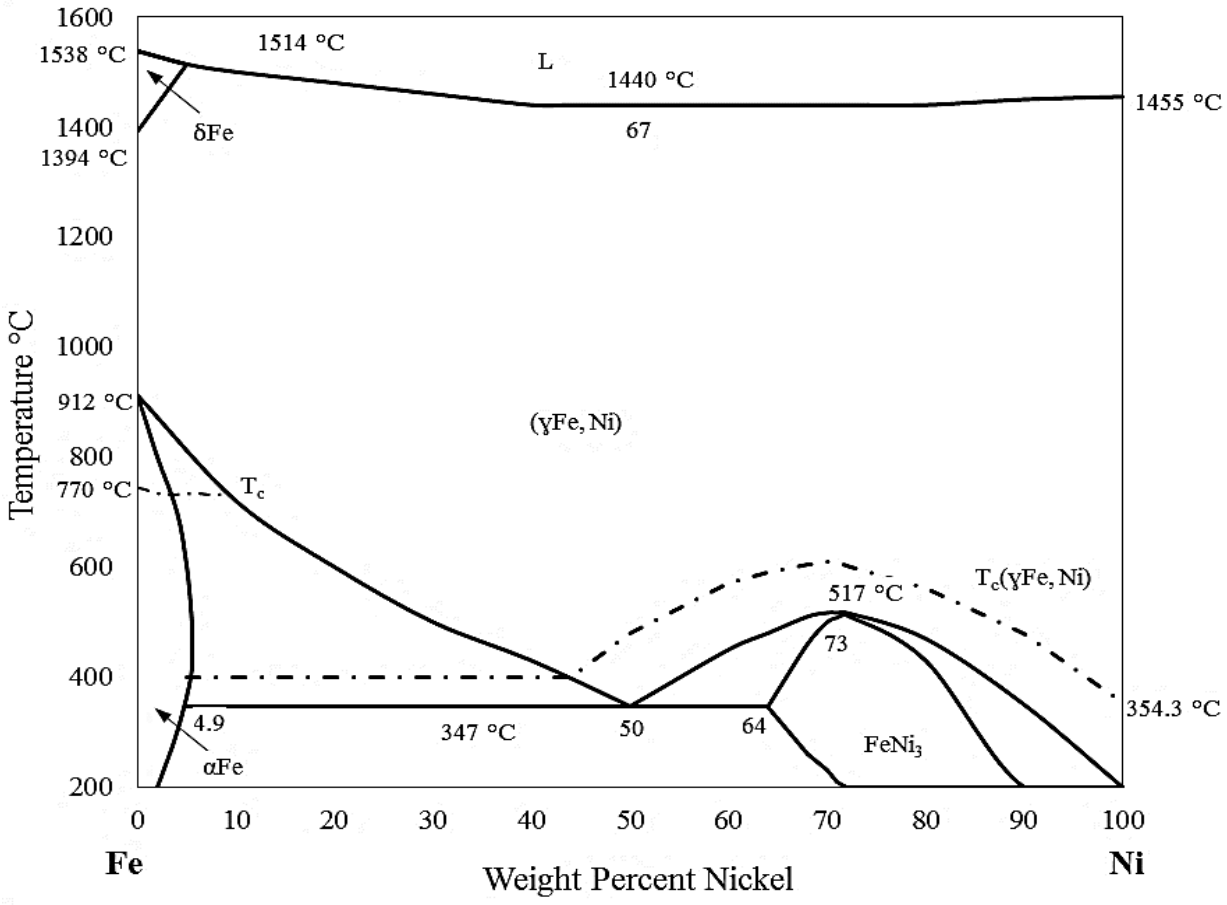

Figure 7-4: Fe-Ni binary, temperature-composition diagram showing the solidus and liquidus temperatures in the Fe-Ni binary from 200 °C to 1600°C [Fabrichnaya et al. 2009]

The vapour pressure of the matte species is expected to increase as the operating temperature is increased above their melting point, this statement is based on the general behaviour of liquids discussed by Koutsoyiannis 2012.

Copper, iron, nickel and sulfur were the constituents of matte as discussed in Section 4.2.2. Of these elements nickel was not detected in the off-gas condensate.

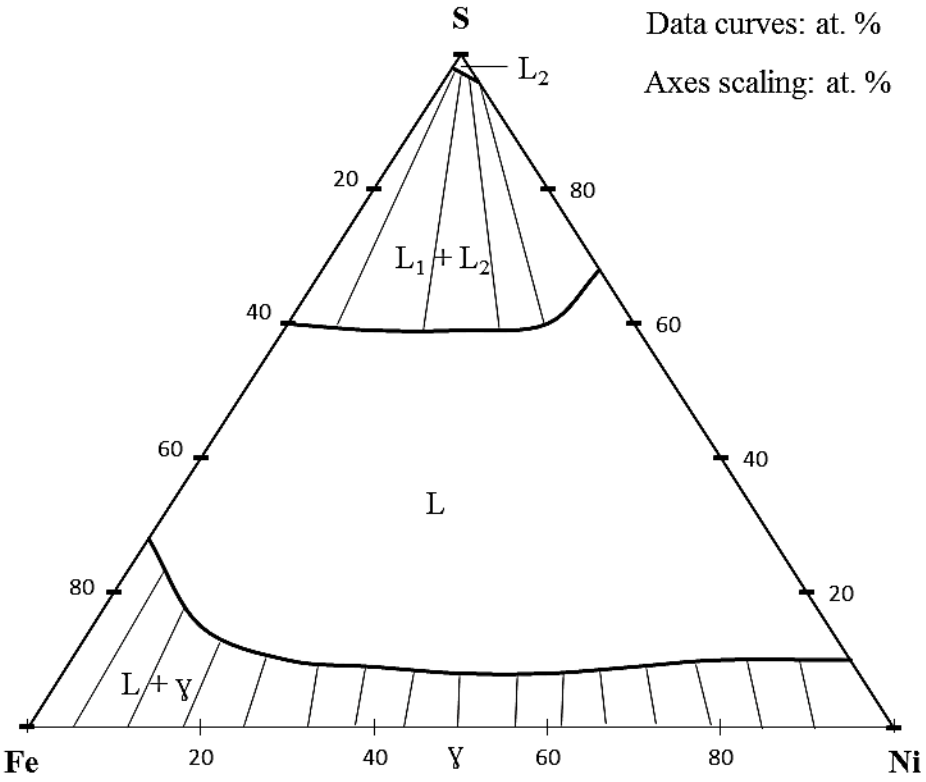

Figure 7-5: Calculated isothermal section in the Fe-Ni-S system at 1350 °C, FeNi is a solid solution, at 1350 °C it is in equilibrium with a sulfide melt [Fabrichnaya et al. 2009]

The gas condensate collected after exposing industrial matte to graphite exposure had elements such as Al, Mg and Si. These elements were the constituents of the oxide-impurities that were in the starting industrial matte sample (Table 4-8). The detection of these elements in the off-gas condensate indicates that during the exposure of industrial matte to graphite, evaporation of the elements that were in the oxide form took place. This is a significant observation since it is the evidence that some species of the slag globule were vaporised during the interaction with matte and graphite.

Matte loss to the gas phase is a significant finding for two reasons:

1) The analysis of a graphite block that was used in the industrial smelter revealed that sulfides get deposited at the cold-face of the graphite block where these sulfides react with copper coolers. This work has confirmed that at operating temperatures the matte species are evaporated and carried to the off-gas.

2) The matte loss to the gas phase results to the formation of a metal/FeNi alloy. Graphite has a higher solubility in a metal than in a sulfide, therefore matte loss to the gas phase will increase solubility of graphite in the melt.

A FactSage (Equilib) simulation confirmed the dissociation of base metal sulfide discussed by Eksteen 2011, the FactSage output is shown in Figure 7-1. Figure 2-1 presents the solid and liquid phase species predicted by the FactSage, the gas phase is reported in Figure 7-2. The FactSage simulation has been discussed in Section 7.1.4 in this report. The reactants for the simulation are the following:

(gram) 2.68 Fe_7S_8 + 62.15 $Fe_{4.5}Ni_{4.5}S_8$ + 12 $CuFeS_2$ + 26.51 FeS +5.36 Fe_3O_4 + C

Fe_xO was added since it was detected by the XRD in the Matte-S sample before exposure.

If a typical matte is heated in the presence of carbon, matte will be fully molten at 1100 °C. As the temperature is increased from 1100 °C to 1500 °C the total mass of the liquid matte decreases by ~2 mass percent. In the liquid matte the element whose mass changes significantly is sulfur, sulfur mass decreases by ~6 mass percent from 1100 °C to 1500 °C. The masses of Cu, Fe and Ni remain constant in the liquid matte according to the FactSage simulation.

Matte loss to the gas phase was observed with both the HG and SG graphite, therefore using a denser refractory does not prevent matte species from evaporating from the smelting vessel.

According to Eksteen 2011, base metal sulfides dissociate according to the Equations 19, 20 and 21.

$$Ni_9Fe_8S_{15}(s) \rightarrow 8FeS(s) + 3Ni_3S_2(s) + \frac{1}{2}S_2 \; at \; 650 \; °C \qquad \text{Equation 19}$$

$$2CuFeS_2(s) \rightarrow 2FeS(s) + Cu_2S(l) + \frac{1}{2}S_2 \; at \; 700 \; °C \qquad \text{Equation 20}$$

$$FeS_2(s) \rightarrow FeS(s) + \frac{1}{2}S_2 \; at \; 796 \; °C \qquad \text{Equation 21}$$

The above equations suggest that even before the matte species are molten a significant amount of sulfur is given off.

7.2.2.2 Penetration of liquid matte prills into the graphite wall

The detection of matte prills in the graphite wall is the evidence that matte species are carried out of the bulk matte in a liquid form. The transport mechanism of matte species embedded in graphite is however different from the evaporation of matte species which forms accretion in the cooled portion of the work tube. The condensate had fine powder particles showing that it had condensed from a gaseous phase. In contrast the matte embedded in graphite were matte prills as big as 0.5 mm diameter, the example of a matte prill is in Figure 5-22.

Calculations of the pressure inside the crucible were reported in Section 5.2.3.4. During the melting of a sulfide, the gas volume can exceed 233% of the crucible volume. In the FactSage simulations the addition of graphite into the matte mixture increased the volume of the gas generated. Therefore it is plausible that there was a positive pressure inside the crucible during the exposure of matte to graphite. Based on the analysis of the gas condensate, it was confirmed that the gaseous species evaporates out of the crucible during the exposure of matte to graphite. From the wettability tests it was observed that graphite is not wetted by matte, therefore penetration of matte through the graphite is not favourable unless the capillary pressure is overcome by excess pressure from the system.

A non-wetting fluid can be forced through the pore of the refractory if the excess pressure exceeds the capillary pressure [Eustathopoulos 2015]. Therefore the mechanism for the transport of matte prills through the wall of graphite was due to a positive gas pressure inside the crucible. The gas pressure can force the liquid matte/slag into open pores or cracks in the wall of the graphite crucible. The infiltration distance of a non-wetting fluid through a pore depends on the excess pressure and time [Eustathopoulos 2015]. Therefore the distance to which the matte prills were deposited on the graphite wall would depend on the gas pressure. At low gas pressure the matte prill would be deposited closer to the graphite-matte interface, at high gas pressure the matte prill could be carried through the thickness of the graphite wall.

It should be noted that matte prills were mostly observed in a Matte-S specimen as well as in the matte/slag setup against the slag-zone. In the industrial-matte specimen, matte prills were not observed, however residual matte was observed in the cracks and pores of the graphite wall due to liquid penetration.

Jetting of the Matte-S was observed during the wettability tests. The example of matte jetting from the Matte-S droplet is shown in Figure 7-6. During matte-jetting, the matte was carried by the gas to the roof of the work tube. The images of the setup (cross-section of the droplet, substrate and roof of the worktube) before melting, after melting and after jetting are shown in Figure 7-7. Before the droplet was fully molten the matte splashes on the furnace roof were negligible, the appearance of the worktube roof is marked in Figure 7-7a. After melting, but before jetting the worktube roof had negligible amounts of matte splashes, this is seen in Figure 7-7b. Matte image during jetting is shown in the images in Figure 7-6. Matte deposits were observed at the roof of the furnace tube after jetting, this is marked matte splashes in Figure 7-7c. Due to high fluidity and non-adherence, the droplet fell off the substrate after jetting.

In the crucible tests, there was no freeboard, the crucible was filled with matte to the top-edge of the crucible. Therefore when the gas accumulates inside the melt, it would escape the crucible through the pores in the graphite crucible.

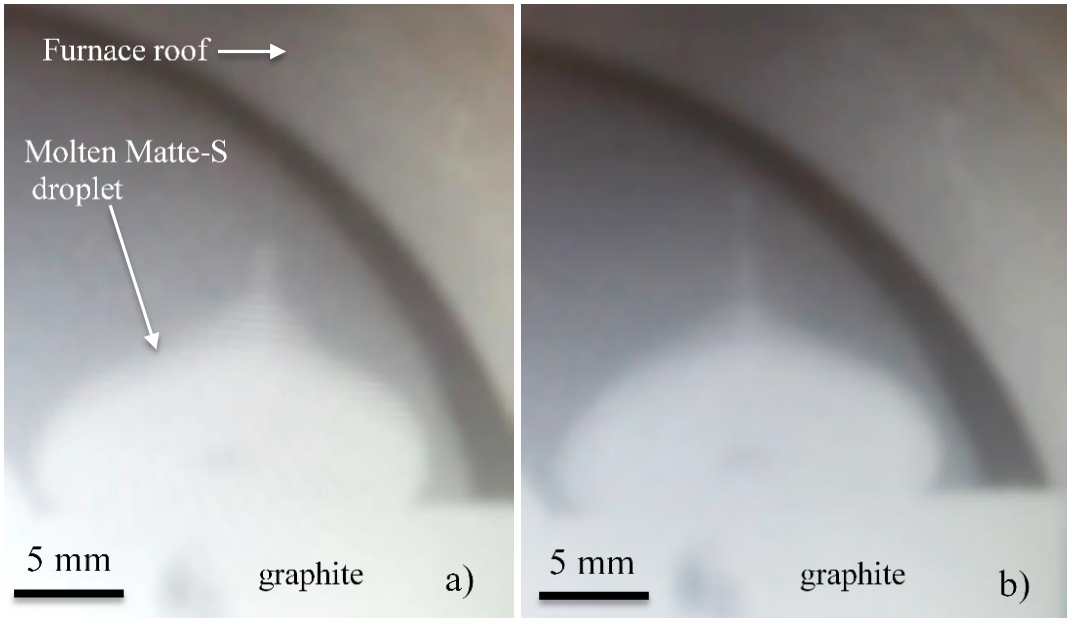

Figure 7-6: Images of a molten Matte-S droplet on a graphite substrate during jetting, a) the furnace roof, the droplet and graphite is annotated and b) shows the matte jetting upwards

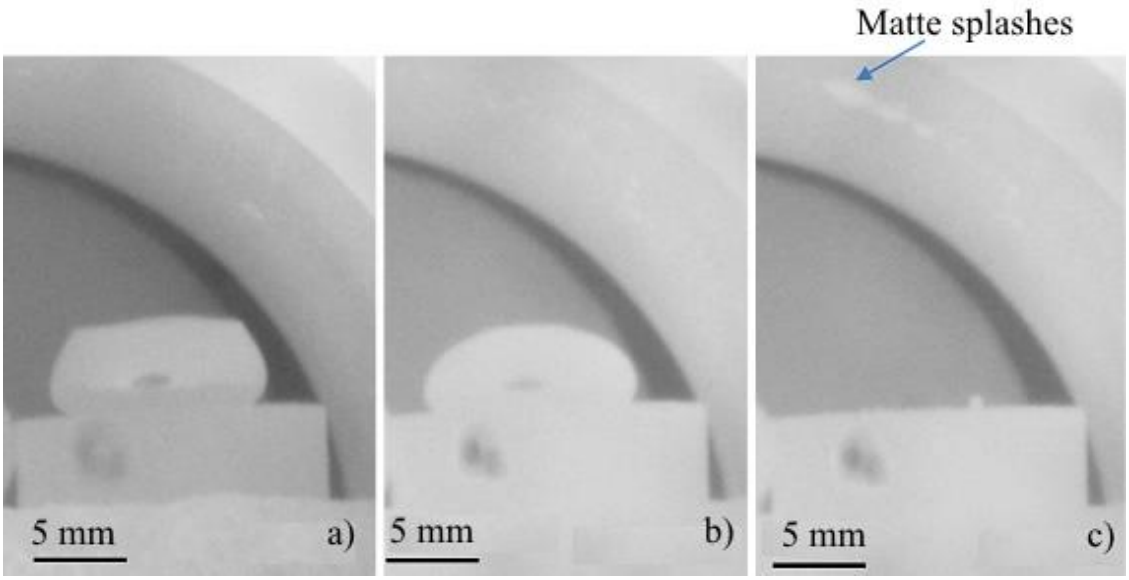

Figure 7-7: Images of Matte-S droplet a) at 1030 °C before melting the matte splashes on the furnace roof are negligible, b) at 1210 °C after melting before jetting the matte splashes on the roof are insignificant, c) at 1220 °C the droplet has dropped off the substrate due to non-adherence, between 1210 °C and 1220 °C the bubbling of matte occurred as seen in Figure 7-6 and matte splashes are observed at the roof of the furnace after jetting

7.2.2.3 Penetration of liquid matte through the graphite wall

A strictly non-wetting liquid can be forced into the pores of a solid by external forces resulting in physical penetration [Rigaud 2011, Lee et al. 2004, Jansson et al. 2004]. For non-wetting liquids infiltration is achieved by applying a sufficiently high pressure to overcome the capillary pressure. The infiltration distance, increases with time, and excess pressure [Eustathopoulos 2015]. In this work, it was established that graphite is poorly wetted by industrial matte however, liquid industrial matte penetrated through the SG graphite. Therefore the industrial matte penetrated through the SG graphite by physical penetration where an external force forced the liquid through the pores of the graphite.

It has also been established that during the melting of a sulfide the volume of the process gas can exceed 233 percent of the crucible volume. Therefore there was a positive pressure inside the crucible during the melting stages of the matte.

Foamability is a tendency of a melt to retain gas bubbles [Sundström et al. 2008]. For a melt to foam, gas bubbles must be present, a melt-foam is characterized by high porosity upon

solidification [Körner et al. 2005]. Viscosity and surface tension determines the foamability of a melt [Körner et al. 2005]. Foamability of a melt is directly proportional to its viscosity [Bhoi et al. 2006, Körner et al. 2005].

It is generally accepted that foamability of a melt is correlated with the presence of solid particles [Körner et al. 2005]. The oxide impurities in industrial matte were still solid at 900 °C (when sulfide phases started melting). This is evinced by the Matte-A residue that only melted at 1350 °C. High porosity was also observed on the matte residue after exposure to 900 °C (during crucible tests). As the temperature increased the porosity of matte decreased, this confirms that as the temperature was increased the solid particles melted and the viscosity decreased.

The proposed mechanism for the penetration of liquid matte through the graphite wall is stated below:

1. During melting, the matte foams and fills the crucible. The foamed matte covers the whole inner surface of the crucible such that the open pores (in the graphite wall) are sealed by the liquid.
2. As the gas pressure increases inside the crucible, it forces the liquid through the pores. Since graphite is non-wetted by the matte, the liquid will only go through the pores if the gas pressure is higher than the capillary pressure.
3. When the gas pressure decreases or drops below the capillary pressure the liquid penetration will cease. The gas generation associated with the melting stage is anticipated to drop with contact time or with increase in temperature, the decrease in gas generation was observed with FactSage simulations (Table 5-18)
4. The foam should collapse with an increase in temperature since the viscosity decreases with an increase in temperature. Once the foam has collapsed, the gas can flow through the open pores then the pressure build-up will be minimal inside the crucible.

The proposed mechanism is based on the discussed properties of matte and the estimated pressure build-up during the melting of matte. The covering of the inner walls of the crucible by the foamed matte was observed at the specimens exposed to 900 °C and 1250 °C (Figure 5-26 and Figure 5-28). The matte layer covered the inner wall of the graphite, although the matte in the centre of the graphite was porous, a continuous layer of matte was observed adhered to the

graphite inner surface. At 1450 °C (Figure 5-29,) no matte layer was observed against the graphite wall, all the matte had segregated to the bottom of the crucible, and the pores in matte had lapsed.

When comparing the behaviour of the synthetic and the industrial matte, the liquid synthetic matte did not penetrate through the graphite crucible but the industrial matte penetrated through the graphite crucible during melting. Synthetic matte maintained its volume during melting; it did not foam or swell (Figure 5-5). In contrast, the industrial matte foamed during melting, matte foaming resulted to pore formation and increased apparent volume of the industrial matte as evident in these images Figure 5-8, Figure 5-12 and Figure 5-15. Industrial matte therefore had a higher foamability than synthetic matte, due to the presence of solids during melting.

The release of process gases alone could not be the main mechanism by which the industrial matte penetrated through the graphite crucible, synthetic matte also released process gases during melting.

Liquid Matte-S did not penetrate through the SG graphite at all tested conditions, only the matte prills were observed embedded in the graphite wall. The liquid industrial matte (Matte-A, Matte-L and Matte-P) penetrated the SG graphite at temperatures around 900 °C. The following discussion only refers to the penetration of liquid industrial matte through the SG graphite.

The HG graphite exhibited a higher resistance to penetration by liquid industrial matte when compared to the SG graphite. The behaviour of the HG graphite was anticipated since it is denser than the SG graphite. The average pore size of the HG graphite was 13 µm and that of SG graphite was 20 µm (Table 4-1). Higher density (less porous) materials usually exhibit higher resistance to penetration by fluid [Lee et al. 2004] when compared to a less dense material. Porosity of the refractory affects the physical penetration of liquid. The resistance of a refractory to penetration by liquids is improved by reducing the open porosity of the refractory [Carniglia et al. 1992]. As seen in the current work, a liquid PGM matte did not penetrate a less porous refractory but it penetrated a refractory with higher porosity.

When selecting the refractory material, the pore size and total porosity of the refractory should be considered. Graphite with low porosity and small pore size depicted higher resistance towards penetration by liquid industrial matte when compared to a porous graphite with larger pore size. However graphite dissolution rate was comparable for HG and SG graphite grades.

Increasing temperature or contact time did not increase the penetration rate of liquid industrial matte through SG graphite.

7.2.2.4 Other mechanisms for liquid-matte penetration through SG graphite

The following factors were investigated to determine other mechanisms that could cause the penetration of liquid industrial matte through the SG graphite wall;

a) Hydrostatic pressure [P=ρgh]
b) Chemical reactions between graphite and matte
c) Effect of restricted crucible volume

The possible mechanisms are discussed in turn:

a) Hydrostatic pressure [P= ρgh]

For a static fluid with a constant density, pressure varies only with the elevation within the fluid [Crowe et al. 2005]. Pressure increases with depth in a fluid. The hydrostatic pressure equation is shown in Equation 18, where ρ is the density of the fluid in kg.m^{-3}, g is the acceleration gravity (9.81 m.s^{-2}), and h is the depth of the fluid in meters [Crowe et al. 2005].

Matte penetration in the current work was not localised to a specific depth in the crucible, it was observed from the top of the lid to the bottom of the crucible. If the hydrostatic pressure had an influence on matte penetration, higher matte penetration would have been observed at the bottom of the crucible. For this reason, the hydrostatic pressure cannot be the main mechanism by which matte penetrated through the graphite crucible. In the current work, the crucible height was about 60 mm, using a matte density of 5200 kg.m^{-3} [Eksteen 2011]; the calculated pressure at the bottom of the crucible is 0.03 atmospheres more than the pressure at the free board, therefore this pressure difference is deemed minimal to cause the degree of penetration that was observed.

An estimation of the hydrostatic pressure in a typical industrial smelter was done using the properties of a typical PGM bath extracted from Eksteen [Eksteen 2011]. The expression used to calculate the head pressure is in Equation 22. The calculations were done for minimum and maximum values of bath height and densities. The properties of a typical PGM-furnace bath (densities and height) and the estimated static fluid pressure are summarised in Table 7-2.

$$P = \rho gh = [\rho_{feed} \times g \times h_{feed}] + [\rho_{slag} \times g \times h_{slag}] + [\rho_{matte} \times g \times h_{matte}] \quad \text{Equation 22}$$

The estimated pressure at the matte zone (industrial furnace) can be 0.69 atmospheres above the pressure in the free board according to the calculations in Table 7-2. In industrial application, hydrostatic pressure can have a significant influence on the penetration of matte through the graphite since the static fluid pressure is the highest at the matte zone.

Based on the estimated static fluid pressure in the matte level of a typical industrial smelter, the effect of static fluid pressure in the industrial smelter seems substantial. The static fluid pressure can cause the liquid matte to penetrate through the spaces between graphite blocks in industrial applications. Snyders et al. 2006 has reported that the bath level affects the flow rate of the matte through a tap-hole, therefore an increase in static pressure owing to the depth of the bath levels (feed, slag and matte) will increase the amount of liquid matte penetration at the matte zone.

Table 7-2: Density, height and estimated static pressure at the feed, slag and matte zone

	Feed	**Slag**	**Matte**
Minimum values			
Density ($kg.m^{-3}$)	1300	3800	4800
Height (m)	0.2	0.8	0.2
Pressure (Pa)	2548	29792	9408
Pressure (atm)	0.025	0.294	0.093
Maximum values			
Density ($kg.m^{-3}$)	1600	4200	5200
Height (m)	0.6	1.1	0.3
Pressure (Pa)	9408	45276	15288
Pressure (atm)	0.093	0.446	0.15

b) Chemical reactions between matte and graphite

Dissolution is one mechanism of refractory wear where a solid refractory reacts with a liquid to form a product with new properties [Carniglia et al. 1992].

Matte residue was analysed using ICP and LECO to determine its elemental composition. The matte remaining inside the crucible (MIC) and the matte collected outside the crucible (MOC) after exposure were analysed separately to determine possible chemical interactions between the penetrated matte and the graphite. Elemental composition of MIC and MOC are shown in Table 7-3.

The carbon content of MIC and MOC was the same (0.1 mass percent), this indicates that the penetrated matte (MOC) did not react with or dissolve carbon while penetrating through the crucible. Therefore chemical reactions between graphite and matte could not be the main mechanism by which matte penetrated through the graphite crucible.

Sulfur, copper and nickel content in MOC were slightly higher than in MIC. In contrast the iron content in MIC was much higher than in MOC. It should be highlighted that iron was present in the starting matte both as a sulfide and as an oxide impurities (FeO and $FeCr_2O_4$). The other elements (Al, Ca, Cr, Mg, Mn and Si) present as oxides in the starting matte remained inside the crucible after exposure. These oxides (slag) have a higher liquidus temperature (1450 ºC to 1500 ºC) [Sundström et al. 2008] compared to that of matte (875 ºC) [Eksteen 2011]. Therefore, at 900 ºC the slag phases should still be solid. If the slag phases were still solid at 900 °C they could not penetrate with the liquid matte.

Table 7-3: Elemental composition of industrial matte residue exposed to SG-graphite at 900 °C (ICP, LECO: mass percent)

	Al	**C**	**Ca**	**Co**	**Cr**	**Cu**	**Fe**	**S**	**Mg**	**Mn**	**Ni**	**Si**	**Zn**
***MIC**	0.2	0.1	0.3	0.5	2.1	8.3	45.1	27.3	0.3	0.1	14.9	0.8	0.1
#MOC	0.0	0.1	0.0	0.5	0.0	11.6	40.4	28.7	0.0	0.1	18.2	0.1	0.2

*MIC_matte remaining inside the crucible after exposure

#MOC_matte collected outside the crucible after exposure (penetrated matte)

c) Effect of a restricted crucible volume capacity

In all the experiments the crucible was filled to capacity since it was not anticipated that the level of matte inside the crucible could affect its behaviour during melting. The effect of a restricted volume was probed by filling the crucible to different volume of the crucible. In one crucible matte was filled to half its volume capacity while the other crucible was filled to full capacity (to the top edge of the crucible).

A half-filled crucible was not penetrated by a liquid industrial matte while a full crucible was penetrated by a liquid industrial matte. In a half-filled crucible, the matte foamed and filled the volume of the crucible, the matte reached a stable volume before it leaked out of the crucible.

It was concluded that the proportion of liquid matte that penetrated through the crucible was correlated with the extent to which the crucible volume could accommodate the foamed matte.

7.2.2.5 Implication for industrial application (industrial matte penetration)

Penetration of liquid matte through the graphite is envisaged in industrial application since the static pressure at the matte level can be substantial. Liquid matte can leak out of the graphite where there is sufficient connected pores or cracks. On dense graphite liquid matte does not penetrate the graphite. In industrial applications the graphite blocks are lined such that there are gaps between the blocks since the blocks are typically ~100 mm width by ~160 mm thickness [Thethwayo 2010]. The gaps between the blocks may serve as penetration path for the matte.

In an industrial smelter, sulfides start melting at the feed-slag interface after which matte falls through the slag and settles below the slag layer [Eksteen 2011]. The effect of matte swelling should not be a factor in an industrial smelter since there is enough space inside the furnace (at the concentrate-zone) to accommodate changes in the volume of the matte. Expansion of matte due to gas generation may affect the thickness of the slag or matte layer. However static pressure may enhance matte penetration at the matte zone.

The hot-face of the refractory has to be sufficiently cooled to below the liquidus temperature of the melt (875 °C). This will cause the melt to freeze at the hot-face, and consequently prevent the penetration of the matte through the graphite block.

7.2.3 Chemical interaction of graphite with matte

The chemical composition of Matte-S and industrial matte was altered during exposure to graphite. In the Matte-S residue, the loss of sulfur resulted to phase transformation of the sulfides. No new sulfide phases were detected in the Matte-S residue. The industrial matte samples had $(FeNi)_9S_8$, $(CuFe)_xS$, FeS and oxide impurities. During the exposure of graphite to

industrial matte, matte segregated into three phases a metal, a sulfide residue, and a slag-globule. The interaction of graphite with matte is discussed in turn:

7.2.3.1 Formation of the FeNi alloy in the Matte-S residue

The FeNi content in Matte-S increased with exposure time and temperature. Matte-S lost as much as ~ 30 mass percent sulfur. Extensive solid solutions of $(FeNi)_xS$ and $(CuFe)_xS$ were also observed in the Matte-S residue. Metallic Fe, Cu and metal carbides were not observed in the Matte-S residue.

The Matte-S sample had ~60 mass percent $(FeNi)_9S_8$, the metal detected in the matte residue contained Fe-Ni. According to Habashi 2002, sulfides are not reduced by carbon [Habashi 2002], therefore FeNi did not form by carbon reduction of $(FeNi)_9S_8$. Based on the analysis of the gas condensate, significant amount of sulfur reported to the off gas during the exposure.

In the Fe-Ni-S phase diagram, FeNi metal is in equilibrium with pentlandite, $(FeNi)_xS$ and Ni_3S_2 at sulfur below 50 atom percent (Figure 3-3). As the sulfide loses sulfur, the equilibrium shifts to a metal Fe-Ni phase field [Vaughan et al. 1978]. Therefore it is suggested that the formation of the FeNi alloy in the Matte-S residue was driven by the phase transformation that occurred with the increase in temperature that lead to the evaporation of sulfur. Graphite cannot be the main reason for the formation of FeNi alloy in Matte-S. However, it should be noted that according to the FactSage simulations, the presence of carbon increased the volume of gas generated. So the formation of CS_2 is also a possibility.

7.2.3.2 Formation of FeNi-Si alloy in the industrial matte residue

A metal (in the industrial matte residue) consisted of FeNi and FeNi-Si alloy. FeNi possibly formed due to evaporation of sulfur during exposure, analysis of the gas condensate (Table 5-22, Table 5-23 and Table 5-24) evinced that sulfur was the main component in the gas condensate.

The formation of Fe-Ni silicide has been discussed by Schiepers et al. 1993. When a monosulfide such as $(FeNi)_xS$ is reacted with silica or silicon carbide in the presence of a

reductant; FeNi-Si forms [Schiepers et al. 1993]. These authors worked at 850 °C. In the current work, $(FeNi)_9S_8$ would serve as a monosulfide, SiO_2 would provide Si and graphite would serve as a reductant. The conditions in this work were conducive for the formation of the FeNi-Si alloy.

7.2.3.3 Formation of a sulfide in the industrial matte residue

The composition of the residual matte changed during the exposure to graphite. Keilite $(FeMg)_xS$, (FeCr)S, CaS and (FeNi)Si are amongst the phases that were observed after the exposure of graphite to an industrial matte contaminated with oxides. The extraction of Al, Ca, Cr, Fe, Mg, and Mn from silicates (in the oxide-impurities) to the sulfides occurred, Si was extracted from the oxide to the metal and the gaseous phase.

Sulfidation of silicates has been discussed by Fleet et al. 1987 and Lenher et al. 2013. Sulfidation of silicates occurs where there is a reductant, a sulfide to supply the sulfur and the silicates. This process is favoured by high temperature (>1200 °C), low CO and high sulfur environment [Fleet et al. 1987, Lenher et al. 2013]. The overall reaction for the sulfidation of silicates and metallization of sulfides is outlined in Equation 23, where [M] is (Ca, Fe, Mg or Mn) [Fleet et al. 1987].

The composition of FeS changed during the interaction, FeS either had high Cr or high Mg after exposure. Cr has been reported to have high solubility (3 to 21 mass percent) in the FeS structure [Weisberg et al. 1998]. Other authors report that FeS can take up to 4.4 mass percent Cr in its structure [Karwowski et al. 2007, Shimizu et al. 2002, Skinner et al. 1971]. Therefore the formation of Cr enriched sulfide could result from the dissolution of Cr into the sulfide (FeS).

The composition of the phase annotated (FeMg)S in Figure 5-32 and Table 5-25 is similar to the composition of the keilite discussed by Shimizu and co-workers [Shimizu et al. 2002]. This means that during the exposure of matte to graphite, sulfides of Ca, Cr, Mg and Mn formed. These sulfides dissolved in the matte and formed a solid solution. The lamellae lines in the (FeMg)S phase (in Figure 5-32) are the (FeMg)S phase with a higher metal to sulfur ratio. The Mg content of the lamellae is less than that of the bulk phase. Equations 24 and 25 were simulated using the FactSage (reaction), their $\Delta G°$ is shown in the equation. The simulation was done for the MgO and the CrO in the presence of the silica, carbon and excess oxygen. Excess

oxygen was added since there was iron oxide in the matte and the slag globule. Free energy of formation is negative at 1200 °C and 1300 °C for respectively CrO and MgO reduction, therefore the reaction in Equation was feasible at the operating conditions of the current work.

The solubility of CaS in keilite is limited since Ca cations have larger ionic size when compared to other monosulfides [Fleet et al. 1987], as such in the current work CaS is detected as a separate phase.

$$[M]SiO_3 + (Fe, Ni)S + 3C \rightarrow (Fe, Ni)Si + [M]S + 3CO \quad \text{Equation 23}$$

$8CrO + 9SiO_2 + (Fe, Ni)_9S_8 + 28C + O_2 \rightarrow 9(Fe, Ni)Si + 8CrS + 28CO$ $\Delta G° = -342.391$ kJ/mol at 1200 °C Equation 24

$8MgO + 9SiO_2 + (Fe, Ni)_9S_8 + 28C + O_2 \rightarrow 9(Fe, Ni)Si + 8MgS + 28CO$ $\Delta G° = -444.244$ kJ/mol at 1300 °C Equation 25

Intermediate solid solution (Cu, Fe)S is observed in the matte residue, it has significant amounts of Al (6.4 mass percent). Solubility of alumina in the sulfide (Cu, Fe)S has not been reported in the literature. Based on the behaviour of the silicate phases, it is assumed that alumina silicate was sulfidised during the exposure of matte to graphite. Sulfidation of aluminosilicate could lead to the formation of an aluminium sulfide. Aluminium sulfide could further dissolve in a (Cu, Fe)S forming a sulfide phase, this assumption is based on the detection of an Al-rich sulfide (annotated in Figure 5-32 and Table 5-25). Synthesis of this phase was attempted in this work, the details of the synthesis of the (Cu, Fe)S-Al phase is reported in Appendix B.

The operating temperature in this work was 1450 °C, this was above the minimum temperature for silicate sulfidation. The reaction in Equation 23 is a plausible mechanism for the formation of the sulfide phases in Table 5-25 and a metal $(Fe, Ni)_xSi$ discussed in 7.2.3.2.

7.2.3.4 Formation of the slag-globule

The oxide impurities in the matte sample consisted of $(FeCr)_xO$ and $(Al, Ca, Fe, Mg)_xSiO$ (Table 4-8). According to Eksteen 2011, at temperatures ≥1500 °C matte can sulfidise the $MgO\text{-}Fe_xO\text{-}Cr_2O_3$ brick, this brick is used in the hearths of most of the PGM smelters. The brick consists

of the oxides of Mg, Cr, Al and Fe as well as minor amounts of CaO and SiO_2. The sulfidation reactions of the oxide brick by the matte are in Equations 26 and 27, the ΔG° for the reactions were determined using the FactSage.

$$FeCr_2O_4(\text{refractory}) + 2S\ (\text{matte}) + 3Fe(\text{matte}) \rightarrow 2CrS(\text{matte}) + 4FeO(matte)$$

$$at\ 1500\ °C\ \Delta G° = -8.478\ kJ/mol \qquad \text{Equation 26}$$

$$MgCr_2O_4(\text{refractory}) + 2S\ (\text{matte}) + 3Fe(\text{matte}) \rightarrow 2CrS(\text{matte}) + 3FeO(matte) +$$

$$MgO(refractory)\ \Delta G° < 0\ at\ 1650\ °C \qquad \text{Equation 27}$$

The sulfidation of a refractory brick in the matte could be responsible for the presence of the oxide impurities in the industrial matte samples. The industrial matte samples had $FeCr_2O_4$ as an impurity (amongst other oxide and silicate phases) before matte was exposed to graphite. After exposure the matte residue had an oxide globule attached to the graphite. The slag-globule had (Mg, Ca)(Al, $Si)_xO$ and SiO_2 as abundant oxide phases, adjacent to the graphite was a layer of SiC, and adjacent to the SiC was a layer of $(FeCr)_xSi$.

The phases in the slag globule could form as products of the sulfidation of silicates as explained in Section 7.2.3.3. The starting oxide-impurities did not have SiO_2 as a single phase (Table 4-8) but it was part of the silicate compounds. SiO_2 (inFigure 5-31c) detected in the slag globule was a product of sulfidation of silicates, SiO_2 forms according to Equation 7, that is the intermediate step in Equation 23.

Reduction of SiO_2 by carbon has been discussed by Miller et al. 1979 and Bialoskórski 1990. SiC forms when a molar ratio of graphite: SiO_2 is ≥ 3 according to Equation 29 [Miller et al. 1979, Bialoskórski 1990]. In the slag-globule (Figure 5-31c), SiC is in contact with graphite therefore the conditions are conducive for the formation of SiC according to Equation 20. It seems that SiO_2 was reduced by graphite to form SiC, since SiC is observed at the interface of graphite and slag globule (Figure 5-31c). The reaction in Equation 29 was simulated using the FactSage (reaction), the ΔG° is negative at 1600 °C (Equation 29), when the partial pressure of oxygen is at 10^{-9} atmospheres, the ΔG° is negative at 1000 °C (Equation 30). Therefore the reduction of silica by carbon is feasible at the operating conditions of the current

work, the forward reaction is enhanced by the presence of oxygen, or if the silica activity is below since the reaction was occurring in solution.

$$SiO_2 + 3C \rightarrow SiC + 2CO \quad \Delta G° = -27.618 \text{ kJ/mol at } 1600 °C \qquad \text{Equation 28}$$

$$SiO_2 + 5C + O_2 \rightarrow SiC + 4CO \quad \Delta G° = -32.861 \text{ kJ/mol at } 1000 °C \qquad \text{Equation 29}$$

Chrome phases can be present in matte as CrS and as precipitated oxidic and sulfidic chromium spinel phases [Kwatara 2006]. Chromite ($FeCr_2O_4$) is slightly soluble in matte in reducing conditions and high temperatures (1450 °C) [Eksteen 2011]. $FeCr_2S_4$, becomes a more predominant phase in reducing conditions [Kwatara 2006]. FeCr-Si was detected in the slag globule. FeCr-Si could possibly form in three ways either as a direct reduction of $FeCr_2O_4$ by SiC according Equation 31, or the sulfidation of chromite according to Equation 32 as suggested by Eksteen [Eksteen 2011], or the reaction of $FeCr_2S_4$ with SiO_2 and graphite to form CO, SO_2 and FeCr-Si; the remaining FeO could be reduced by SiC since the FeCr-Si appears adjacent to SiC in Figure 5-31c. If the activity of $FeCr_2O_4$ is below 1, the reaction temperature is reduced. If this reaction occurs, the reaction products would be a metal silicide (FeCr-Si) and a CO gas.

$$FeCr_2O_4(s) + 4SiC\,(s) \rightarrow Fe(l) + 4Si(l) + 2Cr(s) + 4\,CO(g)$$

$$at\ 1537\ °C\ \Delta G° = -1.396 \frac{kJ}{mol} \qquad \text{Equation 30}$$

$$FeCr_2O_4 + 3Fe + 2S \rightarrow 2CrS + 4FeO \quad \Delta G° = -8.478 \text{ kJ/mol at } 1500 °C \qquad \text{Equation 31}$$

The formation of the Fe-Cr-Si-C alloy has been discussed by Hayes 2004. When chromite ores are reduced by carbon initially the Fe-Cr alloy forms, on further interaction with the slag this alloy can dissolve Si into the alloy.

As seen in the FactSage simulations, ΔG° is negative at 1600 °C for the carbon reduction of the SiO_2 to SiC. At a slightly oxidising environment ($pO_2 \approx 10^{-9}$) ΔG° is -32.861 kJ/mol at 1000 °C. Due to the presence of an oxide phase $(Mg, Ca)(Si, Al)_xO_y$ there can a supply of oxygen to enhance the formation of SiC at the operating temperatures used at the current work.

The interaction between the chromite and silicon carbide has a ΔG° of -1.396 kJ/mol at 1537 °C, therefore the formation of the alloy is feasible as observed in this work. The presence of oxygen reduces the inception temperature of these reactions.

7.2.3.5 The effect of exposure time on the interaction of slag-globule with graphite

The slag-globule was depleted with increase in exposure time. Wear of graphite around the slag globule also increased with exposure time. The depletion of graphite and slag-globule could occur through two processes, namely; the reduction of the oxide phases and the sulfidation of the silicates. These processes result to the formation of gases that escape the reaction site, the experiments were carried out in an open system therefore the gases could be carried by the purge gas to the off-gas.

Depletion of SiC layer with exposure time could be attributed to the reactions in Equations 29, 30 and 31 [Miller et al. 1979, Bialoskórski 1990] where SiC serves as a reductant for the oxides in the slag-globule. The ΔG° for Equations 29 and 31 were determined using the FactSage, these reactions require a partial pressure of oxygen to go forward, oxygen should be at least 10^{-3} atmospheres.

The reduction of SiO_2 by graphite proceeds to vaporization of all constituents (SiO_2 and C) [Miller et al. 1979]. The intermediate steps in Equation 29 form SiO and Si gas according to the reactions in Equations 35 to 39 [Miller et al. 1979, Bialoskórski 1990]. The ΔG° for the reactions in Equations 35 to 39 was determined using the FactSage (reaction). The reduction of the oxide-impurities by graphite could therefore result to the depletion of graphite and the oxide.

Sulfur released from the metallization of sulfides can react with SiO_2 in the slag-residue and form SiS and O_2 gas according to Equation 40 (taken from Lenher et al. 2013). The formation of these gases would lead to depletion of slag-residue and graphite since oxygen will react with graphite to form a CO gas.

SiO_2 (s) + SiC (s) + ½O_2 → 2SiO (g) + CO (g) ΔG°= -13.698 kJ/mol at 1400 °C Equation 32

SiO (g) + 2SiC (s) + ½O_2 → 3Si (g) + 2CO (g) ΔG°= -108.739 kJ/mol at 1400 °C Equation 33

SiO_2 (s) + C (s) → SiO (g) + CO (g) ΔG° = 117.447 kJ/mol at 1400 °C Equation 34

SiO (g) + C (s) → Si (g) + CO (g) ΔG° = -18.939 at 1400 °C Equation 35

Si (g) + C (s) → SiC (s) ΔG° = -60.193 kJ/mol at 1412 °C Equation 36

SiO_2 (s) + ½S_2 (g) + 2C→ SiS (g) + 2CO (g) ΔG° =-2.327 kJ/mol at 1400 °C Equation 37

7.2.3.6 Graphite wear by chemical reactions with industrial matte

The gas-slag interface and slag-matte interface were the most corroded areas of the graphite wall around the slag-globule. Fleet et al. 1987 suggested that during the sulfidation of silicates the reductant is consumed owing to the formation of the CO gas that escapes the reaction site. CO is the major gas component on all the sulfidation reactions discussed in Section 7.2.3.5. As such, the formation of CO from the silicate-sulfidation reactions lead to the consumption of the graphite crucible. Carbon content in the slag-globule could not be quantified, the slag was attached to the graphite therefore a clean sample of slag could not be attained. SEM-EDS and EPMA could not give accurate carbon content of the bulk sample given that these techniques are generally not used for quantifying carbon and also these techniques give spot analysis.

Graphite lost to the off-gas could not be quantified, online analysis of the process gas was not acquired, and as such the composition of the gas stream was not determined. The off-gas duct was cooled to 0 °C to capture gases that could condense above 0 °C. The carbon containing gases (CO, CO_2 and CS_2) are not solid above 0 °C; as such these gases were not in the gas condensate. The gas condensate mostly consisted of (in a decreasing order) S, Si, Cu, Mg, Al and Fe (condensate analysis are shown in Table 5-22, Table 5-23 and Table 5-24). According to this partial analysis of the off-gas, it is evident that high amounts of S and Si reported to the off-gas during the interaction of graphite with matte and oxide-impurities. Therefore, the reactions proposed above for the consumption of graphite and oxides are plausible since in almost all the reactions Si gas is the product. The Si/SiO_2 compound in the condensate could also form due to

the disproportionation product of the low temperature dissociation of SiO gas outlined in Equation 41.

$$2SiO\ (g) \rightarrow SiO_2\ (s) + Si\ (g) \qquad \Delta G^\circ = -333.924 \text{ at } 800\ ^\circ C \qquad \text{Equation 38}$$

The mechanism that causes severe consumption of graphite is the sulfidation of silicates accompanied by the reduction of oxides by the graphite. Based on the observed consumption of graphite by the slag-globule, oxides and silicates can cause a severe wear of graphite at high temperatures (1450 °C). In industrial application graphite consumption can be minimized by maintaining the graphite hot-face below the liquidus temperature of the melt, thus preventing reactions between the graphite and the melt.

7.2.4 Deductions

The summary of findings from the discussion is presented in this section. The observations from the interaction of graphite with Matte-S, and the interaction of graphite with industrial matte are summarized below.

7.2.4.1 Interaction of graphite with Matte_S

- The species of liquid matte dissociate and vaporise with an increase in operating temperature and contact time. The vaporised matte species escape the crucible in a gaseous form.
- The evaporated matte species are carried with the purge gas, these species condense when they reach the cooled portion of the work tube.
- Copper and sulfur are more prone to vaporisation when compared to iron and nickel, nickel is the least prone to evaporation. The Fe-Ni alloy has the highest melting temperature, this factor possibly contributed to low vaporisation rates of Fe and Ni.
- The rate of evaporation of sulfur depends on the concentration of the sulfur in the melt, as the melt becomes deficient in sulfur (with increase in exposure time and operating temperature) the rate of sulfur evaporation decreases.

- The solubility of graphite in matte is correlated with the rate of sulfur loss by the matte. As the matte losses sulfur the Fe-Ni alloy forms.
- Carbon has higher solubility in the alloy (Fe, Ni) than in a corresponding sulfide.
- The Fe-Ni alloy dissolved up to 0.3 mass percent carbon while a corresponding sulfide dissolved 0.03 mass percent carbon. This observation is in line with the findings of Tsymbulov et al. 2001, which reported that the Fe-Ni alloy has higher carbon solubility than a corresponding sulfide.
- The rate of carbon dissolution and matte loss increases with exposure time. The increase in contact time enhances sulfur losses that indirectly increases carbon solubility in the melt through the metallization of the (Fe, Ni)S in the matte. This finding agrees well with the data of Tsymbulov et al. [Tsymbulov et al. 2001].
- The consumption of graphite by matte is not envisaged with increase in contact time, however formation of a metal or evaporation of sulfur should be avoided to minimise the dissolution of graphite in the matte.
- Foaming of Matte-S is not observed during its exposure to graphite.
- Liquid Matte-S does not penetrate through porous SG graphite, only matte prills are observed embedded in a graphite wall.
- The process gas produced during melting exerts excess pressure on the inner walls of the crucible. As such, any matte droplets covering the pores of the graphite can be forced into the graphite wall by the high gas pressure that is created inside the crucible.

7.2.4.2 Interaction of graphite with industrial matte

- Graphite is non-wetted by industrial matte, however liquid industrial matte does penetrate through the graphite.
- Liquid matte penetration was physical penetration since internal pressure forced the liquid matte through the pores and cracks in the graphite wall.
- Gas generation during the melting of matte created pressure build-up inside the crucible. Due to the presence of solids and gas the matte foamed and covered the inner walls of the

crucible. The gas pressure forced the liquid matte through the pores of the graphite. The distance to which the liquid penetrates depends on the differential pressure between the excess gas pressure and the capillary pressure.

- The liquid matte penetration subsided as the gas pressure dropped due to the decrease in gas generation rate. As the temperature increases the solid fraction should decrease that decreases the viscosity of the melt. The foam collapses as the viscosity decreases.
- The composition of the penetrated matte and the composition of the matte that remains inside the crucible were similar (except the elements from impurities); therefore matte penetration was not driven by chemical reactions between matte and graphite.
- The penetration rate of a liquid-matte through SG graphite was not determined by the final temperature or contact time. The rate of liquid matte penetration through graphite was however affected by the internal pressure that is associated with gas generation during the melting stages of matte. The observed physical properties of matte that changed during melting were the porosity of matte that directly affected the apparent volume of the matte during melting.
- Hydrostatic pressure is not a plausible mechanism responsible for liquid industrial matte penetration since penetration was not localised to the bottom of the crucible.

The phenomenon of industrial matte penetration is due to physical penetration which occurs when a strictly non-wetting liquid is forced into the pores of a solid by excess gas pressure.

7.2.4.3 Chemical interaction between graphite and industrial matte

- Metallization of matte (FeNi)S releases sulfur gas according to Equation 8.
- In the presence of sulfur, graphite and silicates, sulfidation of silicates occurs according to Equation 7 at 1450 °C.
- Graphite is consumed during the conversion of silicates to sulfides since graphite forms CO gas that escapes the reaction site [Fleet et al. 1987].
- Sulfidation of silicates results to evaporative loss of the elements due to the formation of gaseous products [Lenher et al. 2013].

- Vaporization of elements is enhanced with exposure time if sulfidation of silicates continues. Therefore, loss of elements to the off-gas is inevitable if the reactions (Equations 7, 8 and 23) outlined above are driven forward.
- The interaction between matte and a slag is significant in the presence of graphite. This phenomena results to the formation of a metal silicide and a sulfide phase which is enriched in the constituents of the slag, such as; Al, Ca, Cr and Mg.
- Metallization of $(Fe, Ni)_xS$ lead to the formation of Fe-Ni alloy and the loss of sulfur by the matte.
- A metal silicide seems to dissolve a substantial amount of carbon up to 0.3 mass percent whereas the corresponding sulfide can dissolve only 0.03 mass percent carbon.
- Although graphite is not directly consumed by matte, the formation of a metal through metallization of the matte can dissolve a substantial amount of graphite. Therefore where graphite is applied, the formation of a metal should be avoided.
- Graphite consumption by the oxide-impurities seems to be a dominant mechanism of graphite wear when graphite is exposed to industrial matte.
- Cooling the graphite such that the hot-face temperature of the refractory lining is below the slag reduction temperatures could minimize graphite wear in industrial application.

7.3 Wear of graphite by industrial melt (matte and slag)

Physical penetration and slag-line erosion were the prominent wear mechanisms of graphite when graphite was exposed to a PGM melt (matte and slag).

7.3.1 Physical penetration of graphite by matte and slag

A strictly non-wetting liquid can be forced into the pores of a solid by external forces during physical penetration [Rigaud 2011, Lee et al. 2004, Jansson et al. 2004]. For non-wetting liquids infiltration is achieved by applying a sufficiently high pressure to overcome the capillary pressure. The infiltration distance, increases with time, and excess pressure [Eustathopoulos 2015]. The infiltration distance is indirectly proportional to the viscosity of the fluid; infiltration can be limited by the viscous friction [Eustathopoulos 2015].

It has been established that graphite is poorly wetted by the tested matte and slag. The physical penetration of the matte and slag could only occur if there was a high pressure to counteract the capillary pressure as explained by Eustathopoulos 2015. Slag penetrated graphite by up to 1 mm depth while the matte penetrated the entire width of the graphite (5 mm). The internal pressure during slag and matte melting could occur due to gas formation. Since the crucible was filled to capacity it is possible that during melting the slag was forced into the pores of graphite wall by the internal pressure inside the crucible such as seen with the matte.

The viscosity of the slag was estimated to be 0.4 Pa.s [Eric 2004] while that of FeS-Ni_3S_2 matte was ~2.2 x 10^{-3} Pa.s at 1500 °C [Sundström et al. 2008]. Since the matte and slag were exposed to the same graphite and at the same temperature and exposure time, the differences were the viscosity and the composition of the two phases. Based on the differences in viscosity it is plausible that the slag penetration was limited to 1 mm depth due to viscous forces.

7.3.2 Chemical interaction between graphite and the industrial melt (matte and slag)

In the matte-slag setup, the slag penetrated up-to 1 mm into the graphite wall. As such the tip of the slag infiltrate was saturated with carbon. Sulfur concentration at the graphite-slag interface is expected to be minimal compared to sulfur concentration above the slag layer (in the free board). The metal layer was not observed at the slag-graphite interface such as seen at the graphite-slag globule (Figure 5-31b) where graphite was exposed to matte only. Low concentrations of sulfur at the tip of the infiltrate could be responsible for the absence of silicate sulfidation reactions at the tip of the slag infiltrate. The atmosphere in these two systems (matte only setup and slag-matte setup) differs slightly. With the matte only setup, the slag-globule is constantly saturated with sulfur since the sulfide phase is in abundance and the slag-globule is above the sulfide layer (free board). In the matte only setup, the sulfidation of silicates and reduction of oxides were favourable due to the abundance of sulfur and carbon.

In the bulk slag the formation of sulfide and metal phases evinced the occurrence of silicate sulfidation. The composition of the slag had changed, the slag was contaminated with sulfide and metal phases, and therefore the behaviour of this slag cannot be directly compared to the behaviour of the slag used in wettability tests.

The conditions in the bulk melt (matte and slag) seemed conducive for the sulfidation of silicates since the graphite is a reductant, the matte below slag would provide sulfur and the slag provided the silicates.

The interaction of matte and graphite has been discussed in Section 7.2.3. In the matte-slag setup the matte residue only had two products, the sulfide phase and metal phase. The slag-globule was not observed since there was a slag layer on top of matte. It is possible that the oxide impurities from matte dissolved into the slag layer. The sulfide and metal had similar composition as observed for matte only setup discussed in Section 7.2.3.

7.3.3 Contrast between the behaviour of industrial matte and slag toward graphite

At the matte-zone, the inner diameter of the crucible remained un-changed. The matte-residue had no apparent adhesion towards the graphite surface based on the gap observed between the graphite surface and the matte (Figure 5-34).

In contrast, uniform penetration of the slag into the graphite wall was observed such that the slag attached to the graphite even after solidification. Similar to matte, the slag was possibly forced to the graphite wall by the internal pressure that builds up inside the crucible during melting. The viscosity of the slag possibly limited the slag from penetrating to the outer wall of the graphite as seen in matte penetration. The data on thermal properties of matte and slag such as coefficient of thermal expansion is not well documented; as such the effects of the cooling properties of matte or slag are not considered in this work.

At the slag-zone, uniform penetration of slag through graphite is observed,

At the matte zone no significant wear of graphite is observed,

At the slag-matte interface erosion of graphite is observed where a graphite surface has been dissolved or washed away, a groove filled with melt is observed after exposure.

7.3.4 Graphite erosion

Erosion of a refractory material by a liquid is associated with the motion of the liquid [Jansson et al. 2004]. For dynamic systems erosion due to forced convection is characterised by uniform corrosion, erosion characterised by a deep groove at the three-phase contact indicates the contribution of Marangoni convection [Vollmann et al. 2013]. Marangoni effect has the highest influence on mass transfer between refractory and fluid where high concentration and surface tension gradients exist [Vollmann et al. 2013].

The graphite erosion observed at the matte-slag interface (Figure 5-36) resembles a slag-line erosion that results from the Marangoni flow as explained by Mills [Mills 2011]. The average surface tension of matte is 0.37 $N.m^{-1}$, it was calculated (based on the composition of matte) from the work of Sundström [Sundström et al. 2008]. The surface tension of a PGM slag varies from 0.42 $N.m^{-1}$ to 0.46 $N.m^{-1}$ based on its composition [Eric 2004]. Since surface tension and concentration gradient exist between slag and matte, Marangoni convection is envisaged.

The appearance of a matte layer between graphite and slag indicates that upward movement of the matte occurred during the interaction. Matte is denser than slag, therefore due to gravity liquid matte is expected to settle below the slag. It is plausible that capillary forces associated with Marangoni effect counteracted gravity and caused matte to remain parallel to the slag at this area. The upward movement of matte could be associated with gas bubbles which rises from the matte through the slag layer; however upon cooling the matte should be released by the gas and settle below the slag layer.

Marangoni flow in the slag-line may cause severe erosion to the graphite. The difference between interfacial tension and surface tension is very blurred; they are in effect the same thing with the name applied in different conditions (liquid/liquid, liquid/gas or interface involving solids). The interfacial tension between graphite and matte as well as interfacial tension between graphite and slag has not been determined hence it is not discussed here. In this instance only the surface tensions of slag and matte are considered.

In industrial applications, the refractory wear is enhanced by the turbulence of the bath and the up-down movement of the bath interface during tapping [McDougall et al. 2012]. In the current work, the turbulence of the bath is minimal since the testing method is static. The up and down

movement of the slag and matte levels owing to tapping is also not simulated in the current work. Erosion of graphite observed at the slag-line demonstrates that, wear of graphite at the matte-slag interface is envisaged owing to the Marangoni effect. Where bath turbulence and up-down movement are present graphite erosion at the matte-slag interface maybe enhanced.

7.3.5 Deductions

- Although industrial slag and matte do not wet graphite, physical penetration of graphite by these materials occur.
- Physical penetration was driven by internal pressure build-up during melting.
- Foaming phenomenon occurs during melting of both industrial slag and matte, this is evinced by porosity of the solidified melt.
- Localised erosion (slag-line erosion) of graphite is observed at the matte-slag interface,
- The penetration pattern of industrial slag and matte differs. The industrial slag gradually penetrates through graphite while the industrial matte penetrates through the entire graphite wall rapidly. Viscosity can be responsible for the contrasting penetration behaviour of slag and matte.
- There was no gradient of the concentration of matte infiltrate in the graphite wall, the composition of matte embedded in graphite and that of the bulk matte were similar.
- It seems that there is no direct reactivity between graphite and matte (sulfides).

7.4 Effect of cooling graphite

From the cooled-graphite tests it seemed that if graphite is sufficiently cooled to below the melting temperature of matte (~900 °C), the matte freezes and attaches itself to the surface of the graphite. With the frozen matte layer at the surface of graphite matte penetration is prevented. Based on the observation from this work, if graphite is sufficiently cooled the matte does form a stable freeze lining. It should be noted that the current work was static so turbulence, or agitation of the bath was not simulated. As such where forced convection is present the behaviour of the frozen skull may be different.

Penetration of gaseous species still occurred even when the graphite was sufficiently cooled. It is the gaseous species that have a tendency of depositing on the cold-face of the graphite. Therefore cooling graphite does not deal with the issue of matte specie dissociation, evaporation and deposition of matte species on the cold-face of the refractory.

Matte was highly porous at low temperatures. As the temperature increased, matte became less porous and at the hot zone (>~1200 °C) the pores were not observed. Porosity of matte was accompanied with unmelted phases. This trend was also observed during the tests at 900 °C, 1250 °C and 1450 °C. The influence of temperature on matte properties was confirmed, during melting, matte became highly porous which could be attributed to the presence of gas bubbles and solids in the matte. The presence of solids in a melt increases its viscosity, as the temperature is increased the solids decrease with a consequent effect on viscosity [Muller et al. 2011, Sundström et al. 2008].

Matte detachment from graphite was observed with increase in temperature. Detachment of matte could be attributed to the change of matte properties with increase in temperature. The formation of Fe-Ni alloy was observed with increase in temperature, this was the evidence that the composition of the bulk matte changes during the exposure, the phase transformations in the sulfide system occurs with an increase in temperature.

7.4.1 The morphology of matte residue as a function of exposure temperature

The effect of temperature on the appearance of the industrial matte is summarised in Table 7-4. The content in Table 7-4 is based on the following images of industrial matte; Figure 5-26: Matte-A exposed to 900 °C, Figure 5-28: Matte-A exposed to 1250 °C and Figure 5-29: Matte-A exposed to 1450 °C.

Table 7-4: Summary of the appearance of industrial matte based on visual observation

	900 °C	**1250 °C**	**1450 °C**
Porosity	high	Low	none
Solid phases	yes	Not clear	none
Metal layer	none	None	yes
Adherence to graphite	yes	Yes	none

The porosity of industrial matte increased during melting, this is evident in Figure 5-14. From ~900 °C to ~1000 °C the porosity increased as seen in Figure 5-14 and Figure 5-15. With increase in temperature the porosity decreased as seen in the matte exposed to 1250 °C and 1450 °C in Figure 5-28 and Figure 5-29.

In a semi-solid melt, the fraction solid decreases with an increase in temperature [Atkinson 2006]. Hence at a 900 °C-sample the solid phases were apparent, as the temperature increased to 1250 °C the solids were not clearly visible. At 1450 °C the matte seemed fully molten.

The presence of solids in a melt increases its viscosity [Muller et al. 2011]; the increase in temperature decreases the viscosity [Muller et al. 2011, Sundström et al. 2008]. For the FeS-Ni_3S_2 melt the viscosity of the melt decreases from 2.8 x 10^{-3} to 2.2 x 10^{-3} Pa.s with a temperature increase from 1250 °C to 1500 °C [Sundström et al. 2008]. Therefore as the operating temperature increased the viscosity of the melt decreased.

The metallic layer was not observed at 900 °C and at 1250 °C, metal segregated below matte after exposure at 1450 °C (Figure 5-29). Based on the analysis of the matte residue, the evaporation of sulfur to the off-gas was enhanced with increasing temperature. The loss of sulfur by a sulfide such as $(FeNi)_9S_8$ produces an alloy as discussed.

Surface tension in the Cu_2S-FeS-Ni_3S_2 system is sensitive to composition [Sundström et al. 2008]. Sulfur has been shown to have the greatest influence on the surface tension of the nickel-iron matte; increase in sulfur content decreases the surface tension of a melt [Sundström et al. 2008]. Increase in metallization of a sulfide melt increases surface tension [Sundström et al. 2008]. Therefore as a metal phase forms the surface tension increases. At 1450 °C there was no adherence of matte to graphite, it is proposed that the non-adherence was caused by higher surface tension associated with the metallization of the melt. It is assumed that the adherence at low temperatures was influenced by a lower surface tension associated with the starting composition of matte that had negligible amounts of metal.

7.4.2 The effect of the cooling rate on the freeze lining

Graphite is already used at the upper sidewall of a PGM smelter where operating temperatures are higher than the operating temperature at the lower sidewall (at the matte level).

The composition and thickness of the frozen skull depend on the hot-face temperature of the refractory [Duncanson et al. 2004]. Therefore the mechanism of the skull formation is a function of the temperature of the graphite hot-face and the composition of the melt. As discussed in Section 2.5.3, graphite is able to form a freeze lining at the hot-face even at high operating temperatures (I industrial application). A typical operating temperature for a slag zone is 1600 °C. A graphite used against a concentrate and slag zone had a stable freeze lining with a thickness of ~1 mm against the concentrate and ~2 mm against the slag [Thethwayo 2010]. Considering that slag operates at a higher temperature than the matte zone, it is envisaged that as far as the hot face temperature is concerned, graphite will be able to form a stable freeze lining against the matte zone. It should however be noted that the current work was done in static conditions, the effect of bath turbulence and up-down movement during tapping has not been simulated. The outcomes of this work cannot be applicable to the industrial conditions where there is forced convection of the bath.

For accurate determination of the formation and stability of a frozen skull on graphite when exposed to matte the effect of forced convection will have to be considered. The heat transfer

calculation should consider the convection transfer between the moving bath and the refractory/freeze lining, as well as the conduction heat transfer through the wall of the refractory.

It is recommended that dynamic tests be done to determine the effect of forced convection on the behavior of matte when in contact with graphite.

As discussed in this work, a frozen skull forms at the hot face of the graphite that is used against the slag-zone. The application of cooled-graphite has not affected the operation of the PGM smelter, the frozen skull is typically below ~2 mm against the hottest portion of the smelter (against the slag zone). A PGM matte operates at a slightly higher temperature than its liquidus temperature, this is due to the treatment of high chrome concentrates (Eksteen et al. 2011). Therefore if cooled graphite is used against the matte level, it is not envisaged that the operation will be affected by the formation of the freeze lining or the cooling. Maintaining the matte refractory hot-face around 900 °C should not affect the operation since the frozen skull is stable at the slag-zone and it does not affect the operation.

7.5 Wear of MPC by a PGM matte

For a porous refractory with a reactive matrix-material, chemical penetration occurs where penetration and dissolution are tied together [Rigaud 2011]. Impurities in the refractories are prone to be attacked by the corrosive liquid; corrosion reactions may proceed through the matrix phase or grain boundary of the refractory microstructure [Sarkar 2017]. Chemical penetration leads to change in composition, porosity, texture and geometry of a refractory. Disrupted structure of the infiltrated refractory causes structural or chemical spalling (fracture or cracking of the refractory) [Rigaud 2011]. A penetrated refractory will have different properties than the unpenetrated refractory; this causes cracking and degradation of the whole refractory structure [Sarkar 2017].

In the current work, the MPC crucible was penetrated by the matte. The penetrated portion of the MPC seemed dense owing to the replacement of the matrix (Al and Si compounds) by the interaction product $(CuFe\text{-}Al)_xS$. There were no apparent pores on the structure of the penetrated MPC wall. The MPC sample had apparent pores, the change in the porosity and composition of the refractory would lead to spalling. Spalling of the MPC refractory is envisaged if it is used against a PGM matte.

7.5.1 Interaction of matte with MPC

The interaction products (between the MPC and matte) seemed immiscible hence they segregated into three distinct layers, a top layer, a middle layer and the bottom layer. In the case of Matte-S the top layer was a sulfide that was enriched in Al (Table 6-2), the middle layer was a matte residue and the bottom layer was the FeNi-Si alloy. With industrial matte, the top layer was enriched in Al, Cr, Mg and Ca (Table 6-3), the middle layer and the bottom layer is similar to that of Matte-S residue in Table 6-1. The conditions in the interaction of the MPC and matte were favourable for the sulfidation of silicates and the formation of an iron nickel silicide as discussed in Sections 7.2.3.3 and 7.2.3.4. The carbon and SiC in the refractory served as a reductant, the SiO_2 in the MPC matrix and the silicate impurities in matte provided the silicon compound required to react with the sulfide, the matte provided the sulfide.

The MPC had SiC and SiO_2 as part of the refractory matrix. An interaction product formed in the matrix of the MPC refractory (Table 6-1) during exposure to matte. This sulfide $(CuFe)_xS$-Al was also detected in the matte residue. In the open literature this phase has not been reported. This phase was synthesised in this work, the outcome is in Appendix B.

The metal (FeNi-Si) had up to 0.5 mass percent carbon while the corresponding sulfide had 0.03 mass percent carbon. This observation confirmed that carbon is more soluble in the metal than in the sulfide as observed for the exposure of graphite to matte.

7.5.2 Deductions

The prominent wear mechanism of MPC when exposed to synthetic and industrial matte was chemical attack of the MPC by the matte.

- When a micropore carbon is exposed to a synthetic and industrial matte chemical reactions occur between the matte and the refractory materials i.e. alumina, silica and silicon carbide.
- Matte species penetrated and reacted with the MPC refractory. The reactions of MPC with matte seemed to be progressive since penetration pattern was uniform and the concentration of the penetrant decreased towards the outer wall of the crucible.
- The refractory gets depleted in Al and Si compounds.
- A sulfide phase forms in the refractory matrix and the refractory becomes disintegrated and dense.
- The matte forms three distinct layers, a top sulfide layer enriched in Al, a middle matte layer deficient in nickel and a bottom layer consisting of Fe-Ni silicide.

Matte-S and industrial matte behaved similarly when exposed to MPC. The matte residue produced by both synthetic and industrial matte segregated into an Al-rich sulfide layer, residual sulfides and the Si-rich Fe-Ni metal. The difference in the composition of Matte-S residue and industrial matte residue is that industrial matte residue had other elements that originated from the oxide impurities. The industrial matte had higher amounts of matte loss.

- Interaction between refractory and matte leads to gas evolution that enhances matte losses to the off gas.

- Increase in operating temperature enhances matte loss and carbon dissolution in the matte.

7.5.3 Industrial implication

MPC is not a suitable refractory to use against liquid matte at the hot-face refractory lining of the PGM smelter. It is projected that MPC will react with matte resulting to densification and degradation of the refractory as well as contamination of matte by the MPC materials such as, Al and Si. Contamination of matte is undesirable since it leads to significant changes in matte properties, this will create challenges with further steps in matte processing.

8 Conclusions and recommendations

This section contains a summary of the research aims, the work done, the deductions from the observations and the recommendations. It is divided into conclusions and recommendations.

8.1 Conclusions

The aim of this study was to determine the compatibility of carbon-based refractories with a typical industrial matte and slag. The research questions and brief description of the work done as well as the outcomes are entailed in this section. The research question had to do with determining the most prominent refractory wear mechanism when carbon-based refractories are exposed to a liquid PGM furnace melt. The research question was divided into four sub-questions, the conclusions are structured based on research questions.

1) Does a PGM melt (matte and slag) wet graphite?
2) What is the most prominent wear mechanism of graphite when graphite is exposed to a PGM melt (matte and slag)?
3) Does matte form a protective frozen skull when graphite is cooled sufficiently?
4) Does a micropore carbon perform better than graphite when exposed to a PGM matte?

8.1.1 Question 1: "Does a PGM melt (matte/slag) wet graphite?"

Research question 1 was addressed by determining the wettability of graphite by PGM melt. Wettability of the SG graphite by Cu_2S, Ni_3S_2, FeS, synthetic matte, industrial PGM matte and industrial PGM furnace slag was determined using a sessile drop method. The findings of this work concerning wettability of graphite by a primary PGM matte and slag are as follows:

- Graphite is poorly wetted by Cu_2S, Ni_3S_2, synthetic matte, industrial PGM matte and industrial PGM slag. The contact angle between graphite and these materials is >90°.
- Reactive wetting occurs between graphite and FeS.

No interaction is observed between graphite and the primary PGM matte or slag, no interfacial or reaction product is observed in the residual melt droplet. Non-wettability of graphite by the matte and slag as well as non-reactivity of graphite towards the matte and slag indicate that chemical penetration of graphite by a liquid matte or slag is not probable. Changes in the operating temperature and composition of the melt may change the behaviour of the primary PGM matte and slag towards graphite.

The conclusion is that graphite is not wetted by a typical primary PGM matte or slag in an inert environment.

8.1.2 Question 2: "What is the most prominent wear mechanism of graphite when graphite is exposed to a liquid PGM melt (matte and slag)?"

Research question 2 was addressed by assessing the prominent wear mechanism of graphite by synthetic matte, industrial matte and industrial slag using crucible test method. Refractory dissolution and chemical/physical penetration were the refractory wear mechanisms investigated in this work. Extruded graphite, isostatically pressed graphite and the micropore carbon were the refractories that were tested against matte using the crucible test method. The synthetic matte, Lonmin matte, Amplats matte (Waterval and Polokwane), Lonmin slag and Waterval slag were the materials tested against graphite. The operating temperature varied from 800 °C to 1550 °C, the contact time was varied from 1 hour to 5 days.

Prominent wear mechanism of graphite by synthetic matte was investigated as a function of temperature and contact time. The conclusions are outlined below:

- Liquid Matte-S does not penetrate through graphite at all tested conditions.
- Matte prills are forced into the graphite wall by excess gas pressure associated with matte melting.
- Matte species (S, Cu and Fe) in decreasing order vaporise as the operating temperature is increased. The melt becomes deficient in sulfur and copper, and consequently the matte becomes enriched in iron and nickel. The evaporated matte species were carried with the purge gas, these species condensed at the cooled portion of the work tube.

- The vaporisation of matte species is enhanced with increasing operating temperature and contact time. Copper and sulfur is the most prone to vaporisation. Sulfur vaporisation leads to the formation of an alloy (Fe, Ni).
- Graphite solubility in the alloy (Fe,Ni) is up to 10 times more than graphite solubility in the corresponding matte.
- Graphite solubility is directly correlated with the loss rate of sulfur by a melt

Concerning the compatibility of graphite with Matte-S the findings of this work are the following:

- Liquid penetration is not a prominent wear mechanism of graphite by Matte-S.
- Graphite dissolution is not a prominent wear mechanism of graphite by Matte-S, however loss of sulfur by matte can cause severe dissolution of graphite in the alloy that forms.

Prominent wear mechanism of graphite by industrial matte was investigated as a function of graphite grade, temperature and contact time. The observations are the following:

- The dense HG graphite is not penetrated by liquid industrial matte, in contrast;
- The porous SG graphite is penetrated by liquid industrial matte. Therefore when considering using graphite against the liquid industrial matte less porous graphite has higher resistance to penetration by a liquid matte.
- The penetration of liquid industrial matte is not affected by the operating temperature or contact time, penetration occurs during the melting stages of the industrial matte.
- During melting the matte foams, matte foaming increases the volume of the matte, the matte then covers the inner wall of the crucible. As the gas is generated during melting the internal pressure increases, consequently the gas pressure forces the liquid matte into the pores in the graphite wall. Depending on the excess pressure, the liquid matte can infiltrate through the entire thickness of the graphite.
- Physical penetration of liquid industrial matte is a prominent wear mechanism of graphite by liquid industrial matte. Matte foaming associated with gas evolution is the probable mechanism responsible for the penetration of liquid industrial matte through the SG graphite crucible.

Liquid industrial matte only penetrates the SG graphite if it is contained in a restricted crucible volume. If the crucible volume is not restricted liquid matte penetration does not occur.

- The rate of liquid matte penetration through graphite is not affected by the process parameters (operating temperature or contact time); it is however affected by the change in the physical properties of the matte.

In industrial application, the volume of the smelter is not limited like the crucible used in this work. A smelter has a freeboard therefore matte foaming should not be a factor in industrial applications. Sulfides (matte) begin melting at the concentrate-zone where there is enough volume to accommodate the expanded matte without creating positive pressure. Therefore foaming of matte during melting is not a factor in industrial application

- Vaporisation of matte species increase with increasing operating temperature and contact time with consequent losses of matte species to the off-gas.
- Although graphite is not directly consumed by matte, the formation of a metal through metallization of the matte can dissolve substantial amount of graphite. Therefore where graphite is applied, formation of metal should be avoided.

The industrial matte samples had oxide and silicate impurities, these impurities react with both matte species (sulfides) and graphite during the exposure. The interaction of these impurities with matte and graphite is more pronounced at higher temperatures (1450 °C). These interactions result to graphite consumption, sulfidation of the silicates and the formation of a metal silicide (FeNi)Si. Sulfidation of silicates lead to high consumption of graphite through the formation of a CO gas. The residual matte becomes contaminated with the slag elements such as Al, Mg, Cr and Ca. The interaction is enhanced by an increase in contact time.

- Graphite consumption during the sulfidation of silicates seems to be a dominant wear mechanism of graphite when graphite is exposed to industrial matte (contaminated with oxides and silicates).

Industrial slag penetrates through SG graphite. The penetration of slag is through physical penetration that is driven by positive pressure inside the crucible due to slag foaming and gas generation during melting. Viscous forces of the liquid slag limits the depth of slag penetration to ~1 mm into the graphite wall.

Where matte and slag are simultaneously exposed in one graphite crucible, slag-line erosion of graphite is observed at the matte-slag interface.

8.1.3 Question 3: "Does matte form a protective frozen skull when graphite is cooled sufficiently?"

Cooled graphite was exposed to industrial matte; a temperature gradient (700 °C to 1207 °C) was achieved from the cooled lid to the bottom of the crucible. A frozen skull formed at the cooled end of the graphite, no frozen skull was observed at temperatures above 900 °C. Penetration of liquid matte was not observed where a frozen skull had formed. Liquid matte penetration was observed at the hot end of the graphite.

When graphite is sufficiently cooled (surface temperature below 900 °C) liquid matte penetration is prevented. A frozen skull of matte forms at the surface of the graphite in contact with the matte. Cooling the graphite such that the hot-face temperature of the refractory lining is below the melting temperature of matte can therefore minimize graphite wear in industrial application.

- Based on the findings of this work; matte penetration through the graphite wall can be minimised by maintaining the graphite hot-face below the solidus temperature of the matte.

8.1.4 Question 4: "Does a micropore carbon perform better than the graphite when exposed to a liquid PGM matte?"

Prominent wear mechanism of a microprobe-carbon by a synthetic and industrial matte was investigated by examining the penetration of matte through micropore carbon and the chemical interaction between micropore carbon and matte.

The prominent wear mechanism of micropore carbon by synthetic and industrial matte is chemical penetration where matte species penetrate and react with the micropore-carbon. This chemical attack leads to the following:

- Dissolution of the refractory components (Al and Si compounds) into the matte

- This interaction leads to the disintegration of the refractory owing to the consumption of the refractory-matrix (Al and Si compounds). Disrupted structure of the infiltrated refractory may cause structural or chemical spalling (fracture or cracking of the refractory).
- Contamination of matte by the refractory materials
- Formation of the solid products (sulfide) in the refractory wall
- Loss of matte through the formation of gaseous products when matte reacts with a refractory
- Depletion of matte (through vaporisation) and an increase in the proportion of metal silicide in the matte residue. Carbon has high solubility in the metal therefore an increase of metal content in matte indirectly enhances the dissolution of the refractory (carbon) in the matte residue

The interaction between micropore carbon and matte is enhanced by an increase in operating temperature.

The reactions of a micropore-carbon with matte seem to be progressive since penetration pattern is uniform and the concentration of the penetrant decreases towards the outer wall of the crucible.

- Chemical penetration is the prominent wear mechanism of a micropore carbon by a typical PGM matte.

Micropore-carbon is not a suitable refractory to use against a liquid PGM matte (based on the findings of this work). It is projected that micropore-carbon will react with matte resulting to densification and degradation of the refractory and the contamination of matte by the micropore-carbon materials such as, Al and Si. Contamination of matte is undesirable since it leads to significant changes in matte properties, which will create challenges with matte processing.

Graphite is a better refractory to use against the liquid PGM matte since micropore carbon exhibited lower resistance towards chemical attack by matte.

8.2 Recommendations

Based on the findings of this work it is inevitable that liquid and gaseous matte species can diffuse through the spaces between graphite blocks and reach the cold-face of the graphite block in industrial applications. In the current work the liquid matte penetrated through connected pores and cracks in the graphite wall, the penetration was not observed through solid aggregate particles. Therefore penetration of liquid matte is not envisaged through a thick graphite block, but liquid penetration can occur where connected pores or (in industrial application) spaces between blocks can serve as a penetration route for liquid matte. This is already seen in the post-mortem analysis of a graphite block that was used in an industrial smelter (Figure 2-4, Figure 2-5). The post-mortem analysis reported in Section 2 and in Appendix A is evidence that in industrial application matte species do somehow get to the cold-face of the graphite where they interact with waffle copper coolers.

8.2.1 Recommended actions for successful application of graphite in industry

The recommended actions are discussed in turn:

- Dense graphite blocks has to be used.

In the current work the HG graphite was not penetrated by liquid matte. The liquid matte penetrated through the connected pores and cracks in the graphite wall of the SG graphite. Therefore if the connected pores and defects on the graphite walls can be minimised, liquid matte penetration can be minimal.

- Application of carbon paste in the spaces between graphite blocks.

In the current work carbon paste was applied between the lid and the graphite crucible and the carbon paste was not penetrated by the furnace contents. Therefore graphite paste can be applied in the spaces between the blocks to serve as a physical barrier for furnace contents, preventing furnace contents from reaching the cold-face of the refractory.

It is necessary to run preliminary tests to determine whether the application of carbon paste between the graphite blocks will be feasible in an industrial scale and also whether the carbon

paste is able to limit the matte penetration in a larger scale. Therefore test work are recommended where graphite blocks can be exposed to matte and carbon paste must be applied in all the joints in the set-up to determine the application of carbon paste in a larger scale.

- Vertical or horizontal compression of the refractory to keep the joints tight

Containment of the melt in a furnace can only be achieved if the horizontal and vertical joints in the wall are leak tight. Vertical or horizontal compression of the refractory is recommended to keep the joints between refractory and cooling elements tight such that the penetration of melt between joints is minimised [Merry et al. 2000].

- If the graphite blocks can be re-designed such that towards the edge of the cold-face there is a grove or a vertical space through which a thin graphite plate can be fitted between each and every blocks. This plate would have to run from the top graphite block to the bottom graphite block such that when the melt escape between the graphite blocks it is deposited on this graphite plate.

It is envisaged that if the penetration path of the furnace melt can be detoured the deposition of furnace contents on the copper waffle coolers will be minimised. Most of the furnace contents will be deposited on the graphite plate rather than on the surface of the copper waffle coolers.

8.2.2 Future work

The current work did not cover the effect of the interfacial tensions on the interaction between matte and graphite. Such study will add understanding as to why the matte tends to adhere to graphite at low temperatures but detaches at high temperatures. The effect of a reducing environment on the wettability of graphite by matte was also not studied.

It is recommended that different methods of wettability testing be used for FeS, since its reactive wetting with graphite rendered inconclusive outcomes.

Dynamic tests would also add value in understanding the erosion of graphite by matte.

9 REFERENCES

Andrews, L., and Pistorius, P. C., Nickel, copper and cobalt distribution and equilibria in Anglo Platinum furnace slags. Mineral Processing and Extractive Metallurgy, 2010, 119(2), pp. 52-59.

Atkinson, H. V., Experimental determination of the parameters for modelling semi-solid processing. In Solid State Phenomena Trans Tech Publications, 2006, 116, pp. 16-23.

Bale, C.W., Belisle, E., Chartrand, P., Decterov, S. A., Eriksson, G., Hack, K., Jung, I. H., Kang, Y. B., Melancon, J., Pelton, A. D. and Robelin, C., FactSage thermochemical software and databases-recent developments. CALPHAD, 2009, 33(2), pp. 295-311.

Barnes, A. R. and Newall, A. F., Spinel removal from PGM smelting furnaces. Southern African Pyrometallurgy 5-6 March 2006, Southern African Institute of Mining and Metallurgy, 2006, pp. 77-88.

Bhoi, B. Ray, H. S. and Sahajwalla V., Influence of different parameters on wettability of graphite by CaO-SiO_2-FeO molten slag. Journal of the institute of Engineers (India), 2008, 89, pp. 3-8.

Bhoi, B., Jouhari, A. K., Ray, H. S. and Misra, V. N., Smelting reduction reactions by solid carbon using induction furnace: foaming behaviour and kinetics of FeO reduction in CaO-SiO_2-FeO slag. Iron and Steel making, 2006, 33(3), pp. 245-252.

Bialoskórski, J., Studies of the silica reduction process by carbon. Journal of Thermal Analysis and Calorimetry, 1990, 36(6), pp. 2029-2032.

Bruce, D., Mera, R., Leatherdale, D., Taylor, M. and Musgrove, R., Techniques for characterising the wetting, coating and spreading of adhesives on surfaces. NPL report DEPC MPR 020, 2005, pp. 1-40.

Carniglia, S. C. and Barna, G. L., 1992, Handbook of industrial refractories technology: principles, types, properties and applications. Noyes publications, pp. 213-232.

Chen, P. X., Chu, S. J. and Han, P. W. The solubility of carbon in molten iron-nickel-silicon alloy at 1773 K and 1823 K. Infacon XIV, 2015, pp. 528-535.

Chen, X., Li, Y., Li, Y., Sang, S., Zhao, L., Li, L. S., Jin, S. and Ge, S., Effect of carbon aggregates on the properties of carbon refractories for a blast furnace. Metallurgical and Materials Transactions B, 2010; 41B, pp. 420-429.

Crowe, C. T., Elger, D. F. and Roberson, J. A., Engineering fluid mechanics, 8th ed., 2005, Wiley, pp. 35-64.

Dhawan, N., Safarzadeh, M. S., Miller, J. D., Moats, M. S., Rajamani, R. K. and Lin C. L., Recent advances in the application of X-ray computed tomography in the analysis of heap leaching systems, Minerals Engineering, 2012, 35, pp. 75-86.

Duncanson, P. L. and Toth, J. D., The truths and myths of freeze lining technology for submerged arc furnaces, In Proceedings of the Tenth International Ferroalloys Congress; INFACON X, Cape Town, South Africa, 2004, pp. 488-499.

Dunkl, M., Corrosion tests - A very important investigation method for the selection of refractories for glass tanks, Glass Science and Technology: International Journal of the German Society of Glass Technology, 1994, 67(12), pp. 325-334.

Eksteen, J.J., A mechanistic model to predict matte temperatures during the smelting of UG2-rich blends of platinum group metal concentrates. Minerals Engineering, 2011, 24(7), pp. 676-687.

Eksteen, J.J., Van Beek, B. and Bezuidenhout, G.A., Cracking a hard nut: An overview of Lonmin's operations directed at smelting of UG2-rich concentrate blends. Journal of the Southern African Institute of Mining and Metallurgy, 2011, 111(10), pp. 681-690.

Eric, R. H., Slag Properties and Design Issues Pertinent to Matte Smelting Electric Furnaces. Journal of the Southern African Institute of Mining and Metallurgy; 2004, pp. 499-510.

Eustathopoulos, N., Nicholas, M.G. and Drevet, B., Wettability at high temperatures. Pergamon, Amsterdam, 1999, pp. 13-51, 349.

Eustathopoulos, N., Wetting by liquid metals—application in materials processing: The contribution of the Grenoble group. Metals, 2015, 5(1), pp. 350-370.

Fabrichnaya, O., Tomashyk, V. and Kozlov, A., Iron-Nickel-Sulfur, Iron Systems: Phase Diagrams, Crystallographic and Thermodynamic Data. Subvolume D `Iron Systems', of Landolt-Börnstein - Group IV. Physical Chemistry, 2009, 11, pp. 1-61.

Fleet, M. E. and MacRae, N. D., Sulfidation of Mg-rich olivine and the stability of niningerite in enstatite chondrites. Geochimica et Cosmochimica Acta, 1987; 51(6), pp. 1511-1521.

Fleet, M.E, 2006, Reviews in Mineralogy & Geochemistry, Vaughan, D.J., (Editor), 61, pp. 365-419.

Gabriel, A., Gustafson, P. and Ansara, I., A thermodynamic evaluation of the C-Fe-Ni system. CALPHAD, 1987, 11(2), pp. 203-218.

Glaister, B. J. and Mudd, G. M., The environmental costs of platinum–PGM mining and sustainability: Is the glass half-full or half-empty? Minerals Engineering, 2010, 23(5), pp. 438-450.

Goldstein, J. Newbury, D.E., Joy, D.C., Lyman, C.E., Echlin, P., Lifshin, E., Sawyer, L. and Michael, J.R., Scanning electron microscope and X-ray microanalysis, Springer, 2003, pp. 1/10-1/18, 3/75-3/96.

Habashi, F., Textbook of Pyrometallurgy, Métallurgie Extractive Québec, Canada, 2002, pp. 237-242.

Hamuyuni, J., Taskinen, P., Akdogan, G. and Bradshaw, S. M., Measurement of surface tension of molten matte phases by an improved sessile drop method. Mineral Processing and Extractive Metallurgy, 2012, 121(3), 173-177.

Hayes, P.C., 2003, Process Principles in Minerals & Materials Production. 3rd Edition. Hayes Publishing CO, Australia.

Hayes P.C., Aspects of SAF smelting of ferrochrome, Tenth International Ferroalloys Congress INFACON X, transformation through technology, Cape Town, South Africa, 2004, pp. 1 - 14.

Herman, F. C. (editor), Principles of Metallurgy: An Introduction to the Metallurgy of the Metals. 1910. Reprint. London: Forgotten Books, 2013, pp. 244.

Holler, M., Diaz, A., Guizar-Sicairos, M., Karvinen, P., Färm, E., Härkönen, E., Ritala, M., Menzel, A., Raabe, J. and Bunk, O., X-ray ptychographic computed tomography at 16 nm isotropic 3D resolution, Scientific Reports, 4, 2014, 3857, pp. 1-5.

Hou, X. and Jones, B. T., Inductively Coupled Plasma Optical Emission Spectrometry. Encyclopedia of Analytical Chemistry, 2000, pp. 9468-9485.

Hundermark, R. J., Mncwango, S. B., de Villiers, L. P. vS. and Nelson, L. R., The smelting operations of Anglo American's platinum business: an update, Southern African Pyrometallurgy 2011, Southern African Institute of Mining and Metallurgy, Johannesburg, 6-9 March 2011, pp. 295-307.

Ip, S. W. and Toguri, J. M., Entrainment behaviour of copper and copper matte in copper smelting operations. Metallurgical transactions B, 1992, 23B, pp. 303-311.

Jansson, S., Brabie, V. and Bohlin, L., Corrosion mechanism and kinetic behaviour of refractory materials in contact with CaO-Al_2O_3-MgO-SiO_2 slags. VII International Conference on Molten Slags, Fluxes and Salts. The Southern African Institute of Mining and Metallurgy, 2004, pp. 341-347.

Jewell, S. and Kimball, S. M., Mineral commodity summaries 2015, U.S. Geological survey, Reston, Virginia, 2015, pp. 120-121.

Jones, R. T. and Geldenhuys, I. J., The pros and cons of reductive matte smelting for PGMs. Minerals Engineering, 2011, 24(6), pp. 495-498.

Jones, R. T., Platinum smelting in South Africa. South African Journal of Science, 1999, 95, pp. 525-534.

Jones, R.T., An overview of Southern African PGM Smelting, Nickel and Cobalt 2005: Challenges in Extraction and Production. 44th Annual Conference of Metallurgists, Calgary, Alberta, Canada, 21-24 August 2005, pp. 147-178.

Jorgensen, F. R. A., Vaporization during combustion of a complex copper concentrate. Proceedings-Australasian Institute of Mining and Metallurgy, 1985, 290(1), pp. 91-98.

Karwowski, L., Kryza, R. and Przylibski, T.A., New chemical and physical data on keilite from the Zakłodzie enstatite achondrite. American mineralogist, 2007, 92, pp. 204-209.

Ketcham, R. A. and Carlson, W. D., Acquisition, Optimization and Interpretation of X-Ray Computed Tomographic Imagery: Applications to the Geosciences, Computers and Geosciences; 2001, 27(4), pp. 381-400.

King, S. G., Electric Smelting Furnaces in Southern Africa. Proceedings of INFACON 74, 1975, pp. 135-142.

Kitakaze, A., Sugaki, A., Itoh, H. and Komatsu, R., A revision of phase relations in the system Fe–Ni–S from 650 °C to 450 °C. The Canadian Mineralogist, 2011, 49(6), pp.1687-1710.

Körner, C., Arnold, M., and Singer, R. F., Metal foam stabilization by oxide network particles. Materials Science and Engineering A, 2005, 396(1), 28-40.

Koutsoyiannis, D., Clausius-Clapeyron equation and saturation vapour pressure: simple theory reconciled with practice. European Journal of physics, 2012, 33(2), pp. 295-305.

Kowalenko, C. G., Assessment of LECO CNS-2000 analyzer for simultaneously measuring total carbon, nitrogen, and sulfur in soil, Communications in Soil Science and Plant Analysis, 2001, 32(13-14), pp. 2065-2078.

Kwatara, M., Chromium deportment in copper matte equilibrated with CrxO-containing slag, (Doctoral dissertation, Stellenbosch: University of Stellenbosch), 2006.

Lee, W.E. and Zhang, S., Direct and indirect slag corrosion of oxide and oxide-c refractories. VII International Conference on Molten Slags Fluxes and Salts, The South African Institute of Mining and Metallurgy, 2004, pp. 309-320.

Lee, W.E. and Zhang, S., Melt corrosion of oxide-carbon refractories. International Materials Reviews, 1999, 44(3), pp. 77-104.

Lehner, S.W, Petaev, M.I, Zolotov, M.Yu. and Buseck, P.R., Formation of niningerite by silicate sulfidation in EH3 enstatite Chondrites. Geochimica et Cosmochimica Acta, 2013, 101, pp. 34-56.

Liddell, K. S. and Adams, M. D., Kell hydrometallurgical process for extraction of platinum group metals and base metals from flotation concentrates. Journal of the Southern African Institute of Mining and Metallurgy, 2012, 112(1), pp. 31-36.

Liddell, K. S., McRae, L. B. and Dunne, R. C., Process routes for beneficiation of noble metals from Merensky and UG-2 ores. Mintek Review 4, 1986, pp. 33-44.

Loubser, M. and Verryn, S., Combining XRF and XRD analyses and sample preparation to solve mineralogical problems. South African Journal of Geology, 2008, 111, pp. 229-238.

Luz, A.P. Ribeiro, S. and Pandolfelli, V. C., Review article: Use of the wettability in the investigation of the corrosion behaviour of the refractory materials, Ceramica, 2008, 54, pp. 174-183.

Matousek, J. W., Oxidation Potentials in Matte Smelting of Copper and Nickel, Journal of Metal, 2014, 66(9), pp. 1670 – 1676.

McDougall, I. and Eksteen, J.J., Sidewall design to improve lining life in a platinum smelting furnace. International Smelting Technology Symposium (Incorporating the 6th advances in Sulfide Smelting Symposium), The Minerals, Metals and Materials Society, 2012, pp. 47-54.

McLennan, A. R., Bryant, G. W., Bailey, C. W., Stanmore, B. R. and Wall, T. F., Index for iron-based slagging for pulverized coal firing in oxidizing and reducing conditions, Energy and fuels, 2000, 14, pp. 349-354.

Merry, J., Sarvinis, J. and Voermann, N., Designing modern furnace cooling systems. Journal of the Minerals, Metals and Materials Society, 2000, 52(2), pp. 62-64.

Miller, P. D., Lee, J. G. and Cutler, I. B., The reduction of silica with carbon and silicon carbide. Journal of the American Ceramic Society, 1979, 62(3-4), pp. 147-149.

Mills, K., The Estimation of Slag Properties, Southern African Pyrometallurgy, S-5, 2011.

Mudd, G.M., Sustainability reporting and the platinum group metals: A global mining industry leader? Platinum metals review, 2012, 56(1), pp. 2-19.

Muller, J. and Erwee, M. Blast furnace control using slag viscosities and liquidus temperatures with phase equilibria calculations. Southern African Pyrometallurgy, 2011, 6(9), 309-326.

Nell, J. Melting of platinum group metal concentrates in South Africa. Journal of the South African Institute of Mining and Metallurgy, 2004, 104(7), pp. 423-428.

Nitta, M. Nakamura, H. and Ishi, A., Development of carbon blocks for blast furnace hearths,

Nippon Steel Technical report no. 98, (July 2008), pp. 49-54.

Nizhenko, V.I. and Floka, L.I., Contact reaction of graphite with liquid iron and iron base melts, Poroshkovaya Metallurgiya, 1974, 6(138), pp. 64-71.

Pierson, H.O., Handbook of Carbon, Graphite, Diamond and Fullerenes, Properties, Processing and Application. Noyes Publications, 1993, pp. 87-110.

Raask, E., Mineral impurities in coal combustion behaviour, problems, and remedial measures, ed. Dugger E., Brienza, B., and Robey, R., Taylor &Francis, 1985, pp. 158.

Raghavan, V., Fe-Ni-S (Iron-nickel-sulfide). Journal of phase Equilibria and Diffusion, 2004, 25(4), pp. 373-381.

Rigaud, M., Corrosion of refractories and ceramics in: R.W. Revie (Ed.), Uhlig's Corrosion Handbook (3rd ed.), Canada, John Wiley & Sons, 2011, 51, pp. 387-398.

Sarkar, R., Refractory technology fundamentals and applications, CRC press, New York, 2017, pp. 41-42.

Schiepers, R.C.J., Van Beek, J.A., Van Loo, F.J.J. and De With, G., The interaction between SiC and Ni, Fe, (Fe,Ni) and steel: morphology and kinetics. Journal of European Ceramic Society, 1993; 11, pp. 211-218.

Shen, P., Fujii, H. and Nogi, K., Wettability of some refractory materials by molten SiO_2-MnO-TiO_2-FeO_x slag. Materials Chemistry and Physics, 2009, 114(2), pp. 681-686.

Shimizu, M., Yoshida, H. and Mandarino, J.A., The new mineral species keilite (Fe,Mg)S, the iron-dominant analogue of niningerite. The Canadian Mineralogist, 2002, 40, pp. 1687-1692.

Siddiqi, N., Bhoi, B., Paramguru, R.K., Sahajwalla, V. and Ostrovski, O., Slag-graphite wettability and reaction kinetics Part 1, Kinetics and mechanism of molten FeO reduction reaction. Ironmaking and Steelmaking, 2000, 27(5), pp. 367-372.

Silva, S.N., Baldo, J.B., Longo, E. and Varela, J.A., Wear mechanism for blast furnace hearth refractory lining. Ironmaking and Steelmaking, 2005, 32(6), pp. 459-467.

Sinyakova, E.F and Kosyakov, V.I., 600 °C section of the Fe-FeS-NiS-Ni phase diagram. Inorganic Materials, 2001, 37(11), pp. 1130-1137.

Skinner, B.J. and Luce, F. D., Solid solutions of the type (Ca, Mg, Mn, Fe)S and their use as geothermometers for the enstatite chondrites. The American Mineralogist, 1971, 56, pp. 1269-1296.

Snyders, C., Eksteen, J. and Moshokwa, A., The Polokwane smelter matte tapping channel model. In Fifth International Conference on CFD in the Process Industries, 2006, pp. 3-6.

Starykh, R.V. and Sineva, S. I., Study of the liquidus and solidus surfaces of the quaternary Fe-Ni-Cu-S system: V. Refinement and addition of the data on the ternary Fe-Ni-S and Fe-Ni-Cu phase diagrams. Russian Metallurgy, 2012, 3, pp. 189-194.

Sundström, A. W., Eksteen, J. J. and Georgalli, G. A., A Review of the physical properties of base metal mattes, The Southern African Institute of Mining and Metallurgy, 2008, 108, pp. 431-448.

Tesfaye, F. and Taskinen, P., Densities of molten and solid alloys of (Fe, Cu, Ni, Co)-S at elevated temperatures-Literature Review and Analysis, 2010.

Thethwayo, B. M., Sulphidation of copper coolers in PGM smelters, MSc Thesis, University of Pretoria, South Africa, (2010).

Tomala, J. and Baista, S., Micropore carbon furnace lining. INFACON XI, 2007; pp. 722-727.

Tsymbulov, L. B. and Tsemekhman, L. S. H., Solubility of carbon in sulfide melts of the system Fe-Ni-S. Russian Journal of Applied Chemistry, 2001, 74(6), pp. 925-929.

Vaughan, D.J. and Craig, J.R.: Mineral Chemistry of Metal Sulfides, Cambridge University Press, 1978, pp. 278-294.

Vollmann, S. and Harmuth, H. (2013). Marangoni Convection as a Contribution to Refractory Corrosion-CFD Simulation and Analytical Approaches. In Proceedings of the Unified International Technical Conference on Refractories (UNITECR 2013) John Wiley & Sons, Inc. pp. 857-862.

Weisberg, M. K. and Prinz, M., Sahara 97096: a highly primitive EH3 chondrite with layered sulfide-metal-rich chondrules. Earth and planetary sciences, 29th Lunar and Planetary Science Conference, 1998, pp. 1741-1742.

Westcott, G., Tacke, M., Schoeman, N. and Morgan, N., Impala Platinum Smelter, Rustenburg-an integrated smelter off-gas treatment solution. Journal of Southern African institute of mining and metallurgy, 2007, 107(5), pp. 281-287.

Willis, G. M. and Toguri, J. M., Yazawa's diagram, The AusIMM Metallurgical Society Special Paper, September 2009, pp. 1 - 8.

Wu, C. and Sahajwalla, V., Dissolution rates of coals and graphite in Fe-C-S melts in direct ironmaking: Influence of melt carbon and sulfur on carbon dissolution. Metallurgical and Materials Transactions 2000, 31B, pp. 243-251.

Xiao, Z. and Laplante, A. R., Characterizing and recovering the platinum group minerals–A review. Minerals Engineering, 2004, 17(9), pp. 961-979.

Yan, L., Cao, Z., Xie, Y. and Qiao, Z., Surface tension calculation of the Ni_3S_2-FeS-Cu_2S mattes. Calphad, 2000, 24(4), pp. 449 - 463.

Yuan, Y. and Lee, T. R., Contact angle and wetting properties. In Surface Science Techniques, Springer Berlin Heidelberg. 2013, pp. 3-34.

Zhang, Z. Hastings, P., Von der Handt, A. and Hirshmann, M.M., Experimental determination of carbon solubility in Fe-Ni-S melts, Geochimica et Cosmochimica Acta, 2018, 225, pp. 66-79.

Articles from this work:

Thethwayo B. M. and Garbers-Craig A. M., Interaction of graphite with synthetic matte. The Southern African Institute of Mining and Metallurgy, 2012, pp. 261-274

Thethwayo B. M. and Garbers-Craig A. M., Wear of graphite and micropore carbon by synthetic PGM Matte. In Proceedings of the UNITECR2013, John Wiley & Sons, Inc. 2014; pp. 1067-1074

Thethwayo, B. M. and Cromarty, R. D., Compatibility of graphite with primary platinum group metals industrial matte, Materials Research Innovations, 2015, 19, S5, pp. 948- 952

Thethwayo, B. M. and Cromarty, R. D., Wettability of graphite by synthetic and industrial PGM-furnace matte, Cerâmica, 2015, 61(358), pp. 219-223

APPENDIX A: Analysis of a used graphite block

A graphite block used as a refractory in an industrial PGM smelter was analysed using SEM (BSE and EDS). The aim of analysing a used graphite block was to determine the prominent wear mechanism of graphite when it is exposed to a primary matte and slag in an industrial set-up. This graphite block was in operation for approximately 12 months. It was lined at the hot-face of the upper sidewall of a PGM smelter (in contact with the melt). A water-cooled copper waffle cooler was in contact with this graphite block, the copper waffle cooler served to extract the heat away from the graphite block.

The side view of the graphite block is shown in Figure A 1. The dimensions of the graphite block were ~160 mm thickness by ~100 mm width. The hot-face and cold-face are annotated as such in Figure A 1. It should be noted that prior to exposure the graphite block had no curvature, the end-walls were flat. The curvature observed at the hot-face edge was probably caused by the interaction between the graphite block and the matte and slag melt during exposure. A graphite rod was placed at the cold side of the block to minimise the movement of the block during thermal cycling, the graphite rod is annotated as such in Figure A 1.

Three areas of the block were analysed, the accretion at the hot-face, the accretion on the graphite rod and the infiltrate in the cold-face end-wall. Figure A 2 has the image of the graphite block as well as the BSE images of the analysed areas. The SEM analyses of each area are discussed below.

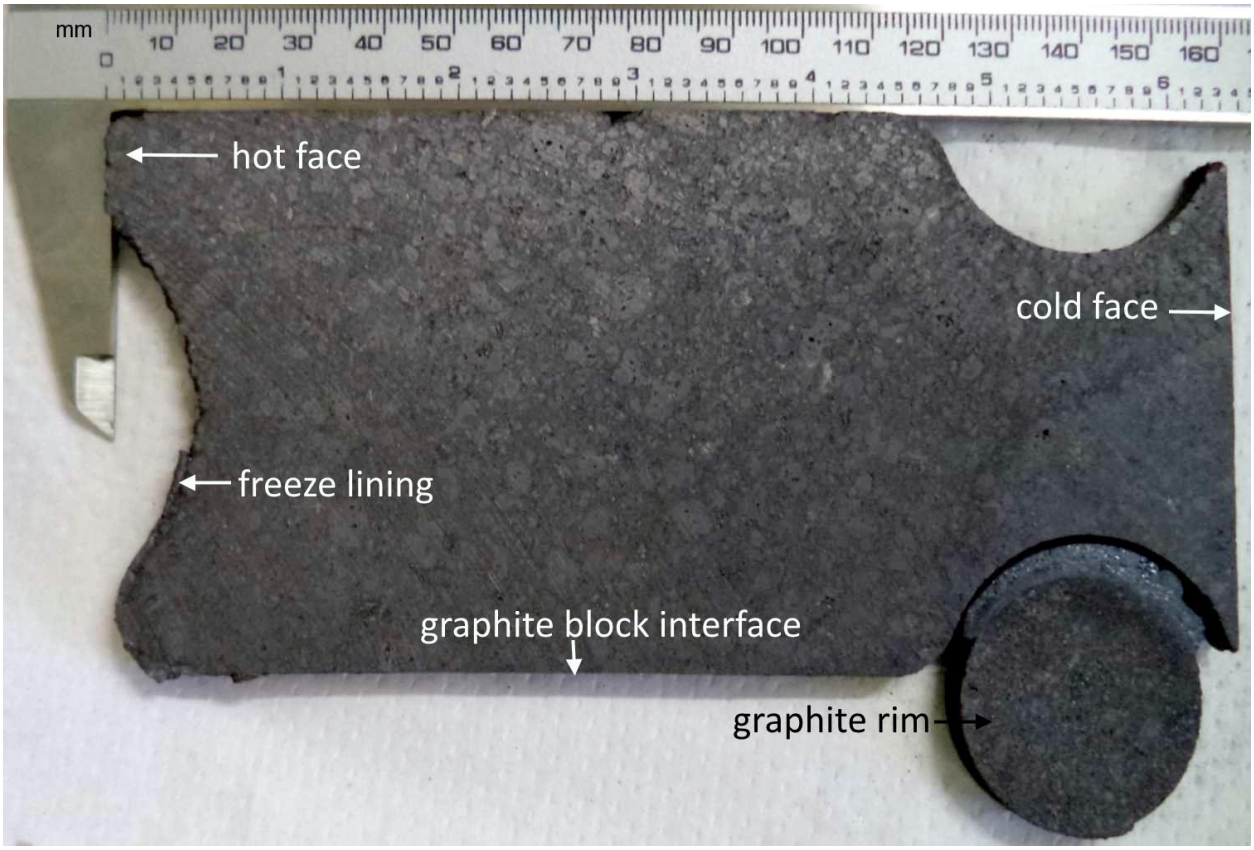

Figure A 1: Side view of a graphite block that was used in an industrial smelter for about 6 months

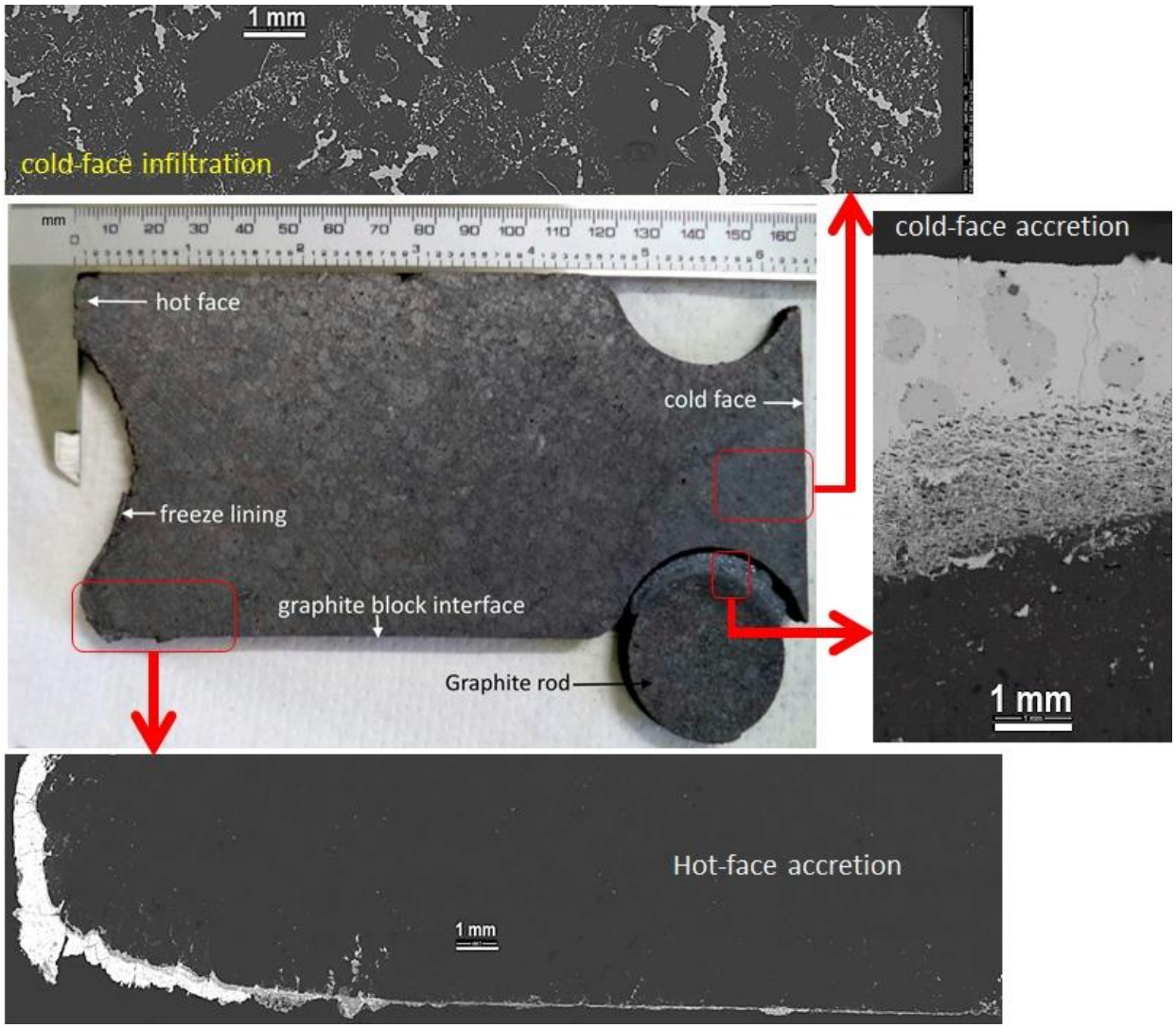

Figure A 2: Side view of the graphite block, BSE images of the analysed spots, highlighted areas are positions that were analysed

1. Hot-face accretion

An accretion was observed at the hot-face of the graphite block. This accretion was at the edge of the graphite block, it extended from the hot-face to the cold-face of the graphite block edges. The BSE image of the hot-face accretion and the EDS spectrum of the detected phases are shown in Figure A 3. The accretion on the graphite hot-face consisted of PbS and ZnCdS-Fe as major phases, Mg-Fe silicate was detected as a minor phase. The sulfides of Pb and Zn form minor phases in the PGM concentrate, these sulfides have high vapour pressure compared to other

metal sulfides. These sulfides vaporised and creeped through the spaces between the graphite blocks and reached the cold-face of the block. The graphite rod was lined at the edge of the cold-face as seen in Figure A 1 and Figure A 2. An accretion was observed around the graphite rod, the BSE image and EDS spectrum for this accretion are shown in Figure A 4.

2. Cold-face accretion (graphite rod sample)

Cu_2S and CuS were major phases in the accretion observed around the graphite rod, the EDS spectrum is shown in Figure A 4. The graphite rod was penetrated by these sulfides at the interface of the accretion and the graphite rod. The infiltrated area has a mixture of the sulfides (bright phases) and graphite (dark phases). This accretion could form as a product of copper waffle coolers reacting with the process gas. In the analyses of the industrial matte discussed in this work copper sulfide typically associated with iron, copper sulfide was not detected in its pure state, hence it is proposed that the formation of the accretion on the graphite rod was as a result of the interaction between the process gas and the copper waffle coolers.

3. Cold-face infiltrate

The graphite cold-face was penetrated by sulfides up to 40 mm depth, the BSE images and the EDS spectra are shown in Figure A 5. The infiltrate consisted of Cu_2S, CuS and other minor phases such as NiS, PbS and ZnCd-S. The presence of PbS and ZnCd-S indicates that the infiltrate is the condensed phases that evaporated from the furnace since these phases were also detected on the accretion observed at the hot-face. Nickel and cobalt are the constituents of the matte, their presence on the cod-face of graphite indicate that the infiltrate originated from the melt. Cu_2S and CuS are constituents of the matte however these phases could form as a result of reactions between the copper waffle coolers and the process gas such as sulfur.

The penetration of melt through the graphite hot-face was limited to ~1 mm, however at the cold-face the penetration depth was up to ~40 mm. There are two probable mechanisms that could lead to a contrast observed on the penetration pattern observed at the cold-face and at the hot-face of graphite.

4. Mechanism of melt penetration through graphite

The accretion on the graphite hot-face could serve as a physical barrier that inhibited the penetration of furnace contents through the graphite. At the cold-face however no accretion is observed except on the graphite rod. The absence of the accretion on the surface of the graphite cold-face could allow gases or furnace melt constituents to find a path to penetrate through graphite. It is proposed that the melt constituents escaped the furnace at high temperatures (in a gaseous form), the gases penetrated through the gaps between the graphite blocks, the gases condensed when they reach the graphite cold-face. At equilibrium the temperature of the graphite cold-face is the same as the temperature of the copper waffle cooler, which is estimated to be ~40 mm [Thethwayo 2010]. Since some of the phases (NiS, PbS and ZnCdS) detected at the graphite cold-face were also detected at the hot-face, it is plausible that these phases escaped the furnace and got deposited at the cooler surface (cold-face).

It is alleged that the operating pressure inside the furnace played a role in enhancing the infiltration of sulfides from the cold-face towards the hot-face. If for instance the furnace is operating at a negative pressure, the contents from the cold-face can be sucked back towards the hot-face of the refractory wall.

5. Final remarks

It is evident that furnace contents do creep through spaces between graphite blocks to reach the cold-face of the graphite block. Therefore the vertical and horizontal spaces between the graphite blocks have to be sealed to prevent the deposition of furnace melt on the cold-face of the graphite blocks.

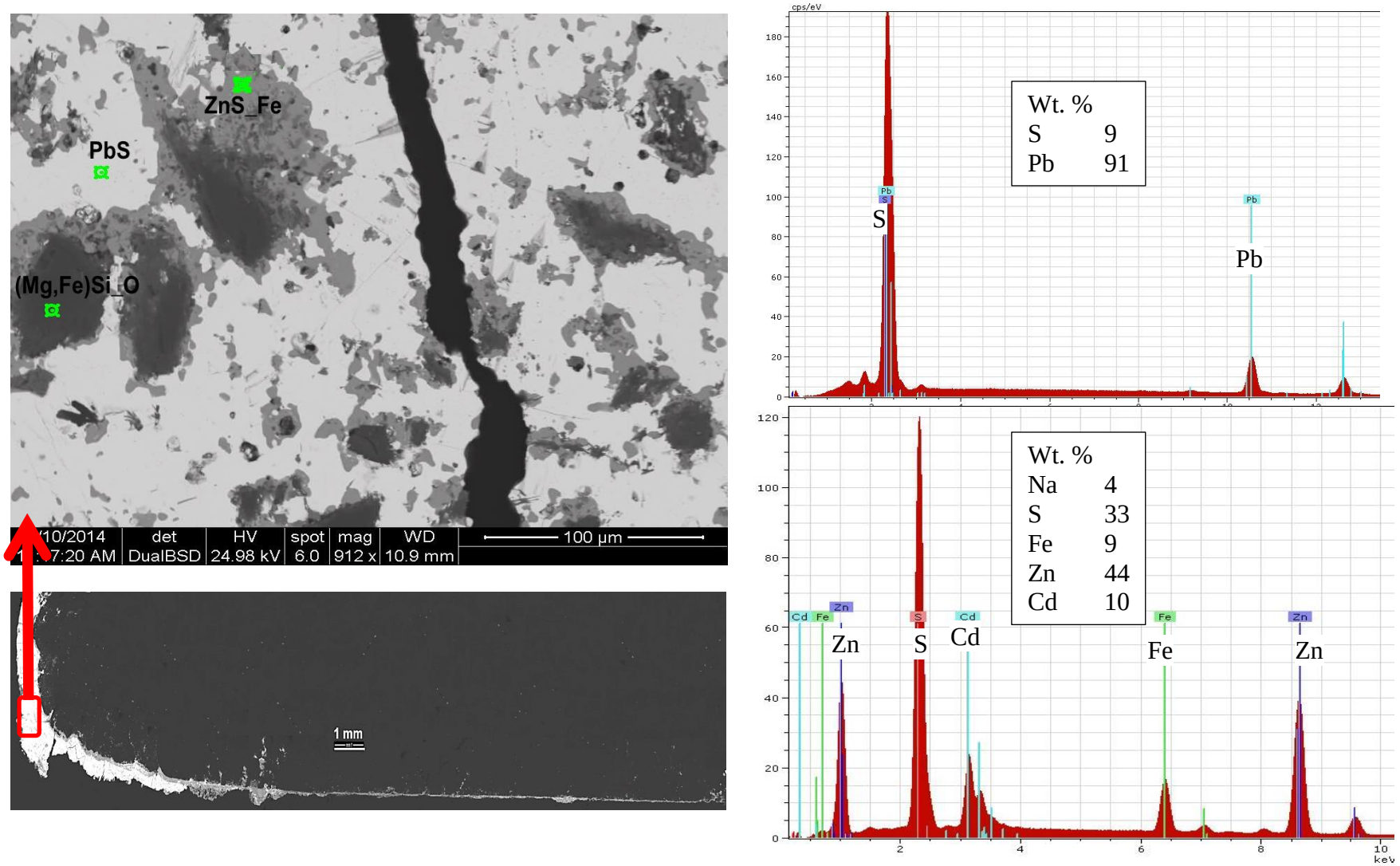

Figure A 3: BSE images of the hot-face accretion of the graphite block and the EDS spectra of some identified phases; PbS and ZnCdS-Fe

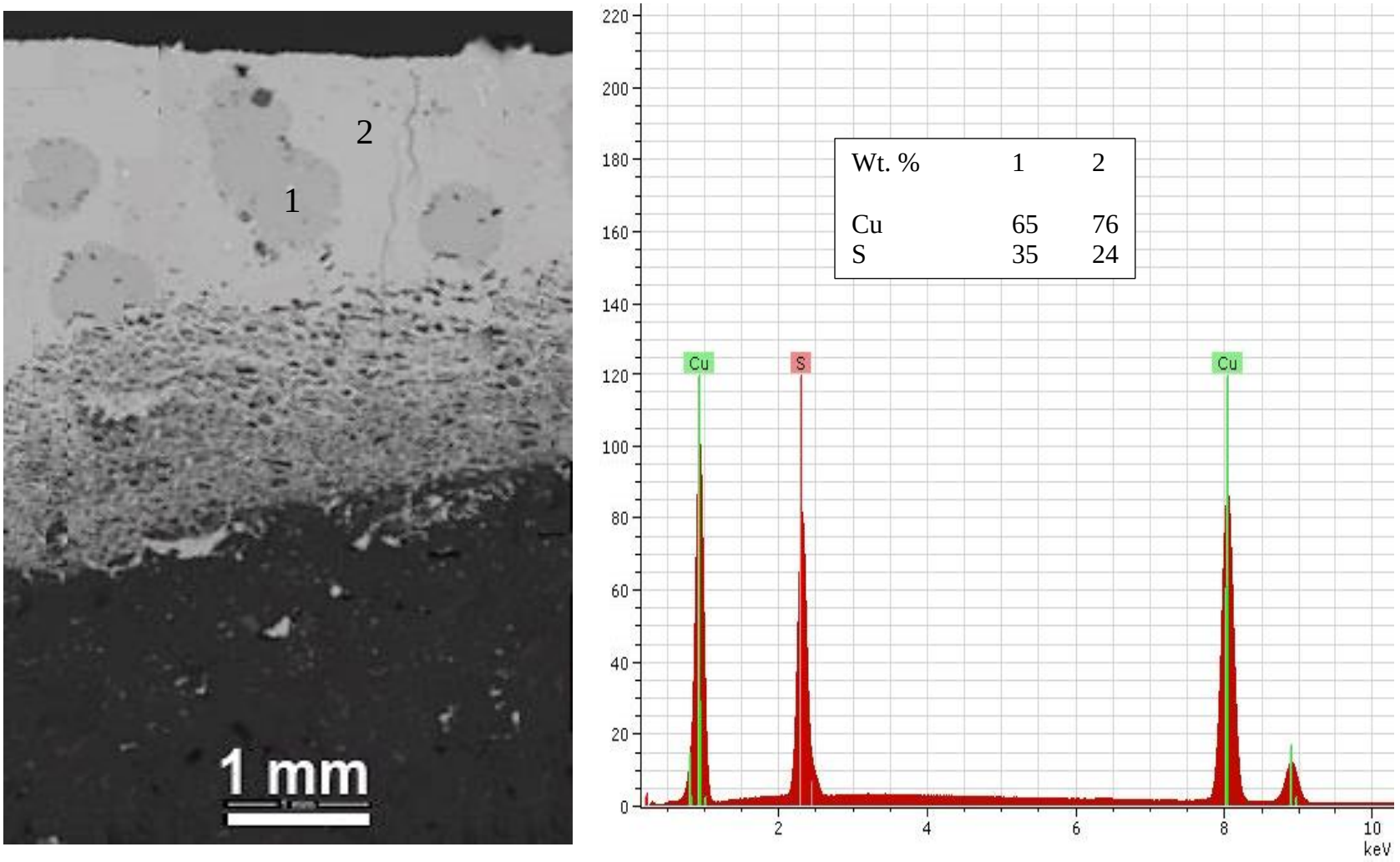

Figure A 4: BSE image of the cold-face accretion on the graphite rod cold-face and EDS spectrum for detected phases; Cu_xS (x=1 or 2)

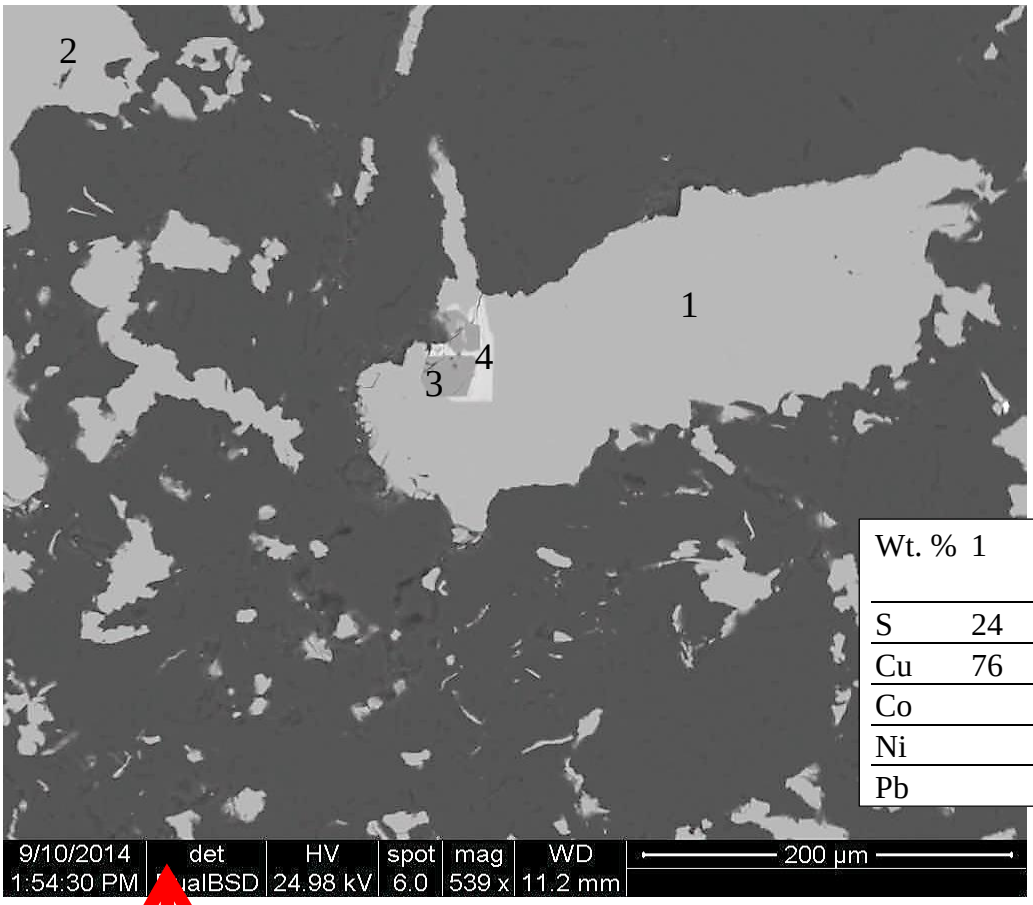

Wt. %	1	2	3	4
S	24	35	54	10
Cu	76	65	6	6
Co			1	2
Ni			39	
Pb				82

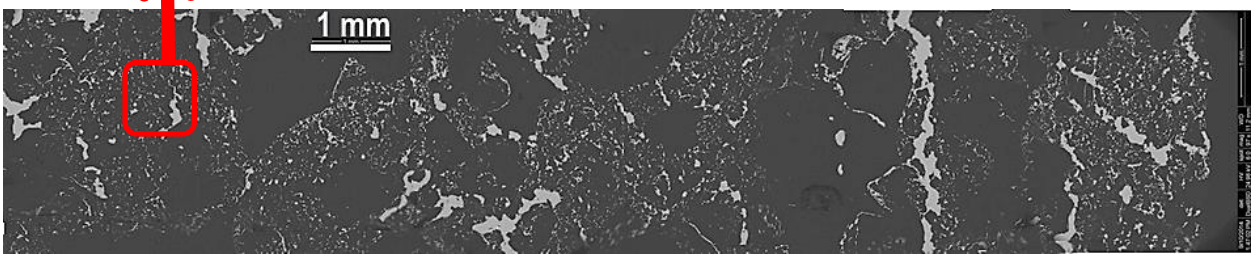

Figure A 5: BSE images of the cold-face infiltrate and the EDS analysis of the identified phases in the infiltrate

APPENDIX B: Synthesis of iron copper aluminium sulfide (CuFe-Al)S

An aluminium-containing sulfide (Cu, Fe, Al)S was detected in the matte residue after matte was exposed to graphite as well as micropore carbon. This sulfide had more than 6 mass percent of aluminium. The existence of this compound has not been reported in the open literature, as such experiments we carried out in the current work to reproduce this compound. Two attempts were made to reproduce this sulfide; aluminium oxide and Matte-S were reacted at 1350 °C, the aluminium metal was reacted with pure sulfides (Cu_2S and FeS) at 1550 °C. The results of the experiments are discussed below.

1. Alumina reaction with Matte-S at 1350 °C

To study the formation of (Cu, Fe, Al)S, Matte-S was exposed to Al_2O_3 at 1350 °C. Al_2O_3 was used as a source of aluminium since Al_2O_3 in its silicate form is a constituent of a PGM slag. Al_2O_3 was also one of the matrix materials of the MPC refractory. Matte-S was used as a source of a sulfide.

The mass fractions of the reactants were 80 percent Matte-S and 20 mass percent aluminium. Matte-S and Al_2O_3 powders were mixed and pressed into a pellet. The pellet was placed on a graphite surface, the graphite served as a reductant. The specimen was placed inside the muffle furnace and heated to 1350 °C. The residual droplet was analysed using SEM; BSE image is shown in Figure B 1. The composition of the phases detected by EPMA is summarized in Table B 1. The reaction between the iron sulfide and alumina was apparent. The alumina reacted at the periphery in contact with the sulfide, it formed Al-Fe-O compound. The core of the Al_2O_3 remained unreacted but the Al-Fe-O phase formed around it. These phase are annotated in Figure B 1. The analysis for the remainder of the sulfides were not included since their composition did not change during the exposure.

Aluminium sulfide was not detected in the residue, therefore this experiment was unsuccessful. It seemed that the experimental conditions were not conducive for the formation of (Cu, Fe, Al)S compound. The operating temperature probably limited the completion of the reaction between the alumina and the matte. Since the first experiment was a trial, the second experiment was conducted but conditions and the reactants were changed. The operating temperature was raised

to 1500 °C; Matte-S was replaced by pure powders of FeS and Cu_2S; Al_2O_3 was not changed; the powders were not made to a pellet; a graphite crucible was used to contain the reactants. These changes were done to enhance the reactions between the sulfides and the aluminium oxide.

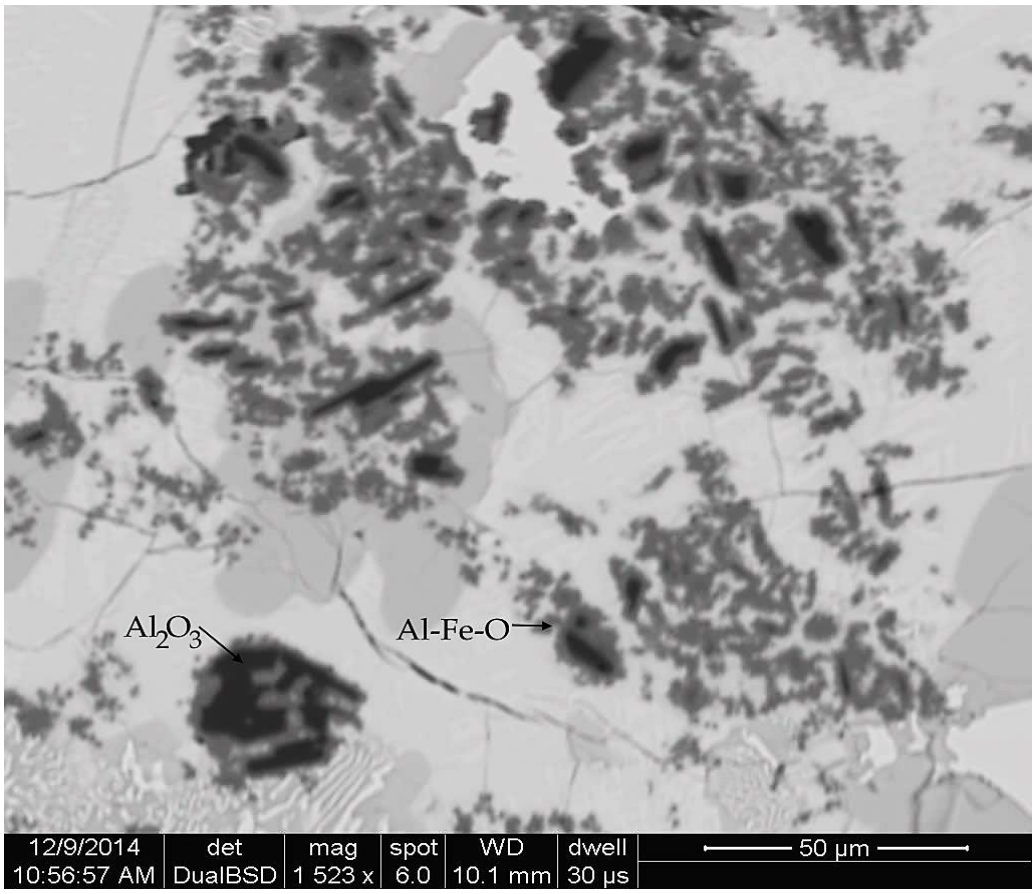

Figure B 1: Matte-S_Al_2O_3 after exposure to graphite at 1350 °C

Table B 1: EPMA analysis of the Matte-S_Al_2O_3 residue reacted at 1350 °C (mass percent)

Mass %	**Al_2O_3**	**Al-Fe-O**	**Al-Fe-O**	**FeS**	**Cu_5FeS_4**
Al	53.0	32.0	32.7	-	-
O	42.3	25.2	35.6	-	-
Fe	3.7	37.3	29.8	59.6	10.1
Cu	1.1	4.0	2.0	2.9	65.5
S	-	1.4	-	37.5	24.4

2. Aluminium reactions with pure sulfides at 1500 °C

Pure sulfides (Cu_2S and FeS) were reacted with aluminium oxide at 1500 °C to produce the (Cu, Fe, Al)S compound. The mass fraction of the starting mixture had 50 percent FeS, 40 percent Cu_2S and 10 percent Al_2O_3. This mixture was loaded into a graphite crucible and heated to 1500 °C in a muffle furnace. After exposure the residue was analysed using an EPMA, the BSE image is shown in Figure B 2. Three major phases detected in the specimen are annotated as 1, 2 and 3 in Figure B 2, their corresponding elemental compositions are in Table B 2. The analysis of some phases were not reported since these phases were residues of the starting materials.

A copper iron sulfide with up to 7.4 mass percent Al was detected in the residue (annotated 1 in Figure B 2 and Table B 2). Therefore the production of (Cu, Fe, Al)S was successful at 1500 °C, when Cu_2S and FeS were reacted with aluminium oxide in reducing conditions. Copper iron sulfide and iron sulfide (phases 2 and 3) are residual sulfide phases.

A copper iron sulfide phase can dissolve up to 7 mass percent Al in its structure and form a stable phase, this statement is based on the detection of this compound when Cu_2S, FeS and Al_2O_3 are reacted at 1500 °C in reducing conditions. It is beyond the scope of this work to characterize this sulfide phase (determine XRD pattern, and other properties). For future work it is recommended that this phase be synthesized in a more controlled atmosphere to be able to characterize it.

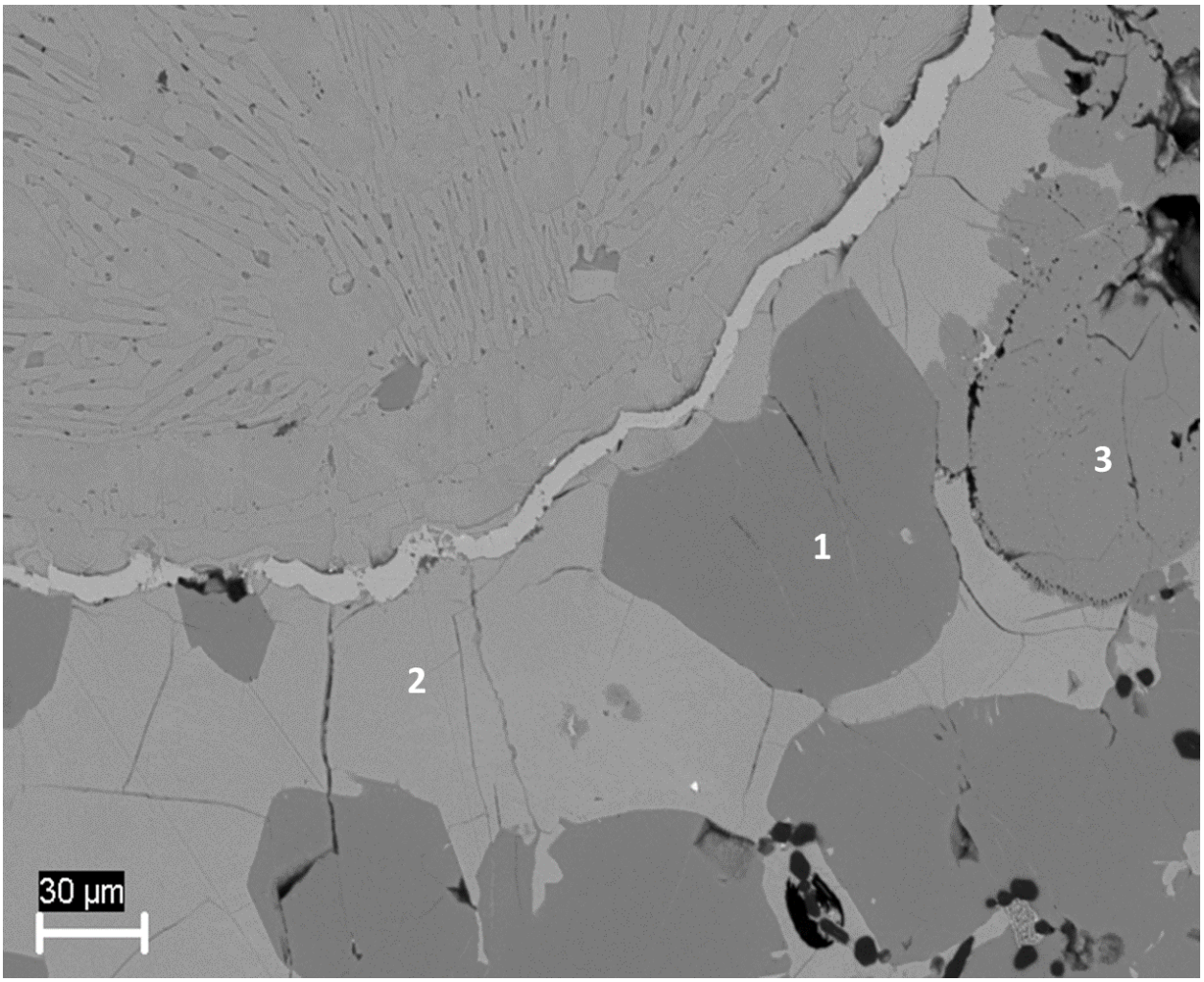

Figure B 2: BSE image of the copper iron sulfide-alumina specimen after exposure to graphite to 1500 °C

Table B 2: EPMA analysis of the copper-iron sulfide reacted with aluminium oxide at 1500 °C in the presence of graphite (mass percent)

Phase	Al	S	Fe	Cu
1	7.4	35.7	32.3	24.6
2	-	25.4	15.3	59.3
3	-	34.0	60.8	5.2

APPENDIX C: Penetration of industrial matte through graphite _ CAF tests

Penetration of a liquid industrial matte was observed during the exposure of industrial matte to SG graphite. CAF tests were conducted to confirm the matte penetration route and the temperature at which the penetration occurred. Experiments were performed in a CAF furnace, the CAF furnace was fitted with a camera to enable visual observation inside the furnace during the operation. Graphite crucibles were filled with industrial matte, the crucibles were closed with the graphite lid; carbon paste was applied between the crucible and the lid. The specimen was heated to 1060 °C at a rate of 5 °C per minute. There was no holding temperature the specimen was heated to 1060 °C and then cooled to 400 °C. To control the operating atmosphere, argon gas was purged through the furnace during operation and cooling of the furnace.

The furnace camera captured images of the specimen every 1 minute from 890 °C to 1060 °C. These images are used to describe the penetration trend of industrial matte. In Figure C 1 the setup of the specimen is shown, each component of the setup is annotated including the sampling time and operating temperature.

At 890 °C (Figure C 1; time 17:49) penetration of liquid matte is not observed. At 900 °C (Figure C 1; time 17:51) initial drops of matte are observed through the lid of crucible 2, matte droplets are highlighted with circles. This observation confirms that matte start penetrating through the graphite crucible at 900 °C. The specimens at 920 °C and 940 °C are shown in Figure C 2. As the time progressed the size of the matte droplets enlarged (droplets circled in Figure C 2). The specimens at 950 °C and 960 °C are shown in Figure C 3.

Matte droplets started dripping from the sides of the crucible at 950 °C (Figure C 3; time 17:57, droplets highlighted with circles). Matte could be seen accumulating in the sample tray (Figure C 3; time 17:57). The specimens at 970 °C and 980 °C are shown in Figure C 4. Matte droplets continued dripping as the time progressed (Figure C 4). The specimens at 990 °C and 1000 °C are shown in Figure C 5.

At 990 °C (Figure C 5; time 18:03) matte stopped dripping. Between 990 °C and 1060 °C the matte droplets adhered to the graphite at the point of penetration. This indicated that gravity did not have significant effect on the dripping of matte. After cooling the matte droplets could still

be observed on the outer surface of the crucible as circled in Figure C 6. The specimen at 1060 °C is shown in Figure C 6.

Based on the images presented in this section it is evident that matte penetration path out of the graphite crucible is through the connected pores present in the crucible wall. Based on the residue of the matte droplets on the crucible wall, the matte penetration is caused by an internal pressure, when the pressure ceases there is no force pushing the matte out so the matte droplets remain on their position.

Head pressure and gravity does not seem to have influence on the penetration of matte, if this was the case, matte penetration would be more prevalent at the bottom parts of the crucible wall; and matte droplets could not be observed leaking through the lid.

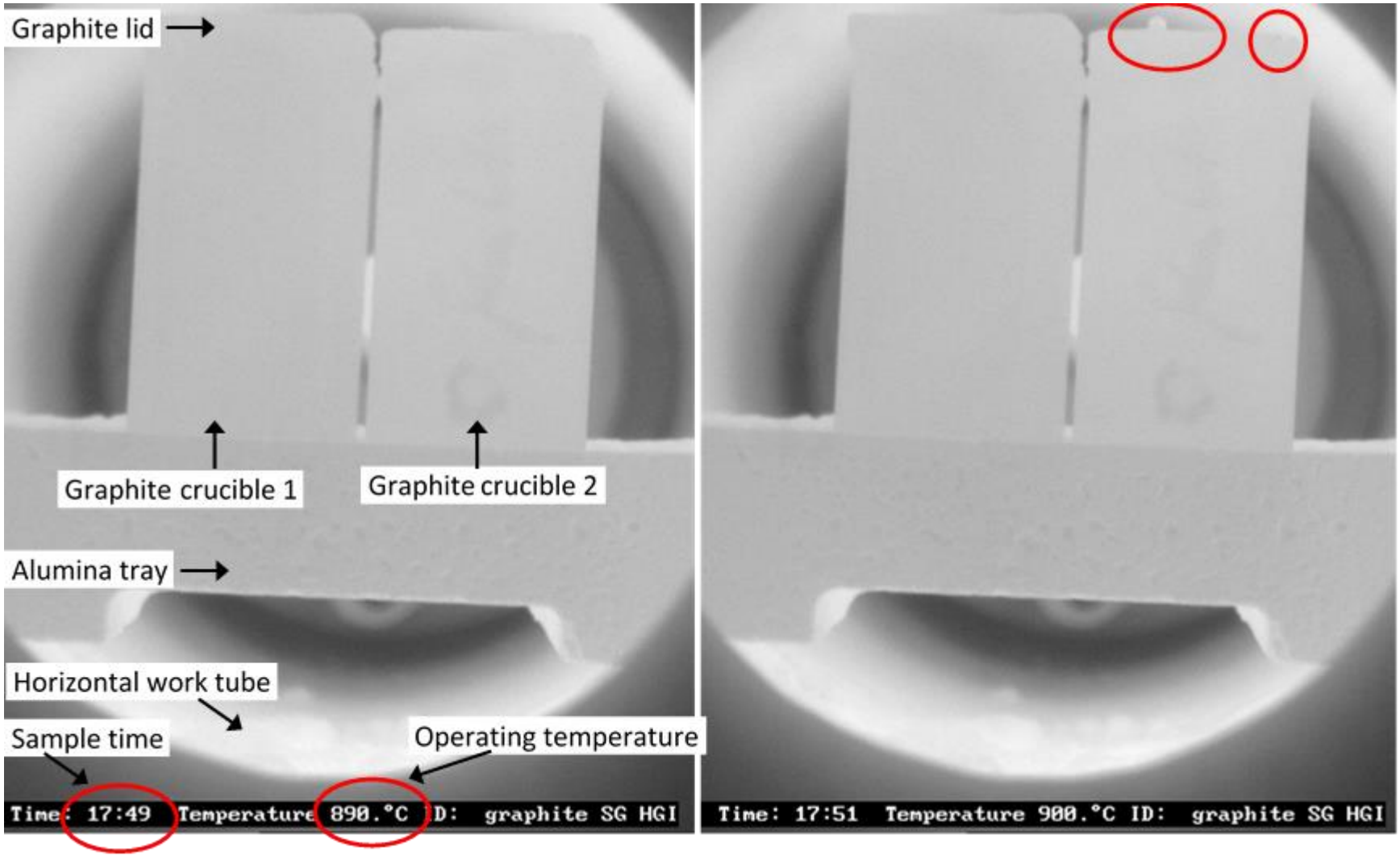

Figure C 1: CAF tests specimen at 890 °C and 900 °C, SG-graphite filled with industrial matte

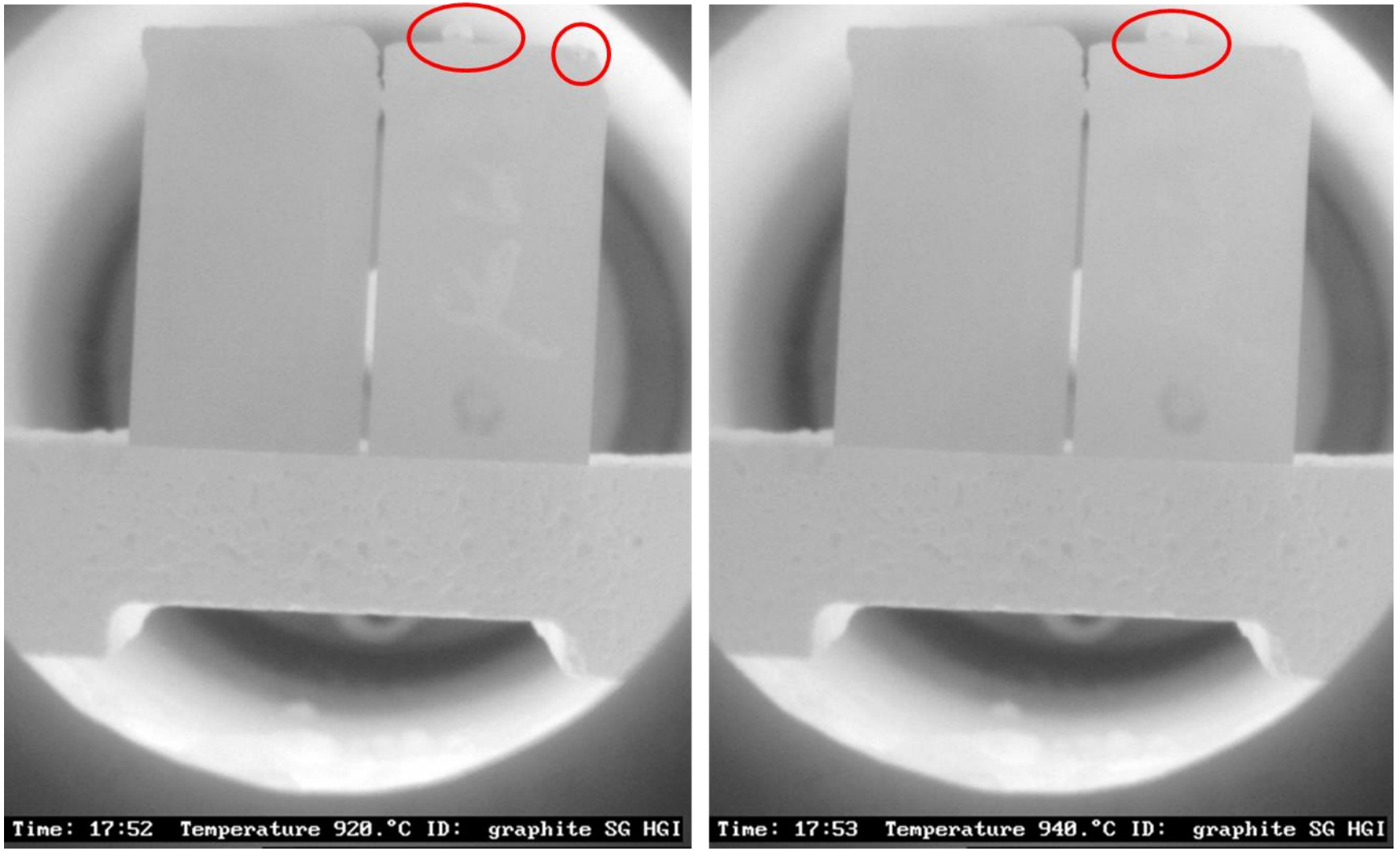

Figure C 2: CAF tests specimen at 920 °C and 940 °C, SG-graphite filled with industrial matte

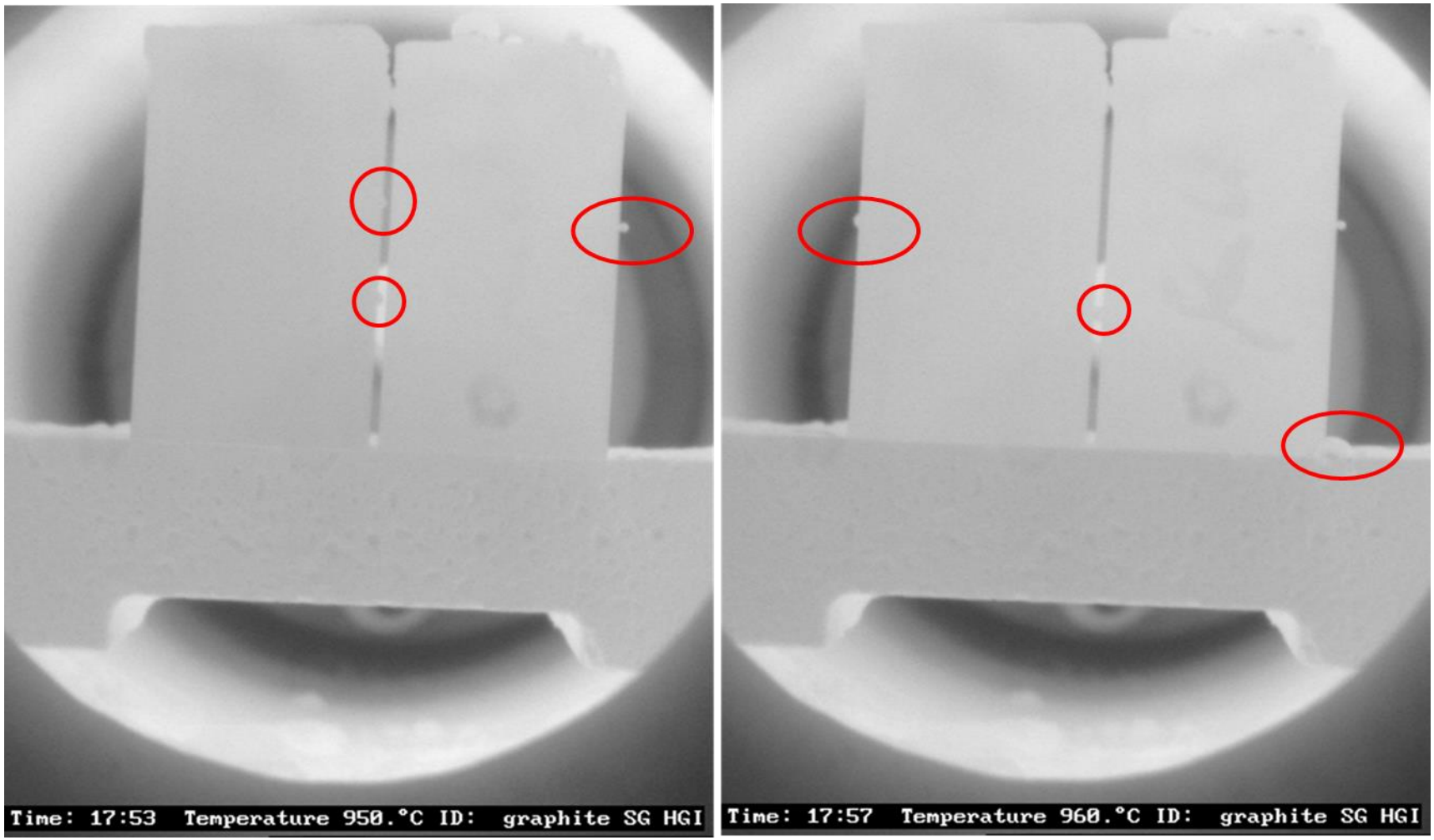

Figure C 3: CAF tests specimen at 950 °C and 960 °C, SG-graphite filled with industrial matte

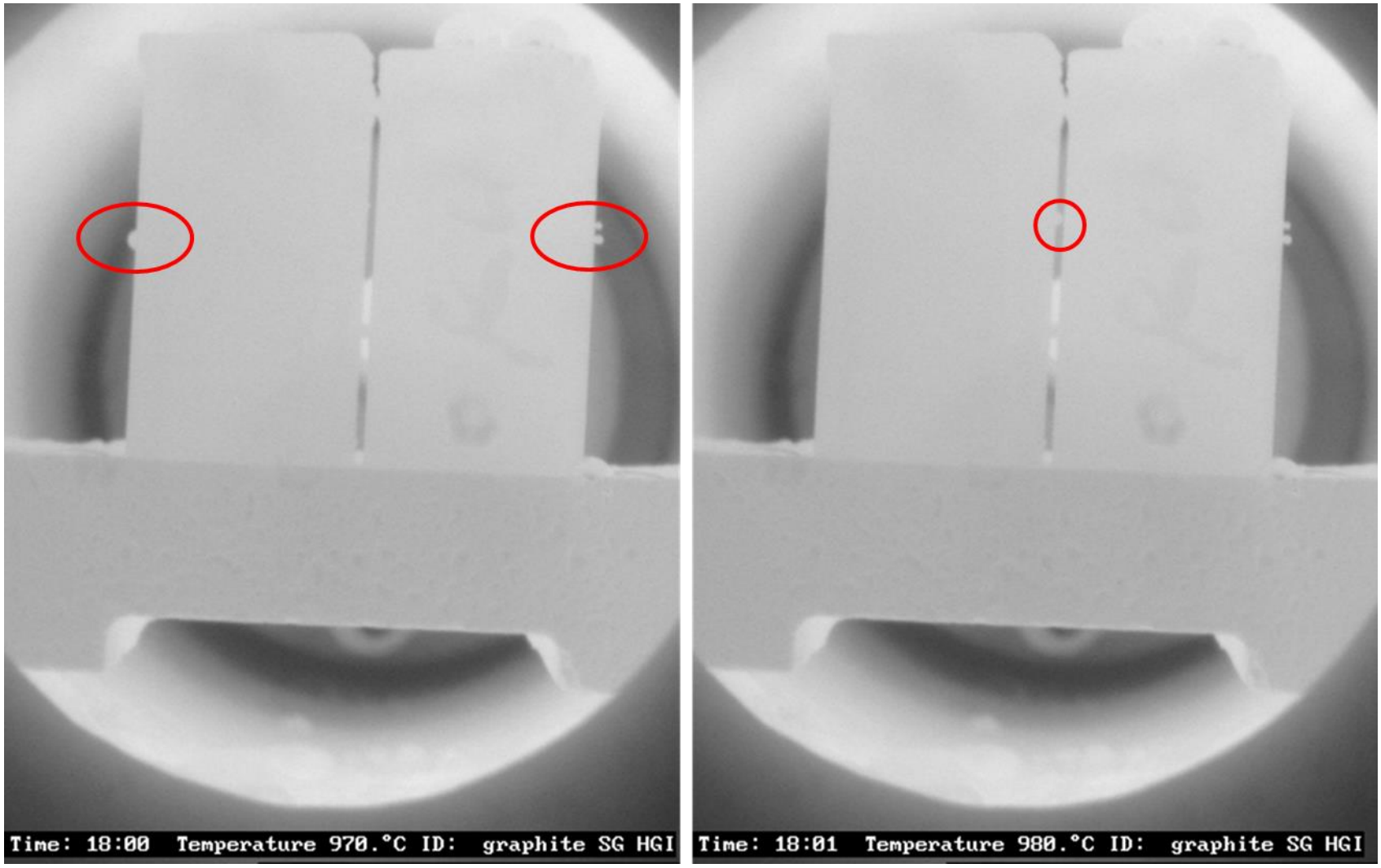

Figure C 4: CAF tests specimen at 970 °C and 980 °C, SG-graphite filled with industrial matte

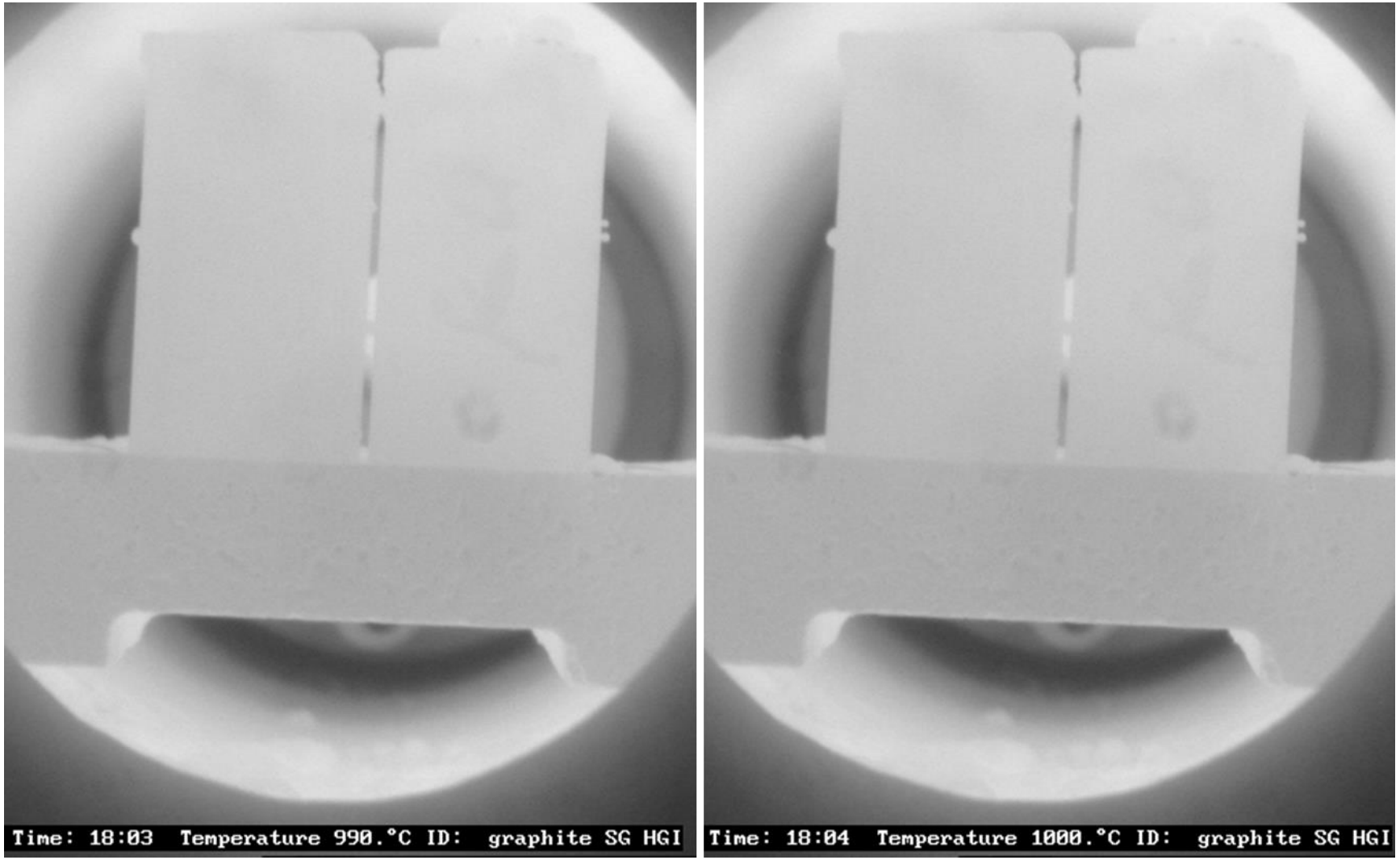

Figure C 5: CAF tests specimen at 990 °C and 1000 °C, SG-graphite filled with industrial matte

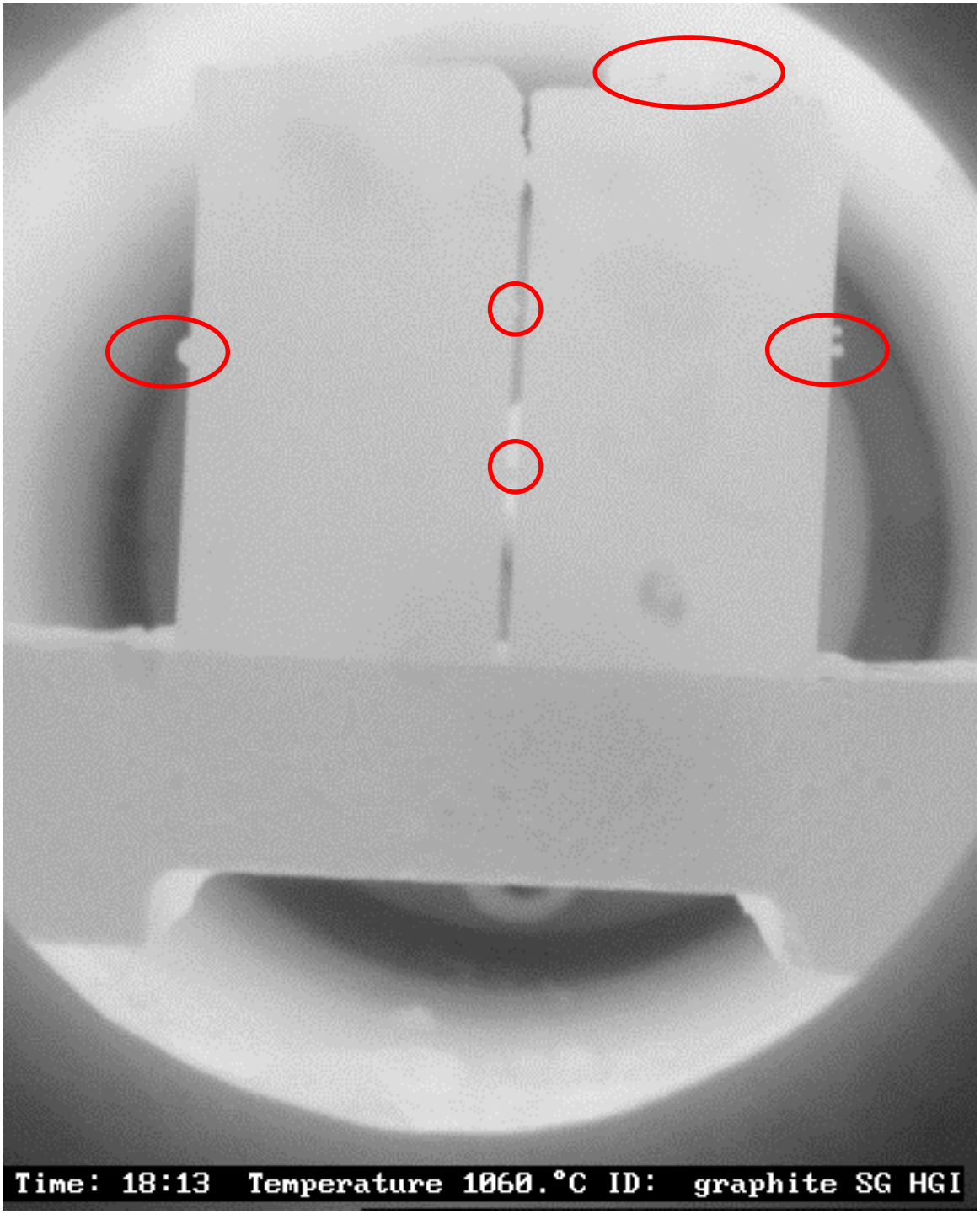

Figure C 6: CAF tests specimen at 1060 °C, SG-graphite filled with industrial matte